ISSN 0916-7501
CODEN : TTEREB

TOYOTA
Technical Review

2018/9 234

TNGA Powertrains

VOL.64

Cover design:

Reflecting the entry of outside companies into the world of vehicle development, the theme of the cover is the spirit to make new discoveries and take on new challenges by applying innovative techniques such as deep learning to systemize the accumulated knowledge of Toyota and the Toyota group in novel ways. This theme is expressed using the Japanese character “知” (pronounced “chi” or “shiru”), which means “wisdom.”

Contents

Preface

▷ Special Feature: TNGA Powertrains

▷ Technical Papers/Technical Articles

Preface

To Achieve an Ever-Better Mobility Society

T. Mizushima

Toshiyuki Mizushima,
former Senior Managing Officer

Looking back, 2017 represented a year that brought significant change to the structure of the automotive industry, with various countries and regions announcing a shift to electrified vehicles for the future and, more immediately, the rapid propagation of advanced driver assistance systems.

In fact, different companies and organizations, including corporations previously tied to different industries, have brought unconventional perspectives to the development of electrified and autonomous vehicles, and are increasingly making their presence felt.

In accordance with the "Know the enemy and know yourself: in a hundred battles you will never be in peril" principle outlined in Sun Tzu's Art of War, we must first know our competitors and where we stand before preparing a strategy. This means we must ascertain the facts with unclouded eyes.

This major turning point should be seen as an excellent opportunity for change, and I believe that we will have to create new value by, for example, utilizing deep learning to systematize the accumulated knowledge and technology continuously passed down by our predecessors.

At the same time, our vision of contributing to the global environment and bringing happiness to people remains unchanged.

In 2017, we celebrated the twentieth anniversary of the launch of the Prius hybrid vehicle, the forerunner of today's electrified vehicles. In those twenty years, we have installed electrification technologies in many models to help reduce CO_2 and produce cleaner emissions.

Nevertheless, to make a sustainable contribution to the global environment and society, simply enhancing vehicle performance will not be enough. We must also successfully popularize the vehicles and technology that we develop. Furthermore, I believe that this will require vehicles and technologies that local people perceive as the achievements of their own countries or regions.

Achieving this calls for planning and development rooted in individual regions. I believe that establishing plans based on local circumstances and technological standards, and then popularizing vehicles developed through the efforts of that region, will help to raise regional technological capabilities.

This must be performed in coordination with the energy policies and traffic environment of each region. What this means from an overall well-to-wheel standpoint (i.e., from energy production to its use for driving the wheels of a vehicle) is as follows: We want to popularize vehicles with enhanced performance from tank-to-wheel, while coordinating these efforts with initiatives such as the establishment of well-to-tank infrastructure that allows convenient charging or filling by users and of a recycling system for batteries and other parts.

Moving forward, let us strive to contribute to the global environment and bring happiness to people by making ever-better cars and realizing an ever-better mobility society.

TNGA Powertrains

Hirohisa Kishi[*1]

1. Introduction

The advent of mass ownership and rapid development of the automobile since the beginning of the twentieth century has been accompanied by increasing awareness of issues such as environmental damage, the depletion of natural resources, and global warming. Consequently, to help reduce CO_2 emissions and improve air quality, the automotive industry is urgently implementing countermeasures to introduce different energy sources and powertrains.

Reflecting this situation, several regions and companies have already announced a shift to various forms of vehicle electrification. This trend has also been complemented by growing recognition of automated driving technology as a key part of vehicle product appeal. Additionally, anticipating further diversification of customer preferences from vehicle ownership to use (such as through vehicle leasing or sharing), automakers are facing a once-in-a-century struggle for their very survival.

Powertrain development at Toyota Motor Corporation has conventionally focused on three fundamental approaches: the conservation of energy, promoting the diversification of fuels, and the development of cars that are both practical and environmentally friendly. **Fig. 1** shows Toyota's 2015 vision for how its powertrain mix might evolve up to 2050.

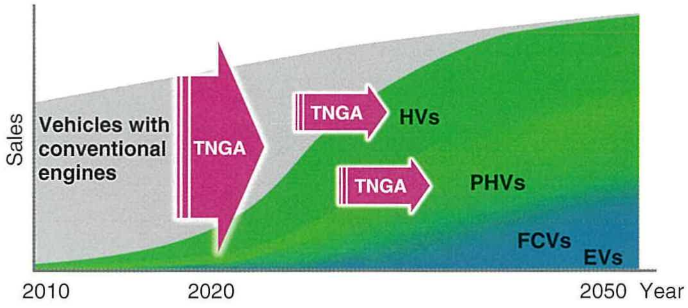

Fig. 1 Powertrain Mix

Currently, the vehicle market is dominated by conventional powertrains, in other words, vehicles powered only by gasoline or diesel engines. However, the market is standing on the brink of a major change, with electrified vehicles such as hybrid (HVs), plug-in hybrid (PHVs), electric (EVs), and fuel cell vehicles (FCVs) poised to take over. To successfully ride out this period of transformation, automakers must focus on enhancing the performance of conventional powertrains, while ensuring that powertrains under development can be utilized with the hybrid and plug-in hybrid systems of the future.

2. Contribution of Powertrains to the TNGA

The Toyota New Global Architecture (TNGA) is Toyota's latest design philosophy, and was formulated with the objective of building ever-better cars. Through the TNGA, Toyota is working to greatly enhance basic performance and product appeal by adopting innovative changes starting with the fundamental vehicle structure.

As part of these efforts and in concert with the development and adoption of new vehicle platforms, Toyota has completely updated its whole powertrain lineup, including engines, transmissions, and hybrid systems. Adopting the TNGA has helped to create ever-better cars by lowering the height of the hood and center of gravity, and by further enhancing both dynamic and environmental performance.

In addition to the development of new technologies, the TNGA was simultaneously applied to the innovation of production engineering and working practices, reflecting the importance of increasing development and production efficiency to bring vehicles to market more rapidly.

3. TNGA Powertrains

The conventional approach to maximizing powertrain efficiency involves the development of engines and transmissions as separate units, before combining and optimizing the two to maximize efficiency as a powertrain.

In contrast, under the TNGA, ideal new powertrain systems were designed as complete systems for different vehicles depending on size and usage environment. The efficiency of these powertrains was maximized as an integrated system, which enabled both fuel efficiency and driving performance to be enhanced.

Fig. 2 shows the underlying development concept for these TNGA powertrains. This concept divides powertrains into three levels: items of the fundamental powertrain structure that remain constant (level 1 of the pyramid), and components that are subject to evolution (levels 2 and 3).

[*1] President of the Powertrain Company

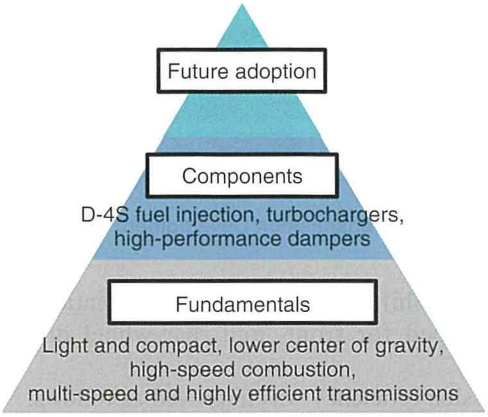

Fig. 2 Development Concept of TNGA Powertrains

More specifically, this concept involves thoroughly optimizing the basic structure to enhance core performance and quality. Technological elements are then added to this basic structure to satisfy changes in the market environment, product requirements, and local characteristics. Finally, the top of the pyramid refers to technological breakthroughs for the future.

The following sections describe the functions and objectives of the components that comprise the TNGA powertrains, as well as how these were accomplished.

3.1 New engines

First, this section describes the reasoning behind the development of the TNGA engines.

Engine development can be categorized into common core technologies that can be evolved regardless of engine displacement or the number of cylinders, and combustion, intake, and exhaust system technologies that depend greatly on engine displacement and geometry.

Efforts to boost thermal efficiency by reducing losses focused on making steady improvements based on past experience. In contrast, despite the difficulty of increasing combustion quality and intake efficiency across different engine types, engine development under the TNGA aimed to achieve both these goals and to apply the resulting improvements to all engine types through a commonly designed basic engine architecture (**Fig. 3**).

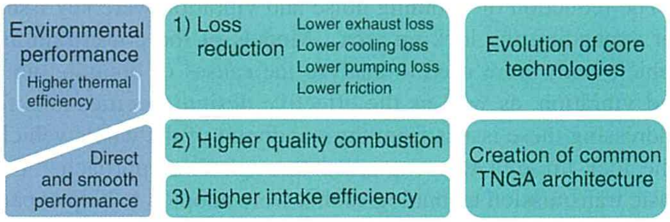

Fig. 3 Engine Development Concept

This common architecture can be defined as follows. **Fig. 4** shows the target objective parameters of the TNGA engines. It was necessary to increase both intake efficiency and in-cylinder turbulence to improve both driving performance and fuel efficiency. These two objective parameters were set as targets for the TNGA engines. Specific targets were set well beyond the conventional trade-off line of these parameters.

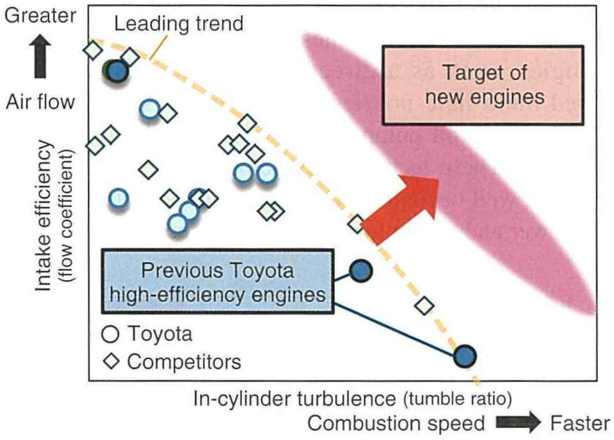

Fig. 4 Objective Parameters of TNGA Engines

The combustion state achieved at this target was defined as the target for the optimized combustion. The common architecture was then visualized using a combustion waveform that expresses the optimum combustion state using the pressure inside the cylinder (**Fig. 5**).

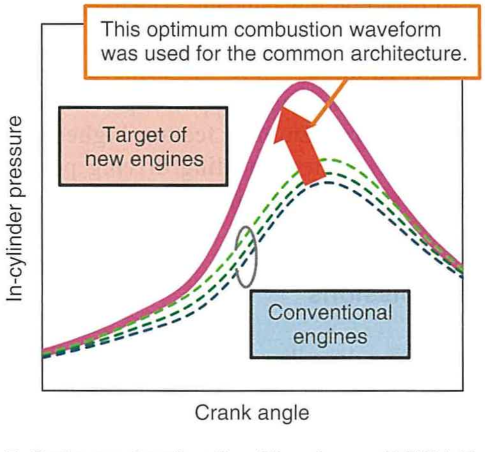

Fig. 5 Optimum Combustion Waveform of TNGA Engines

The ideal port and combustion chamber structure capable of realizing this combustion waveform was defined in terms of design parameters, including tumble ratio, port shape, valve included angle, and the stroke/bore ratio. Modules were created reflecting these specifications and applied to engines with different displacements.

The TNGA engines also adopted a newly developed manufacturing method called laser cladding to help realize a linear port shape. Laser cladding coats a special alloy onto the valve seats, which contact the cylinder head when the valve is closed, to form laser-clad valve seats. This new technology was developed completely from scratch, including the alloy material and the new high-speed laser cladding method, and will be adopted in all the new engines in the future.

Compared with Toyota's conventional highly thermal efficient engines, all the TNGA engines feature a range of the latest technologies, such as a direct injection system with newly developed multi-hole nozzles and the world's first trochoidal variable discharge oil pump, which result in substantially higher performance. These technologies helped achieve world-leading performance, well beyond the conventional trade-off line between specific power and maximum thermal efficiency (**Fig. 6**).

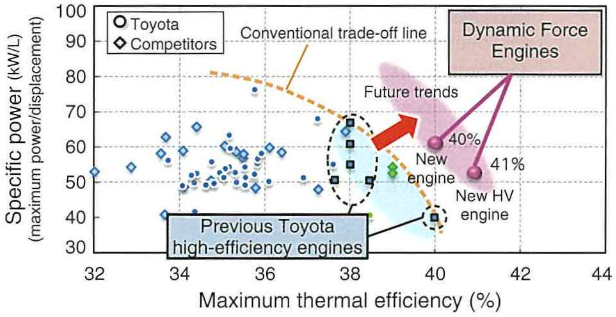

Fig. 6 Specific Power and Maximum Thermal Efficiency

New 2.5-liter inline 4-cylinder and 3.5-liter V6 engines have been developed based on this concept. The engines in these new series are called "Dynamic Force Engines." All new engine series to be launched in the future will achieve similar dramatic improvements in environmental and power performance.

These Dynamic Force Engines feature higher torque in all operation ranges to create appealing driving performance in everyday driving situations, while also substantially lowering emissions.

3.2 New transmissions

Second, this section describes the new TNGA transmissions.

The TNGA transmission development aimed to combine environmental with direct and smooth performance. Three development themes were adopted to accomplish this objective: improvement of transmission efficiency (i.e., the basic performance of a transmission), the utilization of high efficiency engine operation ranges, and the achievement of rhythmical and highly responsive shifting (**Fig. 7**).

These themes were realized by reducing mechanical loss, further expanding the lock-up area, and increasing the number of gear speeds.

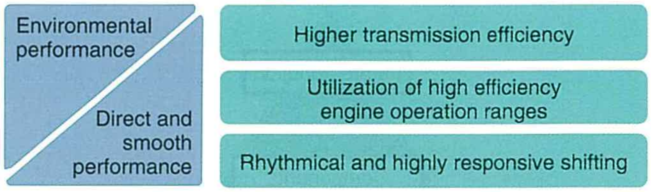

Fig. 7 Transmission Development Concept

New Direct Shift 8- and 10-speed automatic transmissions were developed for front- and rear-wheel drive vehicles, respectively.

Transmission efficiency was improved as follows. Ordinarily, adopting a higher number of gear speeds has a negative effect on transmission efficiency because the number of component parts in the transmission increases. Therefore, the design of key components of the Direct Shift 8- and 10-speed automatic transmissions, such as the gears and clutches, was completely revised to thoroughly reduce loss. One important technology that was adopted was super finishing of the gear faces. This technology creates mirror-smooth gear faces while preserving the concavities used to retain the required amounts of lubrication oil for gear engagement. Technologies developed by combining design and production techniques like these achieved further reductions in energy transmission loss when the gears engage.

These measures were adopted to create a wide gear range and world-class transmission efficiency (**Fig. 8**).

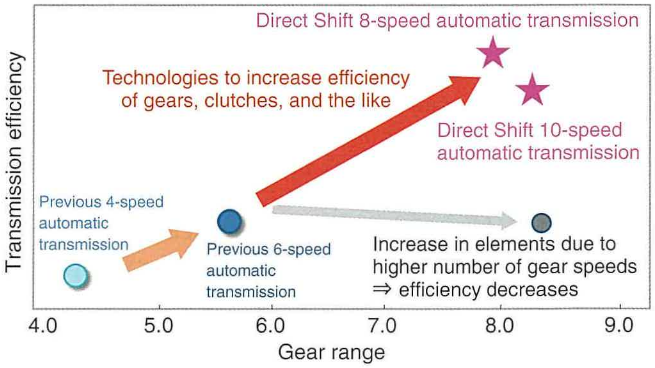

Fig. 8 Transmission Efficiency and Gear Range

The reduction of booming noise and vibration were key issues for expanding the lock-up area. Models of the powertrain and vehicle body were used to analyze the causes of booming noise and vibration, as well as the effective design specifications for addressing these issues from the standpoint of the whole vehicle. The lock-up area was expanded through this approach. Two basic transmission technologies that were adopted to help expand the lock-up area are described below.

First, the layout of the internal automatic transmission parts was optimized to achieve the required inertia. Although higher rotational inertia is desirable for an automatic transmission to reduce vibration, the extra weight this creates is an issue. Therefore, the part layout was altered to achieve the necessary rotational inertia to reduce vibration while maintaining the same mass as an overall transmission assembly (**Fig. 9**).

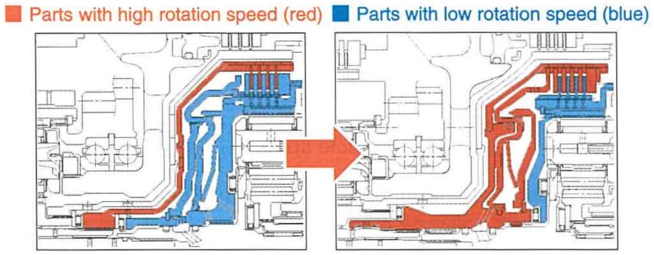

Fig. 9 Optimization of Internal Automatic Transmission Layout Based on Inertia

Second, a new torque converter was developed, featuring a high-performance damper designed through detailed part-level structural analysis, a multi-plate lock-up clutch, and a compact ultra-flat torus (**Fig. 10**).

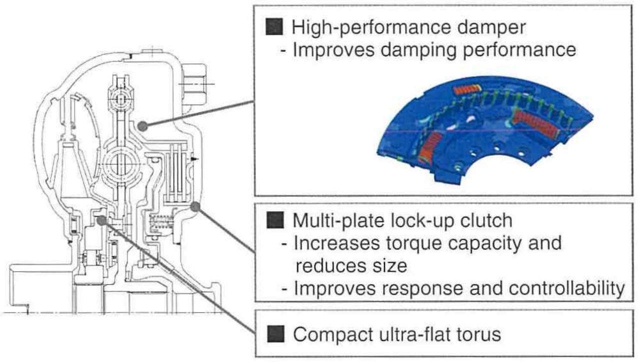

Fig. 10 Newly Developed Torque Converter

In the Direct Shift 8-speed automatic transmission, these features enable lock-up from a lower vehicle speed in all gear stages, thereby reducing engine revving and instability when accelerating or decelerating, and achieving a stronger direct driving feel.

Rhythmical and comfortable acceleration was achieved as follows by increasing the number of gear speeds. Shifting that occurs at equal intervals and a constant rhythm is an important part of achieving comfortable acceleration. This was accomplished in the Direct Shift 10-speed automatic transmission through the development of a gear train with close gear steps (**Fig. 11**).

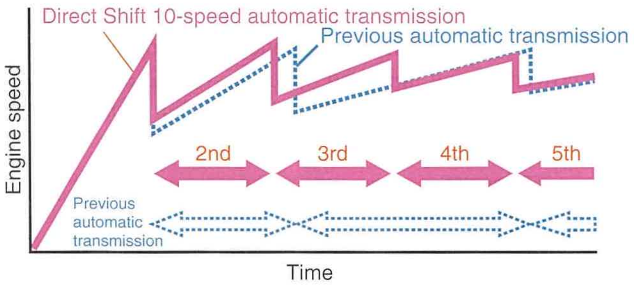

Fig. 11 Rhythmical Shifting

This development also worked to shorten the shifting time. One issue with shorter shifting times is controlling shift shock. In the Direct Shift 10-speed automatic transmission, enhanced hardware response was combined with a newly developed model-based integrated powertrain control. These measures help to achieve the world's fastest shifts that are both smooth and incisive.

New driveline components, such as a propeller shaft and differential, were also developed alongside the high-torque engine and multi-speed transmission for rear-wheel drive passenger vehicles on the new platform.

Driveline losses can be divided into loading loss, rotational loss, and churning loss. These losses were improved to improve fuel efficiency and boost the efficiency of the powertrain.

Conventionally, rubber couplings are used to decrease high-frequency noise. The contribution of radial and axial direction excitation forces was identified to greatly reduce the level of noise.

3.3 New hybrid systems

Third, this section describes the new hybrid systems developed for the TNGA engines. The following hybrid systems were developed. With the aim of combining environmental with direct and smooth performance, the Toyota Hybrid System (THS) II was mated with the 2.5-liter Dynamic Force Engine as a further application of the hybrid system developed for the Prius. Additionally, the Multi Stage Hybrid System and a new plug-in hybrid system were also developed to provide new value to the customer (**Fig. 12**).

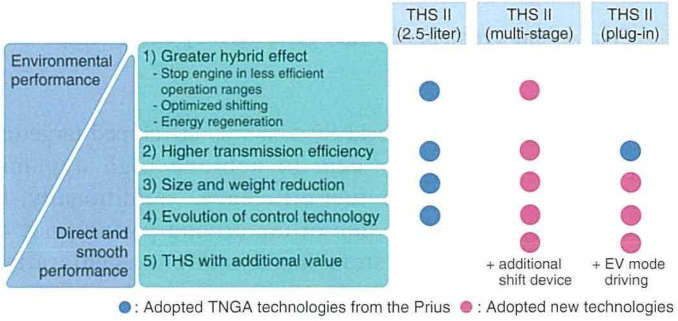

	THS II (2.5-liter)	THS II (multi-stage)	THS II (plug-in)
1) Greater hybrid effect - Stop engine in less efficient operation ranges - Optimized shifting - Energy regeneration	🔵	🔴	
2) Higher transmission efficiency	🔵	🔴	🔵
3) Size and weight reduction	🔵	🔴	🔴
4) Evolution of control technology	🔵	🔴	🔴
5) THS with additional value		🔴 + additional shift device	🔴 + EV mode driving

🔵 : Adopted TNGA technologies from the Prius 🔴 : Adopted new technologies

Fig. 12 Hybrid System Development Concept

First, the new 2.5-liter THS II has the following characteristics. Every main component, including the transaxle, motor, power control unit, and batteries, was re-developed based on the THS II adopted by the Prius launched in 2014 (**Fig. 13**).

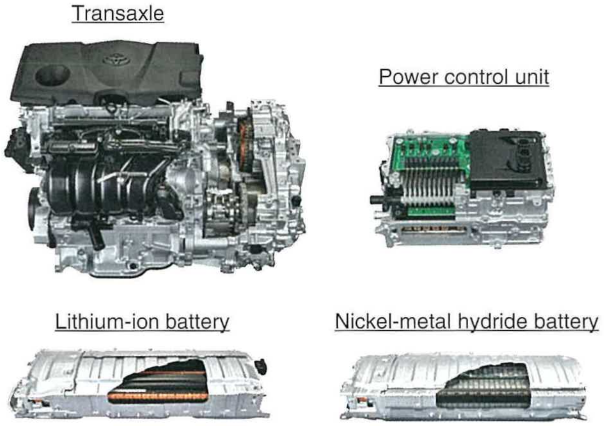

Fig. 13 New THS II (2-5-Liter) System

This system was mated with the 2.5-liter Dynamic Force Engine to improve both fuel efficiency and driving performance. Compared to the previous model, the fuel efficiency of the powertrain was boosted by 20% and intermediate acceleration performance by 10% (**Fig. 14**).

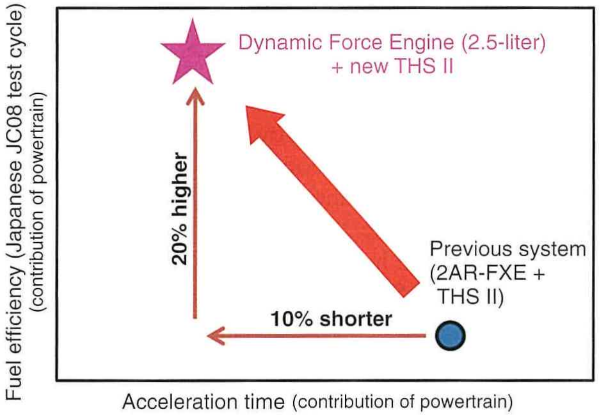

Fig. 14 Improvement of Both Fuel Efficiency and Driving Performance

The new Multi Stage Hybrid System was developed targeting competing luxury sporty cars to achieve high dynamic performance with superior fuel efficiency. Additionally, to create a totally new impression of the driving performance of hybrid vehicles, this system has excellent acceleration performance and adopts a 10-speed shift control. These features achieve a rhythmical and comfortable acceleration feeling in tune with the sound of the engine (**Fig. 15**).

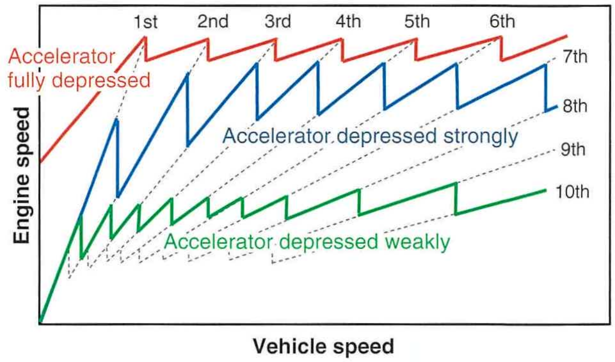

Fig. 15 Operating Points of Engine with 10-Speed Shift Control

This was accomplished by adopting the newly developed Multi Stage Hybrid Transmission, which features an additional shift device in the power split device that controls the shifting performance of the whole transmission. This device allows maximum engine performance to be utilized from low vehicle speeds and greatly increases system power.

This shift device also plays a major role in improving fuel efficiency by adding four high-efficiency operation points that achieve substantially higher transmission efficiency at both low and high speeds.

Finally, the new Prius plug-in hybrid system adopts a dual motor drive system that adds a one-way clutch to the hybrid system of the Prius hybrid. This enables the generator to be used as a motor and ensures powerful EV mode driving.

As a result, power in EV mode is 1.8 times higher than the first generation Prius PHV, increasing both maximum speed and driving force. As a result, the new Prius PHV can be driven in EV mode in almost all situations, including on the highway (**Fig. 16**).

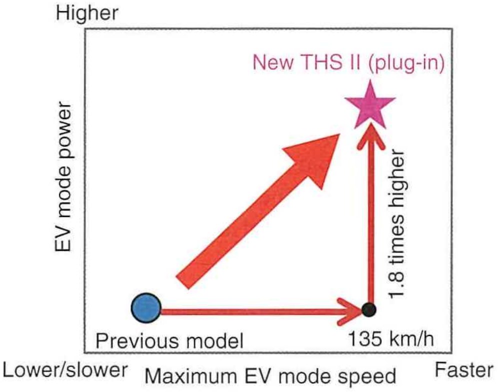

Fig. 16 Expansion of EV Mode Driving Range

4. Improvement of Productivity and Development Efficiency

4.1 Improvement of productivity

This section describes the improvements made to TNGA manufacturing productivity, which is an essential part of product innovation.

To enable flexible and rapid response to powertrain changes due to diversifying customer needs and fluctuating market environments, new production lines have been developed that can produce different components rapidly and flexibly. This was achieved by, for example, adopting uniform machining datums and assembly standards (**Fig. 17**).

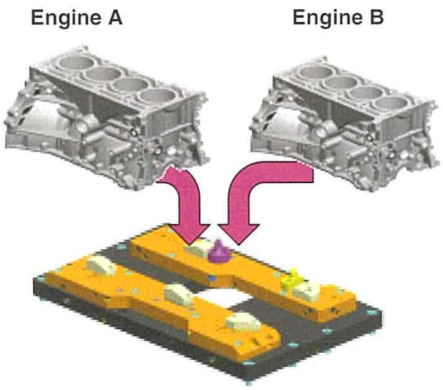

Fig. 17 Example of Commonization of Machining Jigs

Uniform production processes and facility specifications also help to accelerate global deployment by enabling plants around the world to switch production at a rate of around one million units per year.

Other measures to boost productivity include the adoption of the CS core process, an innovative production technique that improves both environmental and casting quality, and manufacturing innovations such as reducing the size, footprint, and energy usage of production facilities. These measures help to reduce the investment required to build a powertrain production line, while also contributing to the environment by reducing CO_2 emissions from plants.

4.2 Improvement of development efficiency

Development efficiency was improved as follows.

Under a conventional approach to engine development, various devices and structures are selected in accordance with various vehicle requirements and characteristics.

In contrast, under the TNGA, all aspects of the powertrain were completely re-designed simultaneously with the vehicle platform. This allowed the center of gravity of the vehicle to be lowered and structures to be unified in line with the optimum installation methods (**Fig. 18**).

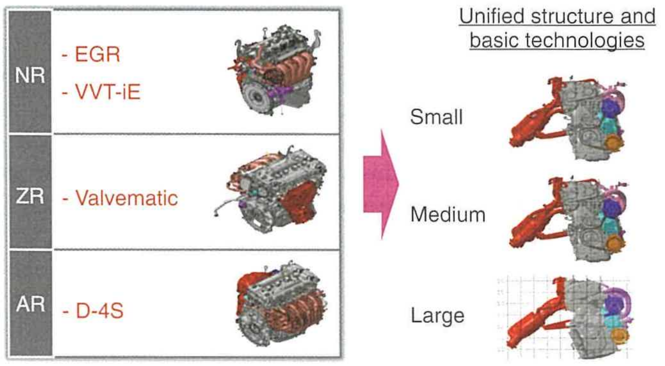

Fig. 18 Unification of Structures and Basic Technologies

At the same time, unified engine combustion chamber and cylinder designs were adopted, enabling engine variations to be configured simply by combining the volume and number of cylinders. This approach eliminated overlap between different engine models with the same displacement, helping to consolidate and streamline the engine lineup, and reduce the number of engines under development by approximately 40% (**Fig. 19**).

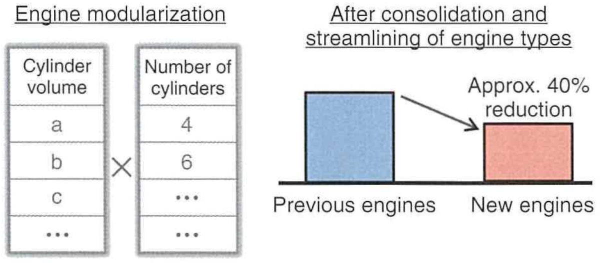

Fig. 19 Reduction of Number of Engines Under Development

The efficiency of combinations with transmissions and hybrid systems was also improved, helping to boost both development efficiency and productivity.

5. Conclusion

Over a five-year period up to 2021, Toyota plans to introduce 37 variations of 19 new powertrains based on the modular development approach of the TNGA. This completely refreshed lineup of TNGA powertrains will be adopted in markets around the world.

Through these plans, powertrain development and production should help to reduce CO_2 emissions by at least 15% a year in 2021 compared to 2015.

In the short- and medium-term, the delivery and widespread adoption of the optimum powertrains at the optimum timings and in the optimum regions, in accordance with the situation of fuel usage and infrastructure establishment around the world can help to reduce energy consumption and lessen environmental impacts. In the long-term, as electrical energy becomes more widely used in the future, Toyota is aiming to help realize sustainable mobility through measures addressing both vehicles and the whole of society. Toyota intends to play a leading role in activities to help achieve this vision through a close partnership with other companies, governments, and its stakeholders.

Authors

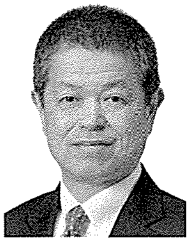

H. KISHI

The New Toyota Inline 4-Cylinder 2.5-Liter Gasoline Engine

Kunihiko Sakata*1
Tadashi Toda*2
Mitsuto Sakai*3
Masashi Hakariya*4
Toshikazu Kato*5

Abstract

The main distinguishing technological characteristic of the new inline 4-cylinder 2.5-liter gasoline engine developed by Toyota Motor Corporation is high-speed combustion, which was achieved by adopting a long stroke design, an expanded valve included angle, and highly efficient intake ports using laser-clad valve seats. This high-speed combustion package was then incorporated into the Toyota New Global Architecture (TNGA) engine series that shares a uniform basic structure. Additional new technologies adopted in this engine include multi-hole direct injection, a redesigned variable valve timing (VVT) system, a variable capacity oil pump, and a variable cooling system.

Keywords: *gasoline engine, high power, high thermal efficiency*

1. Introduction

Toyota Motor Corporation has developed a new inline 4-cylinder 2.5-liter gasoline engine based on the Toyota New Global Architecture (TNGA) design philosophy. This engine was developed to achieve wide-reaching improvements in fuel efficiency and for compatibility with increasingly stringent emissions regulations as part of Toyota's efforts to help realize a sustainable society by addressing future energy-related and environmental issues. Furthermore, this engine was also developed with high power performance to achieve a fun-to-drive experience exceeding user expectations. This article describes an outline of this new gasoline engine and its main technologies.

2. Development Aims

This engine was developed with the objective of further advancing high-speed combustion technologies for conventional engines. As shown in **Fig. 1**, specific development aims including achieving a maximum thermal efficiency of 40%, equivalent to the latest hybrid vehicles (HVs), as well as top-class dynamic performance of 60 kW/L.

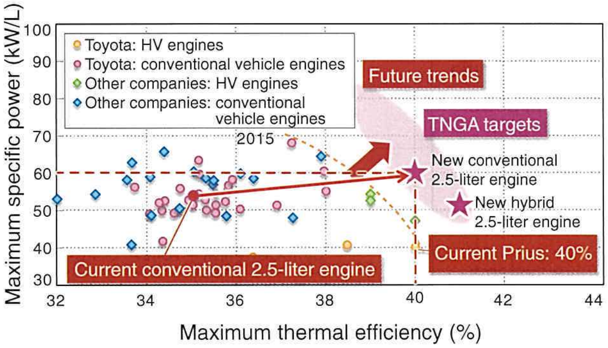

Fig. 1 Trends and Targets for Specific Power and Thermal Efficiency

To achieve these targets, facilitate future development, and ensure productivity, performance was boosted by making the following refinements to the basic engine structure.

- Long stroke design
- Higher compression ratio
- Modified intake and exhaust flows
- Expanded valve included angle

In addition, the following technologies were also adopted.

- Laser-clad valve seats
- The new D-4S system adopting multi-hole direct injection (DI)
- High energy ignition coils
- Electrically variable discharge oil pump
- Cooled exhaust gas recirculation (EGR) system
- An electric variable valve timing system called Variable Valve timing-Intelligent by Electric motor (VVT-iE)

Fig. 2 shows a cross-section of the engine and **Table 1** lists its main specifications.

---

*1 CVZ, CV Company
*2 TNGA Management Div.
*3 Electric Powertrain System Development Div., No. 3, Powertrain Company
*4 Engine Design & Engineering Div., Powertrain Company
*5 Electric Powertrain System Development Div., No. 2, Powertrain Company

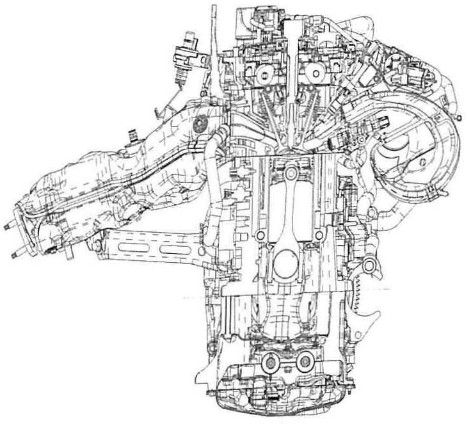

Fig. 2 Engine Cross-Section

Table 1 List of Specifications for the New 2.5-Liter Engine

Engine	Conventional vehicle engines	
	New engine	2AR-FE
Type	Inline 4-cylinder	
Displacement (cc)	2,487	2,494
Bore diameter × stroke (mm)	87.5×103.4	90.0×98.0
Compression ratio	13.0	10.4
Maximum power (kW/rpm)	151/6,600	134/6,000
Maximum torque (Nm/rpm)	250/5,000	231/4,100
Valve systems	4-valve duel overhead cam (DOHC)/ cylinder HLA + roller rocker	
	Dual VVT-iE (motor-driven on intake side)	Dual VVT
Lubrication system	Variable discharge	Conventional
Cooling system	Motor-driven water pump	Belt-driven water pump
Intake system	None	Variable intake
EGR system	Cooled EGR	None
Fuel system	D-4S (multi-hole DI + PFI)	Port fuel injection (PFI)
Aftertreatment	2 air-fuel ratio sensors + 2 catalysts	Air-fuel ratio sensor + O_2 sensor + 2 catalysts

3. Combustion Technology

Thermal efficiency and power performance are generally regarded as having a trade-off relationship. The optimum compression ratio and stroke/bore ratio were selected to achieve the high targets set for both of these items. In addition, breakthrough technology was developed to refine conventional high-speed combustion technologies by increasing the intensity of in-cylinder turbulence.

High-flow, high-tumble intake ports were developed by expanding the included angle between the intake (IN) and exhaust (EX) valves and locating the hydraulic lash adjuster (HLA) inward of the valve axis center (**Fig. 3**). Furthermore, laser clad valve seats were adopted to create a more linear port shape. This helps to maintain a high flow velocity into the combustion chambers and to suppress the generation of reverse tumble, in which the flow separates at the throat portion on the lower port surface. These measures helped to achieve a tumble ratio of 2.9 and a flow coefficient of 0.49, which is a substantial improvement from the conventional trade-off line (**Fig. 4**).

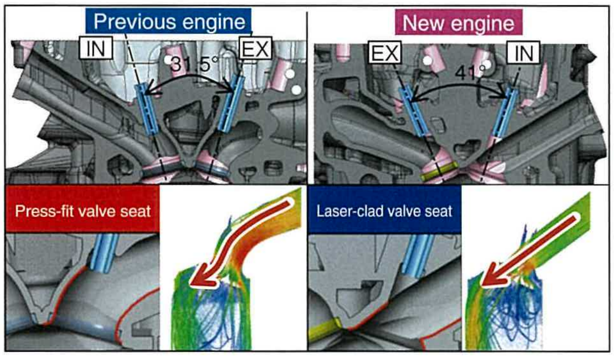

Fig. 3 Cross-Section of Cylinder Head and Combustion Chamber

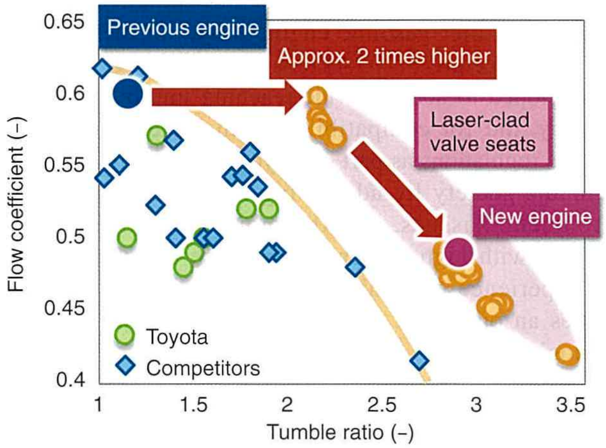

Fig. 4 Target Intake Port Performance

The new D-4S system was developed in consideration of future particle number (PN) regulations. Adopting multi-hole DI injectors shortened the spray penetration and reduced the amount of fuel adhesion on the piston and bore walls. In addition, the stratified cavity on the top of the piston was eliminated as shown in **Fig. 5** to increase the in-cylinder turbulence intensity in the compression stroke.(1)

The valve system was also refined to increase the valve lift and working angle. Applying electric VVT to the intake side enables the optimum valve timing to be realized instantaneously under all conditions. This measure helped to both reduce pumping loss and increase power.

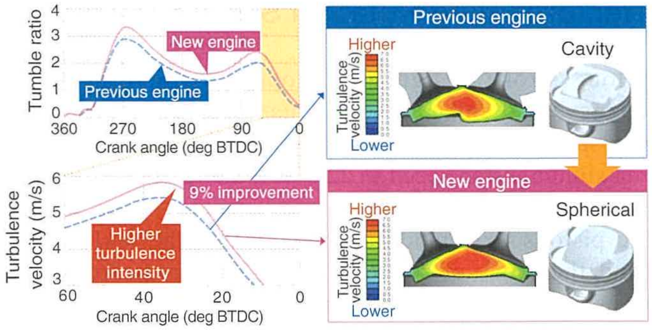

Fig. 5 Comparison of Tumble Ratio and Piston Shape

Furthermore, high energy ignition coils were adopted to stabilize combustion under heavy EGR. The size of the gap of the magnetic circuit passing through each core was reduced to increase the magnetic efficiency (**Fig. 6**).

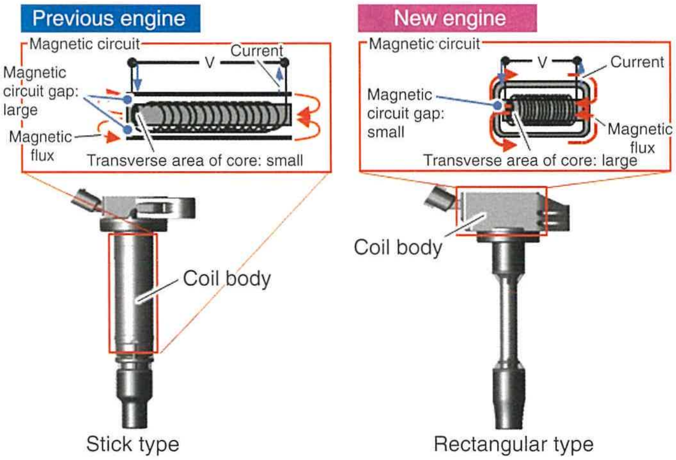

Fig. 6 High Energy Ignition Coils

4. Cooling System

4.1 Improvement of knocking resistance

To suppress deterioration in knocking resistance due to the higher compression ratio, a motor-driven water pump was adapted for use in a conventional engine to control the coolant flow rate regardless of the rotational speed of the crankshaft. The pressure loss was reduced and the cooling performance enhanced to decrease the size of the pump in accordance with the available space. First, a two-level water jacket was adopted for the cylinder head (**Fig. 7**). Changing the flow of coolant in the cylinder head from the vertical to the lateral direction reduced pressure loss by 35%. Additionally, the coolant flow was concentrated between the exhaust valves, the core material of the water jacket was changed, and the sectional area of the core was reduced by 20%. As a result, the coefficient of heat transfer was increased by 20% with around half the flow rate of the previous engine (**Fig. 8**).

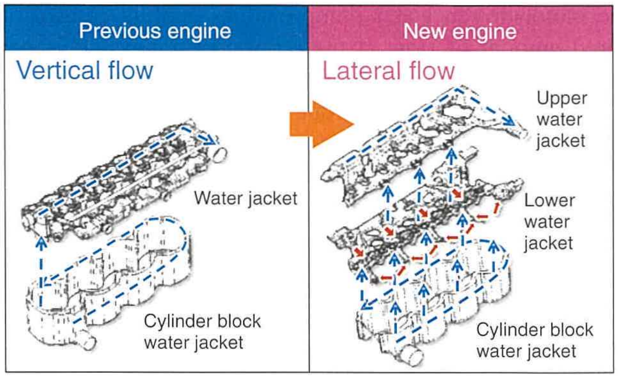

Fig. 7 Comparison of Water Jacket Structures

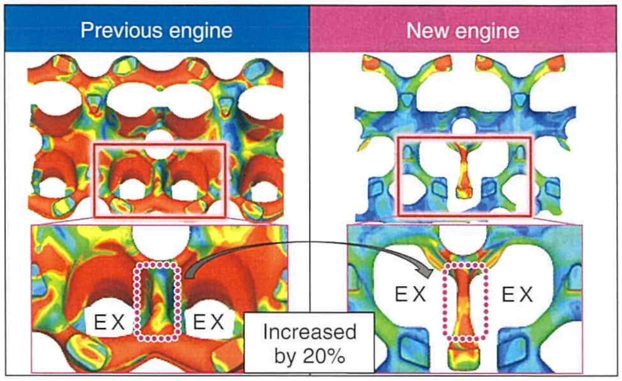

Fig. 8 Comparison of Coefficient of Heat Transfer

A water jacket spacer (WJS) was provided only at the exhaust side of the cylinder block water jacket (**Fig. 9**). This measure concentrates increases in flow velocity to the exhaust side, thereby suppressing higher mixture temperatures due to the high tumble ratio, and equalizing differences in bore wall temperatures between the intake and exhaust side.

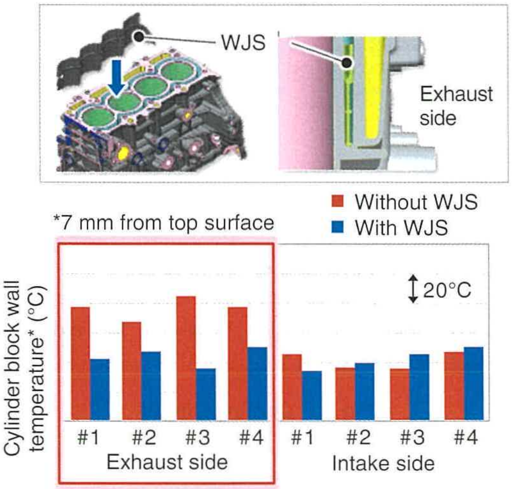

Fig. 9 WJS and Cylinder Block Wall Temperatures

The motor-driven water pump enables cooling control of the required amount of flow at the required timings. This control lowers the cooling loss and friction when driving in the minimum advance for best torque (MBT) region by reducing the coolant flow rate. It also lowers wall temperatures by increasing the flow rate in the restricted knocking region, enabling higher engine torque than the conventional control.

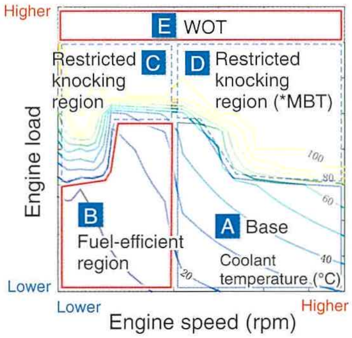

Region	Coolant temperature	Flow rate
A	Lower	Base
B	Higher	Decreased
C	Transient	Increased
D	Lower	Increased
E	Lower	Max.

Fig. 10 Flow Rates and Coolant Temperature Control

4.2 Cold start performance

To warm-up the coolant rapidly under cold conditions, the coolant flow rate control carried out by the motor-driven water pump is supplemented by flow shut valves (FSVs) that switch the flow of the cooling circuit. As shown in **Fig. 11**, the cooling circuit in this conventional engine uses two FSVs. These valves help to optimize the temperature of each component in the circuit, while enhancing fuel efficiency and the performance of the cooler and heater systems.

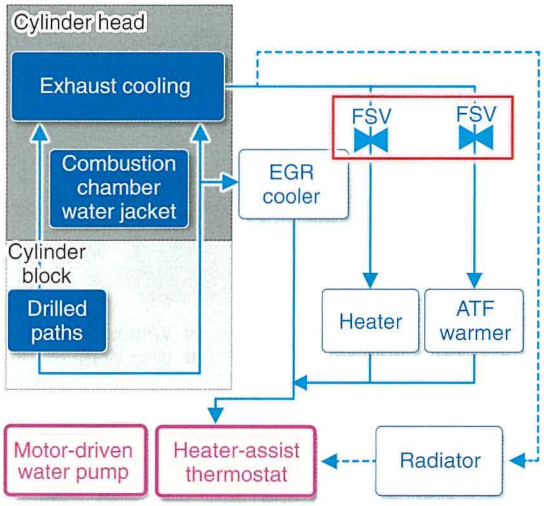

Fig. 11 Cooling Circuit

5. Reciprocating Rotation System

A long stroke design was adopted to increase thermal efficiency. To enhance power performance, the maximum engine speed was increased to 6,600 rpm. Since this increases the maximum piston speed to 22.8 m/s, the reciprocating inertial mass was substantially reduced.

The pistons were modified by adjusting the tool design to expand the areas of reduced thickness for the piston ring grooves, and by adopting thinner walls for the skirts and top surfaces. As a result, the weight of the pistons was reduced by 7%, achieving a world-class weight/torque ratio (**Fig. 12**).

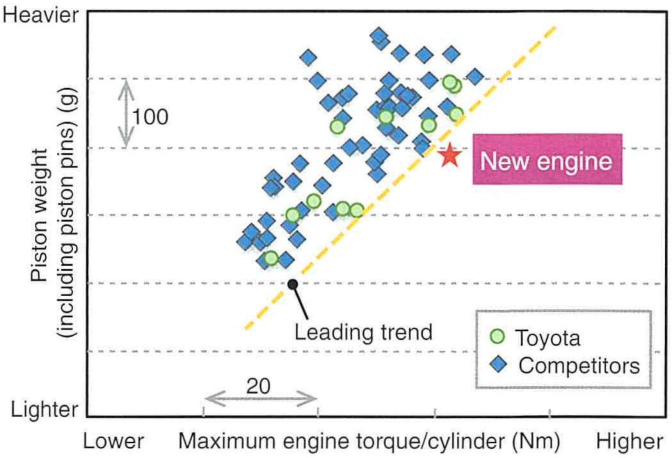

Fig. 12 Relationship between Piston Weight and Torque per Cylinder

Viper head-shaped small ends were adopted for the connecting rods. High-strength steel was also used to decrease the sectional area of the column portions, resulting in lighter and stiffer pistons. Measures to reduce weight and increase stiffness were incorporated to reduce the weight of the crankshaft and suppress tapping noises. The weight-reduction measures focused on parts with a large impact on inertial force, while the measures to increase stiffness focused on parts that contribute greatly to noise and vibration (NV). This approach was applied to optimize each crank journal.

Higher friction and oil consumption are other trade-off effects of increasing the engine speed. These effects were suppressed by reducing the contact area width around the second ring, adopting a diamond-like coating (DLC) around the oil rings, and changing the end position of the oil ring side rail.

6. Lubrication System

This engine includes an electrically variable discharge oil pump that reduces friction loss by using an internal gear type rotor and an electronic oil control valve (OCV) to perform hydraulic control (**Fig. 13**). As a result, the lubrication system is capable of supplying the required amount of oil to the necessary locations in accordance with the main gallery oil pressure.

The oil circuit was divided into passages for the main gallery and the oil jets. This configuration allows the oil jets to be stopped more easily, helping to reduce friction loss and PN by warming up the pistons more rapidly.

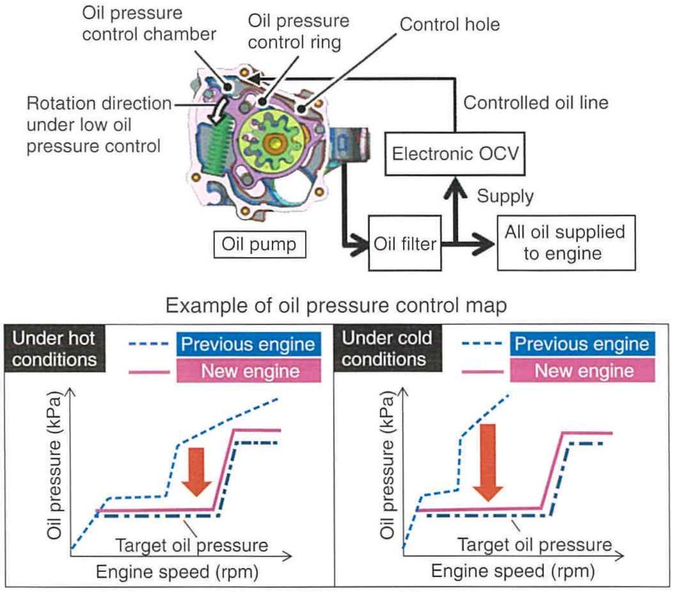

Fig. 13 Electrically Variable Discharge Oil Pump

7. Emissions Control System

The most effective rear exhaust for enhancing the warm-up performance of the catalysts was selected to facilitate compliance with the SULEV30 and Euro 6 emissions regulations. The system is controlled by two air-fuel sensors, which allows the size of the catalysts and the amount of platinum-group metals used to be reduced. The cylinder head exhaust port adopts an exhaust cooling system to enhance power performance and catalyst reliability (**Fig. 14**). This system lowers the exhaust gas temperature and greatly expands the range of stoichiometric engine operation (**Fig. 15**).

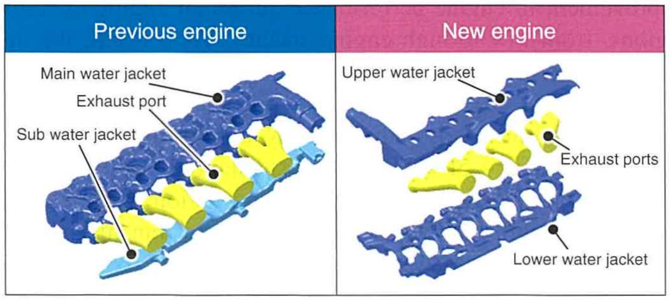

Fig. 14 Structure of Cylinder Head Exhaust Port and Water Jacket

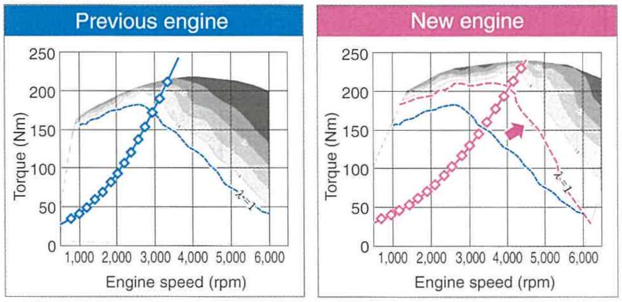

Fig. 15 Comparison of Stoichiometric Engine Operation Range

8. EGR System

The high-speed combustion system enables the maximum EGR rate to be increased up to 25%. In addition, the shape of the intake manifold was optimized to suppress combustion fluctuations and differences in EGR amounts between cylinders. The EGR flow passes through fin-shaped passages surrounded by the cylinder head water jacket before reaching the EGR cooler, thereby helping to lower the gas temperature at low cost (**Fig. 16**).

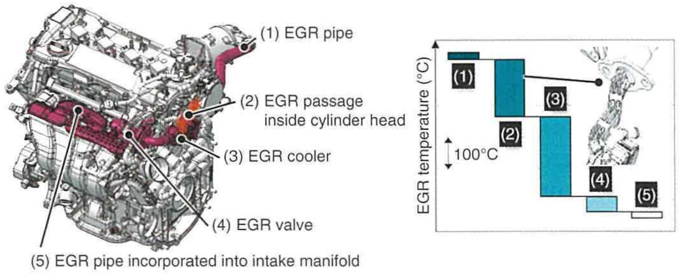

Fig. 16 EGR System Layout and Gas Temperature Reduction Effect

9. Friction

Friction was reduced by 20% compared to the previous engine by adopting the following technologies (**Fig. 17**).

- Resin coated pistons
- DLC coated piston rings (top and oil rings)
- Resin coated bearings
- Plastic chain guard
- Beehive valve springs
- Low viscosity engine oil (SAE 0W-16)
- Elimination of the water pump pulley (adoption of motor-driven pump)
- High-efficiency vacuum pump

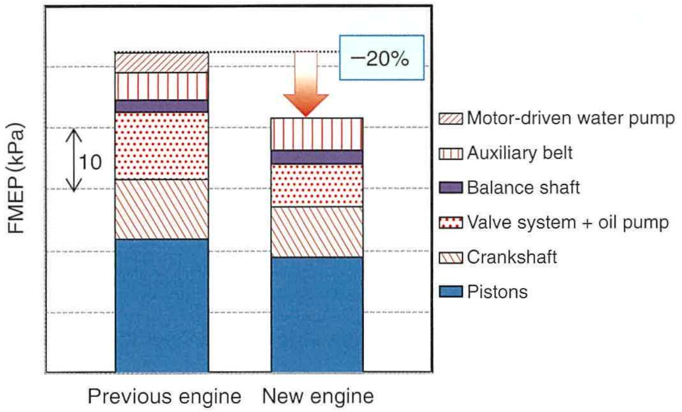

Fig. 17 **Comparison of Friction Mean Effective Pressure (FMEP) (when Motoring at 2,000 rpm)**

10. NV

In addition to increasing engine stiffness, NV was reduced by adopting a new transmission and through the effect of the new vehicle platform.

For low-frequency NV, mountings were installed on the torque roll axis, thereby reducing idling vibration. In addition, locating the power plant over the principal elastic axis helped to reduce vibration when the engine starts up.

In the mid- and high-frequency range, power plant stiffness was enhanced by optimizing the fastening positions of the cylinder block and transmission (**Fig. 18**), enabling a reduction in mounting vibration of approximately 4 dB (**Fig. 19**).

Furthermore, high-frequency noise caused by high-speed combustion was reduced by optimizing the layout of the polyurethane insulators (**Fig. 20**).

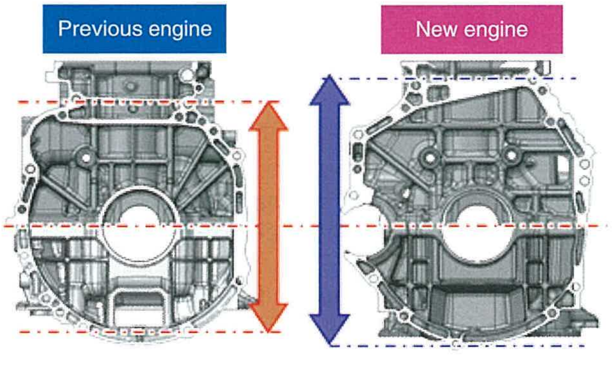

Fig. 18 **Comparison of Transmission Fastening Positions**

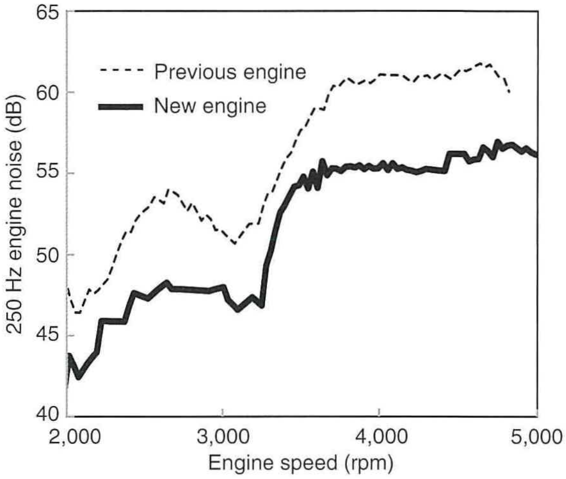

Fig. 19 **Comparison of Engine Noise**

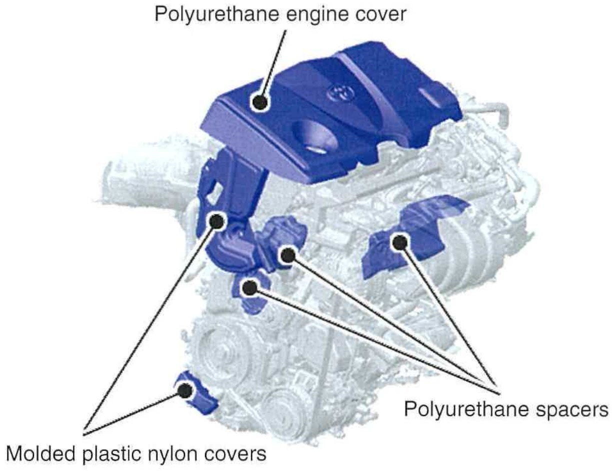

Fig. 20 **NV Insulators**

11. Engine Performance

Compared to the previous engine, high-speed combustion and the new technologies described above resulted in a substantial improvement in engine performance across all engine operating regions, from low to high engine speeds. As a result, the new engine achieves a maximum power of 151 kW (specific power: 60 kW/L) (**Fig. 21**).

Fuel efficiency was enhanced by achieving a maximum thermal efficiency of 40% and by substantially enlarging the 35% thermal efficiency engine operating region (**Fig. 22**). In combination with the new 8-speed automatic transmission, the fuel efficiency of the powertrain was improved by 16%.

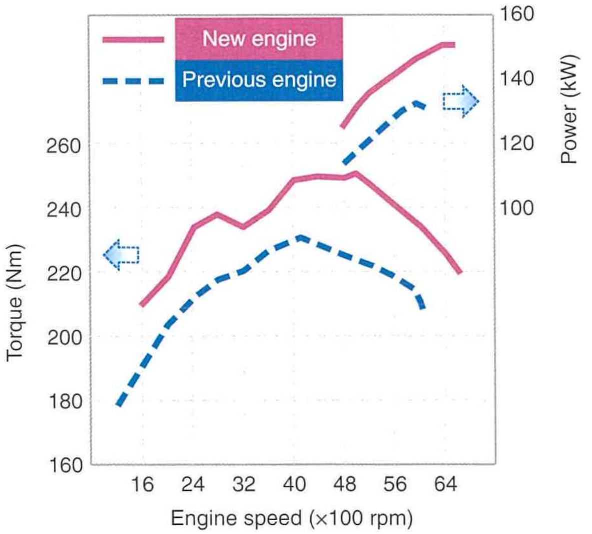

Fig. 21 Engine Power and Torque Curves

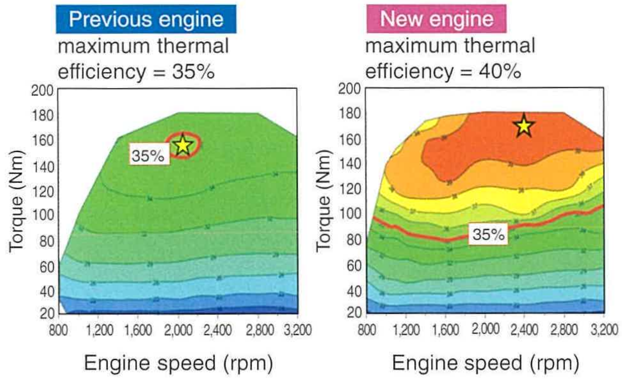

Fig. 22 Comparison of Thermal Efficiency Maps

12. Conclusions

The new inline 4-cylinder 2.5-liter gasoline engine described in this article achieved world-leading maximum thermal efficiency and power performance by adopting a full range of the latest technologies, reflecting its status as a key next-generation engine of Toyota.

The new engine is compatible with emissions regulations around the world and is planned to be adopted in a wide range of models on a global basis.

(1) Its long stroke design and high-speed combustion package achieve intense tumble and high flow rates, which help to realize a maximum thermal efficiency of 40% and a maximum specific power of 60kW/L.

(2) The high-speed combustion package was accomplished through the adoption of laser clad valve seats, high-flow intake ports that achieve a high tumble ratio, a spherical piston top surface that maintains the high tumble ratio, and the new multi-hole DI D-4S system, as well as by optimizing the design of component parts.

(3) The cooling system includes a motor-driven water pump adapted for use in a conventional engine, and a cylinder head incorporating a two-level water jacket and lateral coolant flow that concentrates the coolant between the exhaust valves. The cooling system also adopts FSVs for heat management. By controlling the coolant to the optimum temperature in combination with the motor-driven water pump, the cooling system facilitates both high engine fuel efficiency and power performance.

(4) Friction was reduced by 20% compared to the previous engine by adopting an electrically variable discharge oil pump and optimizing the design of component parts.

(5) The stoichiometric engine operation range was expanded by adopting an exhaust cooling system and cooled EGR.

(6) In addition to the technologies included in the new engine, NV was reduced by a newly developed transmission and vehicle platform, as well as by optimized design.

This is the first of a series of engines incorporating high-speed combustion technologies and other key concepts of the TNGA. Other engines in the same series are planned to be launched in sequence in the future.

Finally, the authors would like to extend their sincere gratitude for the invaluable guidance and support of everyone involved in the development of this engine.

References

(1) E. Murase, Shimizu. "Innovative Gasoline Combustion Concepts for Toyota New Global Architecture." *25th Aachen Colloquium Automobile and Engine Technology* (2016).

Note: this article is based on the following published technical paper.
K. Sakata, Toda, Sakai, Hakariya, Kato. "The New Toyota Inline 4 Cylinder 2.5L Gasoline Engine." *Proceedings of the JSAE Annual Congress* (2017) pp. 1887-1892.

Authors

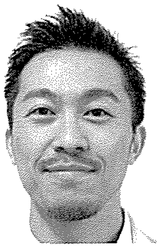
K. SAKATA

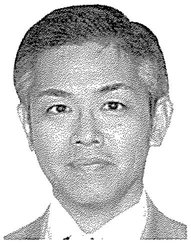
T. TODA

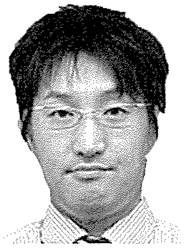
M. SAKAI

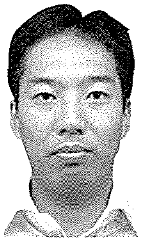
M. HAKARIYA

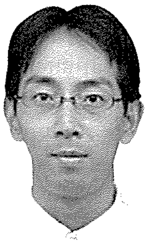
T. KATO

Development of Cylinder System for the New Toyota Inline 4-Cylinder 2.5-Liter Gasoline Engine

Toru Hiranuma[*1]
Chikanori Yamashita[*1]
Tatsuhiro Terada[*1]
Kazuya Nakata[*1]
Mitsuhiro Nakamura[*1]
Takashi Kurauchi[*1]

Abstract

Toyota Motor Corporation has developed a new inline 4–cylinder 2.5–liter gasoline engine with the aim of achieving a thermal efficiency of 40% and a power performance of 60 kW/L. Weight and friction reduction technologies were incorporated into the cylinder system (i.e., the pistons, connecting rods, crankshaft, cylinder block, and bearings), which reduced the weight of the pistons and connecting rods by 13%, and the overall friction of the system by 15%. A 7% reduction in weight compared to the previous engine was achieved by adopting thinner piston walls and by shortening the distance between the pin bosses using viper head–shaped connecting rods. Friction was reduced by changing the surface treatment of the skirts. Operation under actual conditions was analyzed using three–dimensional computer aided engineering (3D CAE) to finalize the shape of the crankshaft and cylinder block, which were designed with careful attention to the portions requiring optimum stiffness. Measures were adopted to suppress increases in weight, and the power performance target was achieved without enlarging the size of the engine compared to the previous generation.

Keywords: *gasoline engine, long stroke, high engine speed, weight reduction*

1. Introduction

Toyota Motor Corporation has developed a new inline 4-cylinder 2.5-liter gasoline engine called the A25A. In addition to re-examining the combustion process and adopting various new technologies, the basic structure of the engine was newly designed and developed with the aim of achieving a thermal efficiency of 40% and power performance of 60 kW/L. This article focuses on the development of the cylinder system for this new engine.

2. Cylinder System Development Concept

The following system specifications were set to achieve high thermal efficiency and power performance: a compression ratio of 13, a stroke/bore ratio of 1.2, a maximum output engine speed of 6,600 rpm, and a 0W-16 engine oil. **Table 1** lists the engine specifications. With these specifications, adopting a long stroke design enabled a piston speed of 22.8 m/s. However, without refinements, the weight of the connecting rods and the size of the engine would likely increase, adversely affecting noise and vibration (NV). Therefore, to satisfy the high system requirements, it was necessary to thoroughly reduce the weight of the overall cylinder system (i.e., the pistons, connecting rods, crankshaft, cylinder block, and bearings). Specifically, it was necessary to minimize the increase in inertial load created by the higher rotational speed of the rotating parts (the pistons and connecting rods) by reducing the weight of these items by at least 10% compared to the previous engine. In addition, this development also aimed to design an engine with lower friction than the previous engine.

Table 1 Engine Specifications

	New engine	Previous engine
Number of cylinders	Inline 4-cylinder	
Displacement (cc)	2,487	2,494
Bore diameter × stroke (mm)	87.5×103.4	90×98
Compression ratio	13	10.4
Fuel injection system	Direct Injection 4-Stroke Gasoline Engine Superior Version (D-4S)	Port fuel injection (PFI)
Other devices	Intake valves: Variable Valve Timing-intelligent by Electric motor (VVT-iE) Exhaust valves: Variable Valve Timing-intelligent (VVT-i) Cooled exhaust gas recirculation (EGR) Motor-driven water pump Continuously variable discharge oil pump	Dual VVT-i Acoustic Control Induction System (ACIS)
Maximum power (kW/rpm)	151/6,600	132.7/6,000
Maximum torque (Nm/rpm)	250/5,000	230.5/4,100

[*1] Engine Design & Engineering Div., Powertrain Company

The parts development process utilized three-dimensional computer aided engineering (3D CAE) to simulate operation under actual conditions. This approach allowed the analysis procedure to consider the dynamic deformation of the whole powertrain, including the engine and transmission. It facilitated studies into NV, as well as into the strength and reliability of the crankshaft, cylinder block, and connecting rods. It also increased development efficiency and enabled weight reduction (**Fig. 1**).

As a result, the weight of the pistons and connecting rods was reduced by 17% and friction was lowered by 15% compared to the previous engine. The following sections describe how these results were achieved.

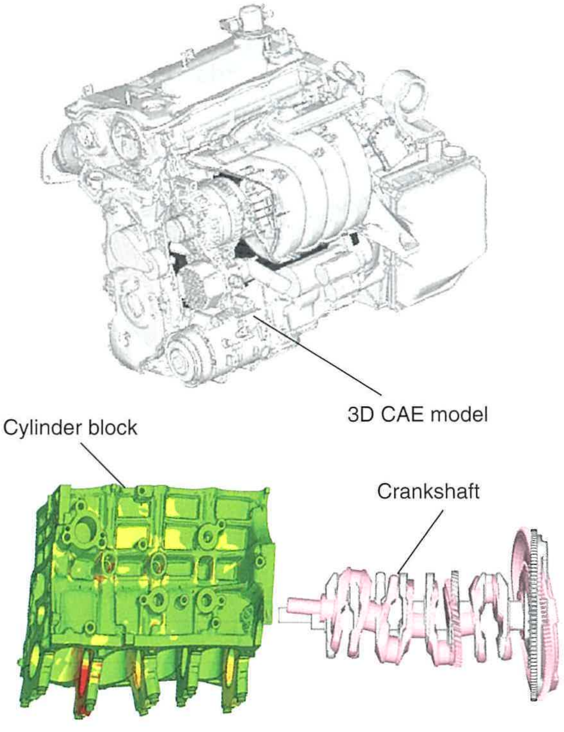

Fig. 1 3D CAE Models

3. Pistons

Lighter pistons were developed by reducing the wall thickness behind the piston ring grooves, as well as by adopting thinner skirt and crown surface designs. The trade-off effect of these measures on stiffness was resolved by adopting a sloping sidewall design that increases the stiffness of the crown surface and restricts piston deformation. Furthermore, cooling was ensured at high piston speeds by reducing the diameter of the oil jets by 0.4 mm to increase the fluid velocity (**Fig. 2**).

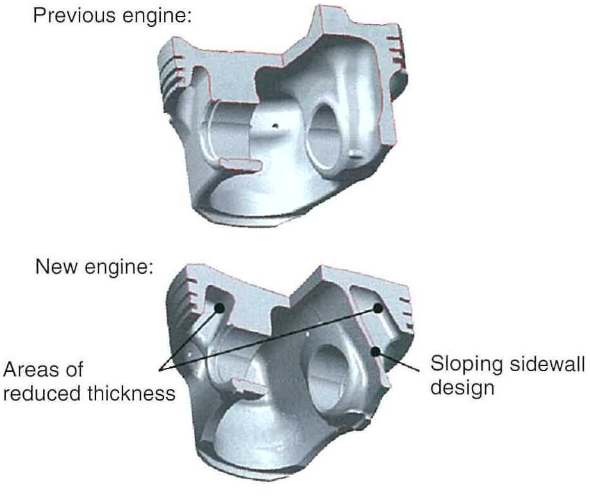

Fig. 2 Piston Design Comparison

One issue with the previous piston skirt design was relatively high surface roughness and friction. To help resolve this issue, micro dimples were formed in the surface. This design ensures seizure resistance and reduces friction by creating a smoother surface while retaining lubrication (**Fig. 3**).

The diameter and length of the piston pins were reduced by 1 and 7 mm, respectively. The side surfaces of the connecting rod piston pin bosses were designed with a viper head shape that flares out at each side toward the end. This design shortens the distance between the pin bosses while ensuring the contact area between the pistons and piston pins, thereby reducing weight while ensuring stiffness (**Fig. 4**).

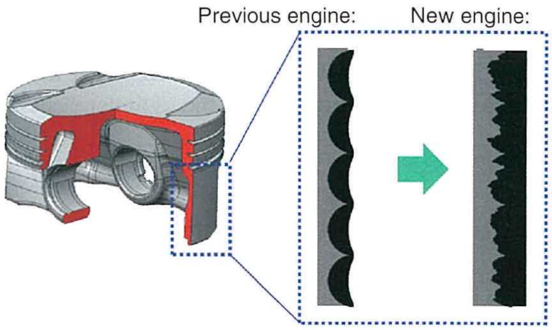

Fig. 3 Piston Skirt Design

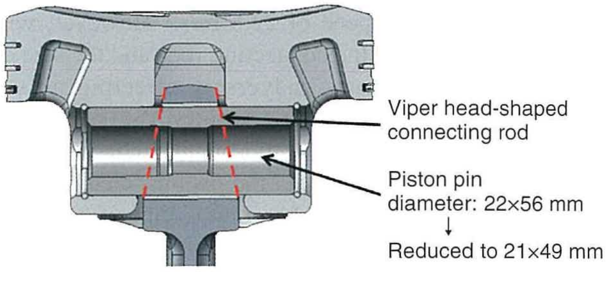

Fig. 4 Piston Pin Design

One of the main issues of increasing the engine speed is oil consumption at high piston speeds. This was addressed by refining the oil rings. By designing a higher side rail end shape than the previous engine, the refined oil rings reduced the thickness of the oil film by 30% and cut down the amount of residual oil. The use of thinner and less stiff oil rings than in the previous engine also helps the piston to track the geometry of the bore more closely (**Figs. 5** and **6**). The trade-off effect on abrasion was addressed by adopting a chromium nitride coating with excellent abrasion resistance. Other refinements, such as the adoption of a diamond-like coating (DLC) around the rings and reducing the width around the periphery of the second ring, also reduced friction while improving oil consumption.

Incorporating these technologies reduced the weight of a single piston by approximately 7% compared to the previous engine (**Fig. 6**).

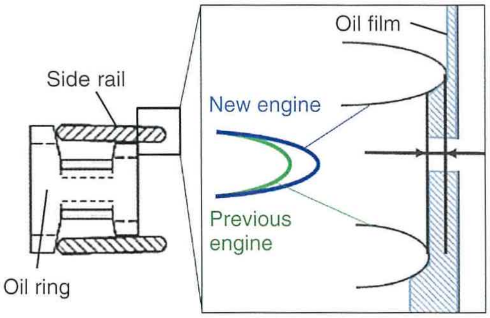

Fig. 5 Side Rail End Design

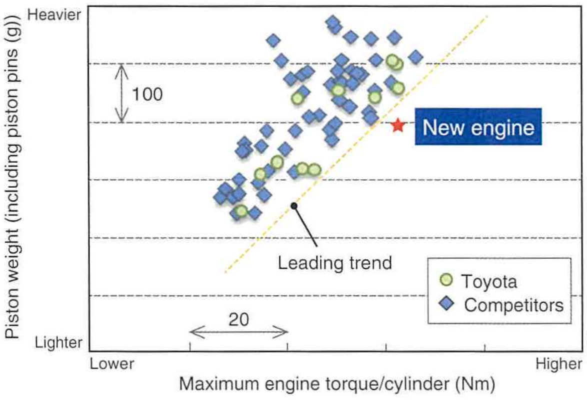

Fig. 6 Piston Weight Comparison

4. Connecting Rods

As described above, the stiffness of the pistons was secured while reducing the weight of the connecting rods by adopting viper head-shaped small ends.

The forging was created using high-strength steel with a tensile strength 30% greater than the previous material.(1) This enabled the adoption of a thinner column than the previous part, thereby reducing the sectional area of the column by approximately 25% (**Fig. 7**).

At the big end, the pin diameter was reduced by 3.5 mm to 48 mm. In addition, the shape around the big end was designed to reduce weight in consideration of the input force from combustion and the inertial load. The input moment of each section was calculated for each angle centered on the big end, enabling the design of an optimum section shape that creates a sufficient geometrical moment of inertia. **Fig. 8** shows the geometrical moment of inertia for each angle from the center of the big end. The geometrical moment of inertia between 40 and 60 degrees was reduced from the previous design, thereby reducing weight.

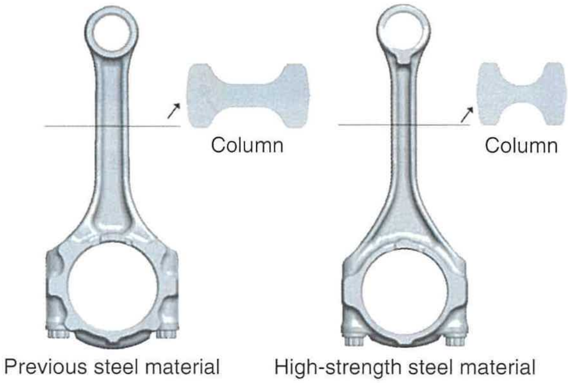

Fig. 7 Connecting Rod Design Comparison

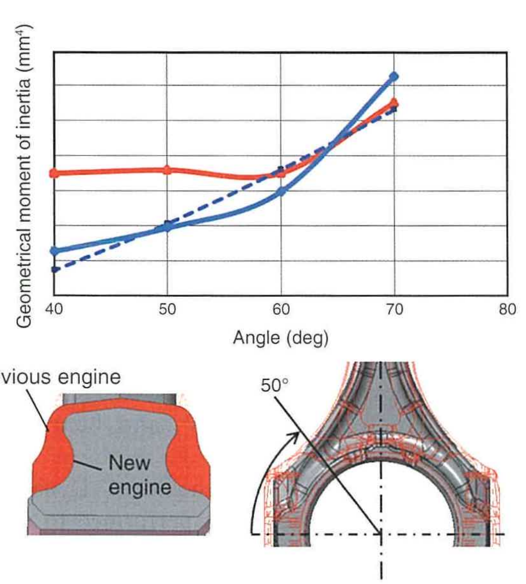

Fig. 8 Distribution of Geometrical Moment of Inertia of Connecting Rod Big End

Although the force of combustion exposes the connecting rod bearings to large surface pressures, reducing the thickness of the top portion of the connecting rod big end disperses the pressure on the bearings and improves bearing seizure resistance (**Fig. 9**).

These changes reduced the weight of the connecting rod by approximately 17% compared to the previous part. Furthermore, the combined improvements to the pistons and connecting rods enabled weight reduction of 13%, greater than the target of 10%.

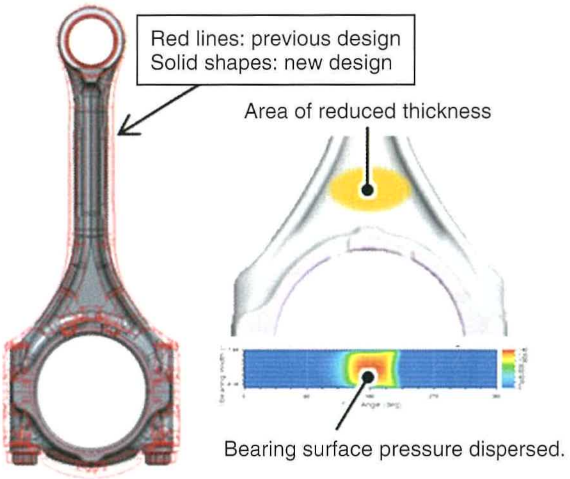

Fig. 9 Surface Pressure of Connecting Rod Bearings

5. Crankshaft and Cylinder Block

The trade-off effects of high engine speeds, high cylinder pressures, and a long stroke design include higher inertial load, greater force applied to the cylinder block due to lower crankshaft stiffness, and deterioration in NV, particularly the tapping noises created by the crankshaft. In response, the development aimed to realize the system specifications while retaining the balance between the cylinder block and crankshaft dimensions, and to maintain the same engine size to ensure vehicle mountability.

First, to increase the stiffness of the crankshaft as a measure against NV, the journal width was shortened by 1 mm and the crankshaft shoulders were widened. However, increasing only the shoulder stiffness creates a vicious cycle of higher weight and deterioration in inertial load, requiring further increases in cylinder block weight. Therefore, well-balanced shoulders that achieve both stiffness and weight targets were required to satisfy the cylinder block strength, NV, and bearing strength requirements.

3D CAE was used to design the shoulders. Dynamic analysis of the whole cylinder system was performed to design each shoulder while confirming the strength and reliability of the cylinder block, NV, and the seizure resistance of the bearings. As a result, the stiffness of each shoulder differs, and a different weight balance is also created (**Fig. 10**). **Fig. 11** shows the stiffness ratio of each cylinder. Since the effects of inertial force due to rotation are particularly high around the No. 3 journal, the design prioritized weight reduction to lower the force applied to the cylinder block. In contrast, since the areas around the No. 1 and No. 4 pins have a major effect on NV, the design prioritized the stiffness of these areas.

For the cylinder block, in addition to reducing the thickness of the journal by 1 mm, stress was reduced by widening the connecting portion with the bottom rail (**Fig. 12**). In addition, the bottom of the water jacket was designed to reduce stress by approximately 25% by adopting an elliptical radius at the cylinder head bolt side, where assembly stress is high (**Fig. 13**).

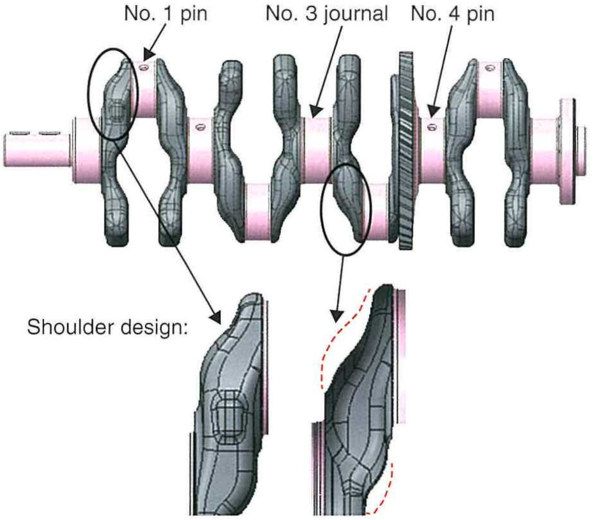

Fig. 10 Crankshaft Shoulder Design

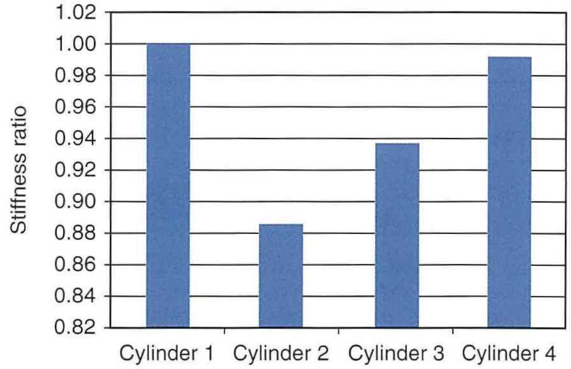

Fig. 11 Crankshaft Stiffness for each Cylinder

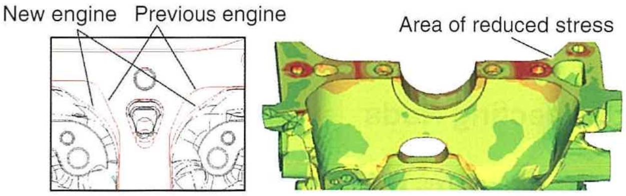

Fig. 12 Cylinder Block Stress Analysis

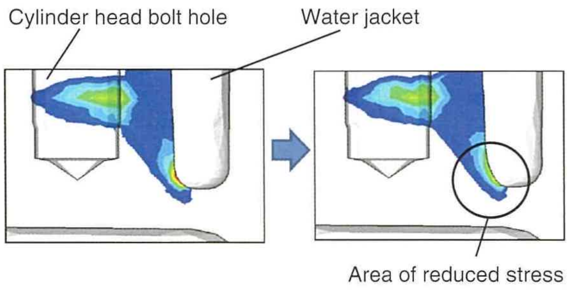

Fig. 13 Stress Generated at Water Jacket Bottom

The size of the engine was maintained by applying a similar stress-reducing approach to other areas in which stress concentrates and increasing the stiffness of only the necessary portions in the design of the cylinder block.

Various friction-reduction technologies were adopted. Friction due to the application of force was reduced by applying a resin coating to the connecting rod bearings and main bearing sliding surfaces. Furthermore, a continuously variable discharge oil pump and low-viscosity engine oil (rated 0W-16 by the Society of Automotive Engineers (SAE)) were adopted in the lubrication system. The combination of low-viscosity oil and variable control of the oil pump discharge volume enables the optimum supply of the required amount of oil, thereby reducing the sliding resistance of the bearings. Since this approach has the trade-off effects of generating heat and increasing input forces, fatigue strength was improved by adopting a stronger bearing lining material and modifying the microstructure by reducing the tin (Sn) content.(2)

By combining the newly designed crankshaft and cylinder block with the lighter pistons and connecting rods described in the previous sections, the cylinder system satisfied the strength and NV requirements without enlarging the size of the engine. Friction was also reduced by approximately 15% compared to the previous engine (**Fig. 14**).

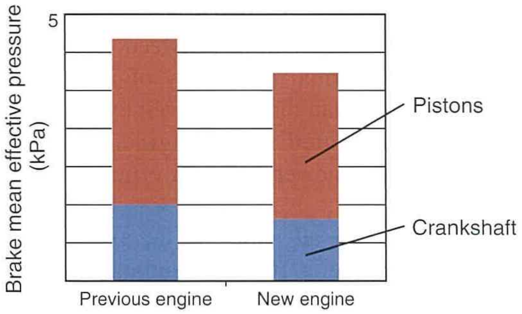

Fig. 14 Friction Comparison

6. Conclusion

Weight and friction reduction technologies were incorporated into the cylinder system (i.e., the pistons, connecting rods, crankshaft, cylinder block, and bearings), which reduced the weight of the pistons and connecting rods by 13%, and the overall friction of the system by 15%.

- A 7% reduction in weight compared to the previous engine was achieved by adopting thinner piston walls and by shortening the distance between the pin bosses using viper head-shaped connecting rods. In addition, friction was reduced by changing the surface treatment of the skirts.
- Adopting high-strength steel and modifying the big end design reduced the weight of the connecting rods by 17%.
- 3D CAE was adopted to finalize the shape of the crankshaft and cylinder block, which were designed with careful attention to the portions requiring optimum stiffness.

Measures were also adopted to suppress increases in weight, and the power performance target was achieved without enlarging the size of the engine compared to the previous generation.

References

(1) N. Shinohara, Tanahashi, Kitano, Fukazawa, Imagawa et al. "High Strength Free Cutting Steel for Connecting Rod." *Transactions of Society of Automotive Engineers of Japan* Vol. 46 No. 4 (2015) pp. 825-829.

(2) T. Desaki, Kamiya. "Development of the New Aluminum Alloy Bearing for Small-sized Diesel Engines." *Proceedings of the JSAE Annual Congress* (1998).

Note: this article is based on the following published technical paper.
T. Hiranuma, Yamashita, Terada, Nakamura et al. "Cylinder System Development of the New Inline 4-Cylinder 2.5L Gasoline Engine." *Proceedings of the JSAE Annual Congress* (2017) pp. 1841-1845.

Authors

T. HIRANUMA

C. YAMASHITA

T. TERADA

K. NAKATA

M. NAKAMURA

T. KURAUCHI

The New Toyota V6 3.5-Liter Turbocharged Gasoline Engine

Takao Yuasa[*1]
Daichi Yamazaki[*1]
Akio Mori[*1]
Shinichiro Nogawa[*2]

Abstract

In association with the completely redesigned Lexus LS, Toyota Motor Corporation has developed a new V6 3.5-liter turbocharged engine. This engine can be installed in vehicles designed based on a low-center-of-gravity, low-hood concept, and is also compatible with future regulations and environmental requirements. The development of this turbocharged engine targeted a power performance of 310 kW (specific power: 90 kW/L) and 600 Nm (between 1,600 and 4,800 rpm), which is equivalent to V8 turbocharged engines in competing vehicles. This target was accomplished by adopting a new highly efficient turbocharger and high-speed combustion, and by incorporating technologies such as laser-clad valve seats in the intake ports. A prototype vehicle installed with this engine and the direct-shift 10-speed automatic transaxle achieved a 0-to-60 mph acceleration time of 4.6 seconds, which is in the same class as competing vehicles installed with V8 turbocharged engines, as well as fuel efficiency of 23 mpg.

Keywords: *internal combustion engine, spark injection (SI) engine, high-speed combustion, turbocharger, performance/fuel efficiency/efficiency, tumble flow*

1. Introduction

In association with the complete redesign of the Lexus LS, Toyota Motor Corporation has developed a new V6 3.5-liter turbocharged gasoline engine. This development aimed to achieve the following three targets to reflect the status of the LS as the flagship model of the Lexus brand.

(1) Dynamic performance and driveability: acceleration time and feeling equivalent to competing models equipped with turbocharged V8 engines, with sharp and flat torque characteristics and response
(2) Environmental performance: fuel efficiency that surpasses competing models and emissions performance that satisfies emissions regulations in the U.S. beyond 2023
(3) Noise and vibration (NV): an evolution of the renowned elegance and smoothness of previous generations of the LS

This article describes an outline of this new gasoline engine and its main technologies.

2. Setting of Development Target Values

Fig. 1 shows the relationship between the dynamic performance and fuel efficiency targeted in the development of the new LS. The development aimed to achieve a 0-to-60 mph acceleration time and fuel efficiency surpassing competing models equipped with V8 turbocharged engines and 8- or 9-speed automatic transmissions. For the engine, the development aimed to achieve maximum power of 310 kW, maximum torque of 600 Nm (at between 1,600 and 4,800 rpm), and a maximum thermal efficiency of 37%, figures that are substantially higher than those achieved by the previous V8 4.6-liter naturally aspirated (NA) engine. **Fig. 2** shows the competitive specific power and fuel efficiency performance of the new LS.

Additionally, to take advantage of the excellent driveability of a turbocharged engine, a 10-speed automatic transmission with rhythmical shifting performance was adopted that makes active use of low engine speed and high-torque engine operating regions to achieve graceful and smooth acceleration. **Fig. 3** shows the torque rate trends of individual engines. Based on vehicle G simulations, a torque rate target was set for the engine that is close to the highest trend line achieved by competing models.

[*1] Engine Design & Engineering Div., Powertrain Company
[*2] Electric Powertrain System Development Div., No. 3, Powertrain Company

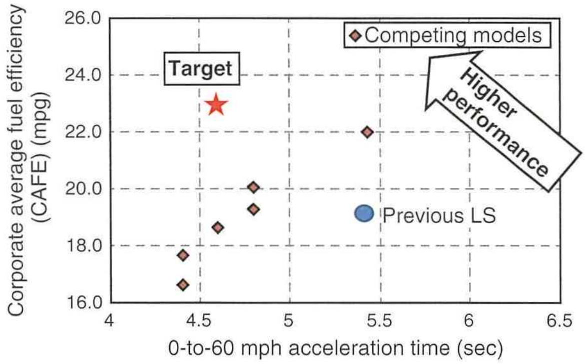

Fig. 1 Power Performance and Fuel Efficiency Targets of the New LS

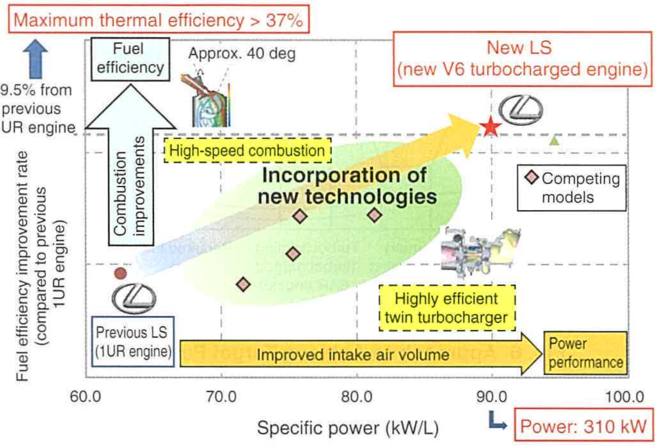

Fig. 2 Competitive Specific Power and Fuel Efficiency Performance of New Engine

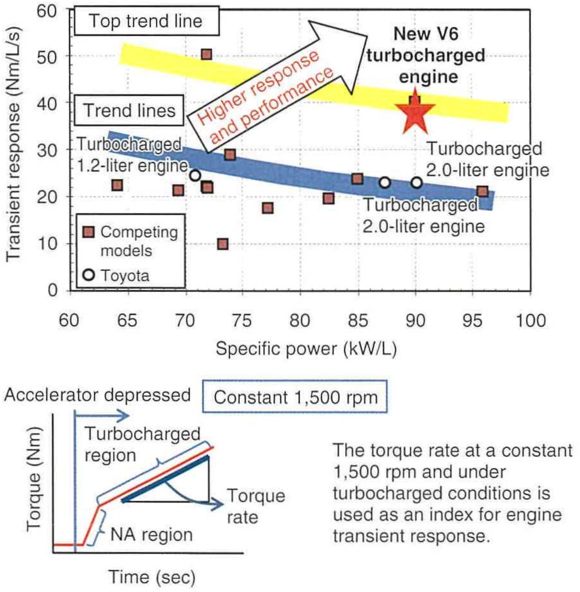

Fig. 3 Engine Torque Rate Trends

In addition to the high performance targets described above, a smartly packaged 3.5-liter V6 engine was selected to realize the low-center-of-gravity, low-hood design concept of the new LS (**Photo 1**), while enabling flexible response to future regulatory and environmental trends related to fuel efficiency and emissions. Furthermore, the new LS adopts Active Noise Cancel (ANC) and Engine Sound Enhancement (ESE) systems to counter the higher vibration of a V6 engine. These systems enable the new LS to uphold and advance the model's renowned quietness, elegance, and smoothness. To complement the smart packaging of the engine and power performance equivalent to rival V8 engines, a highly efficient twin turbocharger was developed and incorporated into the high-speed combustion concept of the Toyota New Global Architecture (TNGA) design philosophy, resulting in improved combustion and higher power. The following sections describe the details of the technologies incorporated into the new engine to achieve these performance targets.

Photo 1 Design of the New LS

3. Technologies Developed to Improve Full Load Performance

3.1 Approach for achieving target performance and torque curve

Fig. 4 shows the bench power performance torque curve target of the new V6 turbocharged engine. Compared to the previous 1UR-FSE V8 4.6-liter NA engine, the development targeted greatly improved performance at both low and high engine speeds.

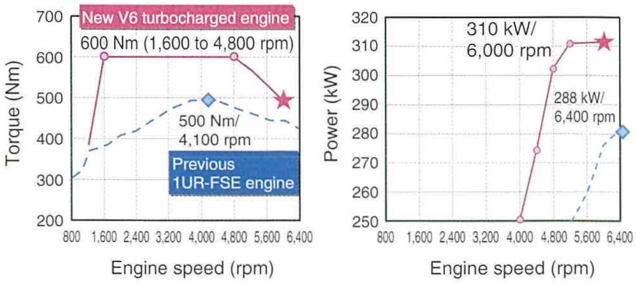

Fig. 4 Engine Torque and Power Comparison with Previous Engine

Reflecting the status of the LS as a flagship model, the development focused on achieving a smooth and comfortable acceleration feeling from low speeds. Turbocharger specifications to achieve a maximum torque of 600 Nm at 1,600 rpm were studied. **Fig. 5** shows the turbocharger compressor maps examined in the development. A turbocharger developed based on the unit used in the 2.0-liter 8AR-FTS engine launched in 2014 generates 600 Nm at an engine speed of 1,850 rpm. This means that the size of the turbocharger had to be reduced to achieve the target of 1,600 rpm while avoiding surging. However, the air flow rate of the compressor would be insufficient at the choke limit to reach the target power performance of 310 kW at 6,000 rpm. Various measures were applied to achieve the required air flow rate, including increasing the efficiency of the intake system and turbocharger, increasing the boost pressure by promoting combustion, and improving knocking. These measures helped to realize the targeted turbocharging characteristics over a wide range from low to high engine speeds.

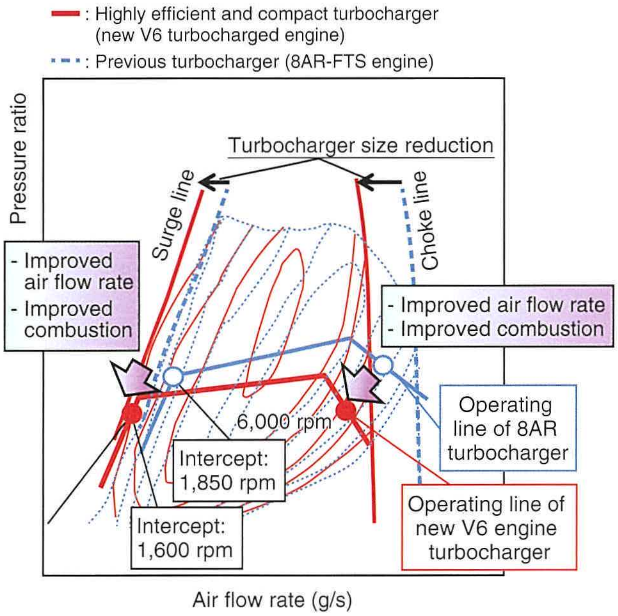

Fig. 5 Operating Points of Turbine Compressor

Fig. 6 shows the cumulative effect of the technological improvements to the turbocharger for power at 6,000 rpm and torque at 1,600 rpm. The shortfall in torque of the compact turbocharger developed based on the turbocharger in the previous 8-AR FTS engine was offset by a combination of improvements to the air flow rate and combustion.

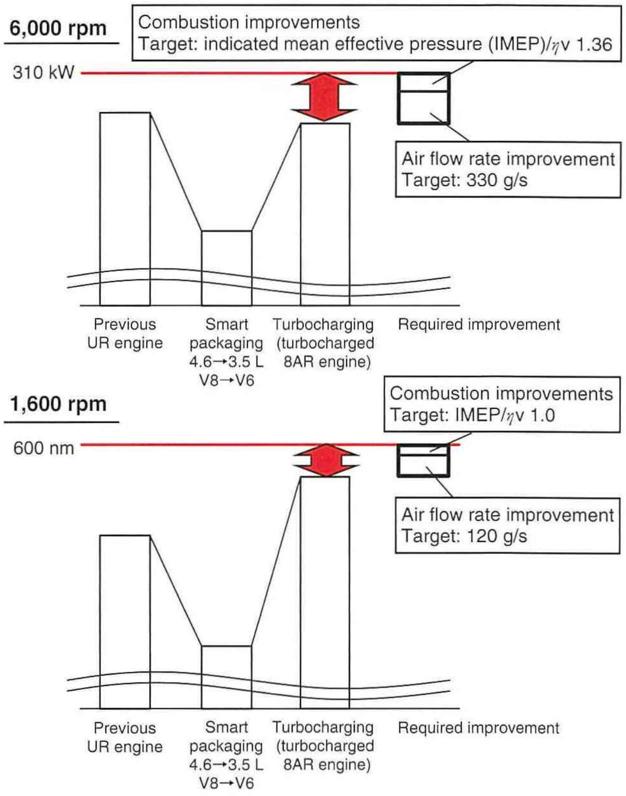

Fig. 6 Approach to Achieve Target Performance

Table 1 outlines the technology adopted to achieve the target air flow rate and combustion improvements. After defining the targets through more specific physical values, the technologies required to achieve the targets were developed and combined. The following sections describe the following newly developed technologies in more detail: improved turbocharger efficiency through the adoption of highly efficient turbine blade geometry, improved boost pressure through the application of turbocharging to Toyota's high-speed combustion concept, the simultaneous achievement of the necessary flow coefficient and high-speed combustion through the adoption of highly efficient intake ports (laser-clad valve seats), and advanced ignition timing through the adoption of multi-point oil jets to facilitate high-speed combustion and cool the exhaust side of the pistons.

Table 1 Technologies Adopted to Achieve Performance Targets

6,000 rpm

Target	Detailed targets		Technologies adopted to achieve targets
Improvement of air flow rate to 330 g/s	Turbocharger efficiency ηtot: A%		Highly efficient turbocharger
	Boost pressure: 194 kPa		Application of turbocharging to high-speed combustion concept
	Improvement of charging efficiency ηvb to B%	Flow coefficient Cf: 0.46	Highly efficient intake ports (laser-clad valve seats)
		Intake pressure loss: C kPa	Surge tank adopting new manufacturing method (welding rib height reduced by carrying out welding after infrared heating)
		Intake temperature: D°C	- Highly efficient intercooler - Installation of intercooler directly onto intake manifold
		Exhaust pressure loss: E KPa	Exhaust pipe clamshell
Improvement of IMEP/ηv of combustion to 1.36	Ignition timing θPmax: F ATDC		Application of turbocharging to high-speed combustion concept
			Higher direct injector flow rate
			Piston exhaust side cooling using multi-point oil jets
			Improved cooling between cylinder bores

1,600 rpm

Target	Detailed targets		Technologies adopted to achieve targets
Improvement of air flow rate to 120 g/s	Turbocharger efficiency ηtot: A%		Highly efficient turbocharger
	Improvement of boost pressure to 194 kPa		Application of turbocharging to high-speed combustion concept
	Charging efficiency ηvb: G%	Improvement of flow coefficient Cf to 0.46	Highly efficient intake ports (laser-clad valve seats)
		Intake temperature: D°C	- Highly efficient intercooler - Installation of intercooler directly onto intake manifold
Improvement of IMEP/ηv of combustion to 1.03	Ignition timing θPmax: H ATDC		Application of turbocharging to high-speed combustion concept
			Higher direct injector flow rate
			Avoidance of scavenging

3.2 Technologies adopted to improve air flow rate

3.2.1 Highly efficient turbocharger

A new compact and highly efficient turbocharger was developed in-house to achieve the targeted turbocharging efficiency. The turbocharger on the 8AR engine utilizes highly efficient curved compressor blades manufactured by an existing cutting technique for forged parts. A new high-efficiency turbine blade design was developed based on this approach. Conventional design approaches emphasize achieving a low moment of inertia by shortening the length of the blades and limiting the amount of curvature to reduce size. In contrast, this development focused on increasing the efficiency of exhaust energy absorption by lengthening the blades and increasing the amount of curvature (**Fig. 7**).

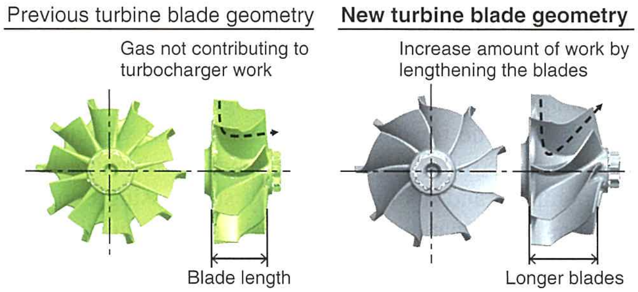

Fig. 7 New Turbine Blade Design

The mechanical efficiency of the turbocharger was further increased by improving the total shut-off performance through the adoption of an electric wastegate valve (**Fig. 8**), increasing the work of the blades by optimizing the inlet blade height through computational fluid dynamics (CFD), reducing the moment of inertia by adopting a thin blade geometry that prevents resonance, and improving aerodynamic characteristics by adopting a die-cast compressor housing. As a result, world-leading turbine mechanical efficiency was realized (**Fig. 9**), and the target turbocharging efficiency of ηtot=42% was achieved.

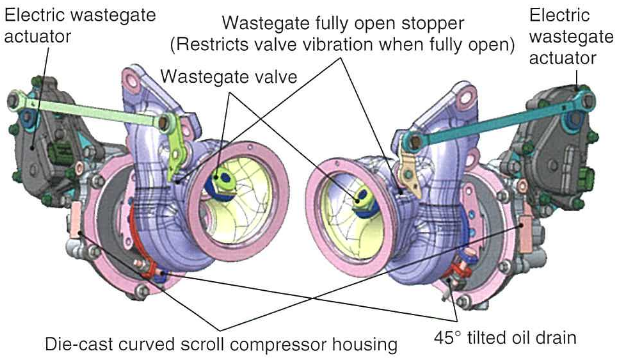

Fig. 8 Electric Wastegate Actuator

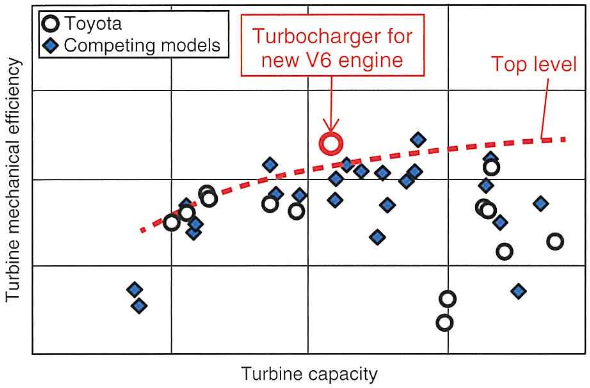

Fig. 9 Turbine Mechanical Efficiency Trends

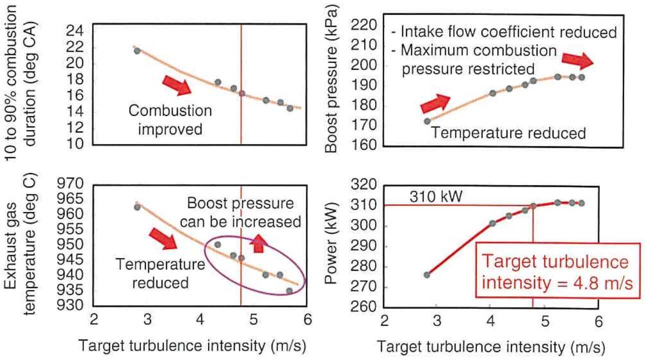

Fig. 11 Relationship between Turbulence Intensity, Combustion Speed, and Exhaust Gas 1/ Temperature in Turbocharged Engine

3.2.2 Application of turbocharged engine to high-speed combustion concept

To realize higher specific power and thermal efficiency, Toyota is developing new TNGA powertrains based on a high-speed combustion concept. The first engine in this series was a 2.5-liter NA engine for conventional and hybrid vehicles (HVs) that was launched in 2017.(1) High-speed combustion helps to reduce pumping and cooling losses by suppressing combustion fluctuations and expanding the exhaust gas recirculation (EGR) limit (point (1) in **Fig. 10**). It also allows higher compression ratios by restricting knocking (point (2)).(2) This development applied a turbocharged engine to the high-speed combustion concept to further increase both specific power and thermal efficiency by raising the boost pressure (point (3)).

As **Fig. 11** shows, the boost pressure can be increased by promoting combustion to lower the exhaust gas temperature. However, substantially increasing turbulence intensity may saturate power improvements by lowering the intake flow coefficient and limiting the maximum combustion pressure of the engine. This development targeted a turbulence intensity of 4.8 m/s to realize the maximum power target of 310 kW.

Therefore, the development determined the specifications for achieving the required turbulence intensity by examining the relevant causal factors. **Fig. 12** shows the time history of the in-cylinder unsteady tumble ratio and turbulence intensity, as well as the combustion specifications that determine these characteristics. Unsteady tumble attenuates as the crank angle advances toward top dead center (TDC), after passing through peak A, which is caused by the intake inflow, and peak B during the compression stroke, which is caused by the formation of the tumble flow. In contrast, turbulence intensity also includes peak C after unsteady tumble peak B, which occurs when the tumble flow is compressed as the piston rises and is transformed into turbulence. Subsequently, turbulence intensity attenuates as the crank angle advances toward TDC and passes through peak D prior to combustion. Based on the results of experiments as well as one- and three-dimensional simulations, the specifications for achieving the target value for peak D were determined based on the four basic engine specifications indicated in **Fig. 11**. After incorporating these assumptions, the development determined the basic combustion-related specifications to achieve the required turbulence intensity of 4.8 m/s in a V6 3.5-liter turbocharged engine.

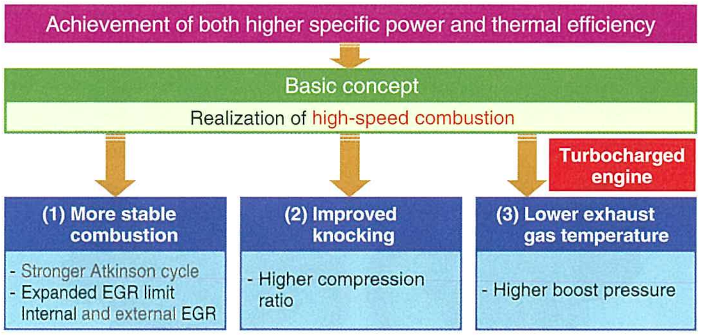

Fig. 10 Application of Turbocharged Engine to High-Speed Combustion Concept

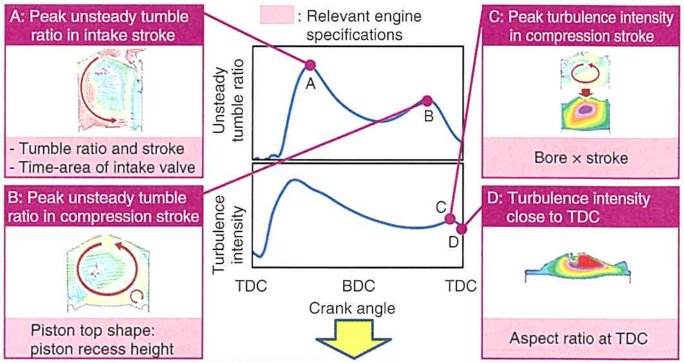

Stroke/bore	1.17
Tumble ratio	2.6
Time-area of intake valve ($mm^2 \cdot CA$)	1,637
Aspect ratio at TDC	0.192
Piston recess height (mm)	3.6

Fig. 12 Target Basic Combustion-Related Specifications of New Engine

The details of the piston top shape are as follows. To intensify (i.e., to inhibit the attenuation of) the turbulence at peaks B and D in **Fig. 12**, it is important to design a piston top shape and aspect ratio that guide the turbulent flow smoothly to the area around the spark plug without blocking the flow path. **Fig. 13** compares the piston shapes used in an inline 4-cylinder 2.5-liter engine and the newly developed V6 turbocharged engine, as well as the turbulence intensity achieved in both engines. The obtainable recess heights differ between an NA engine with a high compression ratio and a turbocharged engine with a lower compression ratio. Therefore, since the piston top shapes capable of achieving the greatest improvement in turbulence intensity also differ, shape B, which is more suitable for the compression ratio of a turbocharged engine, was adopted.

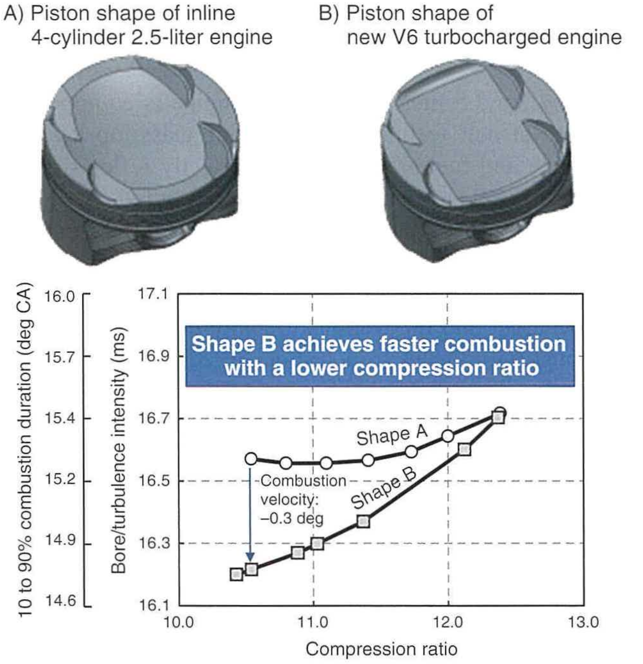
A) Piston shape of inline 4-cylinder 2.5-liter engine

B) Piston shape of new V6 turbocharged engine

Fig. 13 Comparison of Turbulence Intensity Due to Piston Top Shape

3.2.3 Highly efficient cylinder head intake ports

A flow coefficient of 0.46 is necessary to achieve the target air flow rate. At the same time, as described in **Section 3.2.2**, a tumble ratio of 2.6 must also be achieved. Although mainly controlled by the shape of the cylinder head intake ports, these two factors are generally regarded as having a trade-off relationship. As a result, some form of technological feedback is required to achieve both factors. The engine development revised the valve included angle and throat height of the cylinder head intake ports. Laser-clad valve seats were adopted to enable more linear flows into the cylinder and to achieve the targeted throat height. **Fig. 14** compares the relationship between tumble ratio and flow coefficient for the previous 1UR and newly developed engines. The new engine achieves the targets for both tumble ratio and flow coefficient with values at the top of the relationship trend.

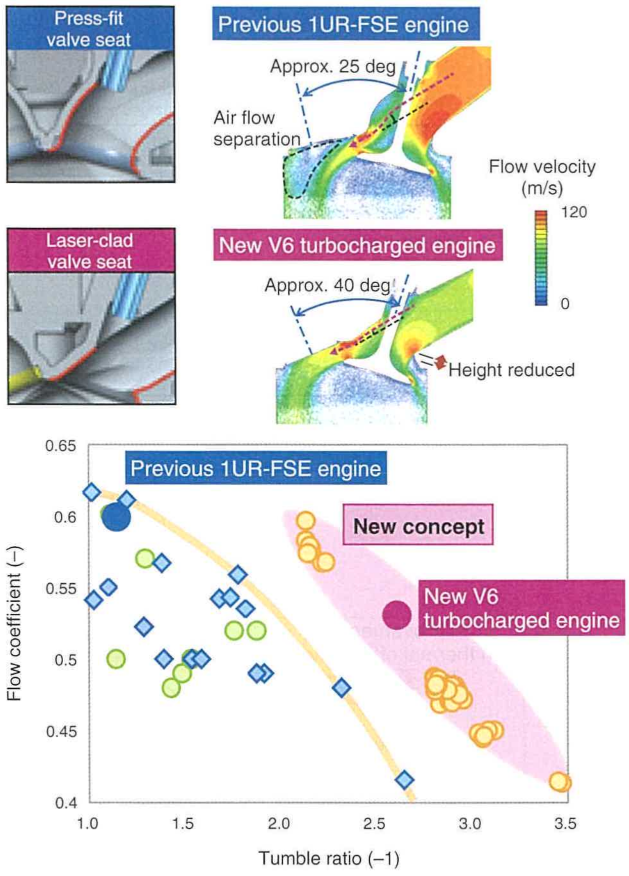

Fig. 14 Comparison of Intake Port Shapes and Relationship between Tumble Ratio and Flow Coefficient

3.3 Combustion improvements (improved knocking through high-speed combustion)

This section describes the evaluation results using a prototype V6 turbocharged engine incorporating the high-speed combustion concept described in **Section 3.2.2**. **Fig. 15** shows the 200-cycle distribution of the 10-to-90% combustion velocity and 50% heat release rate timing (CA50). Compared to the 8AR-FTS engine that uses the conventional concept, the new engine advances the CA50 timing by promoting combustion. In addition, as shown in **Fig. 16**, it also improves knocking while increasing the compression ratio from 10 to 10.5.(3)

As a result, a maximum thermal efficiency of 37% was achieved while also accomplishing the targeted power performance. In addition, the fuel efficiency targets were achieved through measures including the incorporation of heat management technologies through the adoption of a newly developed coolant control valve.

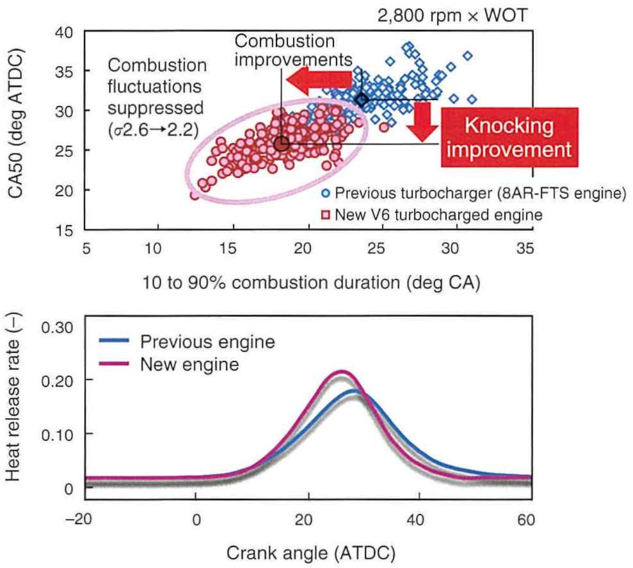

Fig. 15 Results of Combustion Velocity Confirmation

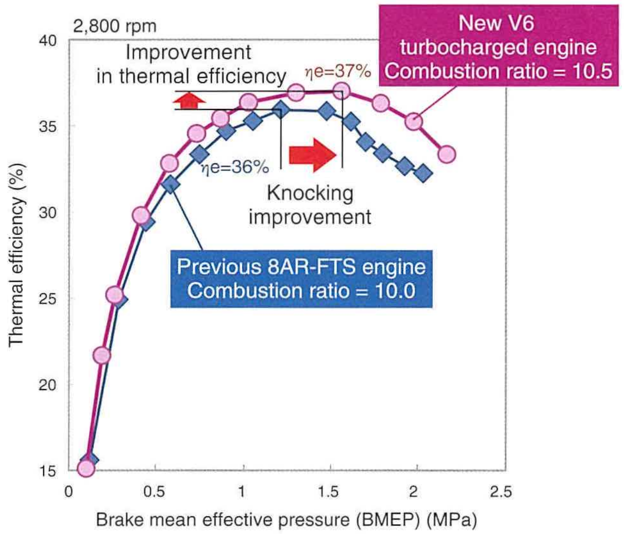

Fig. 16 Thermal Efficiency Confirmation Results

4. Vehicle Performance Summary

This section summarizes the dynamic performance and fuel efficiency accomplished by the new LS installed with the prototype V6 engine described above.

Fig. 17 shows the acceleration time and fuel efficiency of the LS. By combining the low end torque of this V6 turbocharged engine and wide gear ratios of the Direct-shift 10-speed automatic transmission, the rear-wheel drive LS achieved a 0-to-60 mph acceleration time of 4.6 seconds with a combined North American fuel efficiency rating of 23 mpg. This dynamic performance is equivalent to competing models installed with V8 engines, and the fuel efficiency is at the top of its class.

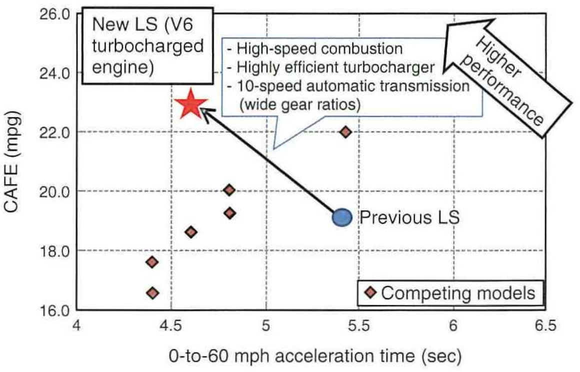

Fig. 17 0-to-60 mph Acceleration Time and CAFE Combined Fuel Efficiency Confirmation Results of New LS

5. Conclusion

This new V6 3.5-liter turbocharged engine is equipped with a wide range of new technologies, enabling class-top level power performance and fuel efficiency and perfectly reflects the status of the LS as the flagship model of the Lexus brand.

(1) Targeting power performance that surpasses competing models equipped with V8 engines, flow rate improvement technology was developed such as a highly efficient turbocharger and innovations to apply the TNGA high-speed combustion concept to a turbocharged engine. Combined with the TNGA high-speed combustion improvement technologies, the new engine achieved the targeted maximum torque of 600 Nm (at between 1,600 and 4,800 rpm) and power of 310 kW (specific power: 90 kW/L). The engine also achieved a maximum thermal efficiency of 37% and the targeted fuel efficiency.

(2) A prototype LS equipped with this V6 3.5-liter turbocharged engine and the Direct-shift 10-speed automatic transmission achieved a 0-to-60 mph acceleration time of 4.6 seconds with a combined fuel efficiency rating of 23 mpg. This dynamic performance is equivalent to competing models installed with V8 engines, and the fuel efficiency is at the top of its class.

References

(1) M. Hakariya, Toda, Sakai. "The New Toyota Inline 4-Cylinder 2.5 L Gasoline Engine." *SAE Paper* No. 2017-01-1021 (2017).

(2) E. Murase, Shimizu. "Innovative Gasoline Combustion Concepts for Toyota New Global Architecture." *25th Aachen Colloquium Automobile and Engine Technology* (2016).

(3) I. Watanabe, Kawai, Yonezawa, et al. "The New Toyota 2.0-Liter Inline 4-Cylinder ESTEC D-4ST Engine-Turbocharged Direct Injection Gasoline Engine." *23rd Aachen Colloquium Automobile and Engine Technology* (2014).

Note: this article is based on the following published technical paper.
T. Yuasa, Yamazaki, Nogawa, Mori. "The New V6 3.5L Turbocharged Gasoline Engine." *Proceedings of the JSAE Annual Congress* (2017) pp. 800-805.

Authors

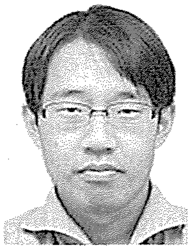

T. YUASA

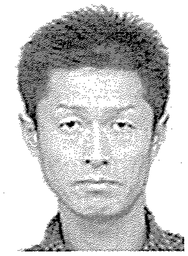

D. YAMAZAKI

A. MORI

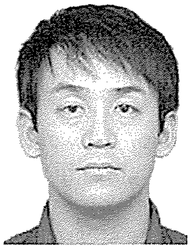

S. NOGAWA

Development of Cooling System for the New Toyota 3.5-Liter V6 Turbocharged Gasoline Engine

Daisaku Morishita*1
Naoya Kawamoto*2
Yusuke Niwa*1
Naoto Hisaminato*3
Mitsuru Yamaguchi*4
Hirokazu Ando*3

Abstract

This article describes the cooling system of the new 3.5-liter V6 turbocharged gasoline engine developed by Toyota Motor Corporation. The cooling system of this engine was substantially redesigned to help achieve high power, while ensuring superlative fuel efficiency with excellent air-conditioning performance. Refinements included greatly reducing the flow resistance of the coolant in the engine, and the adoption of thermal management using a water control valve (WCV). The WCV is capable of controlling how much coolant flows to which engine device, and can prioritize flow to devices requiring coolant. Accordingly, this cooling system supports rapid engine warm-up by reducing coolant flow to zero (thereby helping to improve fuel efficiency), while also enhancing heater performance by prioritizing coolant flow to the heater core.

Keywords: *engine cooling system, thermal management, water control valve, rapid engine warm-up*

1. Introduction

Toyota Motor Corporation has developed a new V6 3.5-liter turbocharged gasoline engine as part of a series of engines based on the Toyota New Global Architecture (TNGA) design philosophy. This engine features an innovative structure that was developed to surpass the power performance of the previous naturally aspirated (NA) V8 4.6-liter engine while achieving acceleration, fuel efficiency, and environmental performance equal to or better than competing models. In addition to the new turbocharging system and basic structure to support the generation of high power, this engine also incorporates substantially refined thermal management (i.e., the optimization of heat energy) using the cooling system to boost the combustion chamber cooling performance. This cooling system helps to warm-up the engine more quickly, boost the cooling and heating performance of the air-conditioning system, lower friction at low engine loads, and enhance knocking resistance at high engine loads. This article describes these points in more detail.

2. Development Aims

2.1 Measures in response to higher engine power

Since the new engine features higher power than the previous engine, the development needed to boost the cooling performance around the combustion chambers. One simple way to raise the coefficient of heat transfer (i.e., the fluid velocity) of the coolant is to increase the lift of the water pump. However, since enlarging the water pump increases the susceptibility to cavitation (a phenomenon in which the saturated vapor pressure of the coolant is exceeded due to the negative pressure created by suction), the flow resistance of the coolant passages was thoroughly reduced in line with the larger water pump lift.

2.2 Measures to enhance both fuel efficiency and air-conditioning performance

Increasing the thermal efficiency (i.e., the fuel efficiency) of an engine can result in delayed engine warm-up or lower the performance of the occupant compartment heater system, which uses coolant as a heat source. Delayed engine warm-up is caused by the coolant temperature taking longer to reach the temperature that permits engine stop control during idling, as well as by delayed transition to the post warm-up control, which reduces the fuel efficiency enhancement effect of the control. This issue was addressed by compensating for the insufficient amount of heat by controlling the coolant flow rate and by appropriately switching the control of the vehicle devices (the radiator, heater core, and automatic transmission fluid warmer (ATF/W)).

Delays in engine warm-up were resolved by completely stopping coolant flow to the vehicle devices. This enables rapid engine warm-up by restricting the thermal mass around the engine combustion chambers. Heater system performance was enhanced by flowing engine coolant to the heater core only, thereby directing all of the heat from the engine to the heater system. To boost the cooling (air-conditioning) performance when required, the coolant flow to the heater is cut, eliminating the effects of heat radiation from the heater core and increasing cooling efficiency. In addition, when higher engine performance is required, the coolant flow to the radiator is increased and the temperature of the engine coolant and combustion chamber walls

---

[*1] Engine Design & Engineering Div., Powertrain Company
[*2] EHV Battery Design Div., Powertrain Company
[*3] Electric Powertrain System Development Div., No. 2, Powertrain Company
[*4] Electric Powertrain System Development Div., No. 3, Powertrain Company

is lowered to raise the knock limit, thereby allowing the ignition timing to be advanced. Furthermore, at low loads, the coolant flow to the radiator is reduced, thereby increasing the temperature of the engine coolant and combustion chamber walls and lowering engine friction (raising the coolant temperature also has the effect of increasing the oil temperature), which results in higher fuel efficiency.

The engine implements the thermal management of the coolant circuit described above using a water control valve (WCV) to switch the connections between the engine and vehicle devices as well as to control the coolant flow rate.

Since the WCV also functions as a thermostat (the part that controls the engine coolant temperature), the thermostat in the radiator coolant passages can be removed. This eliminates the pressure loss generated by the thermostat, thereby helping to increase the cavitation limit and boost the heat dissipation capacity of the radiator.

These refinements to the cooling system help the engine to realize its potential power performance, fuel efficiency, and air-conditioning performance.

Table 1 compares the specifications of the newly developed engine with this cooling system (**Fig. 1**) and the previous V8 4.6-liter NA engine.

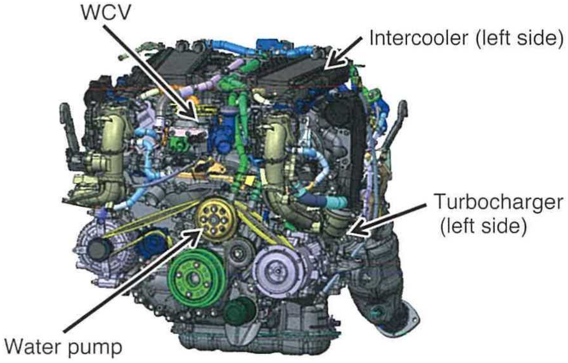

Fig. 1 External Appearance of New Engine

Table 1 Comparison of Main Engine Specifications

Engine		New engine	Previous engine
Engine type		V6	V8
Displacement (cc)		3,445	4,608
Bore diameter × stroke length (mm)		85.5x100	94x83
Compression ratio		10.5	11.8
Maximum power (kW/rpm)		310/6,000	288/6,400
Maximum torque (Nm/rpm)		600/1,600 to 4,800	500/4,100
Cooling system	Turbochargers	Two (right and left banks)	None
	Intercoolers	Water-cooled	None
	Water pump	Belt-driven	Belt-driven
	Component used to vary coolant flow	WCV	None
	Component used to adjust coolant temperature	WCV	Thermostat (valve opens at 82°C)
	Low temperature coolant circuit	For turbochargers and intercoolers	None
	External exhaust gas recirculation (EGR) system	None	None

3. Cooling System Technologies

3.1 Coolant circuit flow resistance reduction

The development investigated the flow resistance of the coolant circuit from the engine to the radiator (**Fig. 2**). Engine flow resistance accounts for approximately 60% of the total resistance, the radiator for 25%, and other cooling pipes for the remaining 15%. The size of the radiator and cooling pipes determines the flow resistance of these components. In contrast, the flow resistance of the engine is determined by the shape of the water jacket and the pressure loss of the thermostat. Since the thermostat was eliminated by the adoption of the WCV, the development focused on optimizing the shape of the engine water jacket.

Flow resistance can be reduced by shortening the distance of coolant flow and increasing the number of coolant passages. The engine cylinder head is rectangular and the previous V6 3.5-liter NA engine flowed the coolant in the long dimension direction from the rear to the front of the engine. In the new engine, coolant is flowed in the short dimension direction from the intake side to the exhaust side (**Fig. 3**), thereby helping to reduce flow resistance by shortening the distance of coolant flow and increasing the number of coolant passages.

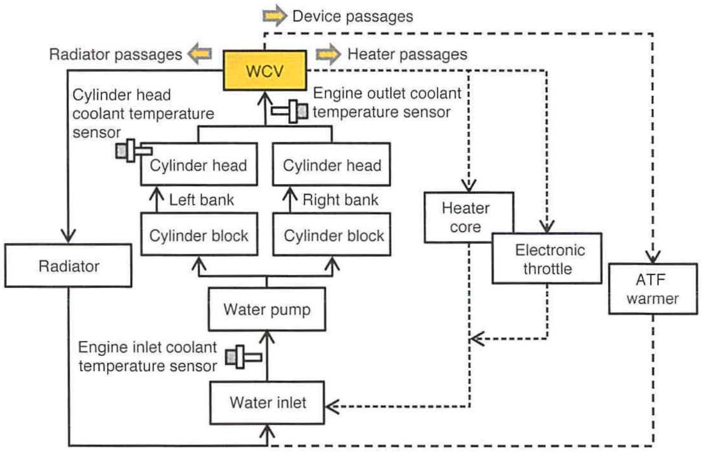

Fig. 2 Diagram of Coolant Circuit of New Engine

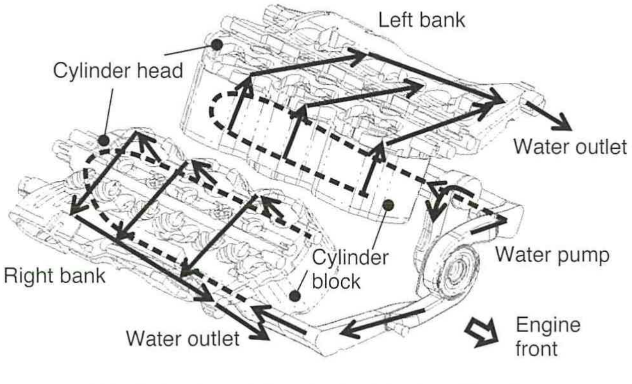

Fig. 3 Engine Water Jacket Coolant Circuit

The passage through which coolant flows into the cylinder block after passing through the water pump was also revised. The double curved structure of the V6 3.5-liter NA engine (**Fig. 4**) was redesigned to reduce flow resistance by creating more gentle curves (**Fig. 5**).

These measures reduced the flow resistance by 30% compared to a V8 4.6-liter NA engine (**Fig. 6**).

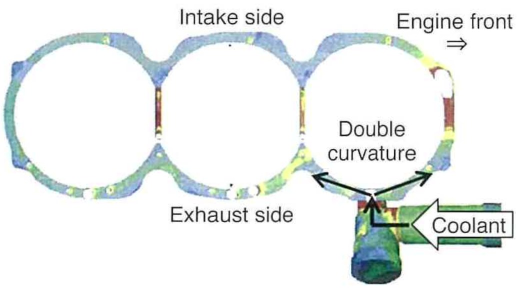

Fig. 4 Top View of Cylinder Block Water Jacket in Previous Engine

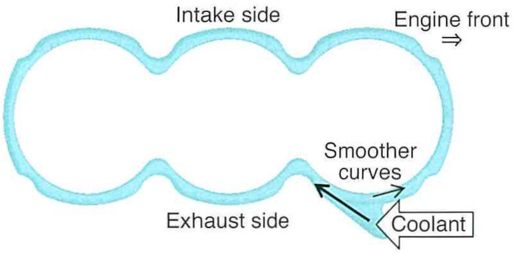

Fig. 5 Top View of Cylinder Block Water Jacket in New Engine

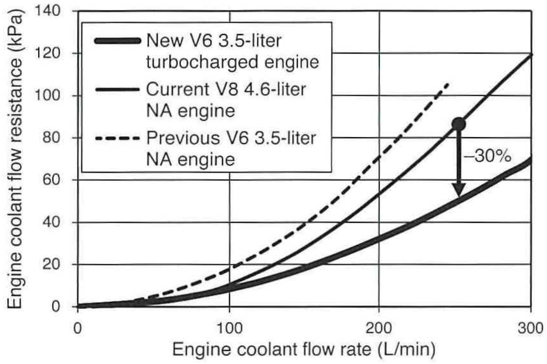

Fig. 6 Comparison of Engine Coolant Flow Resistance

3.2 Compact low coolant volume design

To satisfy both fuel efficiency and power performance requirements, the development needed to reduce the coolant volume (i.e., the thermal mass) and boost the cooling performance (coolant flow rate and heat flux) to enhance the knocking resistance. The following development targets were set: cooling performance equal to or better than a V8 4.6-liter NA engine with coolant volume equal to that of a V6 3.5-liter NA engine. The following two approaches were adopted.

The first approach was to boost the coolant flow rate by increasing the lift capacity of the water pump. Conventionally, the lift of the water pump cannot be raised because of the risk of greater cavitation. Larger lift was enabled in this engine by the flow resistance reduction measures described above. The reduction in flow resistance helps to lower the negative pressure of the water pump created by suction. This negative pressure margin was translated into larger water pump lift. As a result, a coolant flow rate equal to or better than a V8 4.6-liter NA engine was achieved, thereby enabling cooling performance (i.e., radiator heat discharge due to the greater coolant flow rate) suitable for the increase in engine power.

The second approach was to insert a water jacket spacer (WJS) into the water jacket. The development aimed to enhance knocking resistance without increasing the volume of coolant by increasing the heat flux at the top of the exhaust side (EX) of the combustion chambers. It was confirmed that inserting the WJS into the cylinder block water jacket (**Fig. 7**) increased the heat flux at the water jacket EX top (**Figs. 8** and **9**). This measure reduced the wall temperature between the bores of the combustion chambers (**Fig. 10**), thereby enhancing knocking resistance.

Additionally, the structure was simplified to reduce the coolant volume. Adopting the WCV created a unified structure at the engine coolant outlet and enabled the coolant-related parts at the front of the engine to be laid out together.

Due to these measures, the new engine achieved a maximum power performance equal to or better than a V8 4.6-liter NA engine, while restricting the coolant volume to the same level as a V6 3.5-liter NA engine (**Fig. 11**).

Fig. 7 External View of Water Jacket Spacer

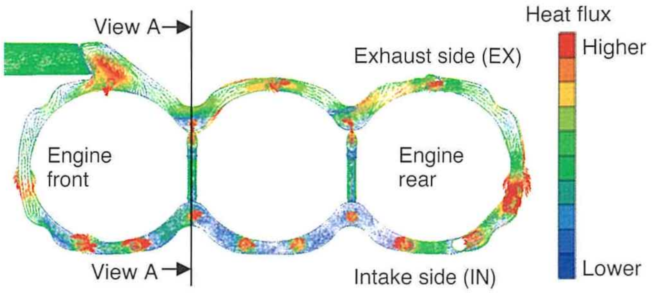

Fig. 8 Top View of Cylinder Block Water Jacket Coolant Heat Flux

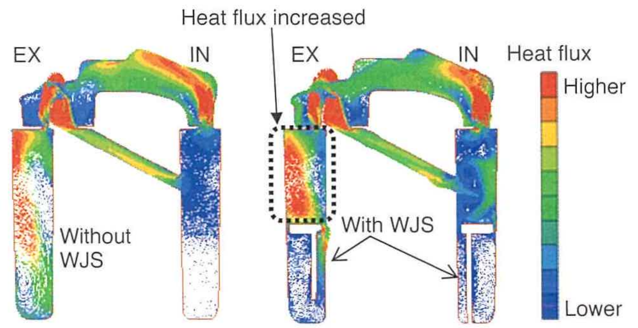

Fig. 9 **Comparison of Coolant Heat Flux with and without WJS (Fig. 8 View A)**

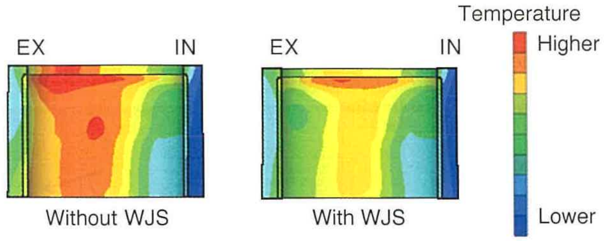

Fig. 10 **Comparison of Cylinder Block Bore Wall Temperature (Fig. 8 View A)**

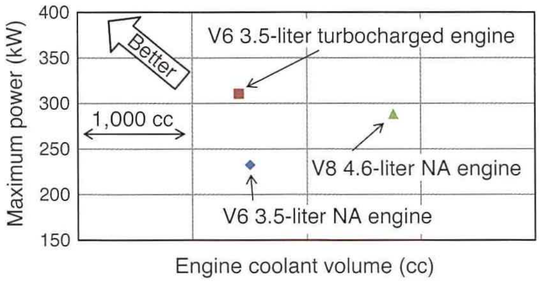

Fig. 11 **Comparison of Coolant Volume and Maximum Power**

3.3 Adoption of water-cooled turbochargers and intercoolers

Because the new engine is turbocharged, the turbochargers and intercoolers must be cooled. Newly developed compact highly efficient turbochargers were adopted with a world-leading efficiency 5% higher than the previous component.

The intercooler development focused on reducing the intake temperature (i.e., enhancing the knocking resistance) and ensuring acceleration response. The intercoolers were installed on the top of the engine rather than at the front to minimize the intake passage surface area after cooling (i.e., to reduce the heat transferred from the engine compartment) and the intake air pressure loss. In addition, since high intercooler efficiency is required to ensure knocking resistance, water cooling was adopted instead of air cooling to secure sufficient heat exchange even when installed on the top of the engine.

Since the intercooler cooling efficiency is insufficient when the engine coolant temperature is high, a coolant circuit separate from the engine coolant (**Fig. 12**) was adopted. To ensure that this coolant circuit is capable of maintaining a low coolant temperature, the radiator of the intercooler and turbocharger circuit was placed in front of the engine coolant radiator and a sub-radiator was positioned in front of the right tire. The aim of this configuration is to ensure heat radiation capacity by flowing large quantities of air at ambient temperatures to the radiator.

Through these measures, an intercooler cooling efficiency of at least 90% at maximum power was ensured, thereby enhancing knocking resistance under boosted conditions and helping to increase power (**Fig. 13**).

Coolant also flows into the turbochargers that are provided in parallel to the intercoolers. The purpose of this coolant is to prevent physical increases in turbocharger temperature created by high boost pressure. Coolant is flowed to the bearing housings of the turbochargers to lower the physical temperature of the compressor and bearing housings, and to suppress oil coking.

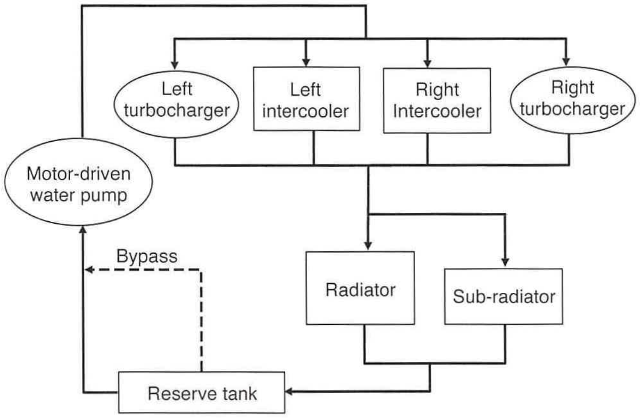

Fig. 12 **Turbocharger and Intercooler Coolant Circuit Diagram**

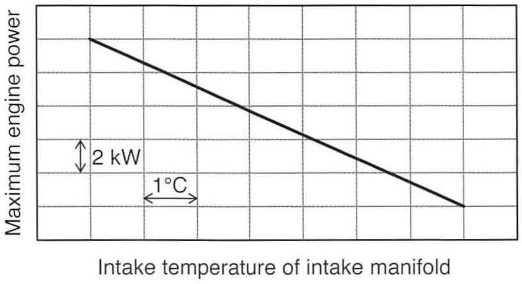

Fig. 13 **Relationship between Engine Intake Temperature and Maximum Power**

3.4 Adoption of exhaust gas cooling

To lower the exhaust gas temperature (for the purpose of part protection), the V6 3.5-liter NA engine utilized the vaporization heat created by fuel injection. However, this is not an optimum approach since it has the potential to worsen fuel efficiency (due to higher fuel consumption) and emissions. The new engine adopted a structure in which the exhaust ports (**Fig. 14**) are surrounded by the cylinder head water jacket (**Figs. 15** and **16**), thereby expanding the range in which fuel consumption does not increase. This structure was created by dividing the cylinder head water jacket into upper and lower levels. The lower first level of the water jacket is used for cooling close to the combustion chambers and lower side of the exhaust ports. The upper second level cools the upper side of the exhaust ports.

Since the exhaust port water jacket receives heat from the exhaust gas, it helps to warm-up the engine coolant more quickly and enhances the heating performance in winter.

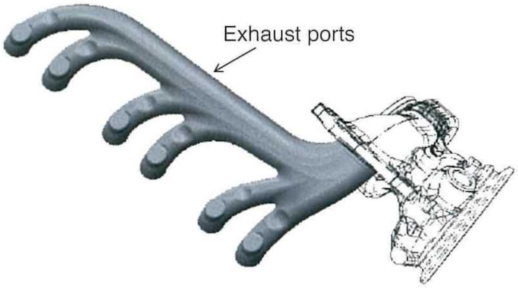

Fig. 14 Exhaust Port Shape inside Cylinder Head

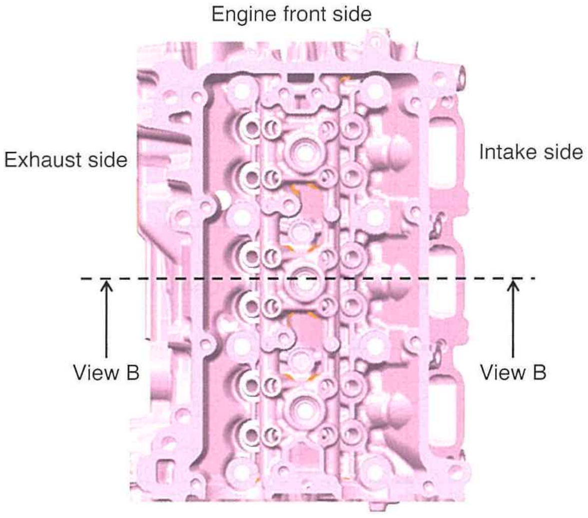

Fig. 15 Top View of Right Bank Side of Cylinder Head

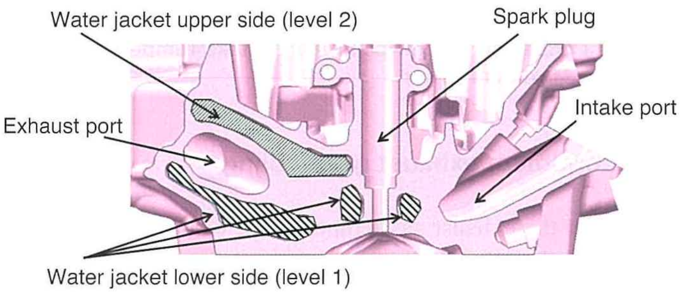

Fig. 16 Right Bank Side of Cylinder Head (Fig. 15 View B)

3.5 Adoption of thermal management using WCV

This section describes the details of thermal management.

The internal structure of the WCV (**Fig. 17**) is shown in **Fig. 18**. The WCV has three outlets (ports) for connecting with the vehicle devices (heater core, radiator, and ATF/W). The valve only opens the passage to the devices that require coolant and controls the amount of coolant in accordance with the engine operating conditions, ambient temperature, and air-conditioning system settings. It uses a highly responsive DC motor to follow accelerator operations by the driver as well as slight fluctuations in coolant temperature. The WCV consists of a spherical rotary valve that is rotated by the DC motor.

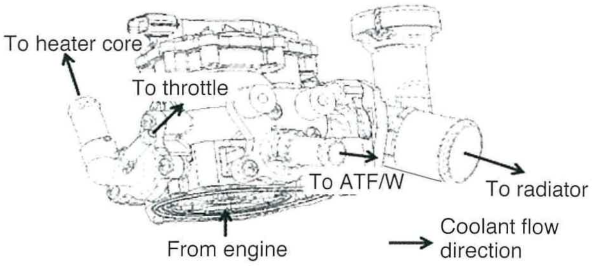

Fig. 17 External View of WCV

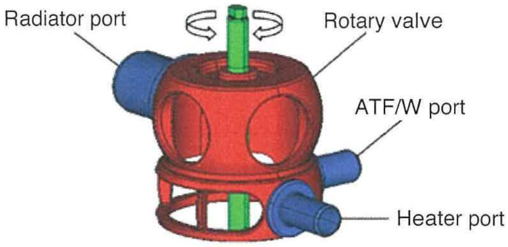

Fig. 18 Internal Structural Components of WCV

3.5.1 Rapid engine warm-up

In the initial engine warm-up phase, all the coolant passages are closed to stop the flow of coolant and reduce the thermal mass. As a result, the engine combustion chambers can be warmed up more rapidly by concentrating heat around the cylinder head and cylinder block and lowering the heat flux close to the water jacket wall surfaces. When the combustion chambers reach high temperature quickly, it is possible to switch the fuel injection and ignition control to the post warm-up control settings, thereby reducing the friction of the cylinder system. As a result, it was confirmed that these measures enhanced fuel efficiency by warming up the engine more rapidly (**Figs. 19** and **20**).

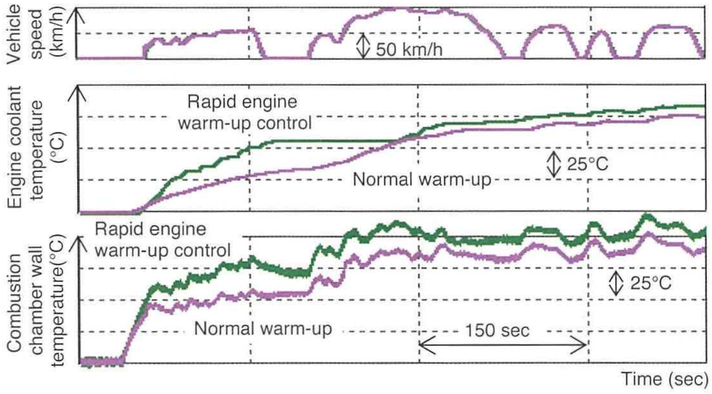

Fig. 19 Effect of Rapid Engine Warm-Up

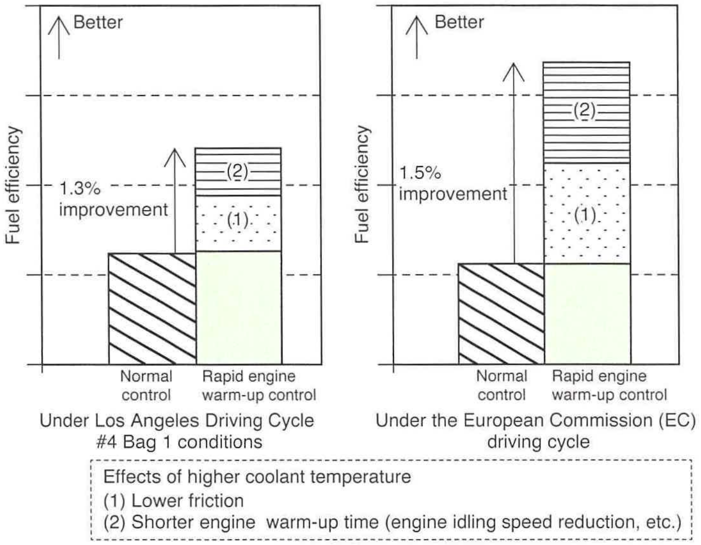

Fig. 20 Higher Fuel Efficiency due to Rapid Engine Warm-Up Control

Since the coolant temperature cannot be detected at the previous outlet coolant temperature sensor position when the coolant is stopped, a coolant temperature sensor was added to the cylinder head (position shown in **Fig. 2**), enabling engine control in accordance with the combustion chamber wall temperature.

3.5.2 Coolant temperature increase

At low and medium loads after engine warm-up, the radiator coolant flow rate is reduced to restrict the radiator heat discharge. Increasing the temperature of the coolant and combustion chamber walls under these conditions reduces friction and increases fuel efficiency.

3.5.3 Coolant temperature decrease

In contrast, at high loads after engine warm-up, the radiator coolant flow rate is increased to boost the radiator heat discharge. Lowering the temperature of the coolant and combustion chamber walls under these conditions restricts knocking and advances the ignition timing (1.1 deg CA/15°C of coolant temperature). This helps to increase both dynamic performance and thermal efficiency.

3.5.4 Air-conditioning performance

The reduction in cooling loss at low engine loads in accordance with the increase in thermal efficiency has the adverse effect of reducing the amount of heat channeled to the heater. When the heater is required in the initial phase of engine warm-up, coolant is flowed to the heater core passage only. This boosts the performance of the heater system (1.5°C) by concentrating engine heat in the heater.

In addition, when maximum cooling is required, stopping coolant flow to the heater core boosts cooler performance (1.5°C) by lowering the discharge temperature of the air-conditioning system.

4. Conclusions

The new V6 3.5-liter turbocharged engine features thoroughly enhanced cooling performance due to lower coolant flow resistance and the adoption of WCV-based thermal management. These measures help the engine to achieve high levels of power performance, fuel efficiency, and air-conditioning performance.

4.1 Measures in response to higher engine power performance

The coolant passage design, including the shape of the water jacket, was revised to meet the requirements of higher engine performance.(1) As a result, coolant passage flow resistance was reduced by approximately 30% compared to a V8 4.6-liter NA engine, ensuring sufficient cooling performance for the higher engine power.

4.2 Enhancement of both fuel efficiency and air-conditioning performance

To satisfy both fuel efficiency and power performance requirements, more compact coolant passages were developed (thereby reducing the coolant volume), and cooling performance efficiency was increased (thereby enhancing the heat flux). A unified cooling part structure was achieved by adopting a WCV and the heat flux to the top of the exhaust side was increased by adopting a WJS. These measures helped the engine to achieve higher power performance than a V8 4.6-liter NA engine with a coolant volume equivalent to a V6 3.5-liter NA engine.

In addition, thermal management in accordance with vehicle requirements (prioritization of the heater, cooler, fuel efficiency, or power) was realized using the WCV. High levels of performance, fuel efficiency, and air-conditioning performance were achieved through increasing the speed of engine warm-up by stopping the coolant (fuel efficiency improvement effect: 1.5% under the European test cycle), enhancing the performance of the heater system (1.5°C) by prioritizing coolant flow to the heater core, enhancing cooler performance (1.5°C) by stopping coolant flow to the heater core, and lowering friction (i.e., increasing fuel efficiency) by reducing the radiator coolant flow.

4.3 Summary

The engine equipped with this cooling system achieved its development targets for power (310 kW, engine speed of 6,000 rpm), fuel efficiency (+9.5% compared to a V8 4.6-liter NA engine), and air-conditioning performance (equal to or better than a V8 4.6-liter NA engine),(2) ensuring that the performance of the new V6 3.5-liter turbocharged engine is suitable for its intended models.

Finally, the authors would like to extend their sincere gratitude to everyone that supported the development of this cooling system.

References

(1) K. Sakata, Toda, Sakai, et al. "The New Toyota Inline 4 Cylinder 2.5L Gasoline Engine." *JSAE Annual Congress (Spring)* (2017).
(2) A. Mori, Yamazaki, Nomura, et al. "The New Toyota V6 3.5L Turbocharged Gasoline Engine." *26th Aachen Colloquium Automobile and Engine Technology* (2017).

Note: this article is based on the following published technical paper.
D. Morishita, Kawamoto, Niwa, Hisaminato, Yamaguchi et al. "Development of Cooling System for the New 3.5L V6 Turbo-Charged Gasoline Engine." *Proceedings of the JSAE Annual Congress* (2017) pp. 240-245.

Authors

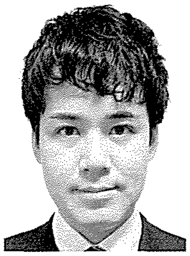

D. MORISHITA

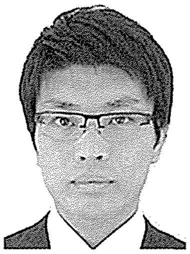

N. KAWAMOTO

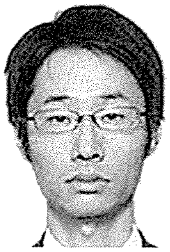

Y. NIWA

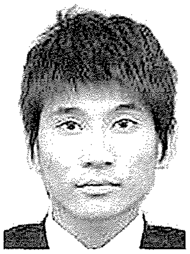

N. HISAMINATO

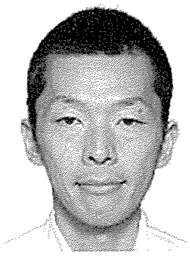

M. YAMAGUCHI

H. ANDO

Development of Engine Lubrication System with New Internal Gear Fully Variable Discharge Oil Pump

Takayuki Hosogi[*1]
Michitaka Yamamoto[*2]
Tetsuji Watanabe[*3]
Yuki Nishida[*4]

Abstract

Over the past decades, faced with growing awareness of global environmental issues and increasingly stringent rules and regulations, the development of fuel efficient technologies capable of reducing CO$_2$ emissions has become even more important to automakers. This article describes technology that was developed to reduce engine friction under both cold and hot conditions using a new internal gear fully variable discharge oil pump (F-VDOP). In combination with hydraulic pressure feedback control, this newly developed oil pump reduces friction and achieves highly responsive oil pressure supply to each engine part, helping to improve fuel efficiency by 1.2% under the Los Angeles Driving Cycle #4 (LA#4).

Keywords: *lubrication system, fuel efficiency improvement, oil pressure response, oil pressure feedback control, pumping ratio*

1. Introduction

Improving fuel efficiency has become one of the most important objectives for automakers, and the electrification of powertrains has accelerated into the mainstream, particularly through the growing popularity of hybrid vehicles (HVs) and plug-in hybrid vehicles (PHVs). However, since the engines used by HVs and PHVs require longer to warm-up from cold conditions than conventional engines, the average engine oil temperature remains lower. This increases engine friction due to higher engine oil viscosity. In response, one important method to lower friction under cold engine conditions is to lower the pressure of the oil supplied to each engine part to the minimum necessary.(1)(2)

A number of other automakers have adopted vane-type fully variable discharge oil pumps.(3) In contrast, Toyota Motor Corporation has only adopted an internal gear dual stage variable discharge oil pump, which cannot fully reduce engine friction under cold conditions.(4)(5)

To address this situation, Toyota has developed a new internal gear fully variable discharge oil pump (F-VDOP). Although conventional internal gear oil pumps are considered to have low efficiency,(6)(7) the new pump was designed to achieve greater total efficiency than a vane-type pump through the adoption of a new rotor with a refined tooth profile that enhances both volumetric and mechanical efficiency.(8)

This article describes the adoption of this internal gear F-VDOP incorporating a new rotor with a refined tooth profile in a 2.5-liter engine developed following the Toyota New Global Architecture (TNGA) design philosophy. It also describes the verification of the fuel efficiency improvement effect of this new pump. This pump helps to increase fuel efficiency by 1.2% in the Los Angeles Driving Cycle #4 by simultaneously lowering the oil pressure from cold conditions and switching the oil jets on and off hydraulically.

2. Aims of Newly Developed Fully Variable Discharge Oil Pressure System

Two types of conventional variable oil pressure systems are the mechanical variable discharge oil pump (M-VDOP) and the electronically switching variable discharge oil pump (S-VDOP). However, both types of oil pumps are affected by the following two issues. First, because these pumps are not capable of oil pressure feedback control, the pumps have to adopt a slightly higher oil pressure than the minimum engine oil pressure demand in consideration of lubrication system part tolerances (**Fig. 1**).

Second, because these pumps control the oil pressure by switching the reserve valve on and off, neither are capable of fully lowering the oil pressure under cold conditions when the oil

---

[*1] Electric Powertrain System Development Div., No. 2, Powertrain Company
[*2] Unit Parts Purchasing Div.
[*3] Engine Design & Engineering Div., Powertrain Company
[*4] Aisin Seiki Co., Ltd.

pressure is high. As a result, an additional switch valve is required or a high oil jet value opening pressure must be set to stop the oil jets used to enhance engine warm-up performance under cold conditions. Increasing the valve opening pressure prevents oil jet operation under high oil temperature low engine speed conditions, which adversely affects knocking resistance. Consequently, these lubrication systems are not ideally suited for the high compression ratio engines commonly used by HVs and PHVs.

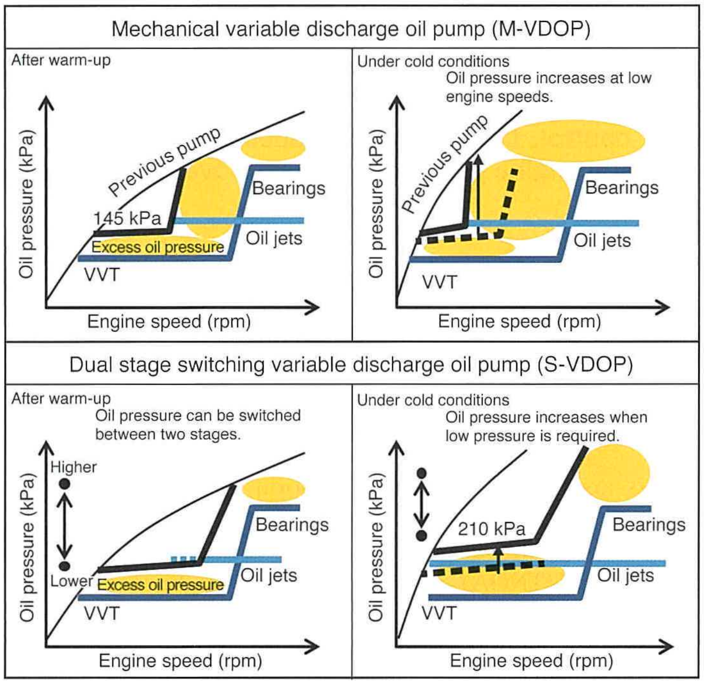

Fig. 1 Oil Pressure Control Ranges of M-VDOP and S-VDOP Pumps

To help resolve these issues, the newly developed F-VDOP and lubrication system use oil pressure feedback control to minimize the effects of part tolerances. Furthermore, since the new pump is capable of tracking set oil pressure targets, engine friction was reduced by controlling the oil pressure to the required minimum level (**Fig. 2**).

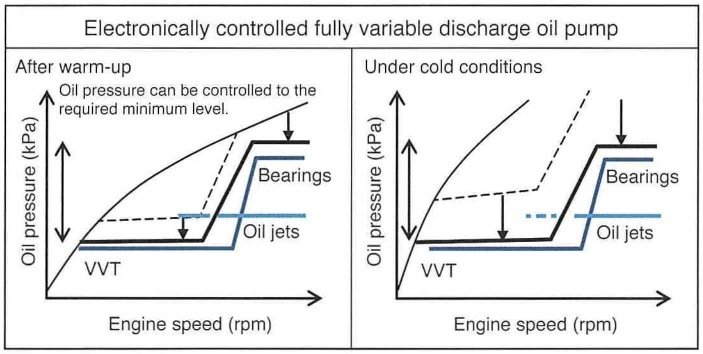

Fig. 2 Oil Pressure Control Ranges of F-VDOP

The oil temperature at which the oil pressure feedback control starts was set to -10°C to ensure the reliability of the main bearings under low oil pressure. The target main gallery oil pressure was lowered to 100 kPa considering the reliability of the variable valve timing (VVT) system and main bearings. Therefore, after factoring in the oil filter loss, the target oil discharge pressure of the F-VDOP was lowered to 125 kPa. In addition, the oil pressure control response target was set to 0.4 sec or less to ensure the required oil pressure on-demand when the engine speed drops suddenly due a manual transmission shift change (**Table 1**). Consequently, the oil jet valve opening pressure target was set to 170 kPa. At this value, the minimum engine speed at which the oil jets can be operated would be 1,400 rpm (oil temperature: 90°C).

Table 1 F-VDOP Development Targets

Oil: 0W-16 Engine speed: 1,600 rpm			**F-VDOP (new)**	S-VDOP
Target oil pressure (main gallery) (kPa)	Oil temperature (°C)	–10	**100**	–
		20		210
		80		145
Target oil pressure (oil pump outlet) (kPa)	Oil temperature (°C)	–10	**125**	–
		20		–
		80		–
Oil pressure response time constant (sec)	Oil temperature (°C)	–10	**0.4**	–
		20		0.6
		80		0.2
Oil jet valve opening pressure (kPa)			**170**	200
Oil jet start engine speed (rpm)	Oil temperature (°C)	90	**1,400**	2,200

3. Development of Fully Variable Discharge Oil Pump System

3.1 Outline of oil pressure control system

The oil pressure control method adopts oil pressure feedback using an oil pressure sensor, engine control unit (ECU), and oil control valve (OCV). The oil pressure is adjusted by changing to the OCV command current in accordance with the difference between the target oil pressure and the oil pressure detected by the sensor.

When the OCV command current is 0.1 A, the OCV closes, and the maximum oil pump discharge pressure is reached. The OCV opening angle increases as the OCV command current rises, and the oil pressure gradually decreases (**Fig. 3**).

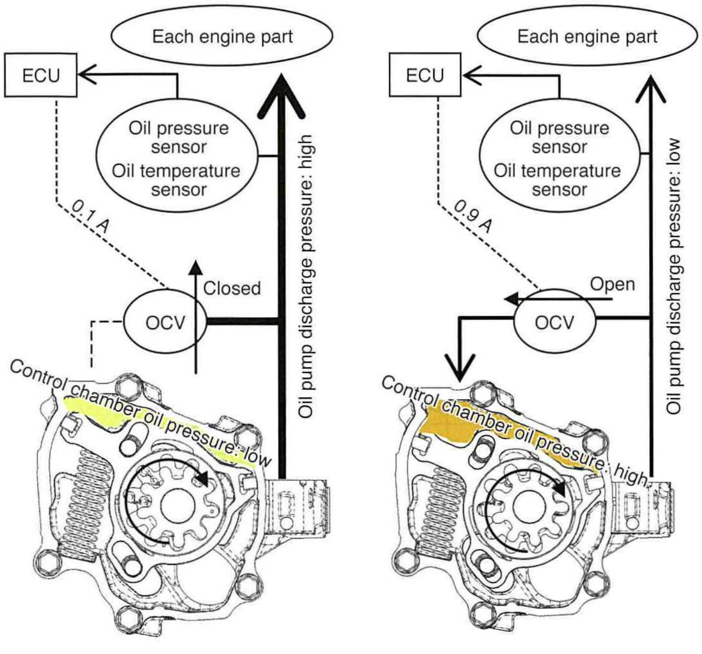

Initial position (maximum discharge pressure)

Under low oil pressure control

Fig. 3 Overall View of Oil Pressure Control System

3.2 Internal F-VDOP structure

The F-VDOP structure includes seven additional elements (underlined in **Fig. 4**) compared to a conventional internal gear fixed-discharge oil pump.

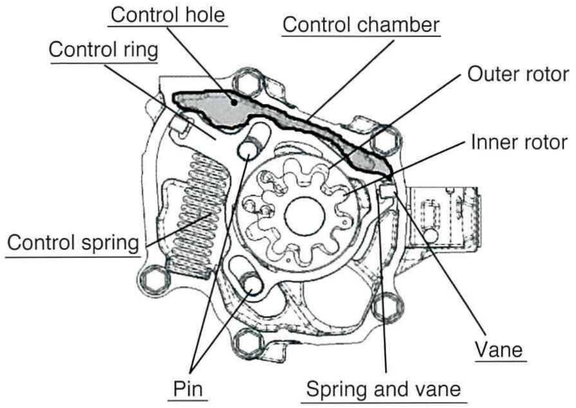

Fig. 4 Component Parts of F-VDOP

In the initial position (maximum discharge), the oil pump draws in oil between the rotors at the suction port. This oil is then discharged from the discharge port after passing through the cut-off position (**Fig. 5**).

The oil pressure is changed by varying the volume formed by the inner and outer rotors when the oil passes through the cut-off position of the housing (**Fig. 6**). The maximum volume is rotated by offsetting the eccentric angle of the outer rotor with respect to the inner rotor to change the volume of oil passing through the cut-off position.

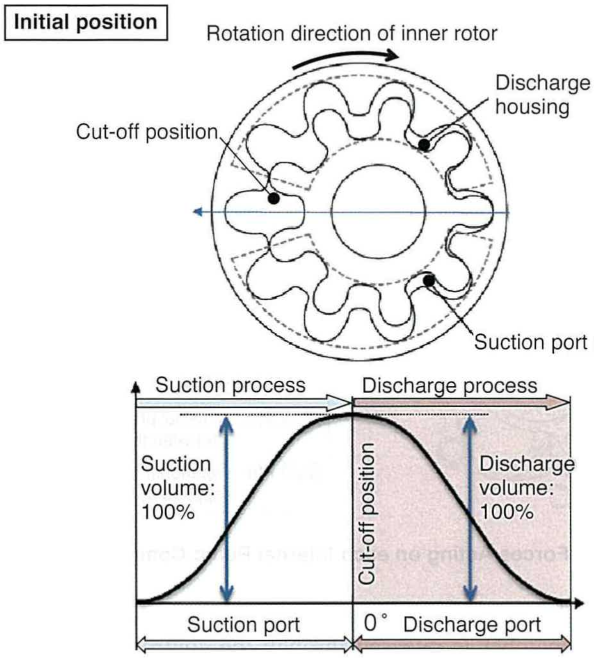

Fig. 5 Pumping Process in Initial Position

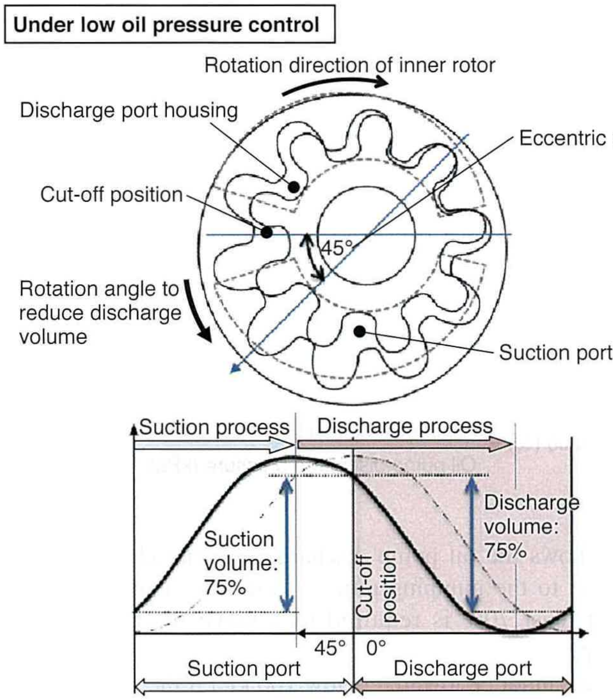

Fig. 6 Pumping Process under Low Oil Pressure Control

The offset eccentric angle of the outer rotor is controlled using a control ring that supports the rotor on the external circumference of the outer rotor (**Fig. 7**). This ring controls the path of the rotor using two guide pins. In the initial position, the rotor is fixed in the upward direction of the figure by the control spring. The oil pressure in the control chamber above the control ring rises as it fills with oil. The control ring starts to move and the discharge pressure drops when the pressure applied by the control chamber (Fcon) exceeds the reaction force applied by the control spring (Fspr) and the internal pressure between the rotors (Frot).

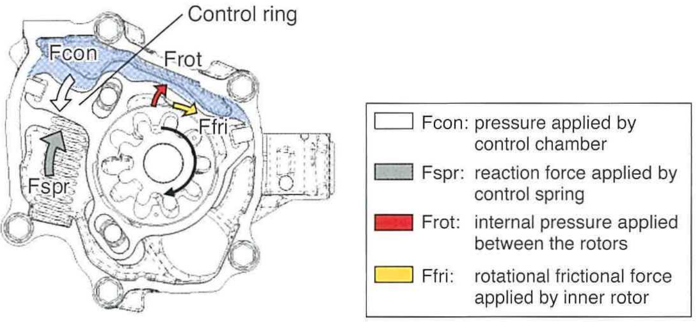

Fig. 7 Forces Acting on each Internal Pump Component

To make the oil pump discharge pressure increase, the oil in the control chamber is released through the control hole. This lowers the internal control chamber pressure and the eccentric angle of the outer rotor is returned by the force of the control spring. The development also examined the drain port of the OCV as a potential method of releasing the control chamber pressure. However, the speed of the decrease in control chamber oil pressure may be affected by the pressure loss in the oil circuit between the control chamber and OCV. Since this may delay the process to increase the main gallery oil pressure it was decided to abandon this idea.

3.3 Design index for oil pressure characteristics

The ratio between the oil pump discharge pressure and control chamber pressure is defined as the pumping ratio. This was used as a design index for oil pressure characteristics.

$$\text{Pumping ratio (\%)} = \frac{\text{Control chamber pressure (kPa)}}{\text{Oil pump discharge pressure (kPa)}}$$

Fig. 8 shows the oil pump discharge pressure characteristics with respect to the pumping ratio. It indicates that a pumping ratio of at least 70% is required to achieve the target pump discharge pressure of 125 kPa. In other words, the main gallery oil pressure cannot be lowered below 100 kPa if the pressure loss between the oil pump outlet and control chamber (including the OCV) is 30% or more. Therefore, a maximum pressure loss target of 30% was set when designing the oil circuit between the oil pump outlet and control chamber. Although the target F-VDOP discharge pressure can be lowered below 125 kPa, this would require making the control spring weaker and the control hole smaller. Since these measures would have a negative impact on the oil pressure increase response, specifications that allow a good balance between oil pressure response and the minimum oil pressure were selected.

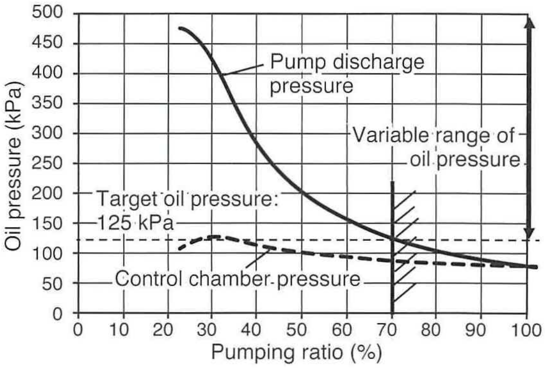

Fig. 8 Pumping Ratio and Pump Discharge Pressure Characteristics (1,600 rpm, Oil Temperature: 20°C)

3.4 F-VDOP oil pressure response

The development aimed to achieve the oil pressure response target by optimizing the control spring force, control hole diameter, and control ring shape. Since this system uses oil pressure feedback control, oil pressure response is an important characteristic to help avoid sudden drops in oil pressure when the engine speed decreases and to protect the engine.

Fig. 9 shows the response time constant results. A response time constant of 0.17 seconds was confirmed when the oil pressure was changed from 120 kPa to 200 kPa, satisfying the target time of 0.4 sec.

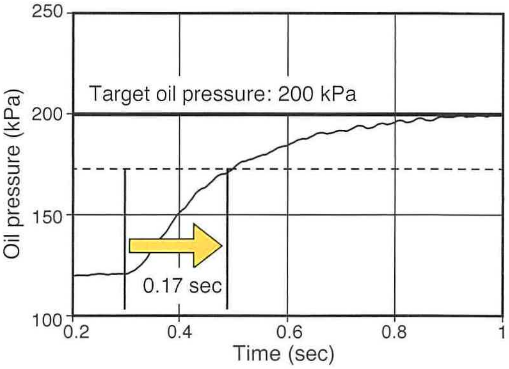

Fig. 9 Oil Pressure Time Constant Confirm ation Results (1,600 rpm, Oil Temperature: 20°C)

3.5 Installation layout

The F-VDOP is installed at the bottom of the engine and driven by a chain. This layout, in which the oil pump is constantly immersed in oil, was designed to meet the frequent intermittent operation requirements of HVs by speeding up the increase in oil pressure after intermittent engine restarts (**Fig. 10**).

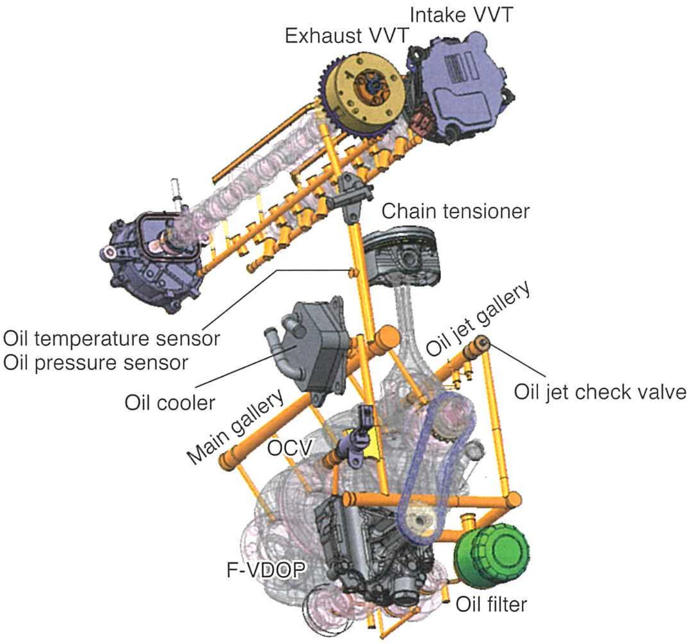

Fig. 10 **Installation Layout**

The oil pressure sensor is installed close to the VVT following the concept of locating the sensor near devices requiring high oil pressure response. Other parts with high oil pressure demand, such as the main bearings and chain tensioner, are consolidated in the low pressure loss oil circuit (**Fig. 11**).

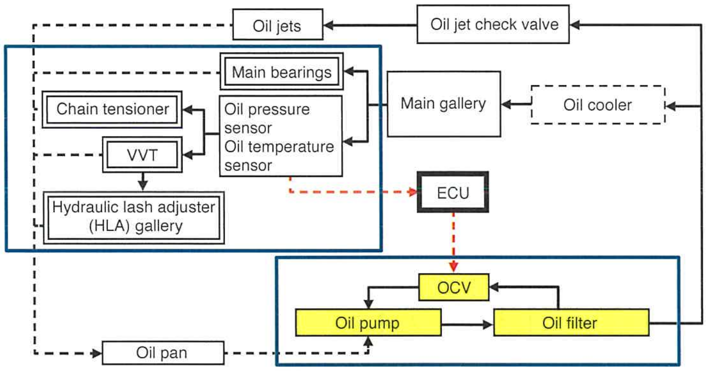

Fig. 11 **Overall View of Oil Circuit**

The layout is designed to reduce loss by not locating devices between the F-VDOP and OCV and between the OCV and control chamber. Particular care was taken with parts such as the oil cooler, which have high pressure loss and are installed depending on the market. These parts were installed outside the oil circuit because layout inside the circuit may increase the minimum oil pressure and require changes to the control characteristics.

3.6 Summary of F-VDOP characteristics

Table 2 summarizes the results of the F-VDOP development. The development targets were achieved, except for the oil pressure at -10°C. However, the effect of this item is limited and the specifications were determined considering the overall oil pressure response from cold to hot conditions.

Table 2 **Results of F-VDOP Development**

Oil: 0W-16 Engine speed: 1,600 rpm			Target values	Results
Oil pressure (oil pump outlet) (kPa)	Oil temperature (°C)	–10	125	177
		20		111
		80		80
Oil pressure response time constant (sec)	Oil temperature (°C)	–10	0.4	0.3
		20		0.17
		80		0.24
Oil jet valve opening pressure (kPa)			170	170

4. Results of Engine Verification

4.1 Confirmation of oil pressure at each engine part

Table 3 shows the specifications of the TNGA engine used for the evaluation. The tests were carried out using low-viscosity SAE 0W-16 engine oil at an engine speed of 2,000 rpm and an oil temperature of 20°C. The tests aimed to verify whether the targeted main gallery oil pressure and pressure loss for each part of the oil circuit were achieved. **Fig. 12** shows the results. The oil filter pressure loss was restricted to 29% and a pumping ratio of 71% was achieved, confirming that the development targets were satisfied. The tests also confirmed that the main gallery oil pressure was lowered to below 100 kPa and that the oil jets were stopped.

Table 3 **TNGA Engine Specifications**

		TNGA 2.5-liter engine (F-VDOP)	2AR–FE (M-VDOP)
Displacement (cc)		2,487	2,494
Number and alignment of cylinders		Inline 4-cylinder	
Bore diameter × stroke (mm)		87.5×103.4	90×98
Compression ratio		13	10.4
Maximum power (kW)		151/6,600	132.7/6,000
Maximum torque (Nm)		250/5,000	230.5/4,100
Lubricant		0W-16	0W-20
Oil pump specifications	Capacity (cc/rev)	18	
	Drive method	Chain	Crankshaft
Oil jet valve opening pressure (kPa)		170	180

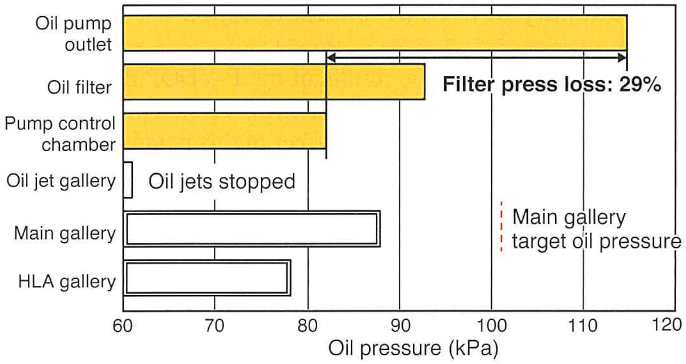

Fig. 12 Confirmation Results of Oil Pressure at each Engine Part (2,000 rpm, Oil Temperature: 20°C)

4.2 Confirmation of oil pressure controllability

Assuming a sudden drop in engine speed due a manual transmission shift change, the engine oil pressure response evaluation conditions decreased the engine speed from 2,000 to 1,400 rpm in 0.3 sec. Calculations indicated that the oil pressure would drop approximately 30% in accordance with the decrease in engine speed. However, this was restricted to 12% by optimizing the oil pressure feedback control (**Fig. 13**).

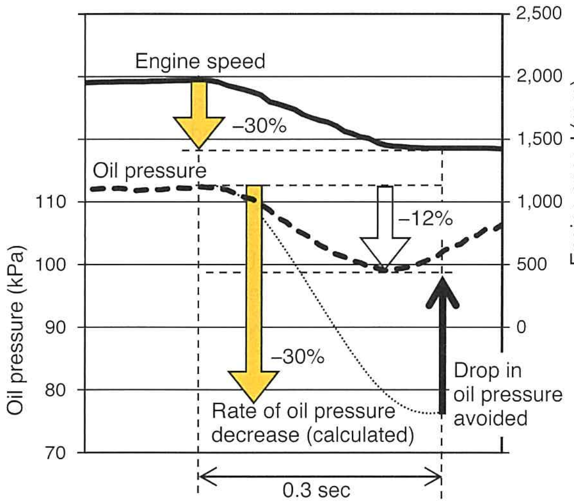

Fig. 13 Confirmation Results of Oil Pressure Controllability

4.3 Engine friction measurement results

Fig. 14 shows the engine friction reduction effect of the developed oil pump at different main gallery oil pressures, measured at an engine speed of 2,000 rpm and an oil temperature of 80°C. It was confirmed that engine friction could be reduced by 1.4 Nm when the main gallery oil pressure was reduced from approximately 350 to 100 kPa. It was also found that the friction reduction effect does not saturate and is in virtual linear proportion with the main gallery oil pressure.

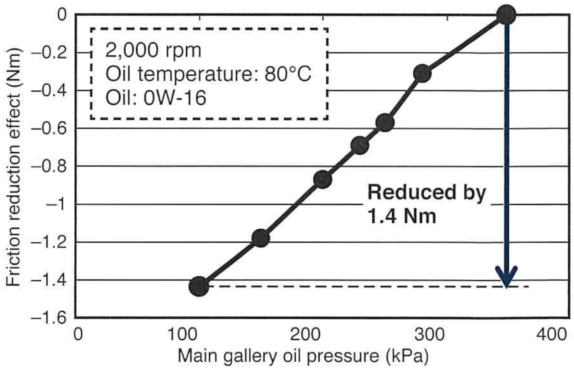

Fig. 14 Engine Friction Reduction Effect

4.4 Effect on actual vehicle fuel efficiency

Figs. 15 and **16** show the oil pressure reduction effect of the developed oil pump at oil temperatures of 40 and 80°C under the LA#4 cold test cycle. The shaded areas of the figures indicate the reduction in oil pressure compared to the previous oil pump. It was confirmed that the developed system control satisfied the oil pressure demands of each part and improved vehicle fuel efficiency by 1.2%.

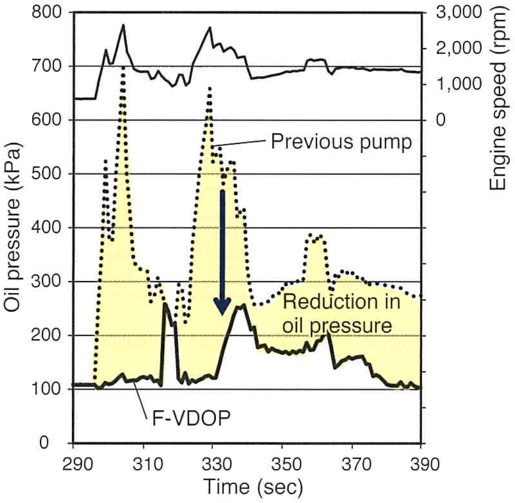

Fig. 15 Oil Pressure Reduction Effect of F-VDOP (Oil Temperature: 40°C)

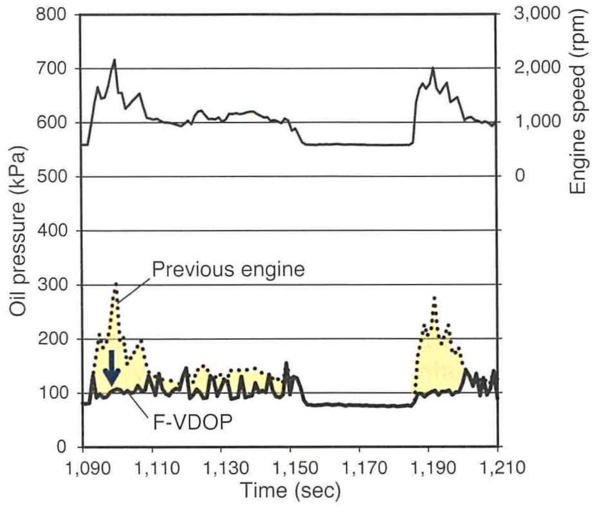

Fig. 16 Oil Pressure Reduction Effect of F-VDOP (Oil Temperature: 80°C)

5. Conclusion

The newly developed F-VDOP oil pump and oil pressure control system helped to enhance engine fuel efficiency and reliability.

(1) The developed oil pump is capable of controlling oil pressure from -10°C and reduces engine friction under cold conditions as well as after the engine has warmed up.
(2) Under the LA#4 test cycle, a 2.5-liter TNGA engine equipped with the developed oil pump improved fuel efficiency by 1.2%.

Finally, the authors would like to extend their sincere gratitude for the invaluable contribution of all companies involved in the development and adoption of this system.

References

(1) M. Rundo, Squarcini. "Experimental Procedure for Measuring the Energy Consumption of IC Engine Lubricating Pumps during a NEDC Driving Cycle." *SAE Paper* No. 2009-01-1919 (2009).
(2) P. Shayler, Cheng, Li, et al. "A Modified Oil Lubrication System with Flow Control to Reduce Crankshaft Bearing Friction in a Litre 4 Cylinder Diesel Engine." *SAE Paper* No. 2016-01-1045 (2016).
(3) F. Toyoda, Kobayashi, Miura, et al. "Development of Variable Discharge Oil Pump." *SAE Paper* No. 2008-01-0087 (2008).
(4) T. Arata, Novi, Ariga, et al. "Development of a Two–Stage Variable Displacement Vane Oil Pump." *SAE Paper* No. 2012-01-0408 (2012).
(5) J. Meira, Filho, Melo, et al. "Strategies for Energy Savings with Use of Constant and Variable Oil Pump Systems." *SAE Paper* No. 2011-36-0150 (2011).
(6) J. Hadler, Neußer, Szengel, et al. "The New TSI." *Internationales Wiener Motorensymposium* (2012).
(7) N. Ardey, Wichtl, Steinmayr, et al. "The New BMW 3-Cylinder and 4-Cylinder Diesel Engines with TwinPower Turbo Technology." *Internationales Wiener Motorensymposium* (2014).
(8) Y. Nishida, Ono, Terashima, Toyoda, Nunami. "Development of Continuously Variable Discharge Oil Pump." *Proceedings of the JSAE Annual Congress* (2017) pp. 1942-1945.
(9) A. De Vizio, Senatore, Buono, et al. "A Simulated Analysis of the Lubrication Circuit of an In–Line Twin Automotive Engine." *SAE World Congress and Exhibition* (2014).

Note: this article is based on the following published technical paper.
M. Yamamoto, Hosogi, Watanabe, Nishida. "Development of Engine Lubrication System with New Internal Gear Fully Variable Discharge Oil Pump." *Proceedings of the JSAE Annual Congress* (2017) pp. 1769-1774.

Authors


T. HOSOGI


M. YAMAMOTO


T. WATANABE


Y. NISHIDA

Development of Laser-Clad Valve Seats

Hironori Aoyama*1
Naoyuki Miyara*1
Natsuki Sugiyama*2
Kohei Yanaka*3
Kimihiko Ando*4
Tadashi Oshima*5

Abstract

Laser-clad valve seats are a unique technology developed by Toyota Motor Corporation in which wear-resistant alloy is directly deposited onto cylinder head valve seats. Compared with conventional press-fit sintered valve seats, this direct deposition process enhances knocking resistance by raising thermal conductivity, and improves combustion efficiency by increasing design flexibility around the ports. This technology has been adopted in the Toyota New Global Architecture (TNGA) engine series and enables an innovative cylinder head design that helps to improve the trade-off relationship between tumble flow and intake resistance by simultaneously generating intense tumble while reducing resistance. As a result, these laser-clad valve seats help to achieve the world's fastest combustion and greatly increase engine thermal efficiency and specific power. To enable the application of this technology as a global standard in Toyota's engine lineup, a new wear-resistant material was designed for use with alternative fuels, which are becoming more common around the world. In addition, a new energy-saving manufacturing process featuring highly reliable equipment was developed to facilitate deployment of this technology to production plants outside Japan.

Keywords: *laser cladding, valve seat, wear resistance, tumble, coefficient of flow*

1. Introduction

Automakers are facing growing demand for more fuel efficient vehicles to help preserve the global environment. As part of its efforts to develop engines with greater thermal efficiency, Toyota Motor Corporation has already achieved a maximum thermal efficiency of 38% in a series of highly efficient gasoline-powered engines designed following the ESTEC (Economy with Superior Thermal Efficient Combustion) development concept. In addition to thermal efficiency, engines also require a high level of dynamic performance to achieve an enjoying driving performance.

Consequently, Toyota has developed a key series of engines under its Toyota New Global Architecture (TNGA) design philosophy to realize world-leading levels of thermal efficiency and specific power (**Fig. 1**).(1)(2)

These goals are realized by high-speed combustion, which is achieved through the formation of intense tumble flows and the reduction of intake resistance, which tend to have a trade-off relationship. In addition, since these are designated as globally strategic engines, it was necessary to incorporate common design elements that enable the use of various fuels and displacements. Therefore, the component parts needed to be designed with excellent productivity and durability for use with a wide range of fuels. To meet these requirements, port design technology incorporating laser-clad valve seats, which were developed for race car engines, was applied to mass-production vehicles. The developed valve seats help to realize high-speed combustion with a world-leading tumble ratio of 2.9 and a coefficient of flow of 0.49. As a result, a targeted engine thermal efficiency of at least 40% and a specific power of 60 kW/L were achieved.

This article describes the development of a new and highly efficient cladding process dedicated specifically to enable the adoption of laser-clad valve seats in TNGA engines as a key technology to realize high-speed combustion. It also describes the development of a new material that allows this technology to be adopted in Toyota's strategic global engines.

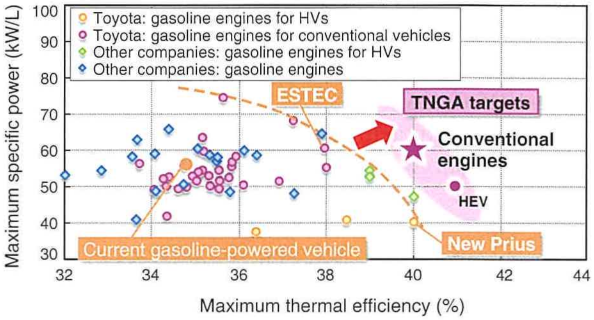

Fig. 1 Development Targets and Relationship between Maximum Thermal Efficiency and Specific Power

---

*1 Engine Design & Engineering Div., Powertrain Company
*2 Production Engineering Development Div., Powertrain Company
*3 Forging & Surface Modification Engineering Div., Powertrain Company
*4 Inorganic Material Engineering Div., Advanced R&D and Engineering Company
*5 Toyota Central R&D Labs., Inc.

2. Outline of Laser-Clad Valve Seats

A widely adopted method of achieving high wear and heat resistance is to use press-fit sintered valve seats. In contrast, Toyota has developed a technology that directly clads highly wear-resistant alloy onto an Al alloy using laser cladding. Valve seats manufactured using this process were adopted in the ZZ engine series in 1997. This technology enables (1) increased design flexibility around the port outlet by manufacturing a smaller valve seat and (2) enhanced valve cooling performance by improving heat transfer (**Fig. 2**).

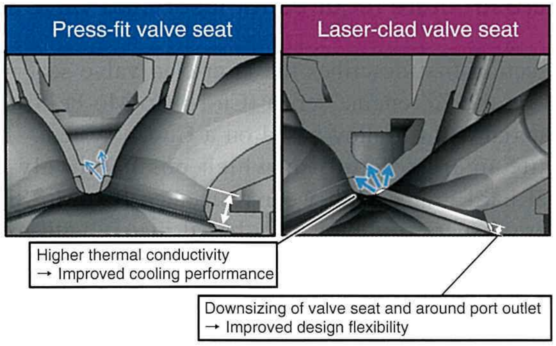

Fig. 2 Comparison of Valve Seats and Port Shapes

In general terms, tumble (which is required to achieve high-speed combustion) and the coefficient of flow (which is required to improve specific power) have a trade-off relationship (**Fig. 3**). Therefore, an innovative intake port design was required to achieve both high tumble and the required coefficient of flow. **Fig. 4** compares the port shapes and intake flow streamlines with press-fit and laser-clad valve seats. Conventional press-fit sintered valve seats require a certain thickness to hold the seats in place. This places constraints on the port shape and generates pressure loss. However, laser clad valve seats allow the intake port to be designed with a straight flow path, which enables the intake air to be drawn into the combustion chamber while maintaining a high flow speed. In addition, the flow can be separated at the throat portion located at the bottom surface of the port. This helps to suppress reverse tumble and can increase the coefficient of flow by at least 20% with the same degree of tumble.

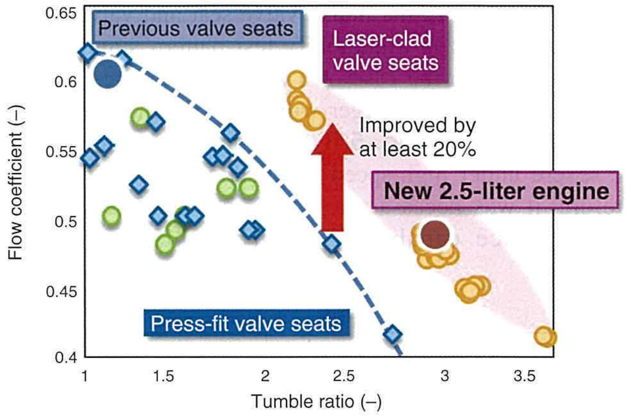

Fig. 3 Relationship between Tumble Ratio and Flow Coefficient, and Effect of Adopting Laser-Clad Valve Seats

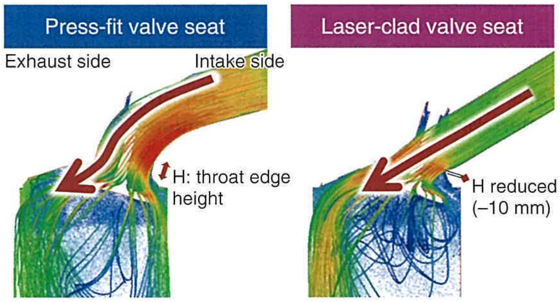

Fig. 4 Comparison of Port Shape and Flow Streamlines between Press-Fit and Laser-Clad Valve Seats

3. Issues for Global Adoption

3.1 Production process

The production of laser-clad valve seats started at the Shimoyama Plant in 1997,(3) using a process that involved rotation of the cylinder head and a CO_2 laser. Issues for global adoption included lowering energy consumption and reducing the equipment footprint, which meant it was necessary to develop an innovative and more efficient cladding process.

3.2 Global fuel compatibility

Since this technology had previously only been adopted in engine models produced for Japan, the valve seats manufactured by this process were only designed for use in gasoline engines. One issue for adopting laser-clad valve seats in TNGA engines was compatibility with fuels blended with ethanol. Greater use of blended ethanol fuels is being encouraged around the world due to heightened awareness of environmental preservation. Some regions, primarily South America, have introduced fuels blended with up to 25% ethanol. For this reason, it was decided that the TNGA engine series for global adoption should be compatible with 30% blended ethanol (E30) fuels.

Fig. 5(A) compares the intake valve seat and valve wear loss with different fuels in a durability test pattern simulating real-world conditions in the case of a ZZ series engine. The valve seat wear loss is clearly larger with E30 fuel than gasoline. In addition, as shown in **Fig. 5**(B), the wear environment is much more severe under high-speed combustion in a TNGA engine. Therefore, it was necessary to develop a valve seat with high wear resistance capable of enduring this kind of usage environment.

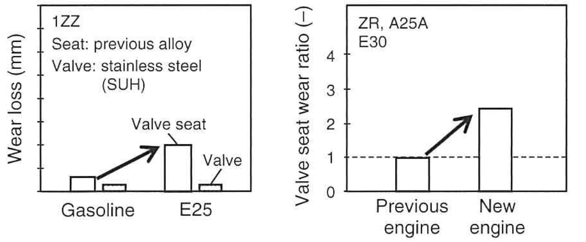

(A) Difference due to fuel type (B) Difference due to engine

Fig. 5 Valve Seat and Valve Wear Loss after Engine Durability Test Pattern Simulating Real-World Conditions

4. Development of New Cladding Process

To reduce energy consumption and the equipment footprint, a highly efficient diode laser with a compact optical system and a shaped beam were adopted. A new angled forming technique that uses a coaxial nozzle to integrate the delivery of a laser beam, powder, and shielding gas was developed, which enables the cladding to be accomplished by rotating the laser with respect to the cylinder head. These measures reduced energy consumption to less than one-fifth and the equipment footprint to less than one-third of the conventional process (**Fig. 6** and **Table 1**).

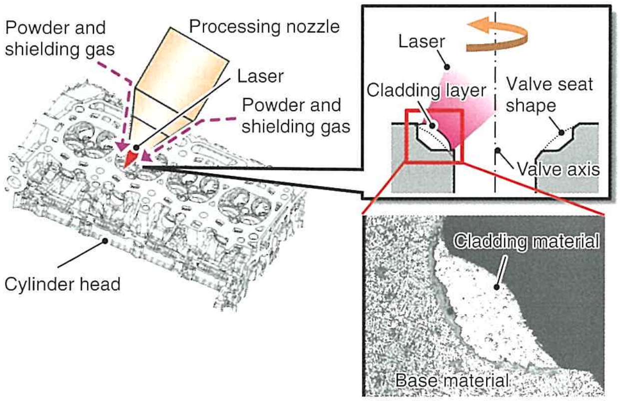

Fig. 6 New Cladding Process Enabling Highly Efficient Valve Seat Formation by Laser Rotation

Table 1 Comparison of New and Previous Cladding Processes

	Previous technique	New technique
Laser	CO_2 + oscillated beam	Laser diode (LD) + shaped beam
Process	Work rotation	Tool rotation
Power consumption	1	0.17
Equipment footprint	1	0.3

5. Development of New Material

5.1 Microstructure required for laser-clad valve seats

This section first describes the laser-clad valve seat material adopted on the ZZ engine series (Cu-Ni-Co-Mo-Fe-Si-Cr).(4)(5) This material is a Cu alloy based on a Cu-Co system. It has a composite microstructure in which comparatively coarse spherical hard grains with wear resistance (Co-Mo-Si Laves phase) are dispersed within a Cu-based matrix with excellent weldability to an Al-based substrate, heat resistance, and mechanical strength (**Fig. 7**).

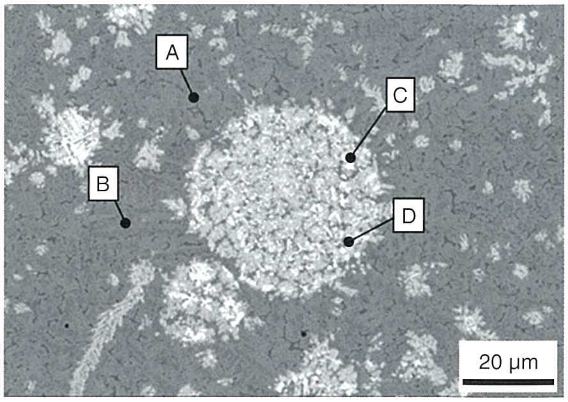

	Matrix	Hard grains
Constituent phases	A Cu-Ni-Co-Fe <S.S.> Co-Ni-Fe-Si <S.S.> B (Ni, Co, Fe)$_5$Si$_2$	C (Co, Ni, Fe)$_3$Mo$_2$Si D Co-Ni-Fe-Si <S.S.>
Function	Weldability Strength Heat resistance	Wear resistance

<S.S.>: solid solution

Fig. 7 Microstructure of Previous Alloy

Wear resistance can be further improved by the following methods.

(1) Increase the volume fraction of the hard grains
(2) Increase the hardness of the hard grains

The results of high-temperature sliding wear tests show that wear resistance can be improved by either of these two approaches. However, these methods may generate weld cracks that start from the hard grains. For this reason, it would be difficult to improve both wear resistance and weldability any further using the previous alloy. Therefore, it was decided to develop a new alloy by adopting an innovative base alloy system.

5.2 Elemental composition of liquid immiscible alloys

The development of the new alloy focused on refining the hard grains to reduce the risk of weld cracks following the approach identified with the previous alloy. The development also focused on machinability, which was one of the issues of the previous alloy.

The composite structure of the previous alloy is formed by a particular metallurgical phenomenon that creates two separate liquid phases, similar to oil drops in water (**Fig. 8**). This forming method takes advantage of the stirring and rapid solidification (10^3 K/sec) that occurs in laser cladding. The development of the new alloy also followed this microstructural formation approach.

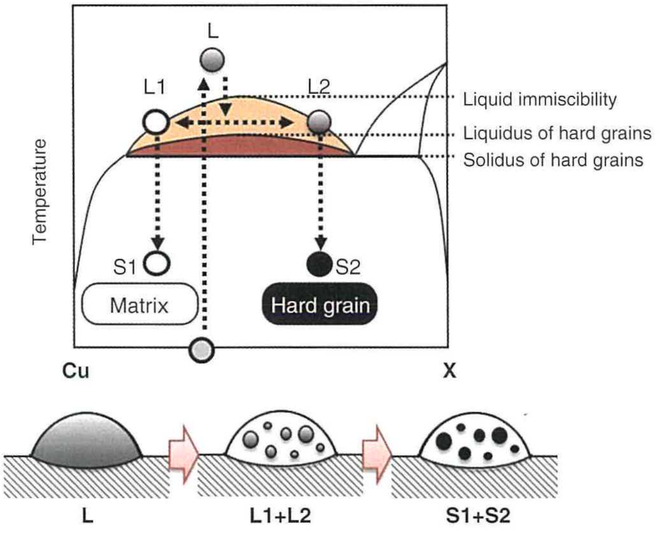

Fig. 8 Schematic Phase Diagrams Showing Liquid Immiscibility

Pb and Tl are known alloying elements that can create liquid immiscibility in a copper alloy. However, these were excluded as toxic elements with a high vapor pressure that are not suited for powder manufacturing and the laser cladding process.

Although the state diagrams show that Cu-Co and Cu-Fe alloys are peritectic systems that resemble each other, the liquidus line is close to the horizontal across a wide composition range (**Fig. 9**). It is known that liquid immiscibility can be created by rapidly cooling this system from a molten state.(5)

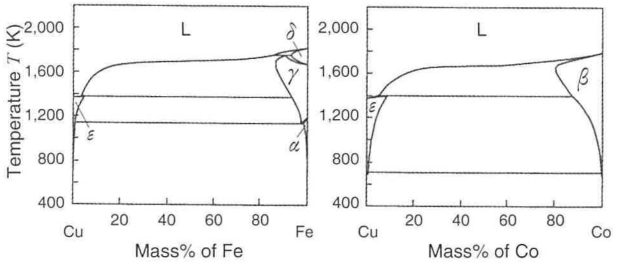

Fig. 9 Binary Phase Diagrams of Cu-Fe and Cu-Co(6)

In addition, it has been reported that Cu-Fe systems containing Cr, V, or Si convert into a monotectic system, and cause liquid immiscibility between around 1,500 and 2,000 K.(7)(8) Therefore, this new alloy development studied adopting a base Cu-Fe system to reduce the risk of cracks and to improve wear resistance.

Laves phases, which are intermetallic compounds that strengthen heat-resistant steel, are regarded as effective hard grains for improving wear resistance. The feasibility of Laves phase formation was confirmed from the ternary phase diagram,(9) and it was decided to use Cu-Ni-Fe-Mo-Si as the elemental composition of the new alloy.

As a result, similarly to the previous alloy, a new alloy microstructure was formed with coarser spherical hard grains dispersed in a Cu-based matrix (**Photo 1**).

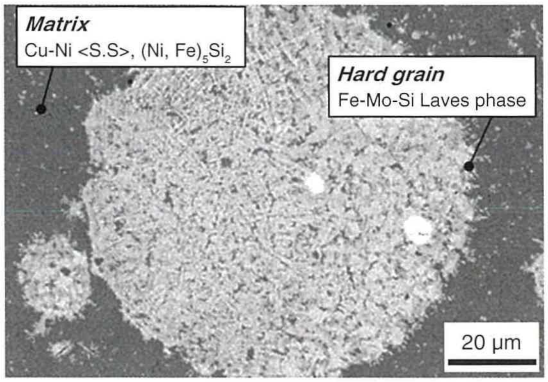

Photo 1 Microstructure of Developed Alloy (Cu-Ni-Fe-Mo-Si)

Fig. 10 shows the relationship between the volume fraction of the hard grains and wear loss, as well as weld cracks. No cracks occurred with the developed alloy system even when the volume fraction of the hard grains was high, showing that it can achieve a higher wear resistance than the previous alloy. However, one concern is that the coarse hard grains will cause a deterioration in machinability.

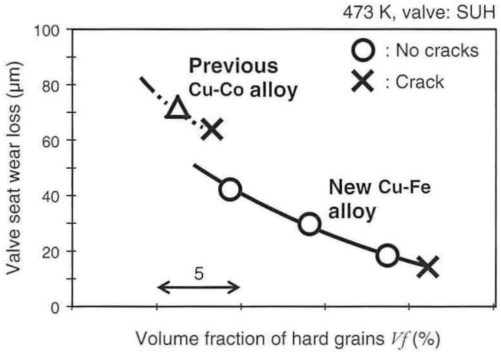

Fig. 10 Relationship between Wear Resistance and Crack Resistance with Previous and New Alloys

5.3 Creation of finer hard grains

With the objective of improving machinability, the following two methods were examined to create finer hard grains.

Method 1: optimization of the elemental composition

The quantity of hard grains and the degree of immiscibility are thought to correlate with the liquid phase separation (L2 in **Fig. 8**) that forms the hard phase in a liquid immiscibility. The development attempted to control the grain size by adjusting the amounts of Mo and Fe (that promote liquid immiscibility) and Ni and Si (that reduce liquid immiscibility). **Fig. 11** shows the relationship of the maximum hard grain size with different Ni and Si contents to reduce liquid immiscibility. The maximum hard grain size can be reduced by increasing the Ni and Si content. It was also confirmed that the volume fraction of hard grains, which greatly affects wear resistance, was approximately the same, despite the reduction in the maximum hard grain particle size.

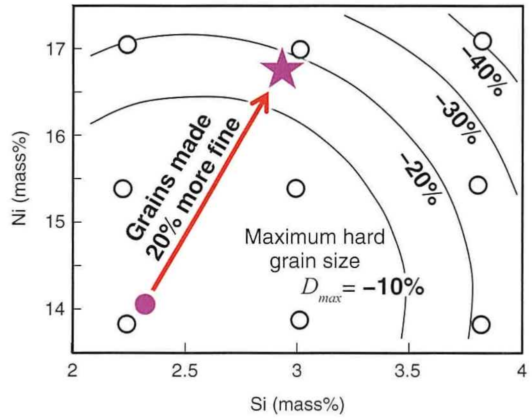

Fig. 11 Effects of Si and Ni Content on Maximum Hard Grain Size

Method 2: addition of minor elements

Simply reducing liquid immiscibility causes a wide variation in the maximum hard grain size at the upper and lower composition limits (**Fig. 12**). Therefore, the addition of minor elements to the developed alloy was considered to control the hard grain size. Carbides were regarded as potential additive elements due to the high melting temperature during laser cladding and the characteristics of powder manufacturing (oxidation, vapor pressure, and volatility). NbC was selected based on factors such as generation trends, specific gravity, and hardness.

Fig. 12 compares the hard grain size with and without the addition of small quantities of NbC. The addition of small quantities of NbC resulted in finer hard grains with smaller variation.

Based on these studies, the final composition of the new alloy was set to Cu-Ni-Fe-Mo-Si-Nb-C. This composition enables the formation of a microstructure that controls the hard grain size (**Photo 2**).

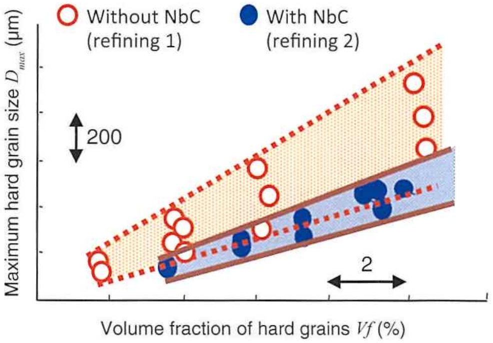

Fig. 12 Relationship between Maximum Hard grain Size and Volume Fraction in Developed Alloy With and Without NbC Addition

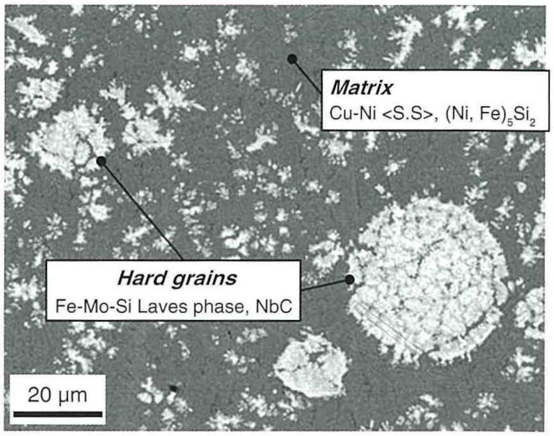

Photo 2 Microstructure of Developed Alloy (Cu-Ni-Fe-Mo-Si-Nb-C)

6. Evaluation of Characteristics

6.1 Corrosion resistance

Corrosion in condensed water was studied, assuming use with an ethanol blend or low-quality fuel. **Fig. 13** shows the corrosion resistance of the developed and previous alloys, and a ferrous sintered material. The Cu-system alloys (i.e., the developed and previous alloys) were confirmed to have higher corrosion resistance than the ferrous sintered material.

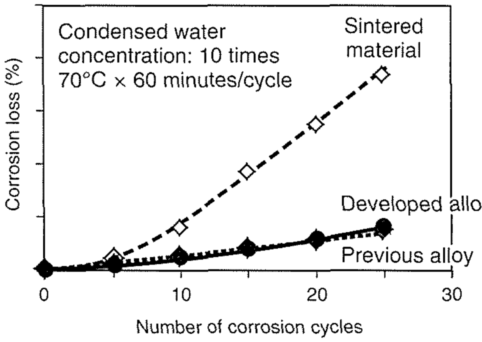

Fig. 13 Corrosion Resistance Test Results in Condensed Water

6.2 Wear resistance

The valve seat wear resistance was tested using three materials: the previous alloy, and the developed alloy with and without NbC content. The results show that the wear loss of the alloy without NbC content was approximately two-thirds of the wear loss of the previous alloy. In contrast, with NbC, the wear loss decreased to approximately one-half of the wear loss of the previous alloy. It was also confirmed that the new alloy caused no issues on the mating side, with virtually the same level of valve wear (**Fig. 14**).

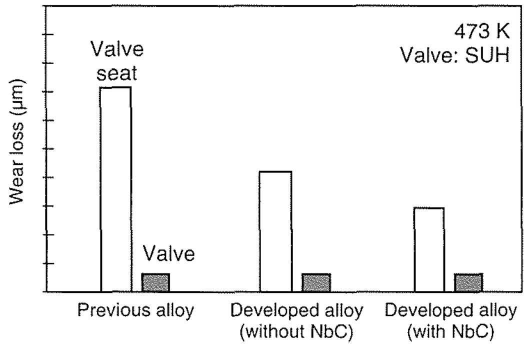

Fig. 14 Results of Valve Wear Resistance Test

6.3 Machinability

Since wear resistance and machinability have a trade-off relationship, this development examined the effects of the hard grain size on machinability.

Fig. 15 shows the effect of the hard grain size on cutting resistance. Although the matrix cutting force remains almost constant, the cutting resistance (i.e., the cutting thrust force) increases in accordance with the hard grain size. In addition, as shown in **Photo 3**, coarse grains cause chipping of the tool tip after cutting. Therefore, the increase in cutting resistance when cutting the large hard grains is likely to lead to greater cutting tool wear. Therefore, the development confirmed that the method to create finer grains described above ensured the same machinability as the previous alloy by controlling the hard grain size (**Fig. 16**).

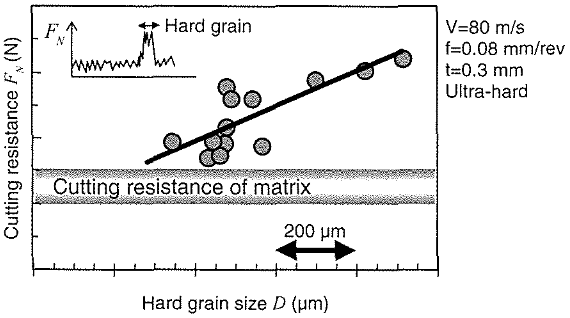

Fig. 15 Relationship between Hard Grain Size and Cutting Resistance in Stand-Alone Machinability Test

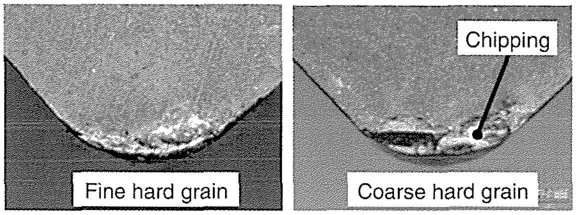

Photo 3 Appearance of Cutting Tool after Stand-Alone Machinability Test

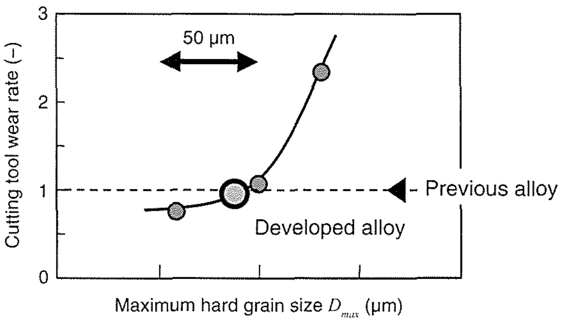

Fig. 16 Relationship between Maximum Hard Grain Size and Cutting Tool Wear in Machinability Test Using Actual Material

7. Actual Engine Durability Test

A durability test was carried out in a pattern simulating real-world conditions by applying the final material microstructure to a new engine. **Fig. 17** shows the valve and valve seat wear loss with different fuels. Lower wear loss with both fuels was confirmed. It was also confirmed that the valve and valve seat surfaces were not damaged after the test (**Photo 4**).

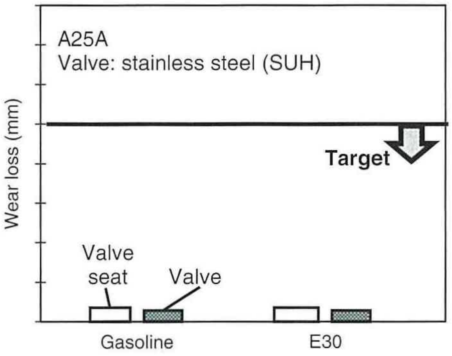

Fig. 17 Durability Test Results with New and Previous Engines

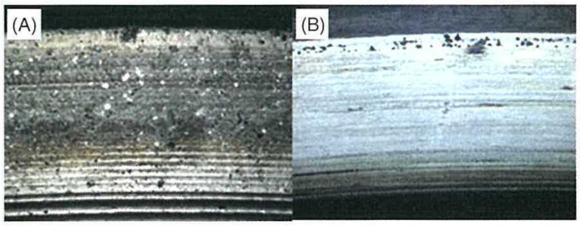

Wear was low enough that the machining striations were not erased.

Photo 4 Appearance of (A) Valve Seat and (B) Valve after Engine Durability Test with E30 Fuel

8. Conclusions

A new highly efficient cladding process and a Cu-Ni-Fe-Mo-Si-Nb-C alloy with excellent performance under global fuel usage environments were developed. Various issues were then resolved to adopt this process and material in the TNGA engine series.

- A compact and highly energy efficient laser rotating cladding system was achieved by adopting a diode laser and developing an angled forming technique that uses a coaxial nozzle to integrate the delivery of a laser beam, powder, and shielding gas.
- Crack resistance during cladding was improved through alloy design using a basic Cu-Fe system alloy and controlling the dispersion of hard grains.
- Excellent wear resistance and machinability were realized to enable compatibility with different fuels around the world.
- Optimization of the alloy components enabled a fine hard grain dispersion and ensured excellent machinability.
- Ideal intake port design using laser-clad valve seats help the TNGA series of engines to achieve a world-leading tumble ratio of 2.9 and a coefficient of flow of 0.49. As a result, these engines achieved a targeted thermal efficiency of at least 40% and a specific power of 60 kW/L.

The laser-clad valve seats and new cladding material (called CuLS11) will be widely used across the TNGA engine series as a fundamental technology to help achieve high-speed combustion.

Finally, the authors would like to extend their sincere gratitude to everyone at Toyota Central R&D Labs., Inc. for their invaluable support in the design and evaluation of the laser-clad valve seat materials.

References

(1) E. Murase, Shimizu. "Innovative Gasoline Combustion Concepts for Toyota New Global Architecture." *25th Aachen Colloquium Automobile and Engine Technology* (2016).

(2) M. Hakariya, Toda, Sakai. "The New Toyota Inline 4-Cylinder 2.5L Gasoline Engine." *SAE Paper* No. 2017-01-1021 (2017).

(3) A. Sato. "Development of Mass Production Technology for Laser-Clad Valve Seat." *GPC* Vol. 16 (2000) pp. 92-101.

(4) M. Kawasaki, Takase, Kato, et al. "Development of Engine Valve Seats Directly Deposited onto Aluminum Cylinder Head by Laser Cladding Process." *SAE Paper* No. 920571 (1992).

(5) J. He, Zhao, Wang, et al. "Microstructure Development in Finely Atomized Droplets of Copper-Iron Alloys." *Metallurgical and Materials Transactions A* Vol. 36 (2005) pp. 2449-2454.

(6) K. Tanaka, Saito, Shimura, Mori, Kawasaki et al. "Development of Copper-Based Composite Material for Valve Seats Compatible with Laser Cladding on Aluminum Alloy" (in Japanese). *Journal of the Japan Institute of Metals and Materials* Vol. 57 No. 10 (1993) pp. 1114-1122.

(7) C. Wang, Liu, Onuma, et al. "Phase Equilibria in Fe-Cu-X (X: Co, Cr, Si, V) Ternary Systems." *Journal of Phase Equilibria* Vol. 23 No. 3 (2002) pp. 236-245.

(8) C. Qang, Liu, Onuma, et al. "Formation of Immiscible Alloy Powders with Egg-Type Microstructure." *Science* Vol. 297 Issue 5583 (2002) pp. 990-993.

(9) P. Villars, Prince, Okamoto. *Handbook of Ternary Alloy Phase Diagrams Volume 1*. ASM International. Materials Park (1995) p. 10487.

Note: this article is based on the following published technical paper.
H. Aoyama, Kawasaki, Miyara, Sugiyama, Ando et al. "Development of Laser Clad Valve Seat." *Proceedings of the JSAE Annual Congress* (2017) pp. 1854-1859.

Authors

H. AOYAMA

N. MIYARA

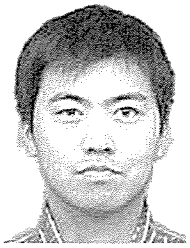

N. SUGIYAMA

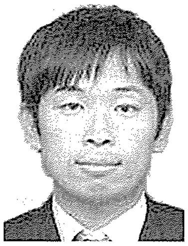

K. YANAKA

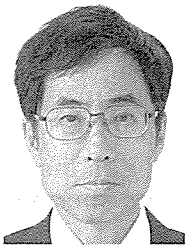

K. ANDO

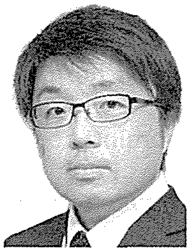

T. OSHIMA

Development of New Front-Wheel Drive Direct-Shift 8-Speed Automatic Transaxle

Ryohei Imanishi*1
Daisuke Kusamoto*2
Hiroomi Toi*2
Nobukazu Ike*3
Takashi Yasuda*3
Masahiro Ito*3

Abstract

A new direct-shift 8-speed automatic transaxle has been developed for 3.5-liter and 2.5-liter class front-wheel drive (FWD) vehicles. To maintain the excellent mountability of the previous 6-speed transaxle while enhancing both vehicle dynamics and fuel efficiency, the new transaxle features a completely redesigned gear train as well as various advanced technologies. This article focuses on the following three key development targets: 1) enhancing efficiency and fuel efficiency, 2) achieving direct and smooth shifting performance, and 3) reducing weight and size. One of the main issues was booming noise in high gear stages, which has a trade-off relationship with the expanded lock-up area adopted to help achieve targets 1) and 2). Booming noise was reduced by setting a tolerance ring between the C1 drum and the rear sun gear to utilize the C1 clutch effectively as inertia. Target 3) was achieved by integrating parts and adopting different materials to reduce the weight and shorten the overall length of the transaxle.

Keywords: *TNGA, automatic transaxle, improved fuel efficiency, shifting performance, lock-up, booming noise, weight reduction*

1. Introduction

Rising awareness of global environmental issues is increasing demand for greater vehicle fuel efficiency to help reduce CO_2 emissions. In developed markets such as Japan, Europe, and the U.S., automakers are actively working to popularize hybrid vehicles (HVs) and to develop zero-emission electric vehicles (EVs).

However, since internal combustion vehicles are likely to make up the majority of vehicles on a global basis for the foreseeable future, the development of technologies for conventional powertrains is a potentially effective way of reducing CO_2 emissions due to the scale that these vehicles are used around the world. Consequently, a new direct-shift 8-speed automatic transaxle has been developed that covers a wide torque band. Two variants of this transaxle were developed with the aim of helping to reduce CO_2 emissions by improving fuel efficiency: the UA80 transaxle for 3.5-liter engines(1) and the UB80 transaxle for 2.5-liter engines. This article describes an outline of this new 8-speed automatic transaxle and the technologies that were adopted.

2. Development Approach

Toyota Motor Corporation has formulated and adopted the Toyota New Global Architecture (TNGA) design philosophy to enhance its competitiveness by developing and manufacturing vehicles with substantially greater product appeal, lower costs, and higher productivity. The objective of the TNGA is to enhance both design and dynamic performance by adopting innovative structural and powertrain technology, as well as by lowering the hood and center of gravity of the vehicle. In the production field, the TNGA aims to streamline steps and equipment in plants by commonizing processes and tools, adjust flexibly to market needs, and achieve rapid product launches. This new 8-speed automatic transaxle was the first to be developed under the concepts of the TNGA. The transmission torque converter, gear train, valve body, and oil pump were commonized and optimized for specific uses based on engine characteristics and the required dynamic performance.

3. Development Aims

Fig. 1 shows a cross-section of the transaxle. An 8-speed gear train was selected from the standpoints of controllability, mountability, and transaxle efficiency with the aim of improving fuel efficiency by increasing the number of gear speeds. The three key development items were as follows.

(1) Design to enhance efficiency and fuel efficiency by enlarging the gear spread, expanding the lock-up area, and reducing transaxle losses
(2) Design to achieve direct and highly responsive driving force through a new control methodology and expanding the lock-up area
(3) Lightweight and compact design: compact design to reduce transaxle weight and to enable installation in a wide range of models by lowering the number of parts and changing materials.

[*1] Kinuura Plant Manufacturing Engineering Service Div., Powertrain Company
[*2] Drivetrain-EHV Design Div. No. 2, Powertrain Company
[*3] Aisin AW Co., Ltd.

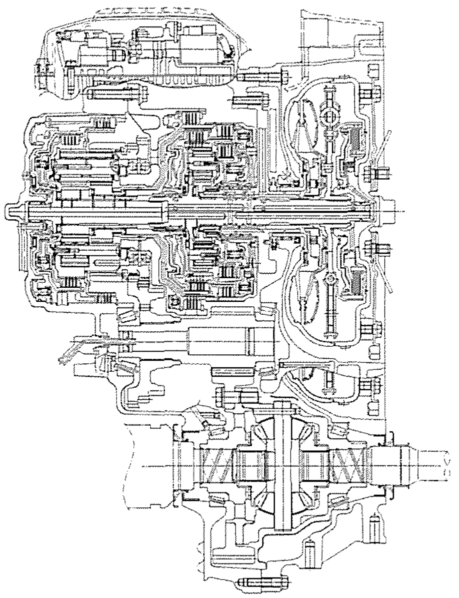

Fig. 1 Cross-Section of New 8-Speed Automatic Transaxle

4. Main Specifications and Basic Structure

The new 8-speed automatic transaxle is configured with the torque converter and gear train on the first axis, the counter gear on the second axis, and the differential gear on the third axis. The variations of the reduction gear are set by the counter gear ratio (**Table 1**).

The oil pump is chain-driven and located on a separate axis, which helps to increase efficiency and shorten the overall length of the transaxle. The location of the valve body was changed from the bottom surface in the previous 6-speed automatic transaxle(2) to the front surface, thereby helping to lower the vehicle center of gravity.

Standing start performance and fuel efficiency were improved by enlarging the gear spread. The transaxle was designed with close gear steps, and rhythmical shifting was achieved, particularly by setting equally spaced gear steps from the 4th to 8th speeds.

The gear train consists of a front planetary gear, Ravigneaux planetary gear, four clutches (C1, C2, C3, and C4), and two brakes (B1 and B2) (**Fig. 2**).

The adoption of new control technology allowed the one-way clutch to be eliminated. This measure helped to restrict the number of component elements to the same as the previous 6-speed automatic transaxle, while reducing the overall length and weight.

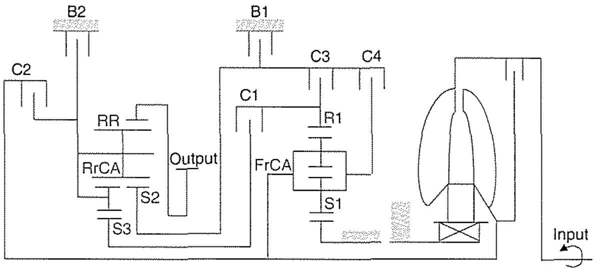

Fig. 2 Skeleton Diagram of Gear Train

Table 1 Main Specifications of New 8-Speed Automatic Transaxle

Transaxle		Previous 6-speed automatic transaxle (V6 engine)	New 8-speed automatic transaxle	
			UA80 (V6 engine)	UB80 (inline 4-cylinder engine)
Torque converter		ϕ260 torus with lock-up clutch	ϕ230 torus with lock-up clutch	
Shifting elements		2 clutches 3 brakes 1 one-way clutch	4 clutches 2 brakes	
Control method		Electronic-hydraulic		
Gear ratios	1st	3.300 >(1.83)	5.519 >(1.73)	5.250 >1.73
	2nd	1.900 >(1.34)	3.184 >(1.55)	3.029 >1.55
	3rd	1.420 >(1.42)	2.050 >(1.37)	1.950 >1.34
	4th	1.000 >(1.40)	1.491 >(1.21)	1.457 >1.19
	5th	0.703 >(1.17)	1.234 >(1.23)	1.221 >1.22
	6th	0.609	1.000 >(1.25)	1.000 >1.24
	7th	–	0.800 >(1.18)	0.809 >1.20
	8th	–	0.673	0.673
	Rev	4.148	4.220	4.015
Counter gear ratio		1.068	0.803	0.846
Final gear ratio		3.238	3.187	3.312
Maximum torque (Nm)		350	380	280
Weight (kg)		94.5	94.3	88.0
Overall length (mm)		384	379	374

This gear train structure is capable of changing to the neighboring gear stage by switching just one component element of the original gear stage, which simplifies the shift control (**Table 2**).

Table 2 Shifting Chart of New 8-Speed Automatic Transaxle

	Clutches				Brakes	
	C-1	C-2	C-3	C-4	B-1	B-2
1st	●					●
2nd	●				●	
3rd	●		●			
4th	●			●		
5th	●	●				
6th		●		●		
7th		●	●			
8th		●			●	
Rev			●			●

Fig. 3 shows the automatic transaxle lineup for each torque band. The torque bands covered by three previous transaxles can be covered by the two new UA80 and UB80 transaxles, thereby reducing the number of transaxle variations while ensuring compatibility with a wide range of vehicle performance requirements.

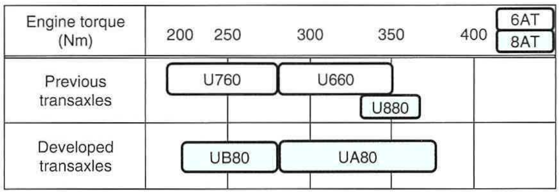

Fig. 3 Automatic Transaxle Types (Front Wheel Drive)

5. TNGA-Based Development

The UA80 transaxle for 3.5-liter engines and the UB80 transaxle for 2.5-liter engines were developed to cover a wide torque range. Parts were commonized and optimized in accordance with torque (**Fig. 4**).

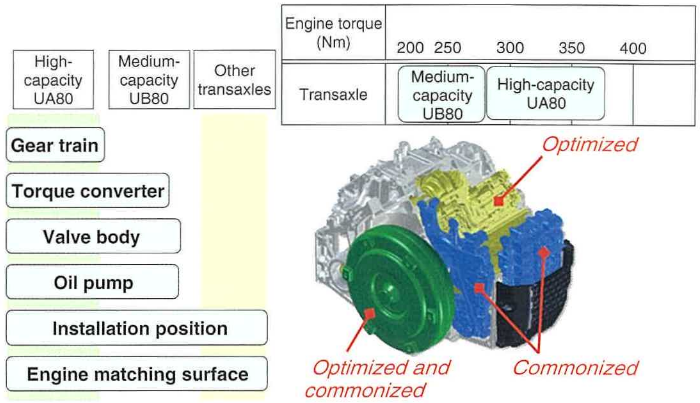

Fig. 4 Example of Optimization and Commonization

5.1 Commonization with other transaxles

Fig. 5 shows the engine attachment parts of the UB80 and HV transaxles for use with the new 2.5-liter engine. This development commonized the attachment bolt positions and assembly knock pin positions between different transaxles. This allows the same engine matching surface to be used for different transaxles (previously, this surface was different for each transaxle) and minimizes new investment in manufacturing processes.

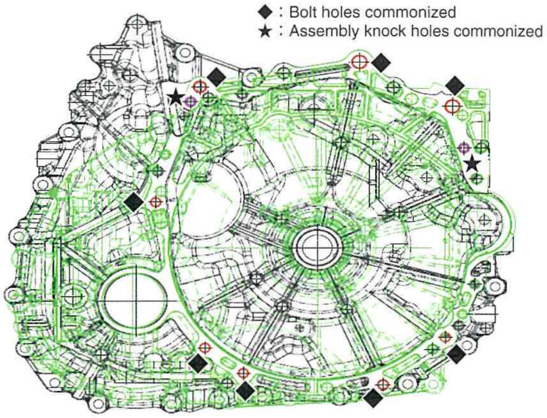

Fig. 5 Comparison of Engine Matching Surface of UB80 and HV Transaxles

5.2 Commonization within UA80 and UB80 transaxles

Two common valve bodies and oil pumps, which are hydraulic system parts that do not depend on torque, were developed: high-capacity and medium-capacity variants.

5.3 Optimization between UA80 and UB80 transaxles

The datum positions for the torque converter, gear train, and transmission case were commonized, and optimum designs with different geometrical specifications were adopted depending on the torque (**Fig. 6**).

Commonizing the datum positions allows the design of general-purpose production lines that can handle a mix of products.

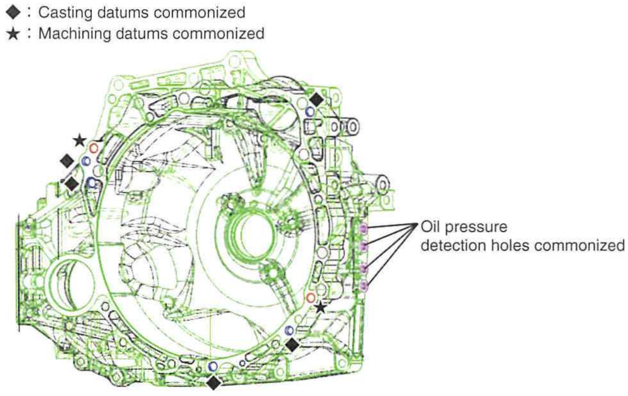

Fig. 6 Comparison of UB80 and UA80 Housings

6. Fuel Efficiency

To increase the efficiency of the new 8-speed automatic transaxle, losses were categorized based on the following three development targets: (1) wider gear train spread, (2) lower transaxle loss, and (3) expanded lock-up area. Newly developed technologies were incorporated to achieve these targets, which helped the new transaxle achieve higher fuel efficiency than the previous 6-speed automatic transaxle (**Fig. 7**).

This section describes some typical examples of the new technologies that were adopted to improve fuel efficiency.

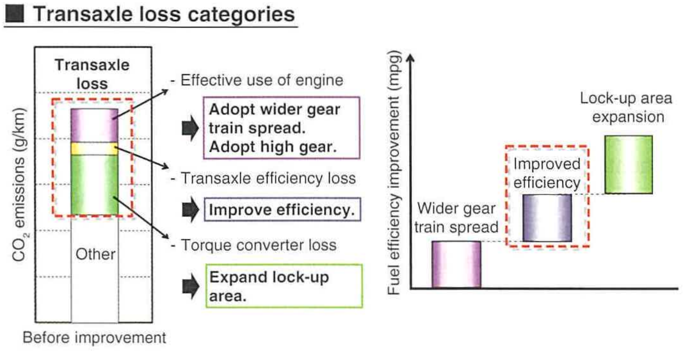

Fig. 7 Analysis of Transmission Losses

6.1 Wider gear train spread

The new 8-speed automatic transaxle features a 1st speed gear ratio that is 24% lower and a top gear ratio that is 24% higher than the previous 6-speed automatic transaxle. This helps to improve acceleration from both a standing start and low speeds, while also ensuring fuel-efficiency and low noise while cruising (**Fig. 8**).

The lower 1st speed gear ratio helps to expand the lock-up area to lower speeds, facilitating both a strongly direct driving feel and improved fuel efficiency. The gear spread of both transaxle variants was enlarged compared to the previous 6-speed transaxle (UA80: 5.4→8.2, UB80: 5.4→7.8) to match the characteristics of the engine.

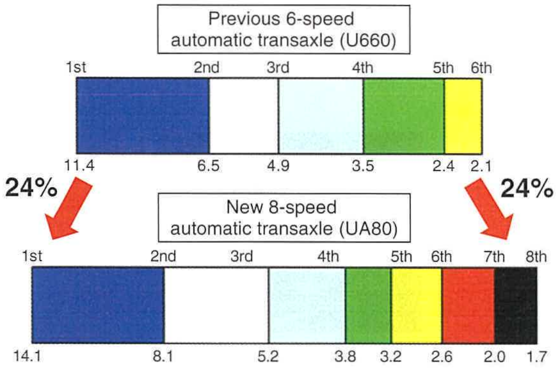

Fig. 8 Comparison of Gear Spreads

6.2 Reduction of transaxle loss

The new 8-speed automatic transaxle achieves world-class transmission efficiency compared to other FWD automatic transaxles in the same torque band, which makes a major contribution to improved vehicle fuel efficiency (**Fig. 9**). The main items adopted to increase transmission efficiency are described below.

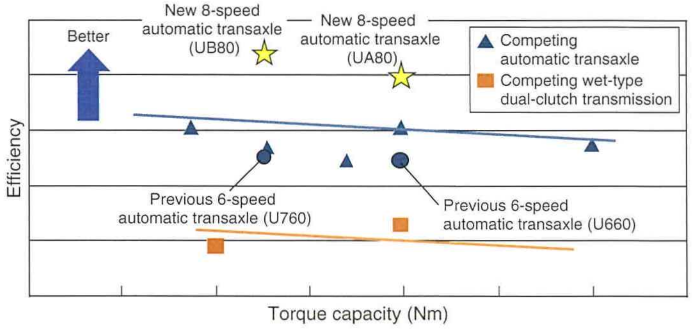

Fig. 9 Comparison of Transaxle Efficiency

Gear meshing loss is a major factor that affects transmission efficiency.

As shown in **Fig. 10**, meshing loss depends on the friction coefficient, load distribution, and sliding velocity.

$$\begin{bmatrix}\text{Meshing}\\ \text{loss}\end{bmatrix} = \int \begin{matrix}\text{Engagement}\\ \text{direction}\\ \text{length}\end{matrix} \int \begin{matrix}\text{Simultaneous}\\ \text{contact}\\ \text{length}\end{matrix} \underset{\substack{\uparrow\\ \text{Super-finished surfaces}}}{\begin{bmatrix}\text{Friction}\\ \text{coefficient}\\ \mu\end{bmatrix}} \times \underbrace{\begin{bmatrix}\text{Load}\\ \text{distribution}\\ \text{P}\end{bmatrix} \times \begin{bmatrix}\text{Sliding}\\ \text{velocity}\\ \text{V}\end{bmatrix}}_{\text{Optimized tooth profiles}} d/dt$$

Fig. 10 Gear Efficiency Calculation Formula

A super finishing process was applied to the counter and final gears of the new 8-speed automatic transaxle to smooth tiny convex irregularities in the gear tooth surfaces while preserving the concavities used to retain the required amounts of lubrication oil.

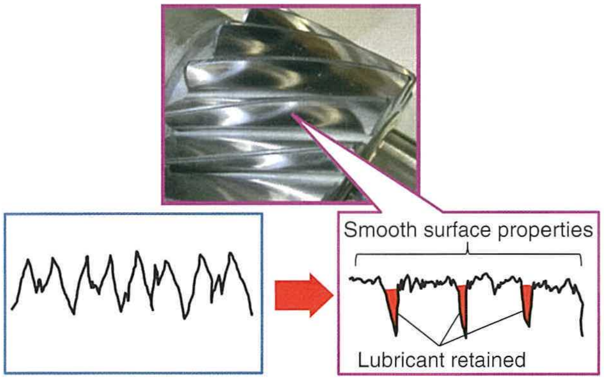

Fig. 11 Gear Tooth Surface Properties

6.3 Lock-up area expansion

One of the main component parts of the transaxle is the torque converter. The lock-up area of the torque converter was expanded by adopting a multi-plate lock-up clutch and optimizing the inertia, resulting in improved fuel efficiency and more direct shifting response. **Fig. 12** compares the lock-up areas of the previous 6-speed and new 8-speed automatic transaxles.

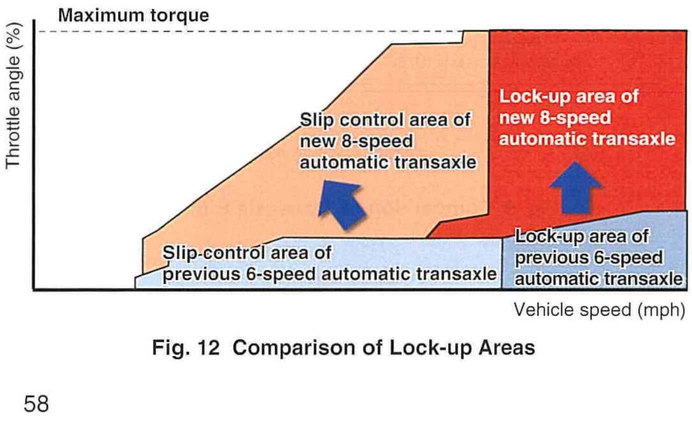

Fig. 12 Comparison of Lock-up Areas

The transmission paths of booming noise include the engine mountings, exhaust system hanger bushings, and suspension mountings. When lock-up occurs at low engine speeds, driveshaft torque fluctuations worsen, causing the transmission of booming noise from the suspension mountings. In the new 8-speed automatic transaxle, the component parts of the C1 clutch are integrated with the C1 drum parts that rotate at high speed. This increases inertia without increasing the weight of the transaxle, thereby reducing booming noise at high gear stages (**Fig. 13**).

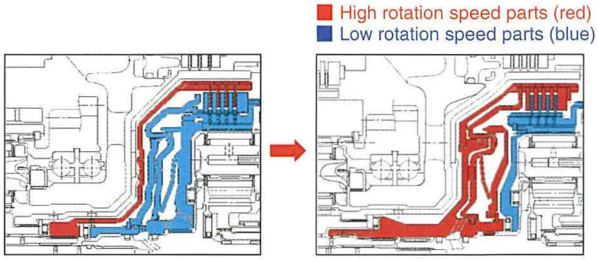

Fig. 13 Changes to C1 Clutch Structure

In the expanded lock-up area of the UB80 transaxle, which is used for 4-cylinder engines, the development identified an area in which the additional C1 inertia does not function over a certain rotation speed and the driveshaft torque fluctuations do not decrease in accordance with the rotation speed (**Fig. 14**).

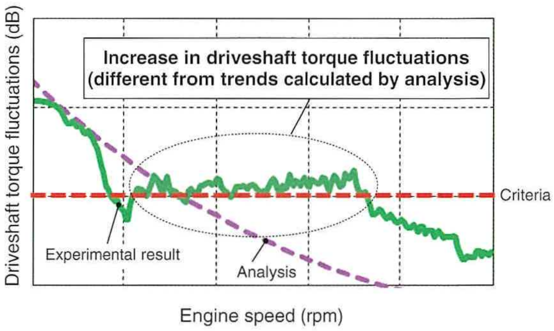

Fig. 14 Comparison of Simulation and Experimental Results

Using the 8th speed as an example, the C1 clutch generates unloaded inertia that rotates together with other rotating elements. In this case, the only freedom is provided by the back lash of the spline engagement portion. **Fig. 15** shows the results of an evaluation using an actual transaxle with the C1 clutch removed. The graph illustrates that the inertia element behavior is extremely unstable and that the additional inertia does not function.

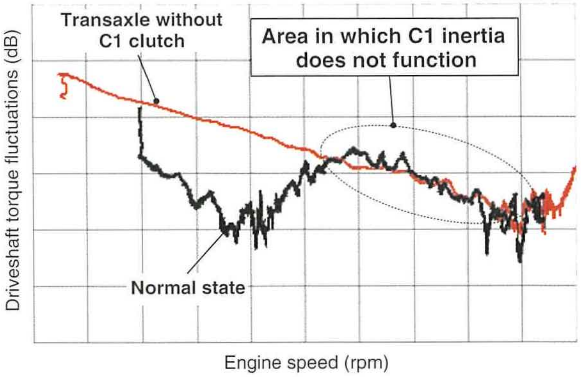

Fig. 15 Results of Confirmation of C1 Clutch Inertia Effect

Analysis focused on the back lash of the spline engagement portion, which is the cause of the unloaded inertia. The analysis identified the same trend as with the actual transaxle, and found that reducing the amount of back lash could lower booming noise (**Fig. 16**).

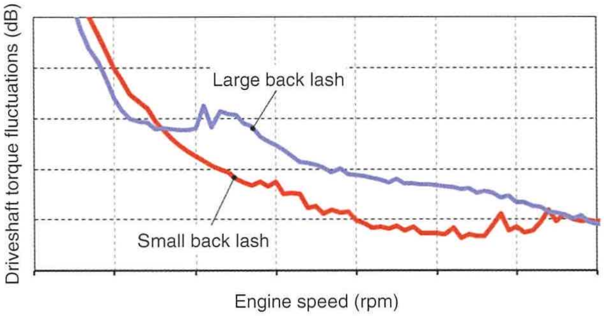

Fig. 16 Comparison of Driveshaft Torque Fluctuations Due to Spline Back Lash

Adopting a press-fit spline was considered as a countermeasure to eliminate the back lash. However, this would require a high press-fitting force, which would be difficult to achieve during production. The development also considered eliminating back lash in the design of the spline structure, but the desired effect could not be achieved due to limitations of dimensional accuracy.

Therefore, a new part called a tolerance ring that absorbs the back lash in the direction of rotation was developed for the UB80 transaxle. This part successfully reduced the torque fluctuations (**Fig. 17**). Production-related issues were resolved by optimizing the material and clearance design to minimize the size of the press-fitting force (**Fig. 18**).

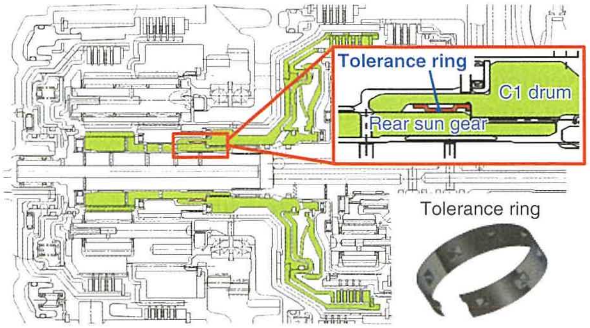

Fig. 17 Tolerance Ring Structure

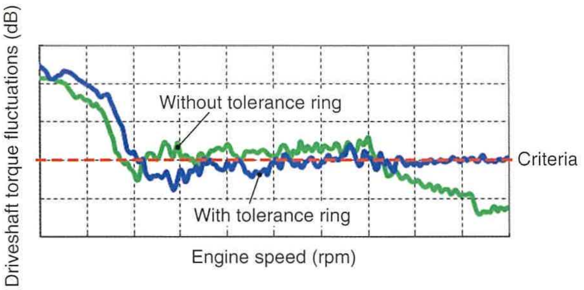

Fig. 18 Results of Confirmation of Tolerance Ring Effect

7. Weight Reduction

To maintain the same weight as the previous 6-speed automatic transaxle while increasing the number of gear speeds, the weight of the new 8-speed automatic transaxle was reduced by changing materials to aluminum and plastic, integrating and consolidating parts, and the like (**Fig. 19**).

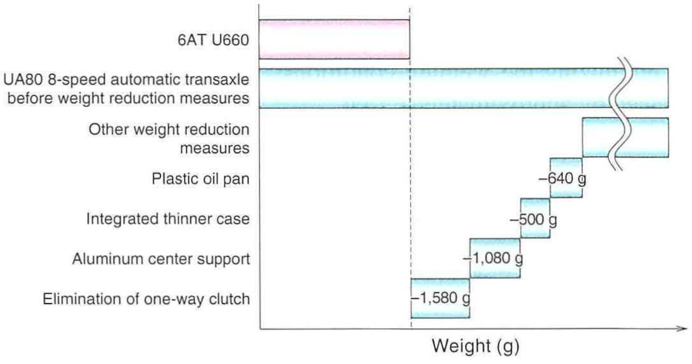

Fig. 19 Weight Reduction Measures

7.1 Center support

Conventionally, center supports are made of steel to ensure sufficient strength to withstand the reaction force of the counter gear. A new aluminum center support was developed for the new 8-speed automatic transaxle with improved elongation performance and lower tensile strength dispersion. Integrating the new center support with the neighboring drum reduced weight by more than 1 kg (**Fig. 20**). The elongation performance of this newly developed aluminum material is more than four times higher than a conventional material, which was achieved by optimizing the amounts of iron, magnesium, silicon, and the like that make up the material. Additionally, integrating the brake structures also helped to increase stiffness, reduce the number of parts, and improve assemblability.

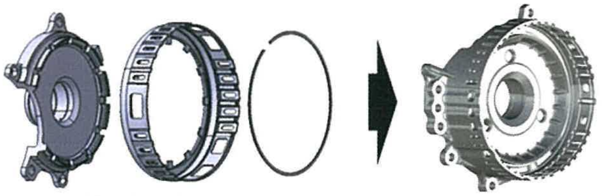
Previous transaxle

New 8-speed automatic transaxle

Fig. 20 Center Support Structure

7.2 C3 drum

The previous 8-speed automatic transaxle$^{(3)}$ used stamped steel parts to form the complex shape of the C3 and C4 clutch structure. In the UB80 transaxle, two aluminum parts are welded together to reduce weight (**Fig. 21**). Two issues identified during this development were cracking generated by the heat of welding and thermal deformation of the rubber seal of the built-in clutch piston. The first issue was resolved by incorporating newly developed material properties. The second was resolved by optimizing the welding conditions. As a result, weight was reduced by approximately 1.2 kg.

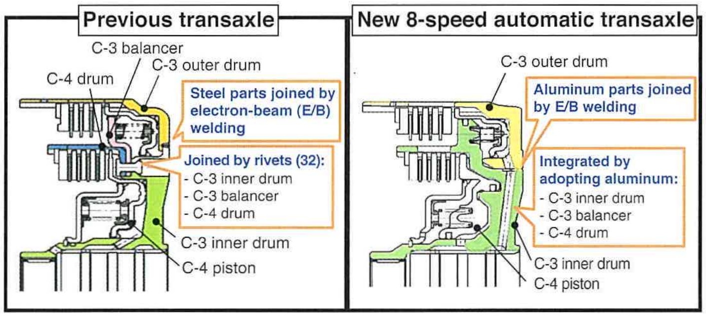

Fig. 21 C3 Clutch Structure

8. Conclusions

1) The rapid adoption of this newly developed 8-speed automatic transaxle in a wide variety of models was facilitated by measures to commonize and optimize parts, as well as to raise development efficiency and productivity.
2) The transmission efficiency of the developed transaxle is 8% higher than the previous 6-speed automatic transaxle. Combined with the expanded lock-up area described in point 3, the developed transaxle helps to improve vehicle fuel efficiency.
3) The lock-up area of the developed transaxle was expanded by 10% compared to the previous 6-speed automatic transaxle, which helps to create a better direct shifting feel.
4) Despite having a larger number of gear speeds, the developed transaxle is at least 6 kg lighter and 5 mm shorter than the previous 6-speed automatic transaxle. As a result, the development maintained the mountability of the transaxle without increasing its weight.

References

(1) Y. Michikoshi, Kusamoto, Ota, et al. "Toyota New TNGA High-Efficiency Eight-Speed Automatic Transmission Direct Shift-8AT for FWD Vehicles." *SAE Paper* No. 2017-01-1093 (2017).

(2) D. Kusamoto, Yasuda, Watanabe, et al. "Toyota's New Six-Speed Automatic Transmission U660E for FWD Vehicles." *SAE Paper* No. 2006-01-0847 (2006).

(3) T. Aoki, Kato, Kato, et al. "The World's First Transverse 8-Speed Automatic Transmission." *SAE Paper* No. 2013-01-1274 (2013).

Note: this article is based on the following published technical paper.
R. Imanishi, Kusamoto, Fujita, Toi, Takebayashi et al. "Development of New FF Direct Shift 8-Speed Automatic Transaxle." *Proceedings of the JSAE Annual Congress* (2017) pp. 1436-1441.

Authors

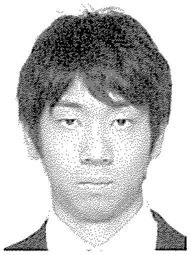

R. IMANISHI

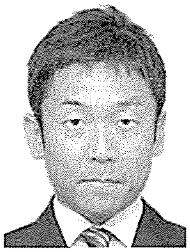

D. KUSAMOTO

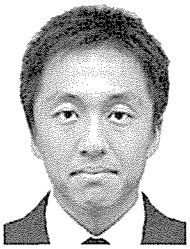

H. TOI

N. IKE

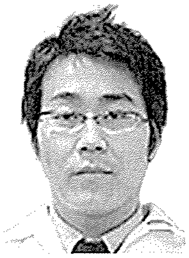

T. YASUDA

M. ITO

Development of New 10-Speed Automatic Transmission for Rear-Wheel Drive Passenger Vehicles

Kazuhiko Yamada[*1]
Terufumi Miyazaki[*2]
Yoshio Hasegawa[*3]
Takahiro Kondo[*3]
Seiji Masunaga[*3]
Ichiro Kitaori[*3]
Akira Takeichi[*2]

Abstract

A new 10–speed automatic transmission has been developed for next-generation rear-wheel drive (RWD) luxury coupes. In accordance with the dynamic performance concept of these vehicles (“sharper and more refined driving”), this automatic transmission was developed with an optimum gear ratio and new shift control technology. These features help to enhance both fuel efficiency and driving performance, while also ensuring an exciting and greatly improved driving experience. This article describes the development concept of the new 10-speed automatic transmission for RWD passenger vehicles (model code: AGA0), the gear ratio design method that was adopted to achieve the targeted driving performance, the details of hardware refinements, and the newly adopted shift control technology.

Keywords: *automatic transmission, 10-speed, gear step, gear spread, shift control, driver intention, driving situation*

1. Introduction

As global environmental regulations grow increasingly stringent, drivers are demanding transmissions that enable both excellent driving performance and high fuel efficiency. In response, multi-speed (continuously variable) automatic transmissions that provide direct feedback to the driver are being developed with an emphasis on higher engine power transmission efficiency. Additionally, in the rear-wheel drive (RWD) segment, transmissions play an important role in creating a more comfortable driving experience for the driver as a way of creating greater product appeal.

Toyota Motor Corporation has developed a new 10-speed automatic transmission for RWD passenger vehicles (model code: AGA0) for installation in next-generation RWD luxury coupes. In addition to fuel efficiency and dynamic performance, the development of this transmission aimed to enhance driving enjoyment under the concept of achieving a “sharper and more refined” experience.

This article describes the development concept of the AGA0 transmission, the gear ratio design method that was adopted to achieve the targeted driving performance, the details of hardware refinements, and the newly adopted shift control technology.

2. Development Aims

The development concept of the AGA0 transmission was as follows.

(1) Rhythmical and sharp shifting

By optimizing the gear ratio of each shift, the developed transmission achieves power-on upshifts with excellent tempo when the engine speed is in the same range during acceleration. Sharp shifting was achieved by shortening the shifting time (i.e., the time taken for the automatic transmission input shaft to reach the same speed after shifting).

(2) Standing start performance and quiet performance during high-speed cruising

The developed transmission is provided with a wide gear spread, consisting of low gears to enhance standing start performance and gears that enable low engine speeds during high-speed cruising.

(3) Driving in tune with driver intentions

The developed transmission incorporates a shift control that estimates the driver’s acceleration intention based on the speed and acceleration of the vehicle, and selects the optimum gear stage in response to the driver’s intention.

(4) Direct response to accelerator operation

This transmission is equipped with a newly developed torque converter that incorporates a multi-plate lock-up clutch and new dynamic lock-up damper, which substantially expands the lock-up area compared to conventional automatic transmissions.

[*1] Drivetrain-EHV Design Div. No. 2, Powertrain Company
[*2] Advanced Powertrain Design & Engineering Div., Powertrain Company
[*3] Electric Powertrain System Development Div., No. 4, Powertrain Company

(5) Excellent fuel efficiency

In addition to the lightness of the gear train, technologies such as the new torque converter that expands the lock-up area and low friction materials help to greatly improve vehicle fuel efficiency. The specifications of the transmission allow the application of an idling stop function. Its structure is also designed to accommodate an accumulator, which is capable of supplying the necessary oil pressure to operate the automatic transmission while the engine is coming back on line.

3. Design of Optimum Gear Ratio

This section describes the gear step and gear spread design process adopted for the AGA0 transmission within the overall gear ratio design process to simultaneously realize the first and second aspects of the development concept (i.e., "rhythmical and sharp shifting" and "standing start performance and quiet performance during high-speed cruising").

3.1 Gear step design method

The development aimed to realize rhythmical shifting when the engine speed is in the same range during acceleration.

First, the target vehicle acceleration was designed. When the vehicle is accelerating with the accelerator pedal at a constant angle, the target acceleration is set to create a continued and consistent acceleration feeling for the driver. As a way of expressing subjective characteristics, the Weber-Fechner law is a well-known method of deriving the relationship between the degree of a physical stimulus and its perception. This relationship can be shown by the following equation, in which the change in perception ΔE is proportional to the Weber ratio (ΔR/R) of the amount of stimulus R. Here, k is the proportionality constant.

$$\Delta E = k\,\Delta R/R \qquad (1)$$

This law can be applied to a transmission as follows, with the change in perception represented as the acceleration felt by the driver ΔV', the stimulus represented by the vehicle acceleration G, and including the proportionality constant k.

$$\Delta V' = k\,\Delta G/G \qquad (2)$$

This equation was used to design the acceleration felt by the driver ΔV' as the target acceleration after obtaining the proportionality constant k experimentally. **Fig. 1** shows the designed target vehicle acceleration. To achieve an equal acceleration feeling, the change in vehicle acceleration becomes larger when the vehicle acceleration is higher.

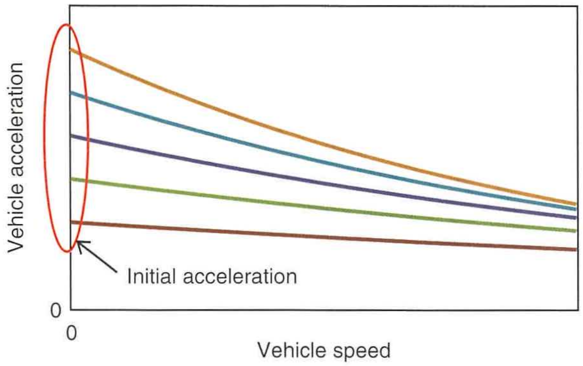

Fig. 1 Target Acceleration for Achieving an Equal Acceleration Feeling

Next, the development designed a target time for the upshift start interval during acceleration. With a conventional automatic transmission, positive driving force characteristics are maintained by elongating the upshift start interval as the number of upshifts increases.

In contrast, the AGA0 transmission achieves excellent driving force characteristics through the engine control and gear ratios. In addition, a target upshift start interval time during acceleration was set to realize rhythmical shifting. **Fig. 2** compares the rotation speed behavior of the automatic transmission input shaft during acceleration from a standing start between the developed transmission and the previous 8-speed automatic transmission (model code: AA80).

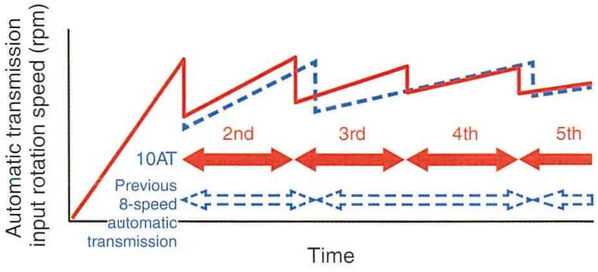

Fig. 2 Comparison of Automatic Transmission Input Shaft Rotation Speed Behavior during Acceleration from Standing Start

As described above, the gear steps between the gear stages were designed with target upshift start intervals to generate changes in rotation speed in the same engine speed area, while realizing the target acceleration. **Fig. 3** shows the rotation speed behavior of the automatic transmission input shaft during acceleration from a standing start, utilizing the designed gear ratio and upshift timings. The figure indicates that the automatic transmission input shaft rotation speed changes within a certain engine speed range and that the upshifts are successfully accomplished.

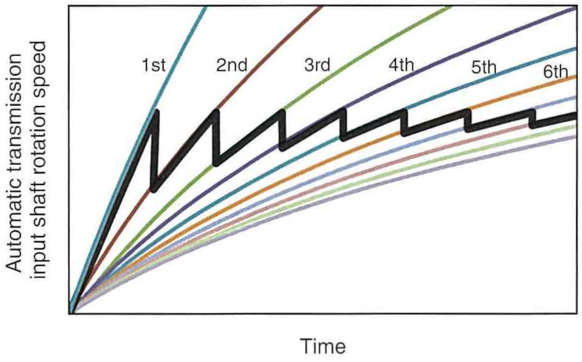

Fig. 3 Automatic Transmission Input Shaft Rotation Speed Behavior during Acceleration from Standing Start

3.2 Gear spread design method

This section describes the design method for the low and high side gear ratios.

In the AGA0 transmission, the first gear stage is used as a dedicated gear stage for standing starts. Therefore, the design focused on the gear ratios from the second to the highest gear stages. In accordance with the greatly expanded lock-up area, the gear ratio for the second gear stage was designed to achieve sufficient driving force for acceleration without relying on the torque amplification function of the torque converter. The gear steps that were designed as described in the previous section were then applied based on this second stage gear ratio to determine the gear ratios for the low speed gear stages.

In contrast, the gear ratios for the highest gear stages were designed in consideration of the available driving force during cruising, in addition to fuel efficiency and silent operation at high speeds. The optimum target engine speed for high-speed cruising was identified and the ideal gear ratios were set based on engine efficiency, engine torque characteristics, as well as noise and vibration (NV) performance.

Following the description above, **Fig. 4** summarizes the gear ratio design method for each gear stage. Compared to the AA80 transmission, the developed transmission required lower gear stages for the lowest gear ratio and higher gear stages for the highest gear ratio.

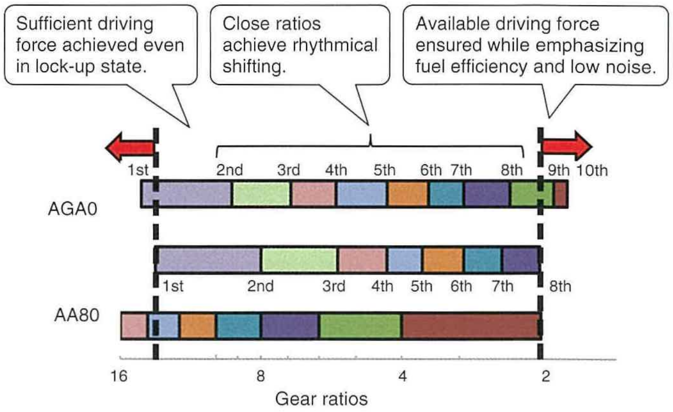

Fig. 4 Gear Ratios and Gear Ratio Design Method

4. Configuration of Transmission System

The automatic transmission was designed to simultaneously achieve the gear steps and spread described in the previous section. Unlike the AA80 transmission, the AGA0 transmission features closer gearing that positions the gear ratio of each gear stage close together to shorten the upshift start interval during acceleration. In addition, the AGA0 transmission features 10 speeds since an extra gear stage was required on the high speed side to ensure silent operation and excellent fuel efficiency during high-speed cruising. This section describes the configuration of the AGA0 system. **Fig. 5** shows the external appearance of the AGA0 transmission.

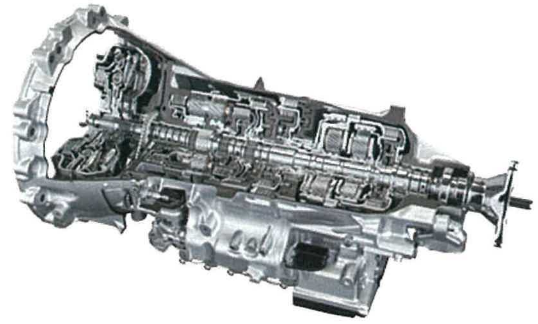

Fig. 5 External Appearance of AGA0 Transmission

4.1 Structure and main specifications

The AGA0 transmission consists of four newly designed planetary gears and the same number of friction elements as the AA80 transmission to realize the targeted gear ratios for 10 forward gears. Additionally, world-leading lightness was achieved by adopting a two-stage engagement structure using separate friction elements for the inner and outer sides of the same portions, as well as aluminum members. Excellent vehicle mountability was ensured by achieving the same axial length and central diameter as the AA80 transmission. **Table 1** shows the technical data of the AGA0 transmission, **Table 2** shows the engagement of the friction elements and the gear ratio of each gear stage, and **Fig. 6** shows a skeleton diagram of the gear train.

Table 1 Technical Data of AGA0 Transmission

Items	Description		
Installation engines	2UR-FSE	V35AFTS	8GR-FKS
Transmission model code	AGA0		
Drive method	RWD	RWD/AWD	RWD
Torque converter format	3-element, 1-stage, 2-phase (with lock-up mechanism)		
Transmission format	Electronically controlled planetary gears		
Name of oil	Genuine Toyota World Standard (WS)		
Oil capacity (L)	8.8		

Table 2 Shift Pattern of AGA0 Transmission

	C1	C2	C3	C4	B1	B2	Gear ratios	Steps
Rev		○	○			○	5.169	
1st	○	○				○	4.923	
2nd	○				○	○	3.153	1.56
3rd		○			○	○	2.349	1.34
4th				○	○	○	1.879	1.25
5th		○		○	○		1.462	1.29
6th	○			○	○		1.193	1.23
7th	○		○	○			1.000	1.19
8th			○	○	○		0.792	1.26
9th	○		○		○		0.640	1.24
10th		○	○		○		0.598	1.07

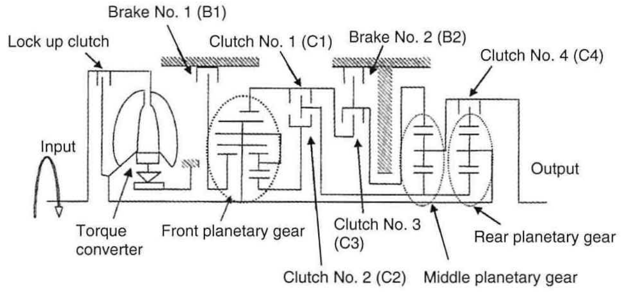

Fig. 6 Skeleton Diagram of AGA0 Gear Train

4.2 Newly developed torque converter

The AGA0 transmission features a greatly expanded lock-up area compared to the AA80 transmission. This was achieved by adopting a newly developed torque converter that incorporates a multi-plate lock-up clutch with excellent oil pressure response and a new dynamic lock-up damper that enables lock-up from low vehicle speeds. **Fig. 7** compares the lock-up area of the AGA0 and AA80 transmissions. By expanding the lock-up control to lower vehicle speeds and higher accelerator pedal angles, the lock-up area extends virtually over the whole range shown in the figure. This helps to realize a driving feeling similar to that achieved by a manual or dual-clutch transmission with direct response to accelerator inputs. The expanded lock-up area also increases transmission efficiency during driving, which makes a major contribution to higher vehicle fuel efficiency.

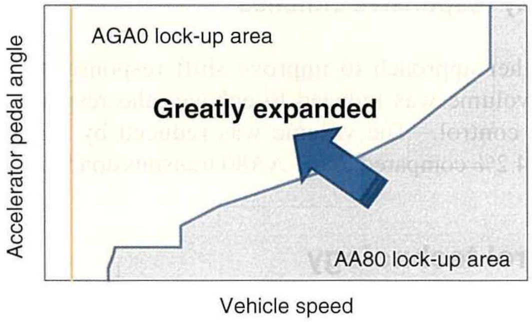

Fig. 7 Comparison of Lock-Up Areas of AGA0 and AA80 Transmissions

Furthermore, the torque converter torus of the AGA0 transmission is flatter (by approximately 13%) and features a smaller external flow path diameter (272 mm reduced to 260 mm). These measures helped to reduce the weight and enhance the mountability of the torque converter. Part commonization was implemented to allow the transmission to be adopted with different engine specifications by changing only the stator and damper. **Fig. 8** compares the external appearance of the torque converter adopted by the AA80 and AGA0 transmissions.

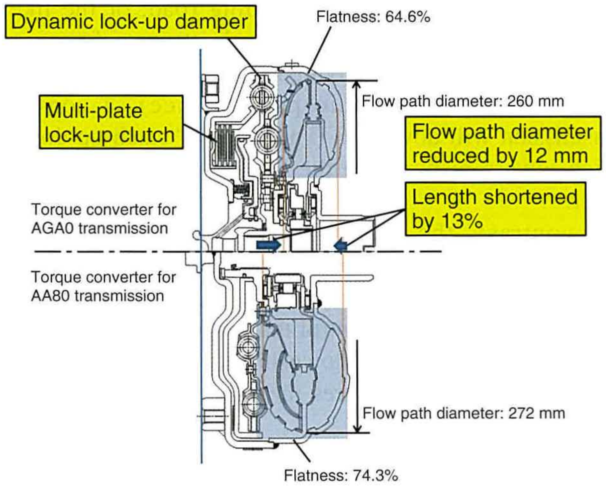

Fig. 8 Comparison of Torque Converter of AGA0 and AA80 Transmissions

4.3 High response and compact valve body

To help achieve highly responsive shifts, the oil pressure response of the AGA0 transmission was improved by 10% compared to the AA80 transmission by adopting linear solenoids. Optimum positioning of the linear solenoids and valves reduced the length of the oil passages and lowered the resistance of the hydraulic lines by 67% compared to that of the AA80 transmission.(1)

4.4 Highly responsive clutches

As another approach to improve shift response, the clutch chamber volume was reduced to enhance the response of the hydraulic control. The volume was reduced by a maximum value of 34.2% compared to the AA80 transmission.(1)

5. Control technology

This section describes the new control technology that was adopted to achieve the following aspects of the development concept: "rhythmical and sharp shifting," "driving in tune with driver intentions," and "direct response to accelerator operation."

5.1 Control in response to driver intention and driving situation

Conventionally, automatic transmissions determine the gear stage based on the shift pattern and road gradient information, using the vehicle speed and accelerator pedal angle set by the driver as parameters. This approach makes it difficult to set gear stages in response to driver intention (i.e., driving emphasizing fuel efficiency, brisk dynamic performance, or the like) and the road environment (highway, winding road, or the like). For example, if the driver wants to accelerate out of a corner on a winding road using high driving force (i.e., a situation that can be defined as brisk dynamic performance), a conventional transmission will downshift (known as a "catch-up downshift"), which lowers response to the driving force demanded by the driver.

In contrast, the AGA0 transmission cancels catch-up downshifts when exiting corners on winding roads only when the driver requires brisk dynamic performance. This is accomplished by a new control that responds to driver intentions and driving situations by downshifting before the vehicle exits the corner. **Fig. 9** compares the gear stages selected with and without this control.

First, the development examined how to determine the driver intention and driving situation to identify the necessary control. If a downshift is carried out when the driver is emphasizing fuel efficiency or during ordinary driving, the engine speed increases and fuel efficiency drops. Therefore, the function that determines the driver intention and driving situation is very important.

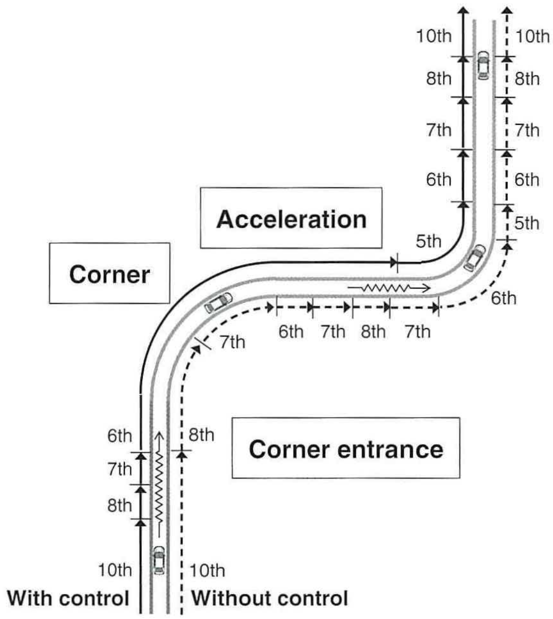

Fig. 9 Comparison of Gear Stages Selected with and without Control Responding to Driver Intentions and Driving Situations (Driver Intention: Brisk Dynamic Performance)

After actual vehicle road tests combining various driving situations and driver intentions, a strong correlation was identified between driver intention and acceleration. Furthermore, lateral vehicle acceleration was identified as an important factor for determining different driving situations on winding roads. **Fig. 10** shows the driving data results analyzed in terms of longitudinal and lateral vehicle acceleration. Longitudinal and lateral vehicle acceleration can be used to identify which driving data refers to brisk dynamic performance on winding roads. As a result, the control can be limited to certain ranges without affecting actual fuel efficiency when driving on highways or urban roads.

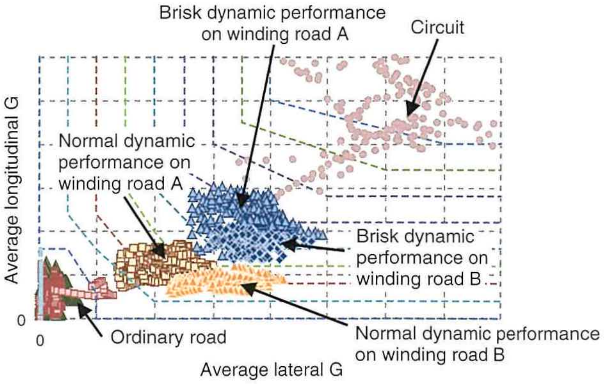

Fig. 10 Driver Intention Determination Results

Next, the development examined how to determine the most appropriate gear stage when entering and driving through a corner on a winding road to help avoid catch-up downshifts when exiting the corner.

When exiting a corner, the gear stage demanded by the driver is determined based on the driving force demand. Therefore, the control must be capable of predicting the driving force demand from the driver when exiting the corner. The combinations of factors involved in entering and driving through a corner (see the list in **Table 3**) that correlate strongly with the factors related to driving force demand when exiting the corner were derived from actual vehicle road tests. As a result, a strong correlation was identified between the vehicle speed when the driver starts to accelerate out of the corner and the maximum absolute acceleration when exiting the corner. The same trend was also found in driving data for other driver intentions. **Fig. 11** illustrates this correlation. As described above, driving force demand when exiting a corner can be predicted from vehicle speed information when entering and driving through the corner.

Table 3 List of Factors when Driving through/Exiting Corner

	Driving situation	
	Driving through corner	Exiting corner
List of factors	Deceleration	Accelerator pedal angle
	Brake master cylinder pressure	Maximum longitudinal G
	Vehicle speed Va when braking starts	Maximum absolute acceleration
	Vehicle speed when entering corner	Target driving force
	Vehicle speed Vb during cornering	Actual driving force
	Vehicle speed Vc when acceleration starts	Engine speed
	Vehicle speed difference (Va vs. Vb)	Gear stage
	Vehicle speed difference (Va vs. Vc)	Difference in vehicle speed between acceleration start and end

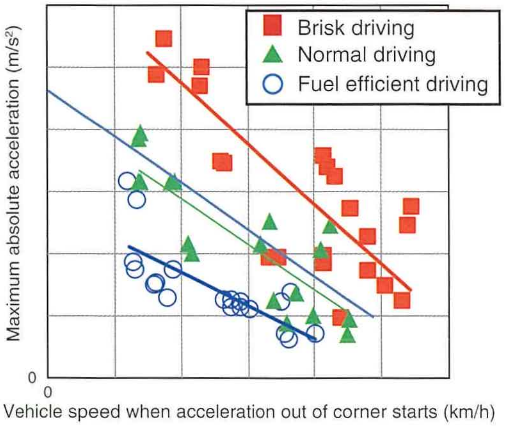

Fig. 11 Vehicle Speed when Acceleration out of Corner Starts and Maximum Absolute Acceleration

In addition, as shown in **Fig. 12**, the control can derive the gear stage capable of achieving the driving force demand in combination with the achievable torque output characteristics of the engine. It should be noted that, when downshifting, the control selects the highest gear stage capable of achieving the driving force demand to restrict the generation of unnecessary deceleration when entering and driving through a corner. As a result, the control can set the optimum gear stage before the driver exits the corner.

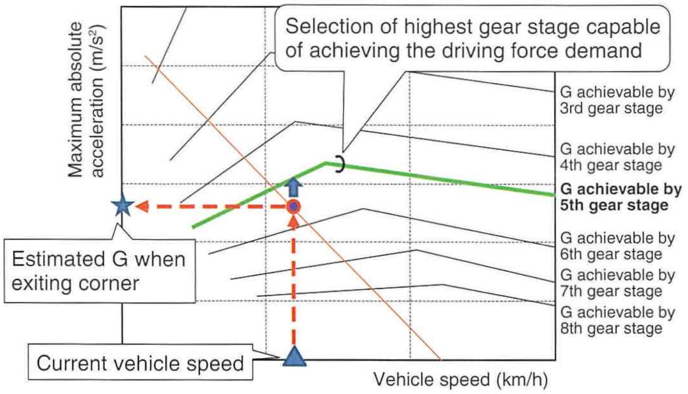

Fig. 12 Target Gear Stage Determination Method

Finally, **Fig. 13** shows the results of a comparative actual vehicle evaluation with and without the control that responds to driver intentions and driving situations on a winding road. The results show the selected gear stage and vehicle acceleration performance with and without the control. When the driver is driving briskly, the control selects a lower gear stage than without the control, thereby eliminating catch-up downshifts. Additionally, when the driver intention changes to more steady driving, the control selects a higher gear stage that emphasizes fuel efficiency as the driving time elapses in the same way as when the control is not implemented.

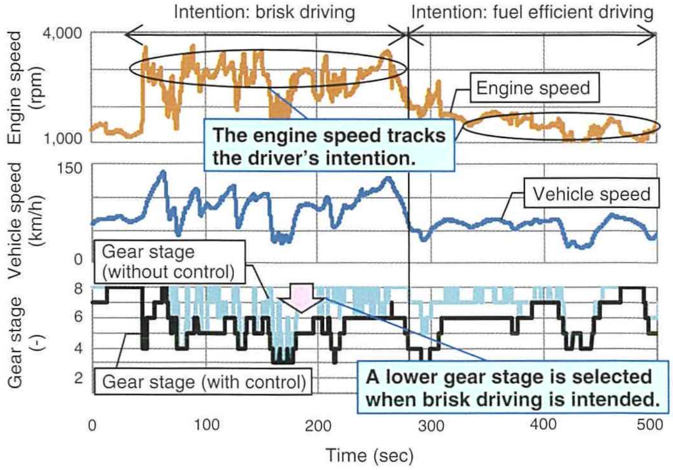

Fig. 13 Actual Vehicle Verification Results

6. Conclusion

Toyota has developed a 10-speed automatic transmission for RWD passenger vehicles. The development researched the optimum automatic transmission gear ratio and shift control designs to achieve the exciting driving performance outlined by the development concept. First, gear step and gear spread design methods were proposed to simultaneously realize the "rhythmical and sharp shifting" and "standing start performance and quiet performance during high-speed cruising" aspects of the development concept. Subsequently, the development proposed a control that responds to driver intentions and driving situations to realize driving performance in tune with driver intention. Actual vehicle tests verified that this control is capable of estimating the driver's intention and selecting the optimum gear stage.

References

(1) M. Hamano, Sugiura, Niinomi, Suzuki, Maezuka et al. "Development of New RWD 10 Speed Automatic Transmission." *Proceedings of the JSAE Annual Congress* (2017) pp. 227-232.

Note: this article is based on the following published technical paper.
K. Yamada, Miyazaki, Hasegawa, Kondo, Masunaga et al. "Development of 10-Speed Automatic Transmission for RWD Passenger Car." *Proceedings of the JSAE Annual Congress* (2017) pp. 1442-1447.

Authors

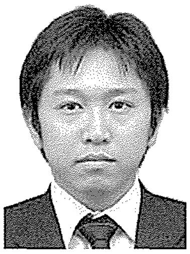

K. YAMADA

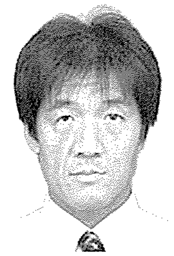

T. MIYAZAKI

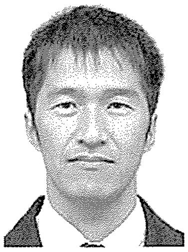

Y. HASEGAWA

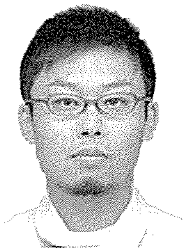

T. KONDO

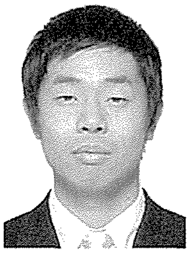

S. MASUNAGA

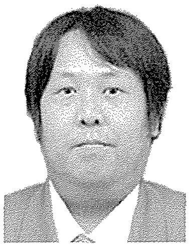

I. KITAORI

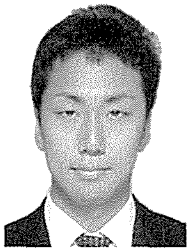

A. TAKEICHI

Design of Highly Efficient Driveline with Low Noise, Vibration, and Harshness for Rear-Wheel Drive Passenger Vehicles

Nobuharu Imai*1
Shinya Takamatsu*2
Takashi Kiten*3
Norihiro Mizoguchi*4

Abstract
Toyota Motor Corporation has developed a new driveline for the Lexus LC500h and LC500 with the objective of achieving the low levels of noise and excellent driving and environmental performance suitable for flagship Lexus models. This article focuses on the technologies adopted to increase the efficiency of the new drivetrain, and the technologies adopted to reduce noise, vibration, and harshness (NVH). High efficiency was achieved by optimizing the differential hypoid gear specifications, bearings, and lubrication structure. Despite increasing the ring gear size by 11% compared to the conventional driveline, fuel efficiency was improved by 0.5% in the European test cycle. NVH performance was improved by greatly reducing booming noise. This was achieved by identifying the effects of propeller shaft axial direction excitation force, and adopting double offset joints and low-stiffness rubber couplings.

Keywords: *driveline, differential, propeller shaft*

1. Introduction

In addition to high levels of dynamic and environmental performance, low noise, vibration, and harshness (NVH) are important requirements for the Lexus LC and LS. The new driveline adopted by these vehicles was developed with the objective of achieving these levels of performance. This driveline adopts either the Multi Stage Hybrid Transmission or a new 10-speed automatic transmission to help realize exciting performance in rear-wheel drive (RWD) passenger vehicles. New technologies have been applied to the driveline to enhance efficiency and reduce noise, while ensuring that the dynamic power of the vehicle is transmitted directly to the tires with minimal loss (**Fig. 1**).

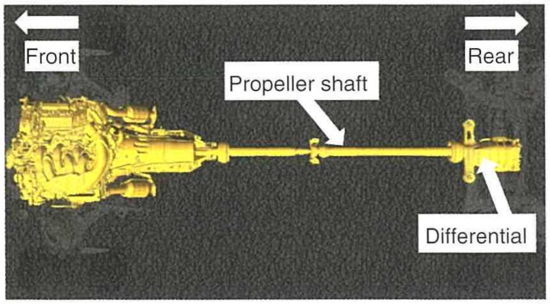

Fig. 1 Outline of Driveline

2. Technologies Incorporated into New Driveline

2.1 Technologies for higher driveline efficiency

Driveline losses affect vehicle fuel efficiency by 2 to 3% and cannot be disregarded when addressing ways of making a vehicle more efficient. These losses can be divided into loading loss, rotational loss, and churning loss. This development optimized the differential hypoid gear specifications, drive pinion bearings, and lubrication structure. As a result, despite increasing the ring gear size by 11% compared to the previous driveline, fuel efficiency was improved by 0.5% in the European test cycle.

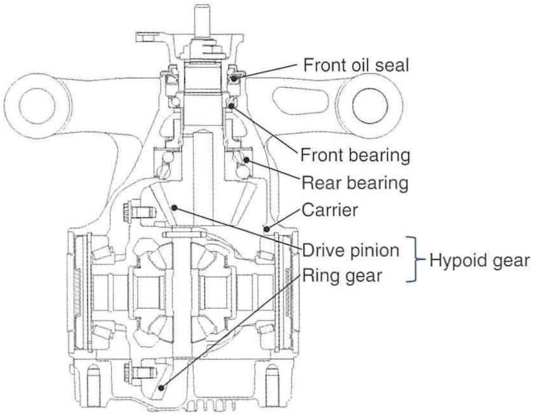

Fig. 2 Outline of New Differential

[*1] Tokyo Engineering Div., Advanced R&D and Engineering Company
[*2] Toyota Motor Europe
[*3] Drive Train, Hybrid Vehicle Powertrain & Chassis Production Engineering Div., Powertrain Company
[*4] R&D and Engineering Management Div., Advanced R&D and Engineering Company

2.1.1 Technologies to reduce loading loss

Loading loss is mainly generated from the hypoid gear of the differential.(1) The previous hypoid gear adopted a large vertical offset and spiral angle (**Fig. 3**) to ensure gear strength and NVH performance. However, this design generates large meshing loss due to sliding between the contacting gear faces.

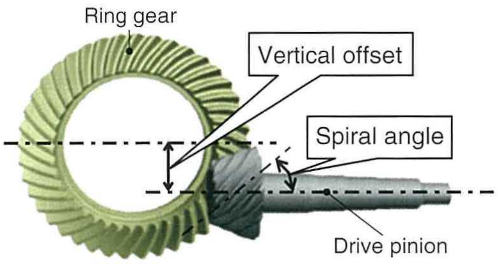

Fig. 3 Offset and Spiral Angle of Hypoid Gear

This development implemented parameter studies and adopted hypoid gear specifications that achieve both high fuel efficiency and strength. **Fig. 4** shows the relationship between the fuel efficiency improvement rate and hypoid gear strength at different vertical offsets. Although fuel efficiency improves as the offset decreases, the strength of the drive pinion falls. Therefore, the thickness of the gear was adjusted to set the optimum offset for achieving the strength target. Additionally, a low spiral angle was adopted to reduce meshing loss and allow the adoption of smaller drive pinion bearings. **Fig. 5** shows the relationship between the fuel efficiency improvement rate and the effective gear contact ratio at different spiral angles. Although reducing the spiral angle improves fuel efficiency, the effective contact ratio decreases and NVH deteriorates. Therefore, the accuracy of the gear face geometry was improved to create the optimum spiral angle for achieving the NVH target.

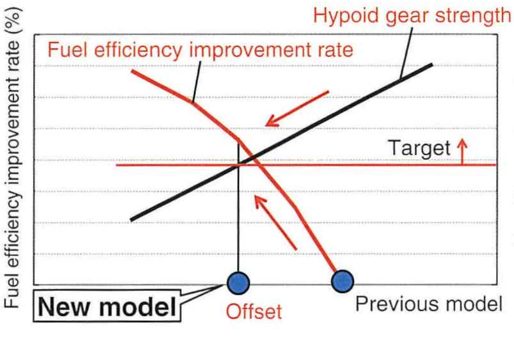

Fig. 4 Offset and Fuel Efficiency Improvement Rate

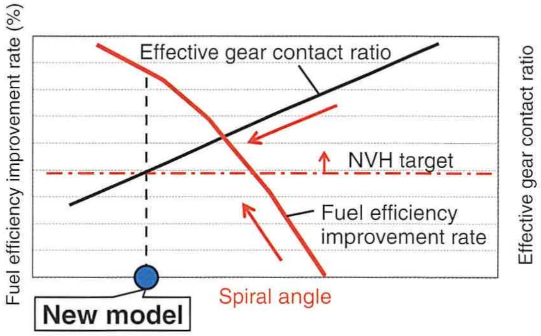

Fig. 5 Spiral Angle and Fuel Efficiency Improvement Rate

2.1.2 Technologies to reduce rotational loss

Rotational loss is mainly generated by the bearings that support the drive pinion. Although this loss can be reduced by switching from tapered roller bearings to ball bearings (**Figs. 6** and **7**), this has an adverse effect on bearing lifetime and hypoid gear support stiffness. However, conventional ball bearings could not be adopted in the new driveline since the size of the bearings needed to be increased to achieve the development targets. Therefore, the new driveline adopted new ball bearings designed to achieve targets for lifetime and stiffness.

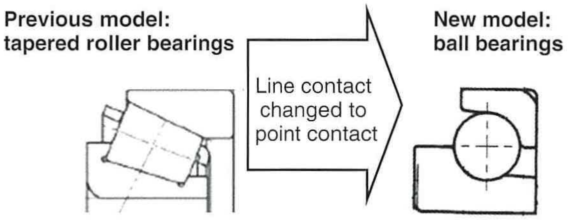

Fig. 6 Outline of Changes to Bearings

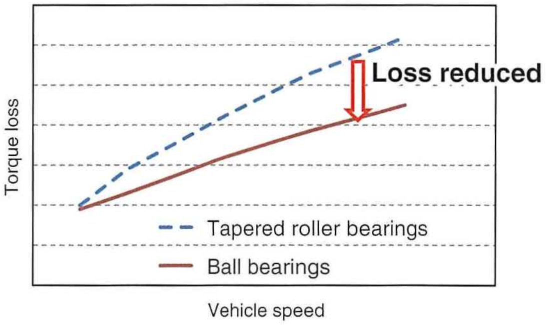

Fig. 7 Comparison of Torque Loss

The target lifetime of the ball bearings was achieved by optimizing the lubrication structure of the carrier. Oil is guided to the bearings by the ring gear following the lubrication structure of the differential. In the lubrication structure of the previous model, which used tapered roller bearings, large amounts of oil are supplied to the front bearing to enhance seizure resistance. Lubrication analysis confirmed that the supply of oil was sufficient (**Fig. 8**). However, if this lubrication structure is adopted with ball bearings, bearing lifetime drops substantially compared to tapered roller bearings (**Fig. 9**) in oil contaminated with foreign matter.

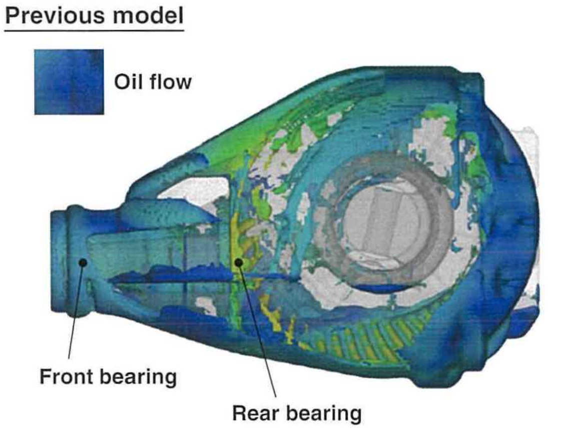

Fig. 8 Lubrication Structure and Analysis Results of Previous Model

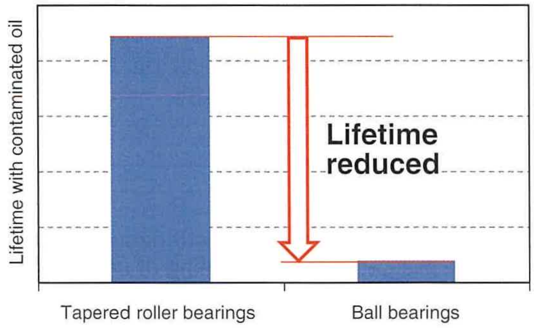

Fig. 9 Comparison of Bearing Lifetime

Therefore, this development revised the lubrication structure so that only the required amount of oil is supplied to the front oil seal by separating the main lubrication flow of the ring gear from the flow to the bearings. This structure ensures a stable supply of oil from the ring gear to the bearings, without over-dependence on the vehicle speed. Analysis confirmed that oil flow to the bearings was reduced compared to the previous structure (**Fig. 10**).

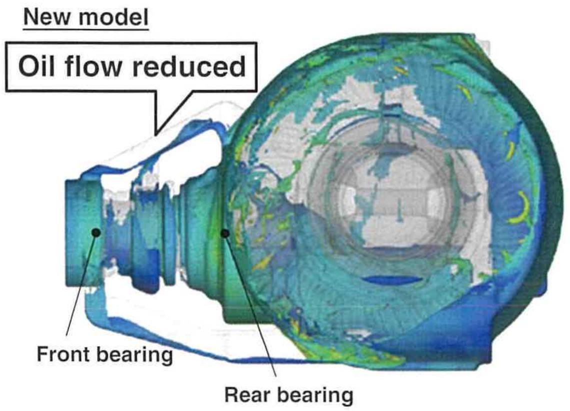

Fig. 10 Lubrication Structure and Analysis Results of New Model

Fig. 11 shows the height of the oil surface at different vehicle speeds as confirmed in experiments. With the carrier structure of the previous model, the oil surface height increased in accordance with the vehicle speed. In contrast, the new model carrier structure maintains a low oil surface height, regardless of the speed of the vehicle. These improvements helped to achieve the bearing lifetime target (**Fig. 12**).

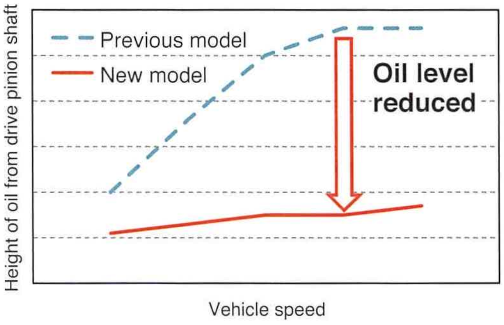

Fig. 11 Oil Level Measurement Results

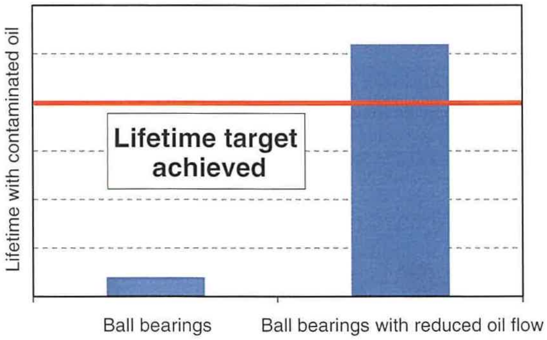

Fig. 12 Ball Bearing Lifetime after Reducing Oil Flow

Support stiffness was secured through the differential assembly including the carrier. Tooth contact movement caused by displacement of each part due to input torque was reduced compared to the previous component by optimizing the geometry of the carrier (**Fig. 13**). The optimized carrier geometry also helped to reduce weight. The required thicknesses for each part were identified. This allowed the thickness of each part to be reduced to prevent the deformation of high stress locations when torque is applied. One issue of this approach is controlling thickness variation during manufacturing. This was addressed by improving die accuracy and optimizing the casting plan by expanding runner sizes and the like to improve the molten metal flow.

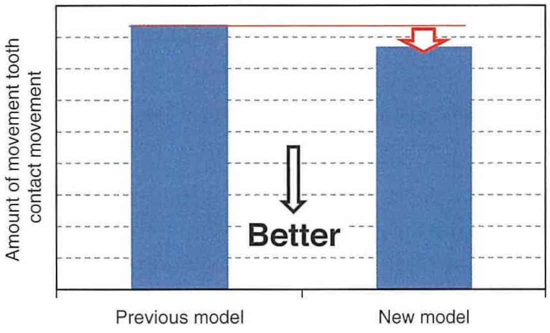

Fig. 13 Comparison of Tooth Contact Movement

2.1.3 Technologies to reduce churning loss

Churning loss is mainly generated by agitation of the oil that occurs when the ring gear rotates. Churning loss was reduced by decreasing the amount of oil in the differential to lower the level of the oil bath used by the ring gear and the like.

2.3 Technologies for lower driveline NVH

RWD passenger vehicles use rubber couplings (**Fig. 14**) to decrease high-frequency noise. One issue when developing vehicles that use these couplings is reducing booming noise during steady-state driving. The level of booming noise is determined by the excitation force of the propeller shaft and the sensitivity of the vehicle mountings.

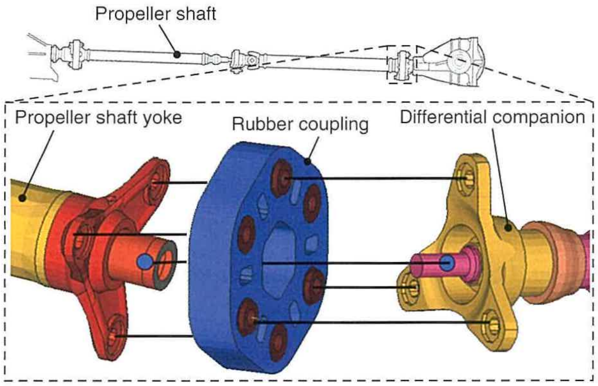

Fig. 14 Outline of Rubber Couplings

Conventionally, this excitation force was thought to occur only in the radial direction caused by propeller shaft imbalance. However, different levels of booming noise were measured in propeller shafts with the same level of imbalance (**Fig. 15**).

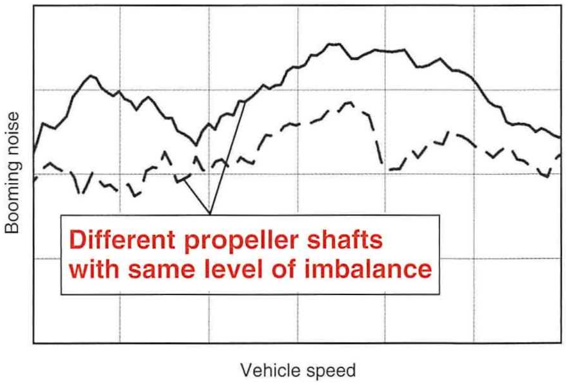

Fig. 15 Booming Noise Measurement Results

The root causes of this difference were analyzed and the effect of axial direction excitation force was identified in addition to radial direction excitation force. The development analyzed this phenomenon using computer aided engineering (CAE). The excitation force was verified on a test bench by modeling the axial direction excitation force, and then calculating the amount of sliding resistance and axial direction excitation force generated by the propeller shaft (**Fig. 16**).

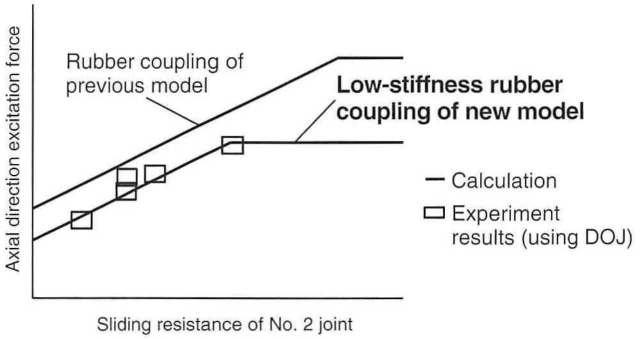

Fig. 16 Sliding Resistance and Axial Direction Excitation Force

The CAE results identified differences in tension values A, B, and C when the propeller shaft and differential yoke are misaligned. Due to these differences, the total of axial direction excitation force is not zero (**Figs. 17** and **18**).

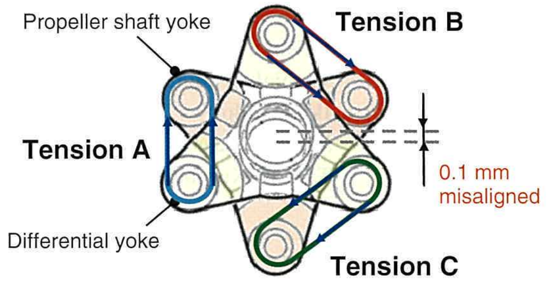

Fig. 17 Outline of Differences in Tension when Misaligned

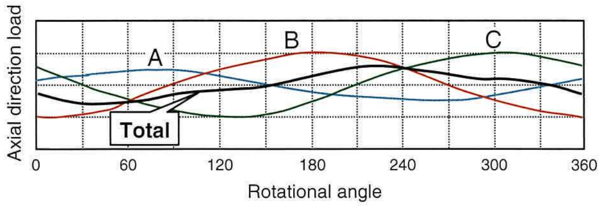

Fig. 18 Axial Direction Load when Misaligned

Additionally, the contribution of the radial and axial direction excitation forces to booming noise was identified,(2) and a target set to reduce the level of axial direction excitation force. Axial direction excitation force was reduced by adopting a double offset joint (DOJ) for the No. 2 joint, which lowered the stiffness of the rubber coupling. These measures achieved a substantial improvement in the level of booming noise (**Fig. 20**).

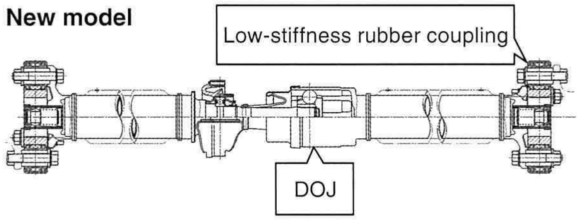

Fig. 19 Outline of New Propeller Shaft

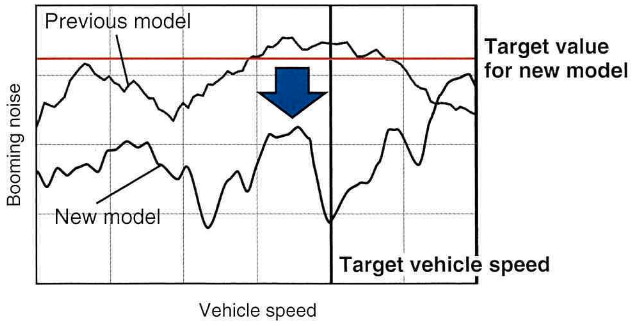

Fig. 20 Effectiveness of Booming Noise Reduction Measures

3. Conclusion

The new driveline technologies described in this article helped to improve fuel efficiency by 0.5% in the European test cycle, and to substantially reduce booming noise.

The authors would like to extend their sincere gratitude to all the partner companies that supported this development.

References

(1) K. Saiki, Watanabe, Shiraki, et al. “Development of High Efficiency Hypoid Gear for Automotive Application.” *Transactions of Society of Automotive Engineers of Japan* Vol. 44 No. 1 (2013) pp. 63-68.

(2) D. Bies, Hansen. Engineering Noise Control. Spon Press. Abingdon. p. 47.

Note: this article is based on the following published technical paper.
N. Imai, Takamatsu, Kiten, Mizoguchi. “High Efficiency and Low NVH Driveline Design for FR Passenger Vehicles.” *Proceedings of the JSAE Annual Congress* (2017) pp. 233-236.

Authors

N. IMAI

S. TAKAMATSU

T. KITEN

N. MIZOGUCHI

Development of Multi Stage Hybrid Transmission

Kazuyuki Shiiba*1
Keisuke Omuro*2
Toshiaki Tamachi*2
Ikuo Ando*3
Shunya Kato*4
Takuro Kumada*5

Abstract
The innovative Multi Stage Hybrid Transmission was developed for the new Lexus LC500h. This transmission was developed with the objective of substantially enhancing the performance of the Toyota Hybrid System (THS II) by achieving high levels of both driving and environmental performance. This system consists of a shift device installed in series with the THS II, which greatly expands the operating range of engine power and provides powerful driving force from a standing start. This configuration combines enhanced and exciting dynamic performance with excellent fuel efficiency by increasing the usage frequency of the most efficient system regions. This article describes the performance of the Multi Stage Hybrid System, as well as the transmission hardware and controls that were developed to achieve this performance.

Keywords: *Multi Stage Hybrid System, transmission, motor*

1. Introduction

Toyota Motor Corporation developed the Lexus Hybrid Drive system for passenger vehicles, which was installed in the GS450h in 2006 and the LS600h in 2007.(1)(2) The fuel efficiency of the Lexus Hybrid Drive system surpasses competing models and its dynamic performance has been highly rated by drivers. With a wide range of refinements having been incorporated since its initial development, the system has contributed greatly to reducing global CO_2 emissions.

Demand for environmentally friendly vehicles has been increasing as environmental consciousness rises and the future outlook for gasoline prices remains uncertain.

At the same time, environmental regulations in many countries and regions are growing increasingly stringent. For these reasons, the development and popularization of vehicles with high environmental performance is very important. As the automotive industry intensifies its efforts to develop environmentally friendly vehicles, various different systems have been commercialized, creating an increasingly competitive market.

The adoption of hybrid systems has accelerated even in the luxury coupe segment that emphasizes high levels of dynamic performance. As a result, it has become necessary to develop vehicles with even better fuel efficiency and driving performance. This article describes the development of the Multi Stage Hybrid Transmission (model code: L310) to achieve excellent fuel efficiency and dynamic performance in luxury coupes.

2. Development Aims

The development aims of the L310 transmission were as follows.

(1) Improved fuel efficiency

One of the key aims of this development was to greatly improve fuel efficiency during high-speed cruising. More specifically, a high-efficiency operating point was added in the speed-multiplication range of the transmission. This was accomplished by setting an appropriate value for the 4th speed gear ratio of the shift device installed in series with the power split device.

(2) Improved dynamic performance

The development aimed to achieve top-class dynamic performance compared to other vehicles with the same displacement. This was accomplished by setting an appropriate value for the 1st speed gear ratio of the shift device installed in series with the power split device, thereby amplifying the engine and motor torque.

(3) Lower noise

The development aimed to maintain or improve upon the top-class levels of noise and vibration (NV) achieved by the previous hybrid transmission (model code: L110) while also ensuring excellent fuel efficiency and dynamic performance. NV was addressed by measures including refining the motor connection structure, adopting a tolerance ring, and designing a separate planetary ring gear structure. This article describes the tolerance ring below.

[*1] Drivetrain-EHV Design Div. No. 1, Powertrain Company
[*2] Drivetrain-EHV Design Div. No. 2, Powertrain Company
[*3] Powertrain Product Planning Div., Powertrain Company
[*4] Electric Powertrain System Development Div., No. 1, Powertrain Company
[*5] Aisin AW Co., Ltd.

(4) Improved shifting performance

The development aimed to achieve a top-class transmission with fast response and a refined shifting feeling. This was achieved through precise model-based shift control of the multi-degree of freedom system comprising the engine, generator, motor, and shift device.

(5) Improved driveability

Conventionally, the Lexus Hybrid Drive has focused on achieving smooth driving performance. The engine mountings were designed to emphasize low noise and the shifting control aimed to keep the engine speed low as far as possible. As a result, if the driver wished to accelerate, it was necessary to increase the engine speed to obtain the necessary power. Occasionally, this generated the so-called rubber band feeling, in which the sensation of acceleration and the operation of the engine do not fully match the perception of the driver. This development aimed to restrict this rubber band feeling. This was accomplished by adopting a 10-speed shift control using a hybrid system with a wider operation range to achieve linear increases in engine speed with respect to the speed of the vehicle, thereby creating a strongly direct driving feel.

3. Multi Stage Hybrid Transmission

3.1 Structure and basic specifications

Figs. 1 and **2** show the main cross-section and an outline of the newly developed L310 transmission. The L310 transmission consists of a motor, generator, power split device, a 4-speed shift device that changes the output rotation speed of the power split device and the motor, a hydraulic mechanism that controls the engagement elements of the shift device, as well as mechanical and motor-driven oil pumps that generate oil pressure. The power split device and shift device are provided co-axially with the engine crankshaft.(3) **Table 1** shows the engagement of the transmission and **Table 2** shows the main specifications.

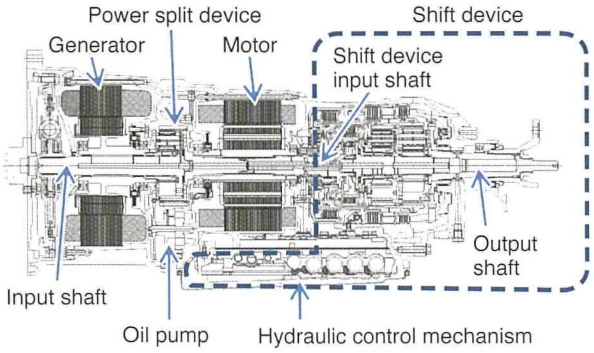

Fig. 1 Main Cross-Section (L310 Transmission)

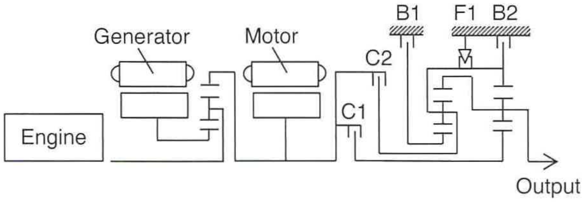

Fig. 2 Skeleton Diagram of L310 Transmission

Table 1 Engagement of Transmission Elements

		Engagement state				
		C1	C2	B1	B2	(F1)
R		○			○	
D	1st	○			○	○
	2nd	○		○		
	3rd	○	○			
	4th		○	○		

Table 2 Main Specifications

Transmission	L310 transmission (new)		L110 transmission (previous)
Gear ratio of 2-stage motor shift device	–		1.9 3.9
Gear ratio of shift device	3.538 1.888 1.000 0.650	1.87 1.88 1.53	–

3.2 Improved fuel efficiency

The L110 transmission was only capable of changing the motor output rotation between two speeds. In contrast, the L310 transmission features a shift device between the power split device and output shaft, which has four speed settings for the power split device and motor output.

Fig. 3 shows the relationship between the theoretical transmission efficiency and gear ratio. When power is supplied and received between the motor and generator, loss is generated due to the conversion between mechanical and electrical power. The theoretical transmission efficiency is the transmission efficiency considering that conversion loss. Therefore, when the generator is rotating at 0 rpm, the electric path power is 0 kW. This state is known as a high-efficiency point.

The L310 transmission has multiple efficiency curves (unlike the L110 transmission, which only had one), which increase the overall transmission efficiency and help to enhance fuel efficiency.

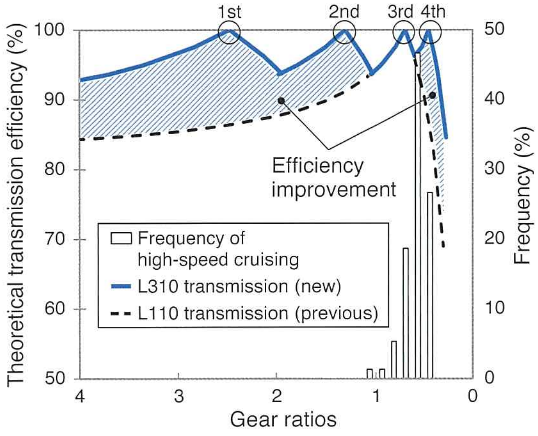

Fig. 3 Enhanced Theoretical Transmission Efficiency

As shown in **Fig. 3**, the power split device enters a speed multiplication state during high-speed cruising in 3rd gear (roughly equivalent to the performance of the L110 transmission). The electric path power increases due to negative rotation of the generator, and the transmission efficiency falls (**Fig. 4**-A). In contrast, by using the highest speed of the shift device as an overdrive ratio, excess speed multiplication by the power split device can be restricted and transmission efficiency increased (**Fig. 4**-B).

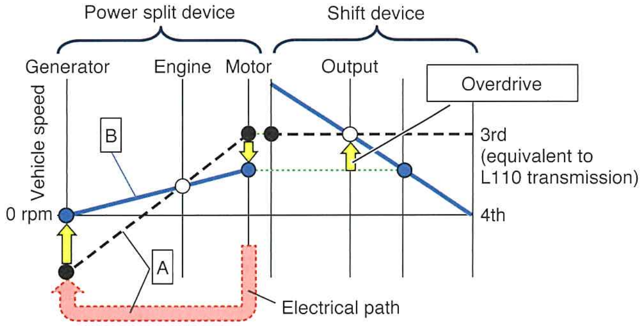

Fig. 4 Gear Speed Map when Cruising at High Speed

3.3 Improved dynamic performance

When accelerating from a standing start with the L110 transmission, the rotation speed of the power split device decreased and the rotation speed of the generator increased (**Fig. 5**). Therefore, the lowest speed of the shift device required an underdrive ratio to attain an engine speed capable of achieving the targeted dynamic performance without changing the maximum rotation speed of the generator.

A gear ratio of 3.538 was set for the 1st speed of the shift device to satisfy the required acceleration performance of the vehicle class targeted by the L310 transmission. As a result, the driving force of the L110 transmission was increased by approximately 50%, as shown in **Fig. 6**.(3)

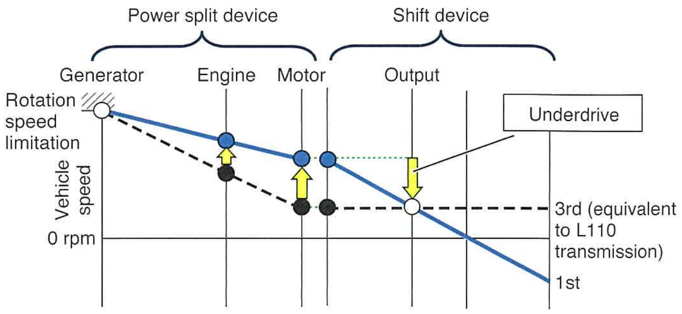

Fig. 5 Gear Speed Map when Accelerating

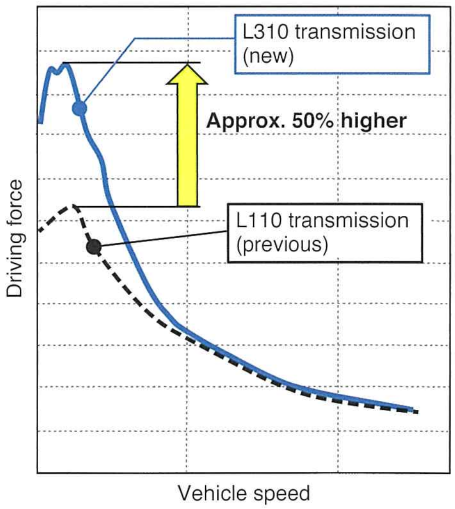

Fig. 6 Driving Force Comparison

3.4 Noise reduction

When the input torque of the shift device is 0 Nm, torque loss may occur at the connection between the mechanism and shift device, which can generate vibration in the engine and motor. Consequently, the connection between the motor and shift device is a potential source of gear engagement noise when the shift device input torque is 0 Nm.

Therefore, as shown in **Fig. 7**, a tolerance ring is provided at the connection between the motor and shift device input shaft. Under ordinary driving conditions, torque transmission is performed through the neighboring spline connection. However, in extremely low torque ranges, torque is transmitted through the tolerance ring. As a result, when the shift device input torque is close to Nm, the gear engagement noise between the two components is suppressed because torque is not transmitted through the spline connection.

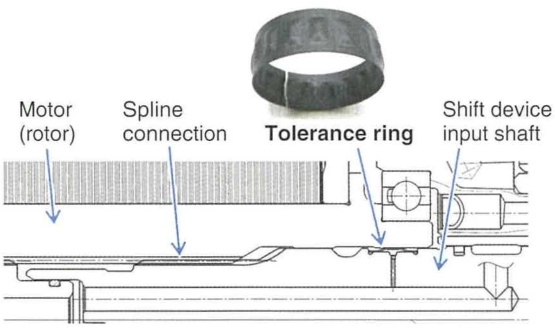

Fig. 7 Adoption of Tolerance Ring

As shown in **Fig. 8**, the tolerance ring helps to improve NV performance by lowering the sound pressure that exceeds the background gear engagement noise by 56%.(4)

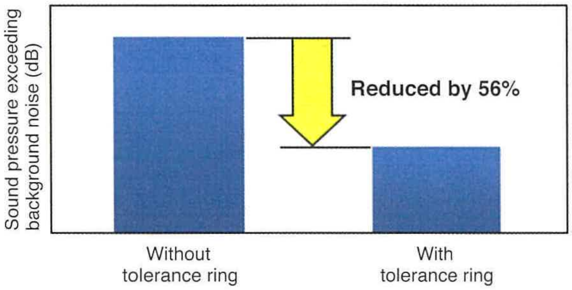

Fig. 8 Gear Engagement Noise Reduction Effect of Tolerance Ring

4. Shift Control Design

4.1 Model-based shift control

Fig. 9 shows the gear speed map during an upshift (from 1st to 2nd gear) by the shift device. In this case, it is necessary to simultaneously control the rotation speed of the engine, generator, and motor, which are connected to the power split device, as well as the battery power supplied to the shift device, generator, and motor.

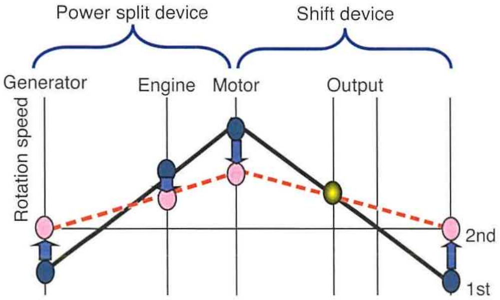

Fig. 9 Gear Speed Map During Upshift from 1st to 2nd

A model-based shift control was developed to control this multi-degree of freedom system. The main design concepts of this control are as follows.

1. Estimate the torque transferred by the engine and transmission using equations of motion.
2. Calculate the target rotation speed of each rotating element from the equations of motion, power balance equation, and boundary conditions. Then, control the torque of the generator and motor to achieve these targets.
3. Control the input torque to the engagement elements, as well as the engine power and torque by combining the model-based shift control with existing automatic transmission technologies.

Fig. 10 shows the configuration of the shift control incorporating this model-based approach. The oil pressure for controlling the engagement elements is set in accordance with the temperature of the transmission fluid, the input torque to the shift device, the rotation speed of each component element, the battery state, and the like.

The generator and motor torque is controlled by a model consisting of the equations of motion, power balance equation, and the boundary conditions (such as maximum battery power, maximum motor torque, and the like), and the target shift map adjusted to ensure shifting performance. Here, the target shift map is adjusted by the rotation speed of the motor and engine during shifting. In addition, even if the boundary conditions described above change due to the limitations of each element, the engine power, engine torque, and oil pressure settings are compensated in accordance with those limitations to ensure the desired shifting performance.(5)(6)

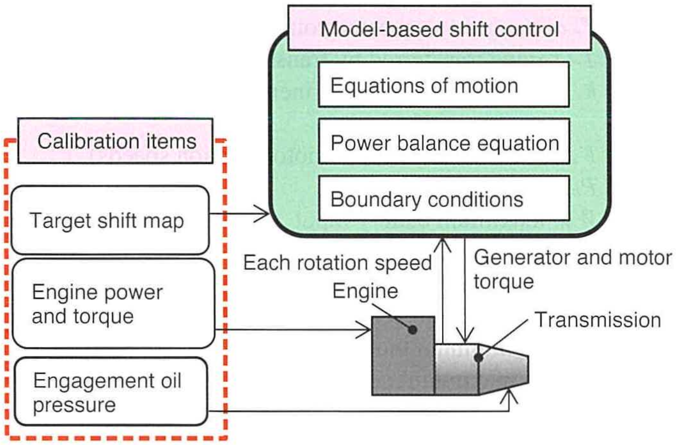

Fig. 10 Configuration of Shift Control

The equations of motion, power balance equation, and boundary conditions are as follows.

Equations of motion:

$$\dot{\omega}_e = k_{eg}T_g + k_{em}T_m + k_{ee}T_e + k_{ec}T_c \tag{1}$$

$$\dot{\omega}_m = k_{mg}T_g + k_{mm}T_m + k_{me}T_e + k_{mc}T_c \tag{2}$$

$$T_o = k_{og}T_g + k_{om}T_m + k_{oe}T_e + k_{oc}T_c \tag{3}$$

Power balance equation:

$$T_e\omega_e + P_b = T_c\omega_m + F_1(\omega_e, \omega_m)\dot{\omega}_e + F_2(\omega_e, \omega_m)\dot{\omega}_m \tag{4}$$

Boundary conditions:

$$W_{in} \leq P_b \leq W_{out} \tag{5}$$

$$T_{gMIN} \leq T_g \leq T_{gMAX} \tag{6}$$

$$T_{mMIN} \leq T_m \leq T_{mMAX} \tag{7}$$

Definitions:

T_o: output torque
T_g: generator torque
T_m, ω_m: motor torque and rotation speed
T_e, ω_e: engine torque and rotation speed
T_c: torque transferred by transmission
k_{**}: coefficient (rotational inertia and gear ratio of power split device)
F_*: function (engine and motor rotation speeds)
P_b: battery power
W_{in}: maximum battery input
W_{out}: maximum battery output
T_{gMIN}: minimum generator torque
T_{gMAX}: maximum generator torque
T_{mMIN}: minimum motor torque
T_{mMAX}: maximum motor torque
$\dot{\omega}_e$: engine rotation angle acceleration
$\dot{\omega}_m$: rotational acceleration of motor/generator 2

4.2 Shifting performance

Fig. 11 shows the time-series waveform during a power-on upshift from 1st to 2nd under wide-open throttle (WOT) conditions for the Lexus LC500h (L310 transmission). Hydraulic control starts from the shift change. The engine torque control and model-based shift control start from the timing at which the input rotation speed of the shift device deviates from the synchronous rotation speed of 1st gear. The model-based shift control is used to coordinate the torque of the generator and motor, thereby enabling the shift to be completed in a short period of time.

Fig. 12 compares the shifting index value of the LC500h with the Lexus LS460 (8-speed automatic transmission) and a rival sporting coupe during a power-on upshift from 1st to 2nd. (The index expresses the shifting characteristics defined in terms of vehicle longitudinal acceleration during shifting.) The L310 transmission achieves top-level response and shifting quality compared to the competing model through precise and rapid shift control.(5)

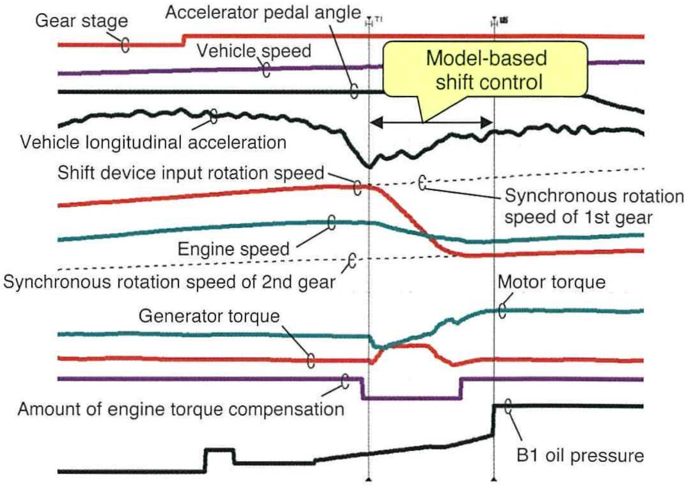

Fig. 11 1st to 2nd Power-On Upshift Characteristics of LC500h (L310 Transmission during Engine Operation under WOT Acceleration)

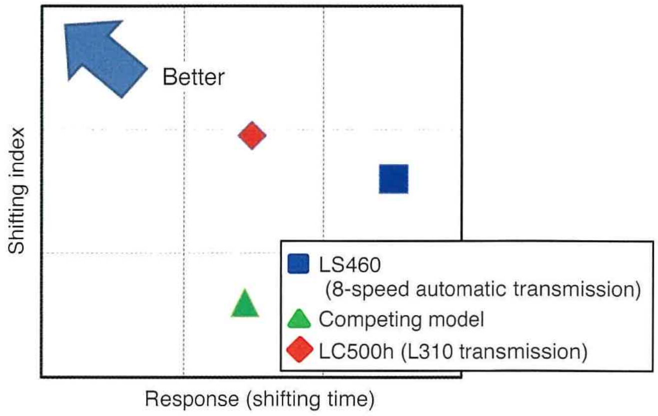

Fig. 12 1st to 2nd Power-On Upshift Index (during Engine Operation under WOT Acceleration)

5. Measures to Improve Driveability

Fig. 13 shows the operational ranges of the L110 and L310 transmissions in terms of the relationship between vehicle speed and engine speed. The speed reduction effect of the lowest gear of the shift device enables the vehicle to be driven at the maximum engine speed from lower vehicle speeds.

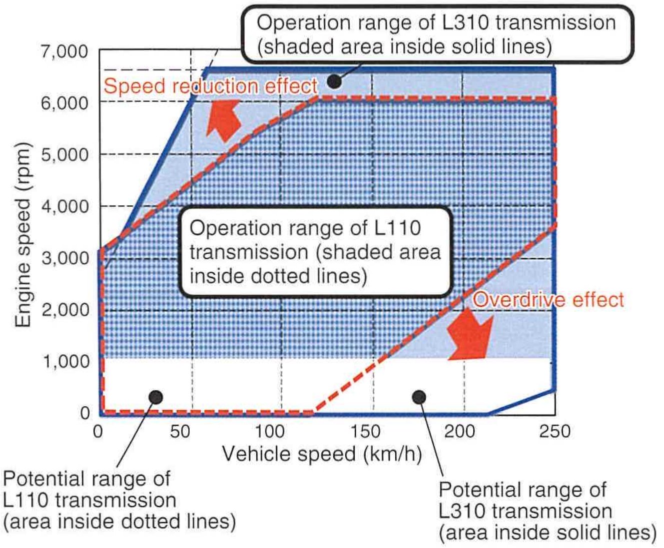

Fig. 13 Expansion of Engine Operation Range

The speed reduction and overdrive effects of the L310 transmission expand the available engine speed range (**Fig. 13**). This expanded range is used to enhance the engine speed transition when the vehicle is accelerating and to increase the speed at which intermittent engine operation is possible. Due to the enhanced engine speed transition during acceleration, it was possible to design an engine speed map that coordinates the engine speed with the speed of the vehicle, using ten close ratios from a lowest gear ratio of 4.7 (**Fig. 14**). In addition, a control that changes between these engine speed settings in accordance with driver demand, vehicle acceleration, and the vehicle driving state was also developed. This control enables rhythmical driving performance even with an electronically controlled continuously variable transmission (CVT). Finally, increasing the speed at which intermittent engine operation is possible helps to further reduce noise during high-speed cruising.[6]

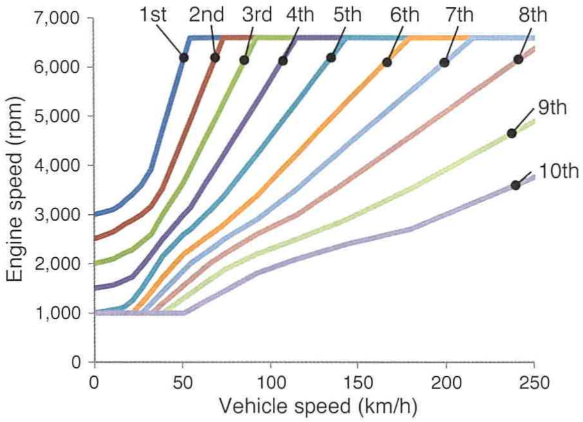

Fig. 14 Engine Speed Map during Acceleration

6. Conclusion

This article has described the details of the newly developed Multi Stage Hybrid Transmission. By installing the shift device in the optimum location on the output shaft of the power split device, this transmission helps to improve both fuel efficiency and dynamic performance.

As a result, this transmission will help to bring a completely new sense of excitement and driving enjoyment to drivers around the world.

References

(1) K. Kamichi, Okasaka, Tomatsuri, et al. "Hybrid System Development for a High-Performance Rear Drive Vehicle." *SAE Paper* No. 2006-01-1338 (2006).
(2) M. Adachi, Endo, Mikami, et al. "Development of a New Hybrid Transmission for RWD Car." *SAE Paper* No. 2006-01-1339 (2006).
(3) K. Okuda, Yasuda, Adachi, et al. "Development of Multi Stage Hybrid Transmission." *SAE Paper* No. 2017-01-1156 (2017).
(4) H. Tateno, Yasuda, Adachi, et al. "Rattling Noise Reduction Technology for Multi Stage Hybrid Transmission." *SAE Paper* No. 2017-01-1157 (2017).
(5) K. Kumazaki, Matsubara, Kobayashi, et al. "Development of Shift Control System for Multi Stage Hybrid Transmission." *SAE Paper* No. 2017-01-1150 (2017).
(6) S. Kato, Ando, Oshima, et al. "Development of Multi Stage Hybrid System for New Lexus Coupe." *SAE Paper* No. 2017-01-1173 (2017).

Authors

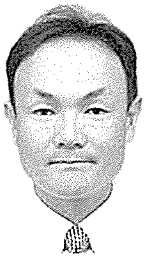
K. SHIIBA

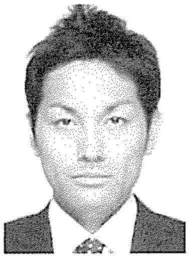
K. OMURO

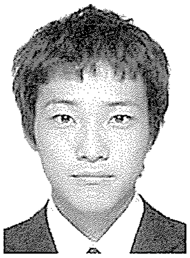
T. TAMACHI

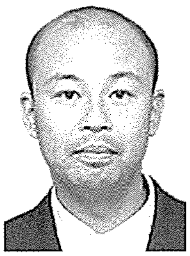
I. ANDO

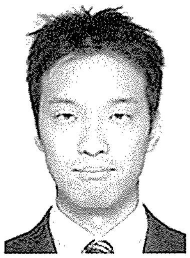
S. KATO


T. KUMADA

Analysis of PHV Charging Behavior Based on Real-World Big Data

Keita Hashimoto*1
Tamaki Ozawa*1
Yuka Tada*2
Haruyoshi Ohashi*3
Shinya Shimada*4

Abstract

Plug-in hybrid vehicles (PHVs) have even higher environmental performance than conventional hybrid vehicles (HVs) due to their higher battery capacity and external charging capability. Since PHVs also run on gasoline when the battery capacity is depleted over longer distances, PHVs can be driven more freely without anxiety about the next charging opportunity. However, analysis of real-world driving data has identified wide variations in charging behavior depending on the vehicle. This article describes how big data was used to analyze the conditions that affect charging behavior.

Keywords: *plug-in hybrid, big data, charging frequency, charging behavior analysis, decision tree*

1. Introduction

In its New Vehicle Zero CO_2 Emissions Challenge, Toyota Motor Corporation has declared its intention to reduce CO_2 emissions from new vehicles by 90% between 2010 and 2050. The electrification of powertrains is an essential step toward reducing CO_2 emissions while driving, and plug-in hybrid vehicles (PHVs), which can be driven with the same level of convenience as conventional vehicles, are regarded as a central pillar of electrification (**Fig. 1**).

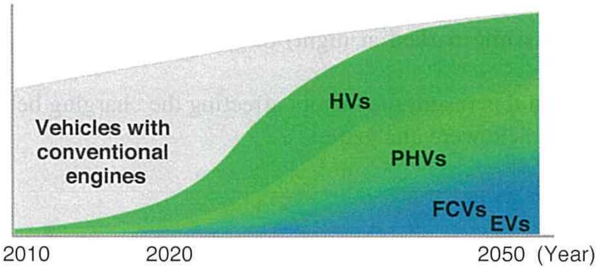

Fig. 1 Predictions for Powertrain Adoption up to 2050

2. History of PHV Development

In 2012, after extensive verification tests, Toyota launched a mass-market PHV with an external charging system based on the Prius, the world's first mass-production hybrid vehicle (HV).

The objective of this PHV was to achieve excellent environmental performance without affecting user convenience by combining the merits of an electric vehicle (EV) over short distances, which tend to be driven more frequently, with the merits of a fuel-efficient HV over longer distances (**Fig. 2**).

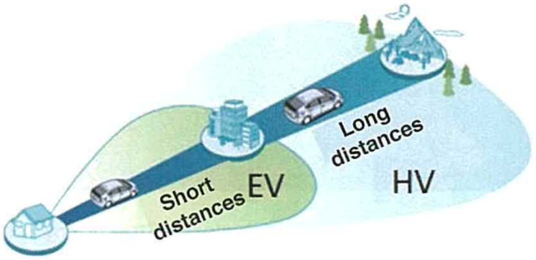

Fig. 2 PHV Driving Modes

After a limited PHV production run in 2007, Toyota initiated large-scale verification tests around the world in 2009 (**Fig. 3**). The largest of these tests to be held in a single city was hosted by Strasbourg in eastern France (**Photo 1**). Based on the range of user behavior, the results of these tests confirmed that a PHV could be driven with the same level of convenience as a conventional vehicle (**Fig. 4**).(1)

[*1] Powertrain Product Planning Div., Powertrain Company
[*2] Technical Administration Div., Advanced R&D and Engineering Company
[*3] DAD Co., Ltd
[*4] Toyota Communication Systems Co., Ltd.

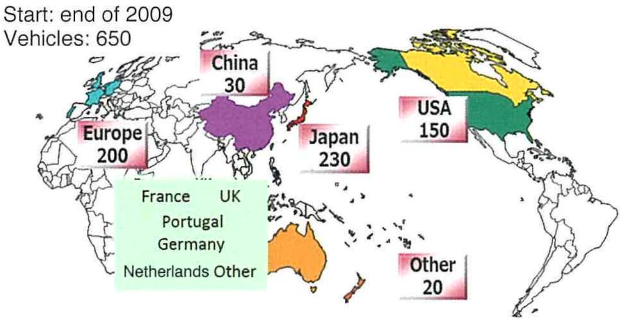

Fig. 3 Locations of Large-Scale 2009 Verification Tests and Numbers of Vehicles Tested

Photo 1 2009 Verification Test in Strasbourg, France

Fig. 4 Routes Driven by Vehicles in Strasbourg Test

Based on these results, Toyota launched a mass-production PHV in 2012 with an EV mode range of 26.4 km (according to the JC08 test cycle). This range was increased to 68.2 km (JC08 test cycle) in the 2017 model, reflecting advances in battery technology (**Fig. 5**).

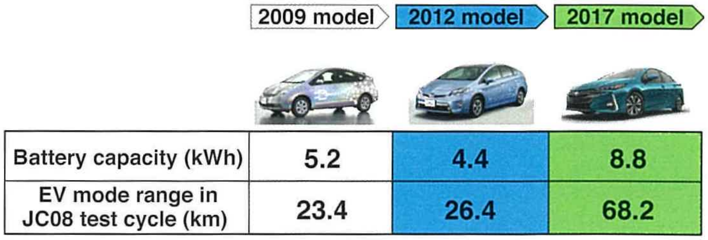

	2009 model	2012 model	2017 model
Battery capacity (kWh)	5.2	4.4	8.8
EV mode range in JC08 test cycle (km)	23.4	26.4	68.2

Fig. 5 History of PHV Development

3. Real-World Data from Mass-Production PHVs

Toyota launched its first mass-production PHV in 2012. Some of these Prius PHVs were equipped with on-board communication units to acquire data about how the vehicle was being driven. Due to its large volume, this data is referred to as "big data" (**Table 1**).

Table 1 Examples of Acquired Data (in Japan)

Number of vehicles	5,388
Data acquisition period	February 7, 2012 to March 31, 2017
Total driving distance (km)	116,521,676
Total number of charges	2,701,738

3.1 Target vehicles for charging behavior analysis

The charging behavior of 1,871 of these vehicles in Japan was analyzed. These vehicles displayed comparatively regular charging patterns, with charging being performed on average at least once a week while parked at night the day before a normal weekday. "Parked at night" refers to vehicles that were parked at least once between midnight and 6 AM. As shown in **Fig. 6**, the proportion of charging while parked at night (i.e., the charging frequency while parked at night) differed greatly depending on the vehicle.

Based on this result, the factors affecting the charging behavior of each vehicle were analyzed.

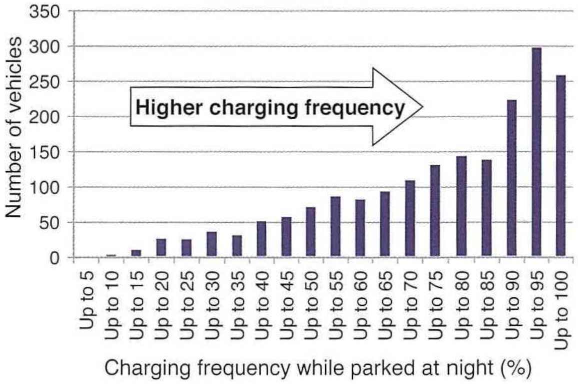

Fig. 6 Charging Frequency while Parked at Night

4. Analysis of Charging Frequency

4.1 Analysis methodology

This analysis utilized a statistical methodology called decision tree analysis to identify universal conclusions independent of subjective or preconceived viewpoints. A decision tree uses a model structured to resemble a tree. In this methodology, the influential factors and threshold values that control target actions are extracted from multiple factors based on an algorithm, and the relative importance of each factor is determined. **Table 2** shows an example with "going out" set as the target action. Factors are set for this target and the contribution of these factors are analyzed. The results of this analysis are shown as a decision tree (**Fig. 7**) and in a chart that shows the importance of each influential factor (**Table 3**). Based on this example, the most important factors affecting "going out" are the weather and temperature. In contrast, the importance of humidity is relatively low.

Table 2 Example Factors (Target Action: "Going Out")

No.	Target action	Factors					
	Did the subject go out?	Weather	Temperature (°C)	Wind speed (m/s)	Humidity (%)	Hours of sunlight (h)	Rainfall (mm)
1	Went out	Sunny	25	4	45	8	0
2	Did not go out	Sunny	23	7	50	7	0
3	Did not go out	Rainy	34	13	69	1	17
4	Went out	Rainy	33	2	64	2	8
13	Did not go out	Sunny	36	8	46	9	0
14	Went out	Cloudy	29	3	46	3	0
15	Went out	Sunny	32	3	46	7	0

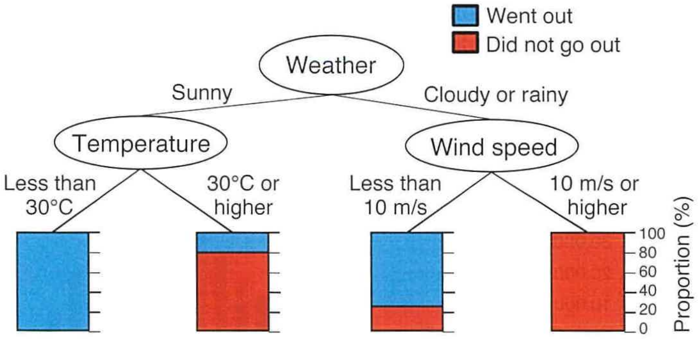

Fig. 7 Example Decision Tree (Target Action: "Going Out")

Table 3 Extracted Factors and Importance

Rank	Factor	Importance
1	Weather	50
2	Temperature	25
3	Strength of wind	20
4	Humidity	5

4.2 Target actions and factors in charging behavior

This analysis selected "charging while parked at night" as the target action. The influential factors were categorized into action factors such as driving and parking, and environmental factors such as the weather, ambient temperature, gasoline prices, and so on.

A decision tree was created to analyze whether charging was carried out while the vehicle was parked at night using a total of 1.78 million charging events.

4.2.1 Action factors

The action factors listed in **Table 4** were set. These factors include those related to vehicle usage, such as the day and time the vehicle was parked and the distance driven immediately before parking, as well as those related to vehicle information, such as the state of charge (SOC) and remaining EV mode range.

Table 4 Action Factors

Day when vehicle was parked	Time driven in immediately previous trip
Time when vehicle was parked	Distance driven in immediately previous trip
Parking duration	Duration of next period of parking
SOC when parked	Whether next period of parking was at night
Final time parked at night that day	Time driven in next trip
Remaining EV mode range	Distance driven in next trip
Duration of previous period of parking	Whether vehicle was charged in previous parking period
Whether previous period of parking was at night	Number of days elapsed since initial data acquisition

4.2.2 Environmental factors

Environmental factors are external factors that do not directly affect vehicle behavior, such as gasoline prices, the weather, temperature, and the like. The factors listed in **Table 5** were set.

Table 5 Environmental Factors (Mainly External Factors)

Gasoline price	Wind speed
Gasoline price fluctuation	Local air pressure
Temperature	Sea level air pressure
Rainfall	Humidity
Snowfall	Dew point
Snow depth	Weather
Hours of sunlight	Visibility
Wind direction	

4.3 Grouping of charging behavior

After creating the decision tree, the analysis was able to categorize the data shown in **Fig. 6**, which shows the charging frequency while parked at night, into three groups with different influential factors, degrees of importance, and decision trees (**Figs. 8** and **9**). These groups were numbered (1) to (3) and are described in more detail below.

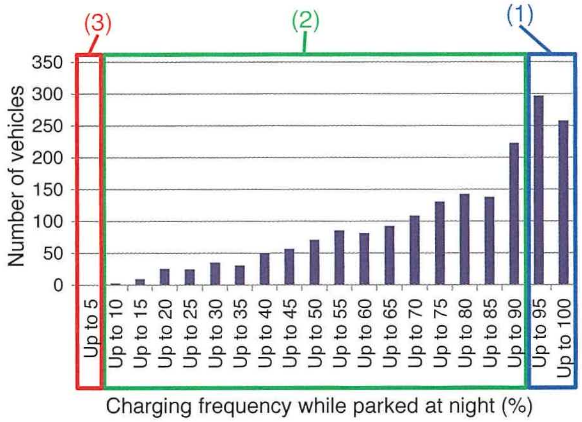

Fig. 8 Charging Frequency while Parked at Night

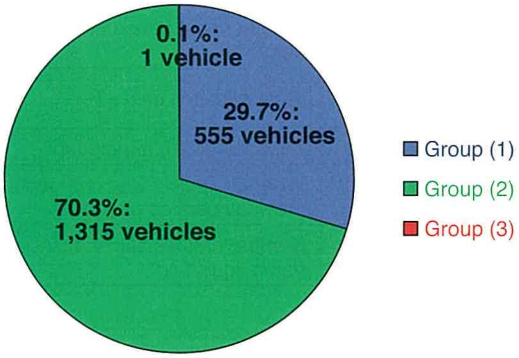

Fig. 9 Number and Proportion of Vehicles in each Group

The decision tree analysis results for group (1) are shown in **Fig. 10** and **Table 6**. The following influential factors affecting charging were identified: whether it was the final time that the vehicle was parked at night that day, the parking duration, and the time when the vehicle was parked. The analysis found that the charging rate when the vehicle was parked at night increased for this group because the user would charge the vehicle if it was parked for the final time at night and planned to park the vehicle for a certain amount of time.

The charging behavior of vehicles in this group was hardly affected by other action factors (such as SOC) or environmental factors.

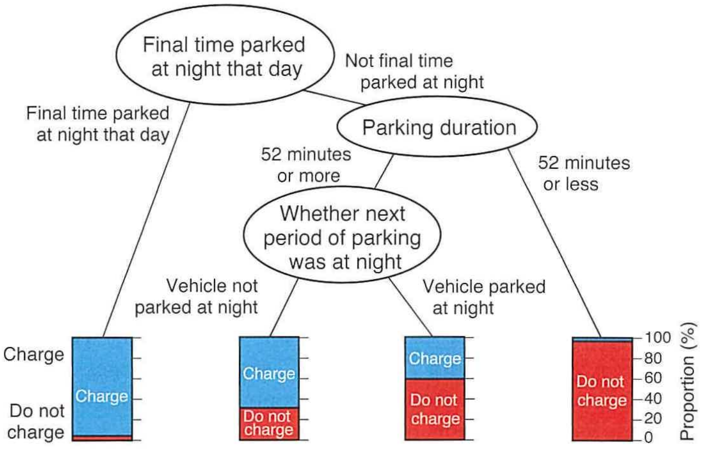

Fig. 10 Decision Tree for Group (1)

Table 6 Influential Factors and Importance for Group (1)

Rank	Factor	Importance
1	Final time parked at night that day	39
2	Parking duration	31
3	Time when vehicle was parked	23
4	Whether next period of parking was at night	2
5	Whether previous period of parking was at night	1

"Time when vehicle was parked" is ranked third in the importance list. Although this time is concentrated in the evening, this factor is not expressed in the decision tree (**Figs. 10** and **11**). When the vehicle is parked in the evening, there is a high possibility that this will be the final time that the vehicle is parked that day, and that the vehicle will be parked for an extended period of time. Therefore, the time when the vehicle is parked may be regarded as included within the "final time parked at night that day" and "parking duration" factors.

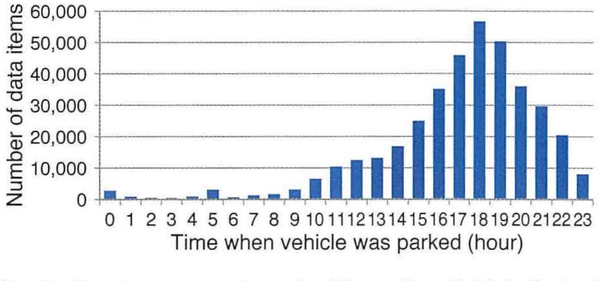

Fig. 11 Number of Data Items for Time when Vehicle Parked (Group (1))

The decision analysis results for group (2) are shown in **Fig. 12** and **Table 7**. The following influential factors affecting charging were identified: SOC when parked, whether it was the final time parked at night that day, the time when the vehicle was parked, and the parking duration.

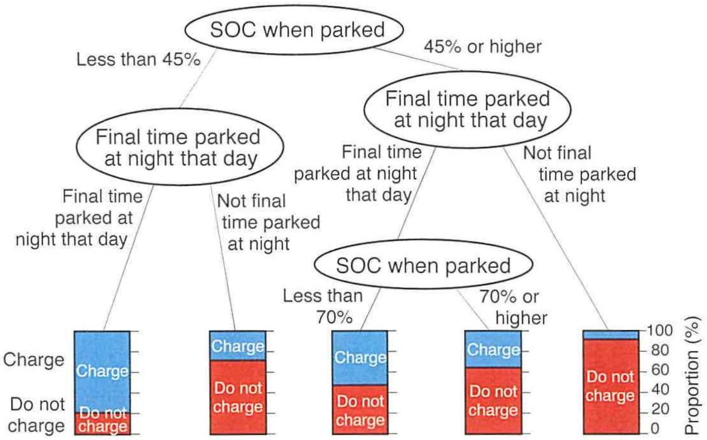

Fig. 12 Decision Tree for Group (2)

Table 7 Influential Factors and Importance for Group (2)

Rank	Factor	Importance
1	SOC when parked	45
2	Final time parked at night that day	22
3	Time when vehicle was parked	13
4	Parking duration	11
5	Whether vehicle was charged in previous parking period	6
6	Duration of previous period of parking	1

The charging behavior of this group is determined by factors such as the battery SOC when the vehicle is parked and the timing of parking. This group optimizes its charging behavior by charging the vehicle when it is effective to do so. In other words, since there are many occasions when effective charging cannot be accomplished (such as when, 1) the SOC is high when the vehicle is parked, 2) it is not the final time that the vehicle will be parked at night that day, and 3) the parking duration is short), decisions not to charge the vehicle during parking that satisfy these conditions can be regarded as falling under the definition of optimized charging behavior.

"Time when vehicle was parked" is also ranked third in the importance list here. Similarly to group 1, this was excluded since it is included within the "final time parked at night that day" and "parking duration" factors.

For group (3), it was impossible to perform decision tree analysis since no constant influential factors could be identified. This was probably because charging behavior was not affected by any particular driving or environmental conditions.

4.4 Re-grouping under potential charging conditions

The analysis results for groups (1) and (2) identified the following potential charging conditions when the vehicle is parked at night.

Potential charging conditions:
1. A SOC of 10% or less when the vehicle is parked
2. The final time that the vehicle parked at night that day
3. A long parking duration (30 minutes or longer)

The charging frequency was analyzed for parked vehicles satisfying these conditions. It was found that the number of vehicles with a charging rate of 75% or higher accounted for at least 80% of the total number of vehicles (**Figs. 13** and **14**). This shows that the charging frequency of most vehicles increased compared to the charging frequency while parked at night (**Fig. 8**).

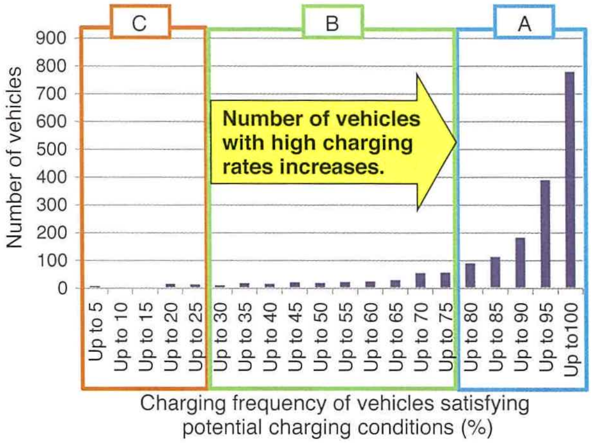

Fig. 13 Charging Frequency and Number of Applicable Vehicles Satisfying Potential Charging Conditions

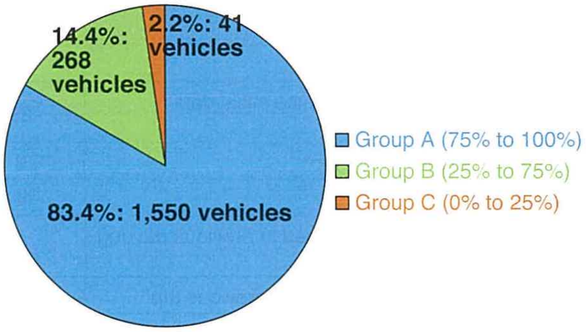

Fig. 14 Number and Proportion of Vehicles in Groups A, B, and C

The charging frequency results for vehicles satisfying the potential charging conditions can be categorized into 75% or higher for group A, 25 to 75% for group B, and 25% or lower for group C. In group A, charging was carried out at a probability of at least 80% when the vehicle satisfied the potential charging conditions. In contrast, the charging frequency results were dispersed widely for group B, ranging between 25 and 75%. Therefore, another decision tree was created to analyze the factors affecting the charging behavior of group B.

4.5 Charging behavior analysis for group B

Fig. 15 and **Table 8** show the results of decision tree analysis for the charging behavior of group B, using the same factors as before. This analysis identified gasoline prices (an environmental factor) and number of days elapsed since initial data acquisition (an action factor) as the most important influential factors.

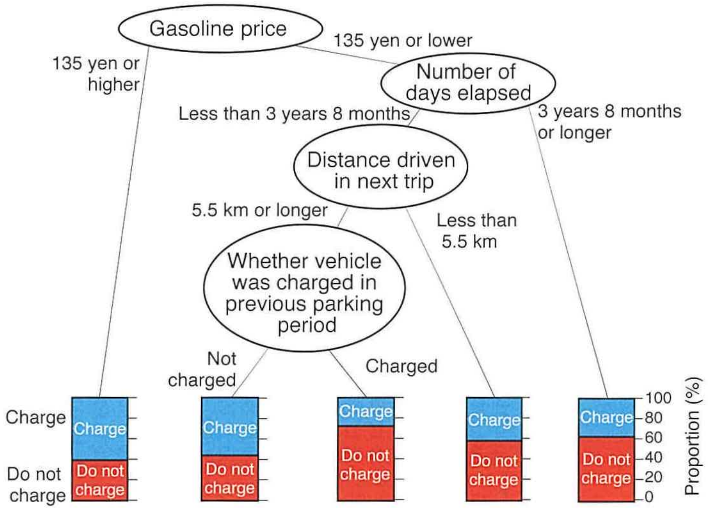

Fig. 15 Decision Tree for Group B

Table 8 Influential Factors and Importance for Group B

Rank	Factor	Importance
1	Gasoline price	51
2	Number of days elapsed since initial data acquisition	29
3	Distance driven in next trip	6
4	Time driven in next trip	4
5	Whether vehicle was charged in previous parking period	4
6	Distance driven in immediately previous trip	1
7	Time driven in immediately previous trip	1

The charging rate of group C was low under all environments and influential factors with a high degree of importance could not be identified. Therefore, the effect of gasoline prices and the number of days elapsed since initial data acquisition on charging frequency was confirmed for groups A and B.

Gasoline prices had virtually no effect on the charging frequency of group A. In contrast, the charging rate of group B rose in accordance with the price of gasoline (**Fig. 16**). It is possible that group B changes its charging behavior in consideration of economic factors due to the economic benefits of driving in EV mode rather than using gasoline as gasoline prices increase.

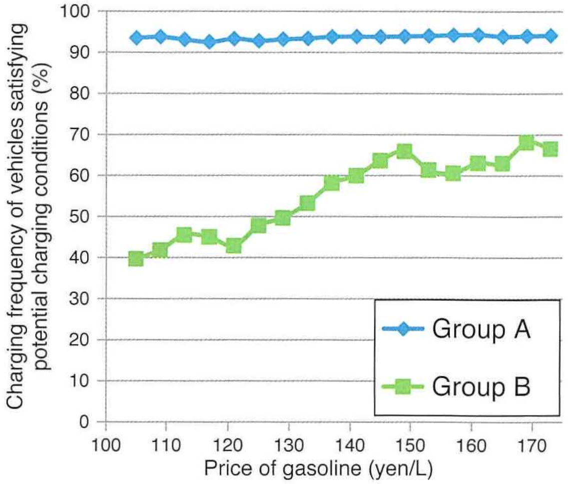

Fig. 16 Effects of Gasoline Prices (Groups A and B)

The charging frequency of group A remained high regardless of the number of days that elapsed since initial data acquisition. However, the charging frequency of group B fell as the number of days increased (**Fig. 17**). This indicates that the motivation of group B to charge the vehicle might have dropped in accordance with the number of days after first acquiring the vehicle, leading to a lower charging frequency. However, it may be possible to reverse this decline in charging frequency by making charging more convenient.

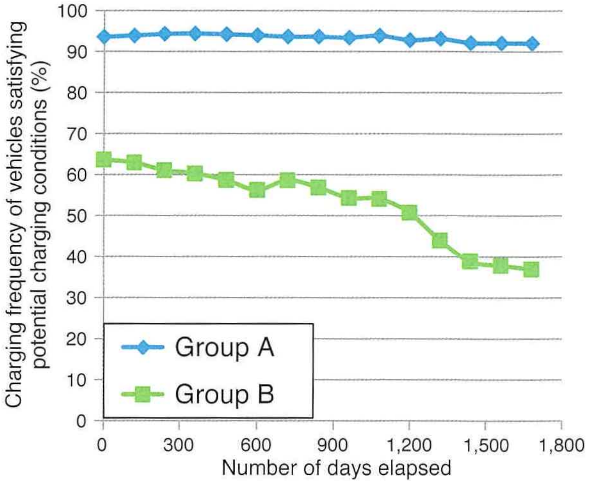

Fig. 17 Effects of Number of Days Elapsed since Initial Data Acquisition (Groups A and B)

5. Conclusion

This analysis found that vehicle charging behavior when parked at night was affected by the SOC when parked, the parking duration, and whether the vehicle was being parked for the final time at night that day. Since the effect of charging is low when these conditions are not satisfied, decisions not to charge the vehicle in this case can be regarded as falling under the definition of optimized charging behavior.

Analysis of Prius PHV charging behavior found that more than 80% of vehicles were charged when parked at night if these conditions were satisfied.

It was also found that the charging frequency of approximately 14% of vehicles when parked at night varied greatly. The charging frequency of these vehicles fell in accordance with current gasoline prices and the number of days elapsed since acquiring the vehicle. However, since it may be possible to reverse this decline in charging frequency by making charging more convenient, further development efforts are required.

References

(1) K. Hashimoto, Takeuchi, Itagaki. "Analysis of the Environmental Performance of the Plug-In Hybrid Vehicle Based on the Validation Test Data." *Transactions of Society of Automotive Engineers of Japan* Vol. 46 No. 6 (2015) pp. 1079-1085.

Authors


K. HASHIMOTO


T. OZAWA

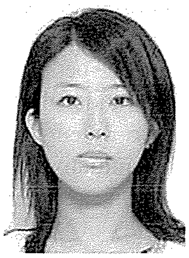
Y. TADA


H. OHASHI

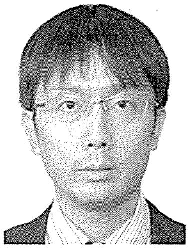
S. SHIMADA

Introduction of Innovative CS Core Process Production Technology Affecting Engine Performance and the Aluminum Casting Process

Hirotsune Watanabe[*1]
Shogo Izumi[*1]
Masaki Okada[*1]

Abstract

This article describes the clean and smooth/circulation sand (CS) core process, an innovative production technology adopted in the aluminum cylinder head casting process of powertrains developed following the Toyota New Global Architecture (TNGA) design philosophy. Developed as an original technology by Toyota Motor Corporation, the CS core process drastically improves the flexibility of cylinder head design to help realize Toyota's Dynamic Force Engine series, which balances high thermal efficiency with high power. The CS core process also enables superior environmental performance and casting quality. It was adopted on the new TNGA production lines as the first new casting technology in fifty years, and is currently being introduced on a global basis. This article details the characteristics of the CS core process as an indispensable part of heat management in engines with high thermal efficiency from the standpoints of developing ever–better cars and ever–better plants.

Keywords: *cylinder head, core, aluminum casting, inorganic core, CS core, foundry*

1. Introduction

1.1 Developing ever-better cars and ever-better plants

For the automotive industry, reducing CO_2 emissions through measures such as improving vehicle fuel efficiency is an issue of utmost importance to help combat environmental changes brought about by global warming, such as the dramatic changes in climate that have occurred in recent years. At the same time, automakers are also working to reduce the energy consumption of foundries and to alleviate the burden on the global environment caused by plant emissions.

1.2 Background of production engineering (PE) technology development

Since the aluminum casting industry requires large amounts of heat, CO_2 emissions from foundries account for a large proportion of overall automotive plant emissions. For this reason, the adoption of more energy efficient technology is regarded as an urgent task. Furthermore, increasingly stringent environmental regulations governing emissions from plants are stimulating global competition to develop technology capable of reducing malodorous gases emitted from foundries to zero. This technology has already started to be adopted in manufacturing processes. However, although commercially available technology is capable of achieving substantial reductions in malodorous gases, various issues remain, such as lower product geometry design flexibility and the lack of recycling technology within manufacturing processes. Consequently, current PE technology has yet to fulfill its potential from the standpoints of developing ever-better cars and ever-better plants.

Therefore, under the concept of improving the environmental performance of engine and aluminum foundries, this article describes an initiative to develop original PE technology that will support the future of aluminum casting.

2. Details of Aluminum Casting and Background of Engine Development

2.1 Cylinder head structure

Photo 1 shows an example of a powertrain and Dynamic Force Engine developed and produced under the Toyota New Global Architecture (TNGA) design philosophy. **Fig. 1** shows a cross-section of a Dynamic Force Engine and the cross-sectional configuration of a cylinder head in this engine. The cylinder head comprises the top portion of the engine combustion chamber. Its main functional parts include the valve train, the intake and exhaust mechanism, as well the oil and coolant passages.

[*1] Foundry Engineering Div., Powertrain Company

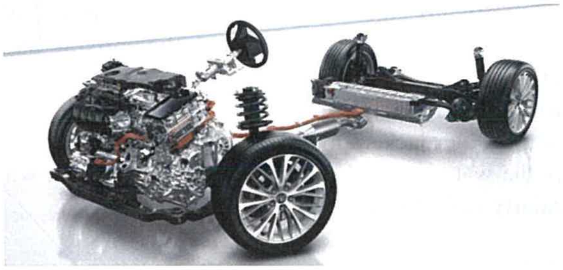

Photo 1 TNGA Powertrain

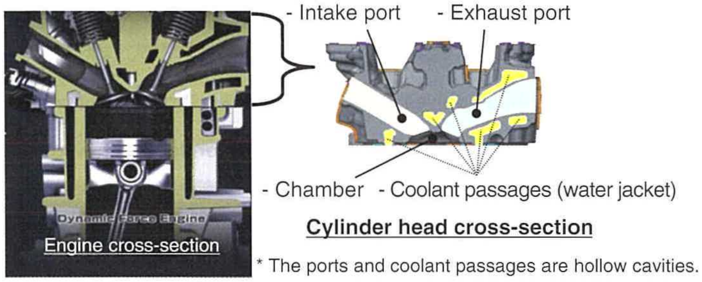

* The ports and coolant passages are hollow cavities.

Fig. 1 Engine Cross-Section and Cylinder Head Configuration

The cylinder head blank is cast at an aluminum foundry and assembled to the engine after being machined at a machining plant. For simplicity, this article treats the cylinder head as an aluminum casting (**Fig. 2**).

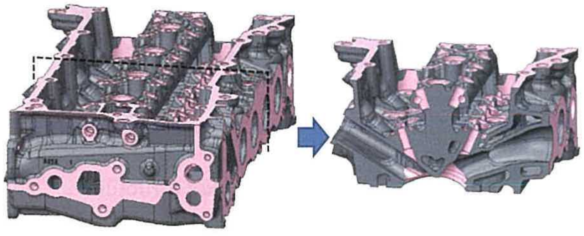

Overall view of cylinder head   Cylinder head cross-section

Fig. 2 Overall and Cross-Sectional Views of Cylinder Head

Although development tends to focus on the shape and strength of the combustion chamber, the interior of the cylinder head also contains a large number of hollow cavities (**Figs. 1** and **2**). These cavities contain the intake and exhaust ports, as well as oil and coolant passages. The mutual relationship between aspects of these cavities, such as wall thicknesses, shapes, accuracy, strength, and sealing performance, play a major role in defining the performance and reliability of the engine.

Additionally, these coolant passages (referred to below collectively as the water jacket), which function to cool the combustion chambers, exhaust ports, and other components, are rapidly becoming more complex as heat management is strengthened to enhance engine thermal efficiency.

2.2 Cast aluminum cylinder head manufacturing method

The aluminum casting process for manufacturing a cylinder head is as follows. Molten aluminum is poured into the cylinder head die body and solidified. Cavities such as the intake and exhaust ports, and the water jacket are formed using cores. The cross-section in **Fig. 3** shows the relationship between the cylinder head, die body, and cores.

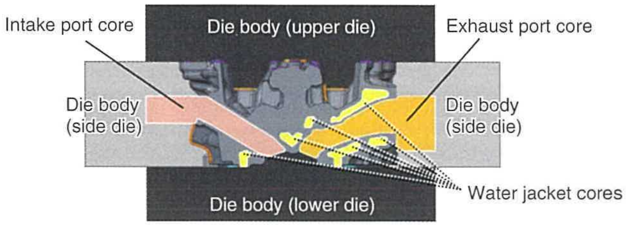

Fig. 3 Explanatory Diagram of Die Body and Core Assembly

Solid refractory materials molded into the shape of the cavities in the product are assembled into the die body in advance. These refractory materials are called "cores." Cores are created using fire-resistant refractory materials (sand) that will not burn or deform even when surrounded by molten aluminum. **Fig. 4** shows the casting process. In the casting process, the cores are assembled into the die body, which is then closed, filled with molten aluminum, and solidified by cooling. After the solidification step, the cylinder head blank is removed from the die body and sent for finishing. In the finishing process, a shock is applied to the cylinder head blank using a vibrator or the like. This shock breaks the cores into sand granules, which are then removed through the holes provided for this purpose. The cavity shapes formed by the cores function as the intake ports, exhaust ports, and water jacket (**Figs. 1** and **2**).

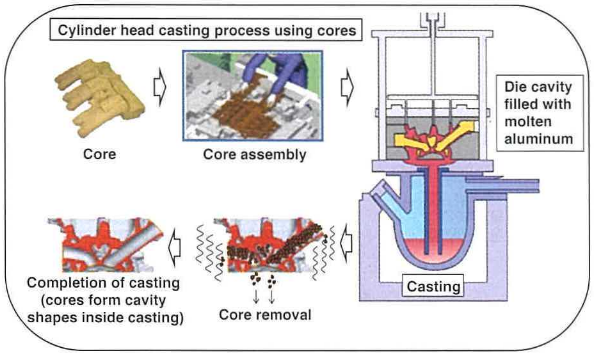

Fig. 4 Aluminum Casting Process and Cylinder Head Manufacturing Method

2.3 Core manufacturing method

Toyota Motor Corporation manufactures cores using shell molding. **Fig. 5** shows the core manufacturing process.

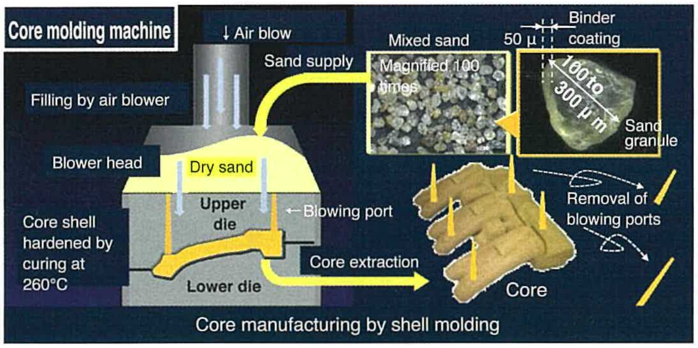

Fig. 5 Core Manufacturing Method (Shell Molding)

Cores are solid refractory materials molded into the shape of the cavities in the product. Naturally occurring silica sand granules with a diameter of approximately 0.1 to 0.3 mm are used as the refractory material. This sand is coated with a phenolic resin, which acts as an adhesive to bind the sand granules together. The sand is filled into the core shell cavities using an air blower, passing through the blower head of the core molding machine and blowing ports. After the cavities are filled, the sand is cured into a core shell at a temperature of approximately 260°C. The core is then extracted from the tool together with the blowing ports. The core is completed when the blowing parts are removed.

2.4 Background of engine development and evolution of shape

The recently developed Dynamic Force Engine series successfully pushes forward the conventional trade-off line for maximum thermal efficiency and specific power. These engines achieve world-leading engine performance with a maximum thermal efficiency of 40% for gasoline-powered vehicles and 41% for hybrid vehicles (**Fig. 6**).

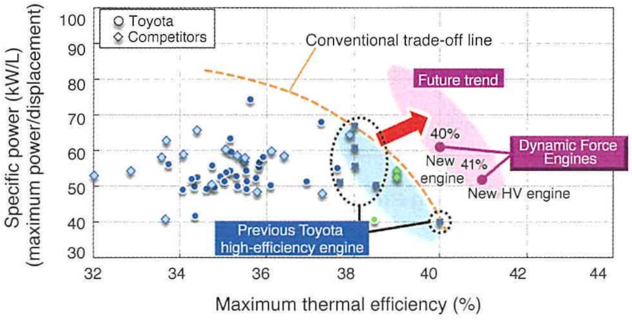

Fig. 6 Thermal Efficiency and Power of New Engine Series

More specifically, these engines adopt a motor-driven water pump and electronically controlled thermostat as a heat management system to expand the knock limit. This change to the cooling control required substantial modifications to the shape of the water jacket around the combustion chambers. **Fig. 7** shows the water jacket between the exhaust valves, which has a particularly delicate shape.

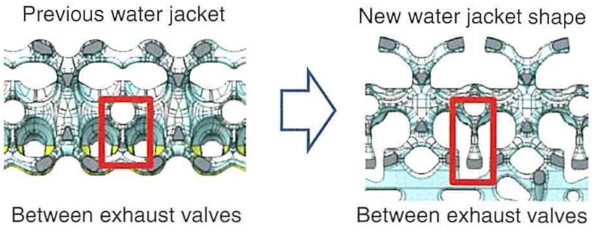

Fig. 7 Comparison of New and Previous Water Jacket between Exhaust Valves

This new water jacket shape can reduce the wall temperature of the combustion chamber by 10°C while cutting the coolant flow rate by one-half compared to the previous shape. As a result of this design change, the new water jacket was divided into separate levels and a complex network structure was created (**Fig. 8**).

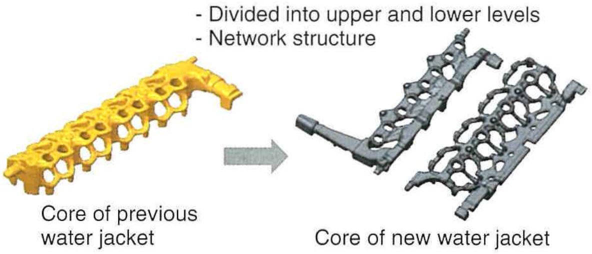

Fig. 8 Change in Water Jacket Structure

The new network structure gave rise to various issues affecting the molding of the core, the aluminum casting process, and finishing, which required innovative PE technology solutions to resolve.

2.5 Background and issues of PE technology development

The conventional shell molding process adopted by Toyota has various merits. For example, it allows comparatively high flexibility in product shape design, is simple to implement during manufacturing, and the sand recovered at the end of the process can be recycled. However, the phenolic resin used as an adhesive coating for the sand generates gas when heated in the core molding and casting processes. The odor, smoke, and contamination caused by this gas is the main reason why foundries are regarded as smelly, dirty, and dangerous.

One commercially available method that eliminates malodorous gases is an inorganic thermosetting core manufacturing process that replaces the adhesive with a water glass binder. **Fig. 9** shows the thermosetting reaction equation using water glass. Although this process enables excellent environmental performance and casting quality since only steam is emitted during the thermosetting process, various issues caused by the properties of the water glass have yet to be resolved.

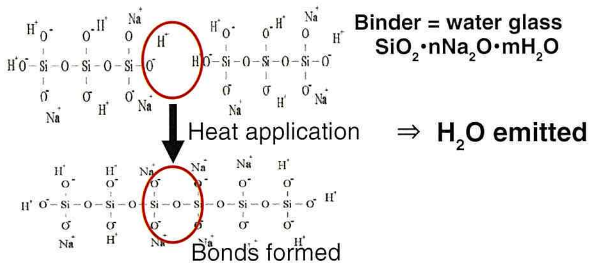

Fig. 9 Curing Reaction of Inorganic Thermosetting Core

3. Issues of Developing Ever-Better Cars and Ever-Better Plants

3.1 Issues related to creation of water jacket network structure (ever-better cars)

This section describes three issues that occurred from the standpoint of core molding when a water jacket with a network structure was adopted to help develop ever-better cars.

3.1.1 Worsening of filling performance

The first issue is the core filling performance. A water jacket with a network structure has a small core sectional area. Consequently, there are insufficient locations to place blowing ports with a large enough area to fill the core using an air blower, which means that the required filling performance cannot be achieved. **Figs. 10** and **11** show a filling defect generated in a molding test using the conventional process. Changing the shape to expand the blowing port area reduces design flexibility.

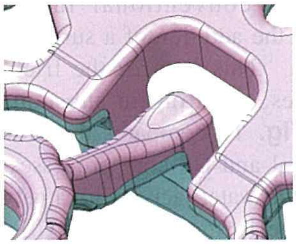

Fig. 10 New Water Jacket Shape

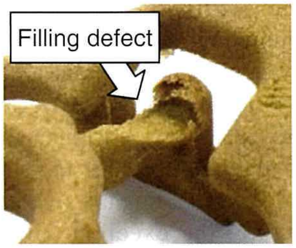

Fig. 11 Results of Test Using Conventional Manufacturing Method

3.1.2 Worsening of sand removal performance

The second issue is the removal of sand from the cylinder head. Since the core sectional area is smaller in a water jacket with a network structure, the paths for removing the sand from the cylinder head are greatly restricted, which worsens the sand removal performance.

Fig. 12 shows the relationship between the water jacket shape and the sand removal performance. A TNGA cylinder head requires a sand removal performance that far exceeds the maximum capability of the conventional shell molding process. Breakthrough PE technology was required to resolve this issue.

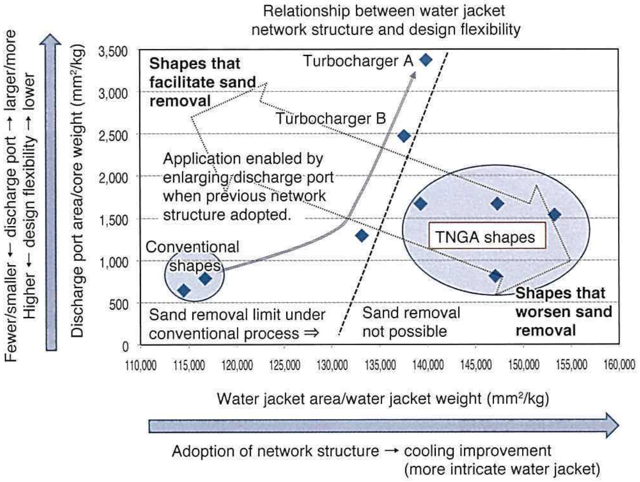

Fig. 12 Relationship between Water Jacket Network Structure and Sand Removal Performance

3.1.3 Increase in water jacket fractures (veining)

The third issue is fracturing of the water jacket caused by the heat load during casting. This is known as "veining." Veining refers to fracturing of the core due to thermal expansion of the sand used in the core, which is caused by the heat of the molten aluminum during casting. Since veining tends to occur in intricate water jackets, it becomes particularly noticeable when the core sectional area is reduced in a water jacket with a network structure (**Fig. 13**).

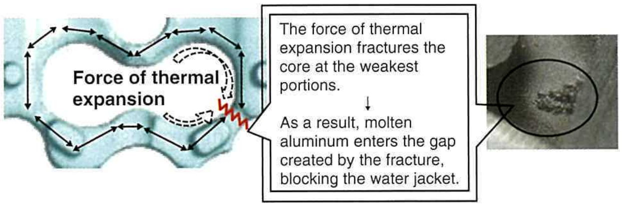

Fig. 13 Veining Mechanism

3.2 Issues of inorganic thermosetting core development (ever-better plants)

3.2.1 Larger equipment and sand logistical difficulty

The mixed sand used by shell molding is dry and has comparatively high flowability when used for air blower filling. It is also a simple process to manage and store at the foundry. The phenolic resin can also be burned off, which allows the sand to be recycled. However, making the mixed sand in a single concentrated mixer and transporting it to several tens of core machines in a plant requires forklifts or another logistical method capable of transporting 1-ton barrels of sand.

In contrast, the mixed sand used for inorganic thermosetting cores is wet because it uses water glass. **Photo 2** shows images of dry and wet sand.

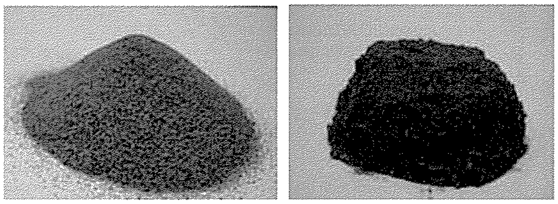

Dry sand Wet sand

Photo 2 Images of Dry and Wet Sand

Wet sand has poor flowability when used for air blower filling and it is more difficult to fill cavities with wet sand, which reduce the flexibility of product shape design. Furthermore, the amount of moisture content causes variations in flowability and core strength, and the core will not harden if it becomes too dry. These issues are addressed by using a high-pressure high-flow air blower, which increases the size of the core machine. Although the mixed sand can be used in a concentrated mixer in the same way as shell molding, it results in a higher workload at the foundry because wet sand is heavier and the moisture content is difficult to manage. Additionally, wet sand cannot be stored in large quantities. It must be used within a few hours and is thrown away once this time limit is exceeded.

3.2.2 Development issues related to recycling used sand

The key element of the shell molding sand recycling process is the thermal efficiency when the phenolic resin is burned off. For this reason, the burning process uses a single concentrated recycling device similar to the sand mixing process. Forklifts or the like are used to transport 1-ton barrels of waste sand from the several tens of sand shakeout machines used in one foundry.

The water glass used by thermosetting cores is difficult to recycle since it is an inorganic substance that does not burn off. Sand granules are fused together at a temperature of approximately 600°C. This results in clumps of sand with poor flowability in a furnace. If solid glass is formed at a temperature of approximately 700°C, yield drops in the process to separate the water glass from the sand.

For these reasons, it has not been possible to establish a recycling process for used sand. Various methods have been researched, but no successful industrial applications have been reported.

The commercial water glass binder mentioned above is compounded with special additives to offset power flowability and sand removal performance, which probably help to make the sand more difficult to recycle. To allow global application of this inorganic process, a general-purpose and reasonably priced binder must be developed at the same time based on a standard product.

Table 1 compares the inorganic thermosetting core and shell molding processes to highlight the development issues of inorganic thermosetting cores.

Table 1 Comparison of Inorganic Thermosetting Core and Shell Molding Processes

Process comparison	Gas emissions	Casting quality	Design flexibility	Operability	Recycling of used sand	Binder
Shell molding process	X	○	○	○	○	Commercial product
Inorganic thermosetting core process	○	◎	X	X	X	Special product

X : poor, ○ : good, ◎ : excellent

4. Issue Resolution and Key Breakthrough Items

4.1 Breakthrough technology for creating water jacket network structure (ever-better cars)

Breakthrough core mold technologies were required to enable the manufacture of a water jacket with a network structure. This development improved flowability by adopting foamed sand, improved sand removal performance by adopting hollow cores, and improved veining by reducing thermal expansion.

4.1.1 Improvement of water jacket filling performance

The developed clean and smooth/circulation sand (CS) core process differs greatly from a conventional inorganic thermosetting core process due to the addition of a surfactant to the wet sand to generate a foam. This reduces the frictional resistance between sand granules, resulting in substantially improved filling performance. **Fig. 14** compares the blowing port area between the conventional and CS core processes. In addition to enabling the creation of a water jacket with a network structure, the excellent filling performance of the CS core process helps to eliminate blowing port areas that are not necessary to form the product shape, thereby further increasing design flexibility.

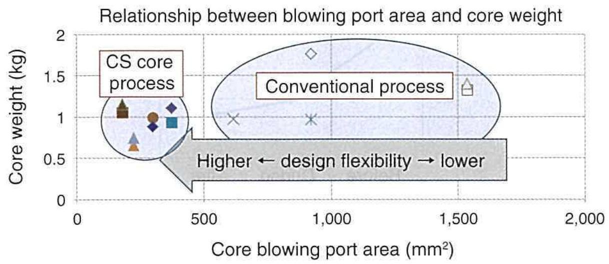

Fig. 14 Comparison of Processes Based on Blowing Port Area and Core Weight

4.1.2 Improvement of sand removal performance

Fig. 15 illustrates how the sand removal performance was improved by the CS core process. It was possible to improve the sand removal performance while maintaining the shape of the core by adopting hollow cores and hardening only the outermost shell of the core.

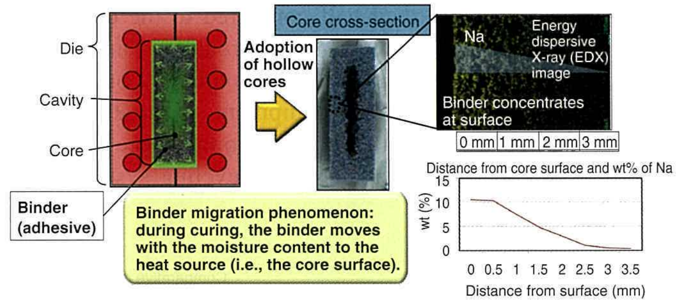

Fig. 15 Hardening Mechanism of Outermost Core Shell

As a result, these measures enabled the manufacture of water jackets with a network structure, which are a key feature of the Dynamic Force Engine series, while achieving sand removal performance that could not be accomplished by the conventional process.

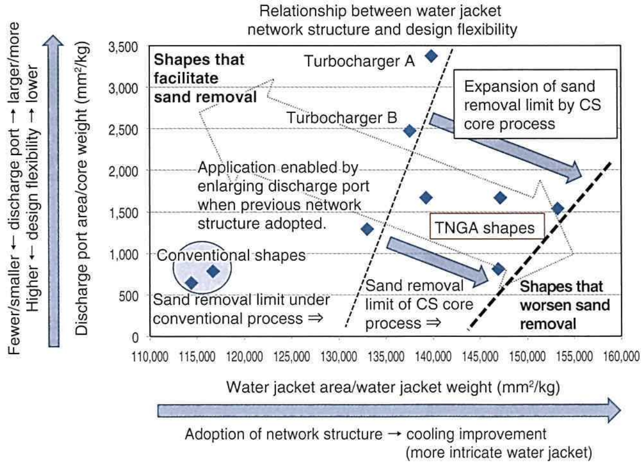

Fig. 16 Sand Removal Performance of CS Core Technology

4.1.3 Veining countermeasures

As described above, veining refers to fracturing of the water jacket when the core is not strong enough to withstand thermal expansion during casting. Therefore, the susceptibility to veining can be defined by the relationship between strength and thermal expansion. The CS core process uses artificial sand to achieve low thermal expansion. As shown in **Fig. 17**, this measure increased veining resistance compared to the conventional process. With the developed process, no veining occurs due to thermal expansion at the minimum sectional area of the water jacket core between the exhaust valves, even at a lower strength limit than the conventional process.

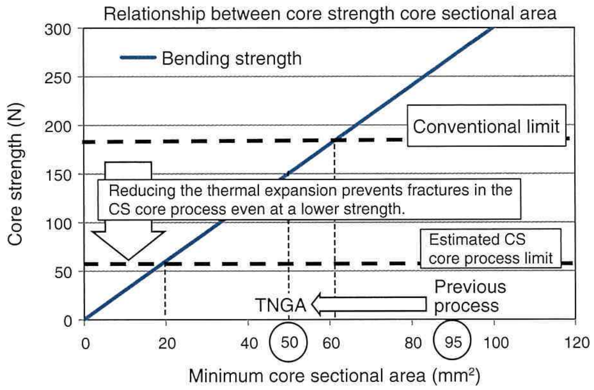

Fig. 17 Relationship between Core Strength and Water Jacket Core Sectional Area

4.2 Key breakthrough items for ever-better plants

4.2.1 Reduction of equipment size and improvement of mixed sand logistics

The CS core process incorporates a mixing machine into the core machine. The developed process eliminates mixing waste by mixing and injection molding sand and additives for a single molding shot. Sand and additives equivalent to the amount of decrease are then added. This eliminates the need for transportation and storage of the mixed sand.

The core molding machine used by the shell molding process included ducts and hoods to collect smoke and odors at the top of the equipment. Since the CS core process generates no smoke or odor, and due to a thorough revision of the positional relationship between the die and filling machine, the equipment structure was redesigned. As a result, the height of the basic equipment structure was reduced to just 1.5 meters. **Fig. 18** shows an external view of the equipment used in the shell molding and CS core processes. These measures helped to greatly improve visibility on the production line.

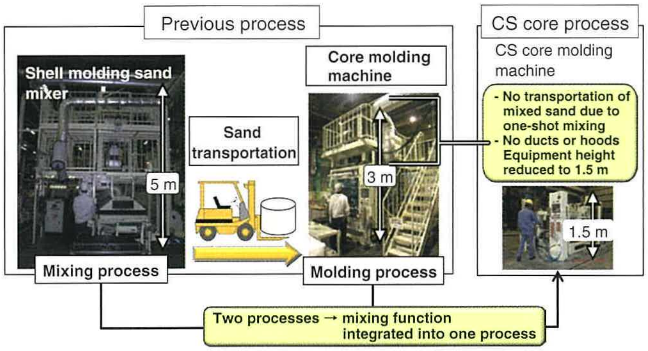

Fig. 18 Molding Machines Used by Conventional and CS Core Processes

4.2.2 Development of recycling technology for used sand

The establishment of recycling technology was inspired by a major change in approach. Normally, a powerful grinding process, a process that heats the sand to high temperatures of at least 700°C and then grinds the result, or a combination of both processes is required to remove the water glass that remains in used sand. These processes have not been practically adopted for the reasons described above. In contrast, this development focused on the fact that water glass also changes chemically when heated to lower temperatures of around 400°C before glassification occurs. Consequently, an inactivation process that prevents glassification was combined with weak grinding that strips away only the inactive content on the sand. This resulted in a breakthrough low temperature heating and low-force grinding process capable of recycling used sand.

This process consists of three steps: a heating step in which the water glass on the sand surface is inactivated at low temperatures of approximately 400°C, a stripping step in which the inactivated water glass is stripped away from the sand by mechanical grinding, and a separation step in which water glass dust and sand are isolated and reused.

As shown in the top graph in **Fig. 19**, the index that expresses the remaining binder decreases during the recycling process. Although the remaining binder does not reach zero, the remaining active content functions as a binder in the next molding process. As shown in the bottom graph in **Fig. 19**, the development verified that the remaining binder index stayed below the standard value after more than 50 recycling processes.

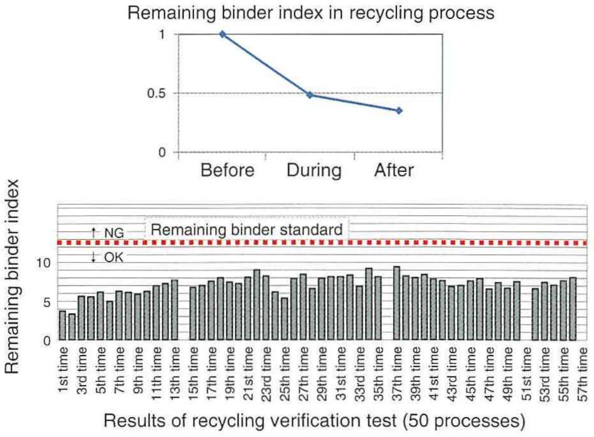

Fig. 19 Remaining Binder Index of Sand Recycling

This low temperature heating and low-force grinding process enabled electrical heaters to be adopted for all the recycling heat sources, thereby helping to reduce the size of the equipment and lower CO_2 emissions. As shown in **Fig. 20**, CO_2 emissions were reduced by more than half compared to the conventional recycling system, and the investment, throughput, and dedicated footprint of the new equipment is approximately one-tenth that of the conventional large-scale equipment. **Fig. 21** shows the external appearance of the conventional large-scale sand recycling system and the small-scale recycling system adopted by the CS core process.

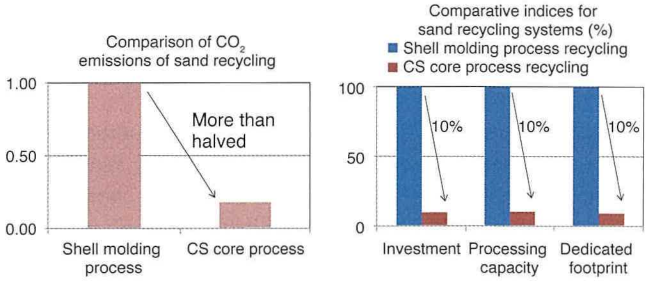

Fig. 20 Comparison of CO_2 Emissions and Other Indices

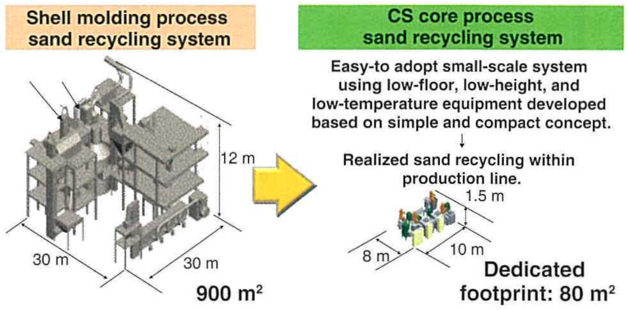

Fig. 21 External Appearance of Sand Recycling Systems

Combining this small-scale recycling system and the core machine with the one-shot mixing function enables the adoption of a self-contained sand recycling system on lines producing 9,000 units per month. **Fig. 22** compares the different sand logistics processes.

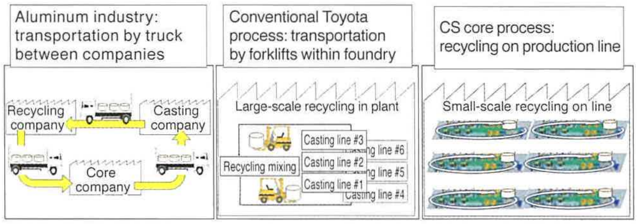

Fig. 22 Comparison of Sand Logistics Processes

In the aluminum casting industry, sand logistics generally involve the flow of sand to and from the recycling company via the core manufacturer and aluminum casting company. In contrast, the CS core process is capable of recycling the sand in a self-contained process on the production line.

5. Conclusion of CS Core Process Development

Table 2 summarizes the evaluation results of the CS core process. Although the table does not list all the evaluation indices, it demonstrates the fact that the CS core process is suitable for global application.

Table 2 Evaluation Results of CS Core Process

Process	Gas emissions	Casting quality	Design flexibility	Operability	Recycling of used sand	Binder
CS core process	○	◎	◎	○	○	Standard product

In addition to simply satisfying targets for environmentally friendliness and cost-reducing technologies, this development aimed to achieve a specific vision for an ideal process and foundry environment capable of contributing to the next generation of ever-better cars. At the same time, this process also demonstrated a potential capability to increase the flexibility of cylinder head design to help enhance engine performance. The development team intends to continue improving this technology to enable further innovations in product performance and plant environments.

Finally, the authors would like to extend their sincere gratitude to the many suppliers and other people involved in every aspect of this process development, including molding equipment and dies, sand recycling equipment, subsidiary materials such as binders and sand, as well as inspection methodologies, for the invaluable advice and support that enabled the successful adoption of this process.

Authors

H. WATANABE

S. IZUMI

M. OKADA

Design Method Using Real-World Vehicle Data

Shin Koike[*1]

Abstract

This article describes an optimum design method through an explanation of various applications of the method to product design. Using real-world vehicle data, this method handles data with large variance caused by differences in vehicle users and usage environments as probability distributions, constructs a model using the probability distributions of multiple different parameters, and then calculates a probability distribution for the target design parameter.

Keywords: *brake control, brake actuator, adaptive cruise control (ACC), automated driving, driver assistance, probability distribution, Perl, Python, MATLAB*

1. Introduction

The future of mobility lies in the development of vehicles that can be driven simply and safely by anyone, and progress is being made toward this objective. Technologies that partially realize automated driving and systems that help to prevent collisions and the like are steadily becoming more widely available. The development of these technologies and systems involves the collection of large amounts of driving and control data, and refinements are being continuously applied for control optimization. This article proposes a method for extracting information from driving data collected during development, processing the extracted information, and utilizing it in design projects.

Data containing large variance caused by differences in vehicle users and usage environments must be handled accurately to achieve high levels of both product reliability and performance. However, the parameters for gauging the required levels of performance and reliability often cannot be directly obtained from information extracted from driving data. Although predictions can be made by creating models of parts and systems, no models are capable of accurately considering large variance to a satisfactory degree. For example, the distribution when plural dimensions with a normal distribution of variance are totaled together (referred to as "σ") is known to form the square root of the sum of the squares. However, if the actual essential variance contains bias, modeling requires the synthesis of non-dimensional parameters through calculations using elements other than sums, i.e., quotients or products.

This article introduces an optimum design method by describing examples of its application to various product design projects. This method calculates the probability distribution of target design parameters by handling variance information extracted from driving data as the probability distributions of various parameters, and applying the four basic arithmetic operations to these parameters.

2. Operational Durability Conditions of Brake Actuators

This section describes the operational durability conditions of brake actuators, which were the inspiration for this probability distribution-based design method. When brake controls were first adopted, the brake actuator operational durability conditions for anti-lock brake systems (ABS) and traction control (TRC) manufactured by Toyota Motor Corporation were regarded as unnecessarily severe compared to the conditions of other companies, and required optimization. Therefore, the frequency of actuator operation (called the "actuating frequency") was investigated to determine the durability conditions. Repeated test drives were performed under real-world conditions outside Toyota and information related to actuating frequency was extracted from the measured data. This information was supplemented with statistical data about the proportion of vehicles driving on what types of roads and under which conditions in the real-world. This enabled the creation of probability distributions that illustrated the variance in actuating frequency based on differences in users and usage environments. The actuating frequency probability distribution was defined as follows. The average number of actuator operations per 1 km was calculated. Then, how this number varied depending on environmental variance in the real-world, and the probability that each resulting number would occur was then illustrated in a

---

[*1] Automated Driving & Advanced Safety System Management Div., Advanced R&D and Engineering Company

graph as a distribution. **Fig. 1** shows an example in which a histogram was created from measured actuating frequency data and then converted into a probability distribution using a kernel distribution. A kernel distribution creates weighted averages of the frequency values in a histogram to convert the values as small normal distributions. It then synthesizes all the converted values and creates a probability distribution. It should be noted that this graph was calculated from the actuating frequency of a different system and does not show the data obtained at the time. Unlike actual ABS and TRC systems, compensation was also not applied to this data in accordance with real-world conditions.

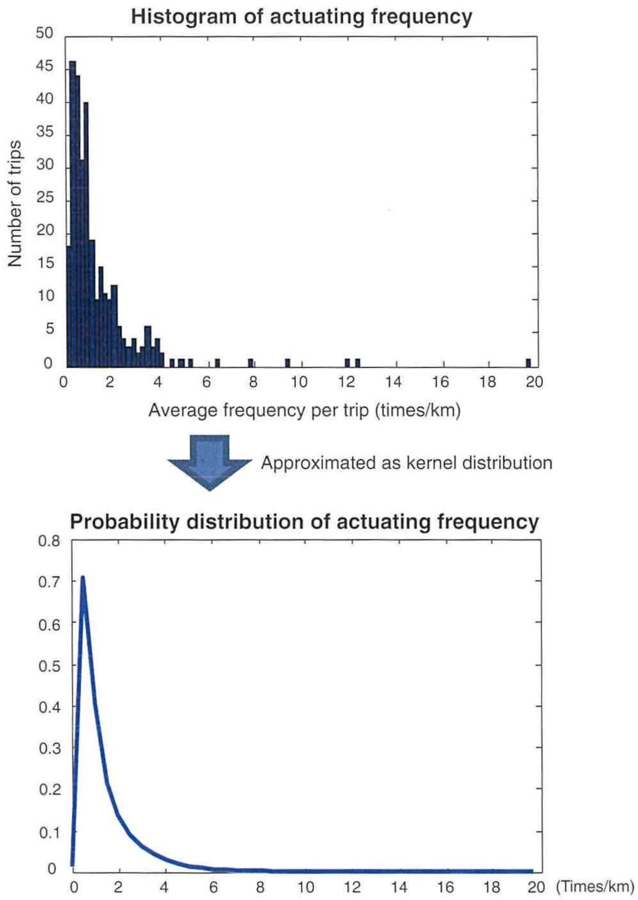

Fig. 1 Probability Distribution of Actuating Frequency (Distribution b)

The probability distribution of the number of operations to be guaranteed over the vehicle lifetime can be calculated by multiplying the vehicle mileage warranty (km) by the probability distribution for the actuating frequency (times/km). However, it should also be noted that the distance that a vehicle is driven over its lifetime may be longer or shorter than the guaranteed number of operations. Therefore, if the probability distribution of the number of actuator operations over the vehicle lifetime can be calculated from the probability distribution data of the vehicle lifetime driving distance and the probability distribution data of the actuating frequency described above, it should be possible to roughly determine the probability distribution (Weibull distribution) of the number of operations before the system malfunctions. Thus, it should be possible to calculate durability conditions in line with real-world usage environments. The method in which the probability distribution of the number of operations performed over the vehicle lifetime and the Weibull distribution are displayed in the same graph to calculate the malfunction rate is called a stress-strength model.

Fig. 2 shows a driving distance distribution estimated from recent data. The description below the graph explains how the number of operations over the vehicle lifetime is calculated from this driving distance distribution and the actuating frequency distribution mentioned above.

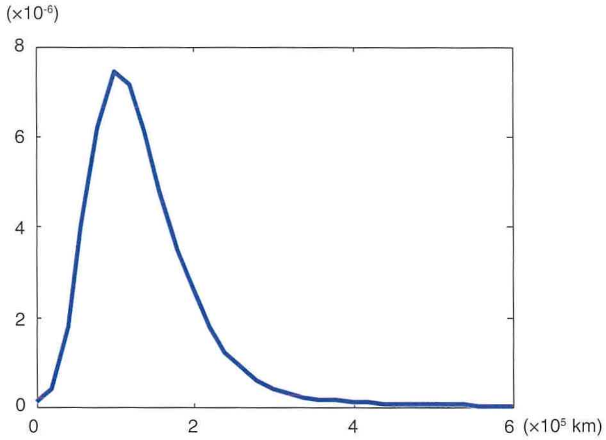

Fig. 2 Driving Distance Distribution over Vehicle Lifetime (Distribution a)

Taking probability distribution a of the vehicle lifetime driving distance (km: horizontal axis of **Fig. 2**) and probability distribution b of the actuating frequency (times/km: horizontal axis of **Fig. 1**), then a probability distribution that is the product of both horizontal axes can be calculated. From this, probability distribution c of the number of actuator operations over the vehicle lifetime (number of times on the horizontal axis) can be obtained.

If the respective occurrence probabilities of a and b are independent, then the probability that a number of operations occurs in probability distribution c is the total probability of all combinations generated by that number of operations. The product of a certain distance in distribution a and a certain actuating frequency in distribution b is, with respect to combinations of the actuating frequencies and all distances matching a certain number of operations in distribution c, the total of the product of the probability that the respective distances and actuating frequencies will occur. This forms the probability of the number of operations. More specifically, each distribution is divided into smaller portions with a minimum width. The width of these portions is constrained to cover the whole area and the respective products of the areas of the portions representing combinations of distributions a and b are totaled over the whole area. This concept can be formulated as follows.

(1) The probability at point xc on the horizontal axis of distribution c is the probability that a combination of two points, i.e., the product of points xa and xb on the horizontal axes of distributions a and b, will become xc. It shows the sum of all the combinations of these points.

(2) The horizontal axis of distribution c is divided into minimum widths dxc. Likewise, distribution a is divided into minimum widths dxa and distribution b is divided into minimum widths dxb. Here, the relationship between each minimum width is the same as the relationship between xc, xa, and xb: (xc+dxc)=(xa+dxa) (xb+dxb). In this case, the minimum width of at least one of the distributions is variable.

(3) The probability at xc in distribution c is defined as h(xc). Likewise, the probability at xa in distribution a is defined as f(xa) and the probability at xb in distribution b is defined as g(xb). If dxb has a variable width, the sum of xa in the following equation substituted into each dxa from the minimum to the maximum values at each xc forms the probability distribution of c (see **Fig. 3**).

$$\begin{cases} h(xc)=[\Sigma\{f(xa)\cdot dxa\cdot g(xb)\cdot dxb\}]/dxc \\ dxb=(xc+dxc)/(xa+dxa)-xb \\ xb=xc/xa \end{cases}$$

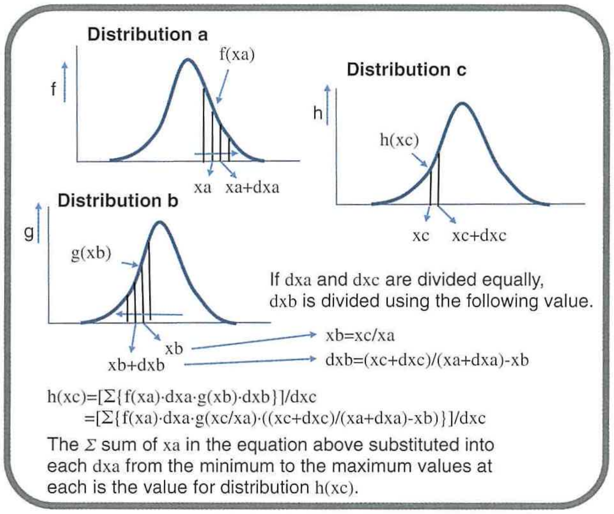

If dxa and dxc are divided equally, dxb is divided using the following value.

h(xc)=[Σ{f(xa)·dxa·g(xb)·dxb}]/dxc
=[Σ{f(xa)·dxa·g(xc/xa)·((xc+dxc)/(xa+dxa)-xb)}]/dxc

The Σ sum of xa in the equation above substituted into each dxa from the minimum to the maximum values at each is the value for distribution h(xc).

Fig. 3 Method of Calculating Distribution c of Product of Distributions a and b

The probability distribution of the number of actuator operations over the vehicle lifetime (distribution xc) can be calculated from the probability distribution of the actuating frequency and the driving distance probability distribution over the vehicle lifetime using the numerical calculations described above (**Fig. 4**).

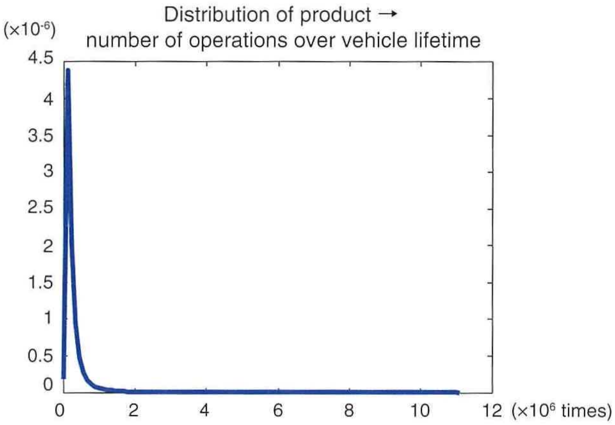

Fig. 4 Number of Actuator Operations over Vehicle Lifetime (Distribution c)

If this probability distribution is defined as (1), the cumulative Weibull distribution incorporating actuator malfunction pattern m (2) is overlaid on a graph with the same number of operations, and the distribution of the product of both values (3) is calculated, then the resulting area is the malfunction rate. **Fig. 5** shows the stress-strength model created so that the malfunction rate reaches a predetermined value. **Fig. 6** is the logarithmic expression that visually illustrates the distribution for calculating the malfunction rate. For example, if the number of operations equivalent to the 80th percentile of this Weibull distribution is defined as S times, and a malfunction does not occur after S cycles of a durability test performed using N samples, the Weibull distribution can be guaranteed with a risk of $(1-0.8)^N$. In this case, it is sufficient to have a number of operations and samples that can be guaranteed at a risk of several percent or less.

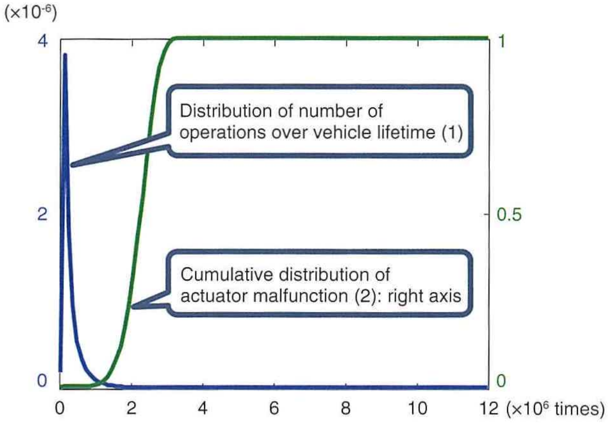

Fig. 5 Stress-Strength Model

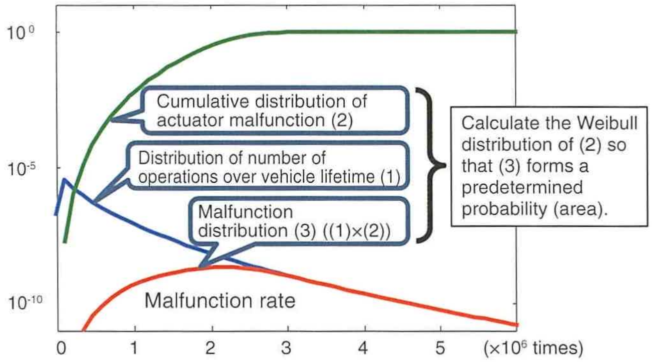

Fig. 6 Logarithmic Expression of Stress-Strength Model

As described above, a probability distribution that is the product of different parameters can be calculated from the probability distributions of the respective parameters. It is also possible to calculate distributions of sums and quotients in the same way by applying the relationship between xc, xa, and xb, and the variation division method described above to the sums and quotients of the parameters.

It has been possible to create sufficiently clear differentiation in reliability and performance in comparison with Toyota's competitors by designing various actuators and control systems using these methodologies.

3. Parameter Design of ACC Control Trigger

This section describes a more recent design case study involving the control trigger for Toyota's adaptive cruise control (ACC) system known as Dynamic Radar Cruise Control. ACC is a driver assistance system that has started to become more widely available as part of the Toyota Safety Sense active safety packages. It allows the driver to set a speed that the vehicle maintains while measuring the distance to the preceding vehicle with radar. This driver assistance system uses data to record real-world behavior that might need refinement. This recorded data can therefore help to optimize the system. However, since ACC may be activated for long periods while driving, it is difficult to distinguish normal data that requires no refinement and data that may need refinement from the whole body of data. Since large volumes of unnecessary data is recorded, it is possible that the dealer may overwrite the memory before the required data is extracted. Consequently, designing when to set the recording trigger must be determined in consideration of the balance between the recording frequency and the extraction timing. Since the recording trigger frequency and ACC usage environment contains large variance, the trigger was designed using the probability distribution method described above.

The trigger design procedure consisted of steps (1) to (6) below.

(1) Multiple candidate operation requirements were created that can reliably extract cases to be recorded, from triggers with a low actuating frequency and triggers with a relatively high frequency.

(2) Using real-world driving data measured under various environments, an actuating frequency (km/times) histogram was created showing the average interval (km) of operations per trip with each trigger (**Fig. 7**), and a probability distribution was created using a kernel distribution (**Fig. 8**). The following section describes the how this real-world driving data was processed.

(3) The daily driving distance probability distribution (km/day) data was collated for a vehicle driving in the real-world (**Fig. 9**). The distribution of the product of the probability distribution of the inverse number of this daily driving distance and the actuating frequency probability distribution created in step (2) was created. Here, since (km/times)/(km/day)=(day/times), the probability distribution of the required number of days for one trigger could be calculated (**Fig. 10**).

(4) The number of cases stored in the memory before overwriting was defined as N, and the distribution of the sum of the probability distribution created in step (3) and the probability distribution equivalent to the number of days required for one operation was created. This was repeated N-1 times. Creating distributions equivalent to N times the required number of days for 1 trigger enabled calculation of the probability distribution of the number of days from N triggers to the number of days that N memory items are overwritten (**Fig. 11**).

(5) The frequency distribution of the number of days between a user encountering an incident and taking the vehicle to a dealer (i.e., the number of days from the date of real-world information generation to the date the vehicle is brought to the dealer) and its probability distribution were calculated (**Fig. 12**).

(6) The cumulative distribution was calculated from the probability distribution obtained in step (4). By overlaying the cumulative probability distribution calculated in step (5) on the same graph, it was possible to visualize the margin for the number of days before memory overwriting occurs with respect to the number of days before the vehicle is taken to a dealer (**Fig. 13**). The cumulative number of days before memory overwriting B and the probability of the number of days before the vehicle is taken to a dealer A were overlaid on the same graph. The value for the number of days A shows the probability that the vehicle will be taken to the dealer at that number of days, and the value for B shows the probability that the memory will be overwritten at that time. The product of both values (A×B) is the probability that the vehicle will be taken to the dealer at that number of days and the memory overwritten. The area of the distribution is the total probability that the memory will be overwritten (**Fig. 14**). **Fig. 15** shows the logarithmic expression of **Fig. 14**.

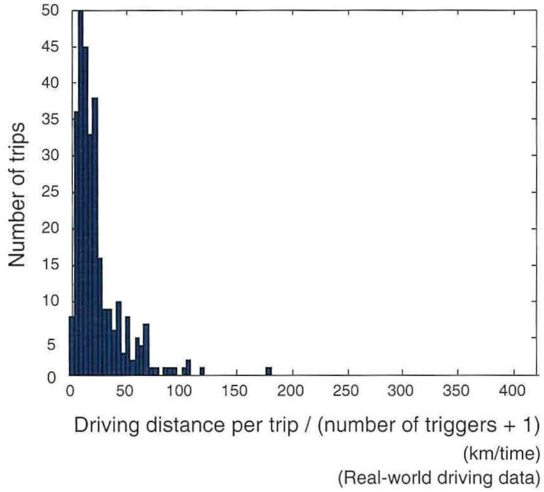

Fig. 7 Trigger Actuating Frequency Histogram

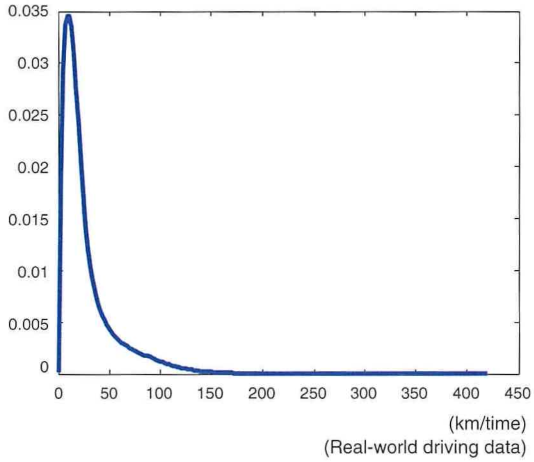

Fig. 8 Probability Distribution of Trigger Operations

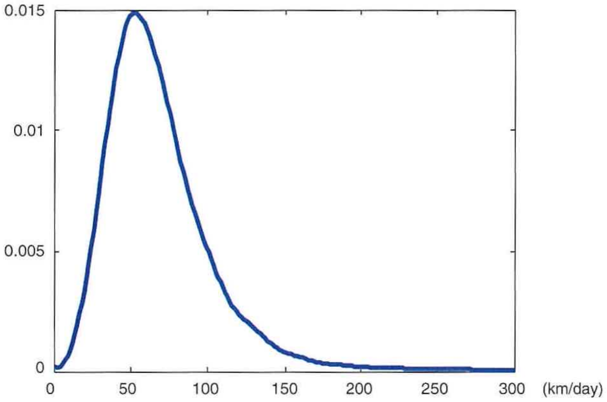

Fig. 9 Probability Distribution of Daily Driving Distance

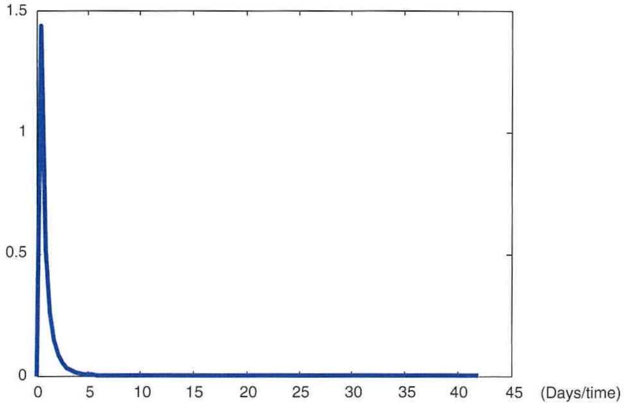

Fig. 10 Probability Distribution of Number of Days for One Trigger Operation

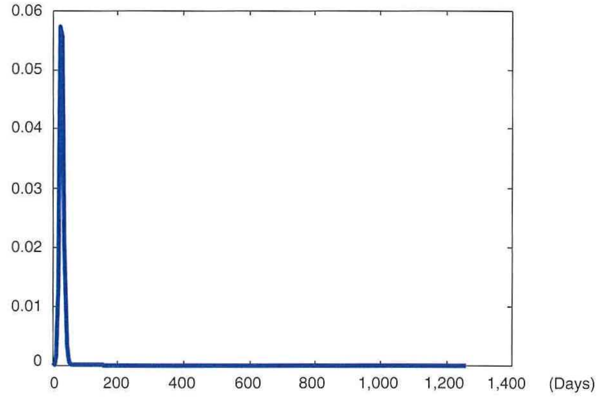

Fig. 11 Probability Distribution of Number of Days for Overwriting N Memory Cases

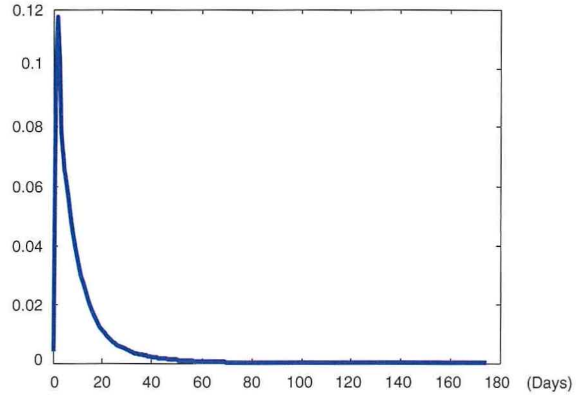

Fig. 12 Probability Distribution of Number of Days before Vehicle Taken to Dealer

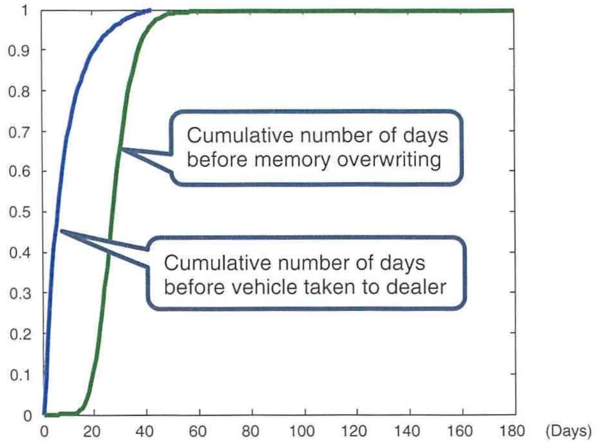

Fig. 13 Relationship between Number of Days before Vehicle Taken to Dealer and Number of Days before Memory Overwriting

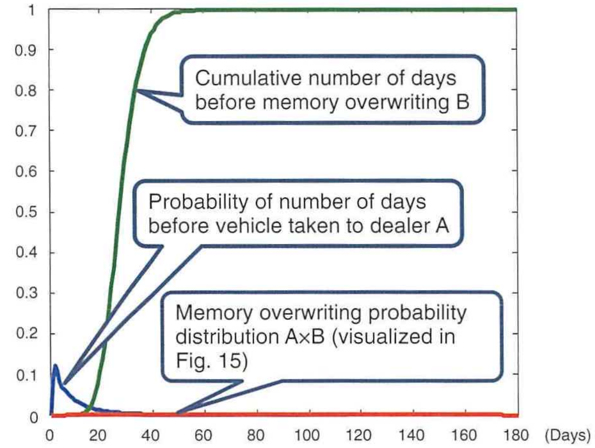

Fig. 14 Probability Distribution of Memory Overwriting

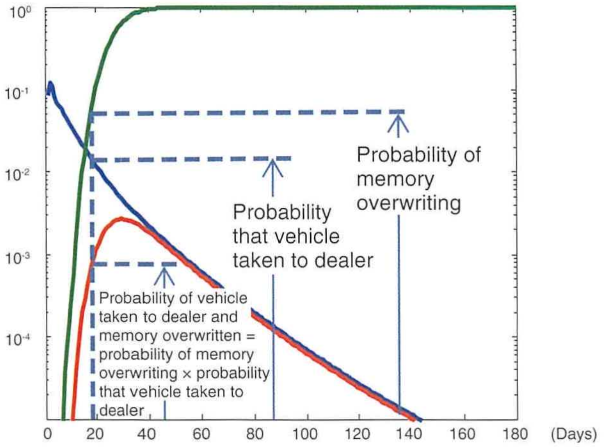

Fig. 15 Logarithmic Expression of Memory Overwriting Probability Distribution

Once the probability that the memory will be overwritten after the vehicle is taken to the dealer can be calculated as described above, that value can be used as a target for designing the trigger requirements and size of the memory. In the case study described above, the probability of memory overwriting at the dealer was calculated as 10% or less. In the event that the vehicle is taken to the dealer within about 10 days, the memory will not be overwritten in at least approximately 99% of cases, indicating that the memory was designed with sufficient margin. Creating a distribution for a target parameter enables the overwriting status to be visualized, something that cannot be understood easily by figures alone.

In this case, the variance of three parameters (trigger actuating frequency, driving distance, and number of days before vehicle taken to dealer) was used as the probability distributions. However, if the probability distribution is not calculated (for example, if the value equivalent to the 80th to 90th percentile of each probability distribution is used under the same conditions to calculate the required memory size), the result shows that a memory capacity between 5 and 18 times greater than N defined above is needed. This represents a substantial degree of excess quality and a massive performance compromise when installed in a system that competes based on performance. In the figures below, the 90th percentile of actuating frequency is defined as X_{90}km/time and the 80th percentile as X_{80}km/time (**Fig. 16**), the 90th percentile of daily driving distance is defined as Y_{90}km/time and the 80th percentile as Y_{80}km/time (**Fig. 17**), and the 90th percentile of the number of days until the vehicle is taken to a dealer is defined as Z_{90}km/time and the 80th percentile as Z_{80}km/time (**Fig. 18**). **Fig. 19** shows an example of the calculated memory size requirement based on each of these values.

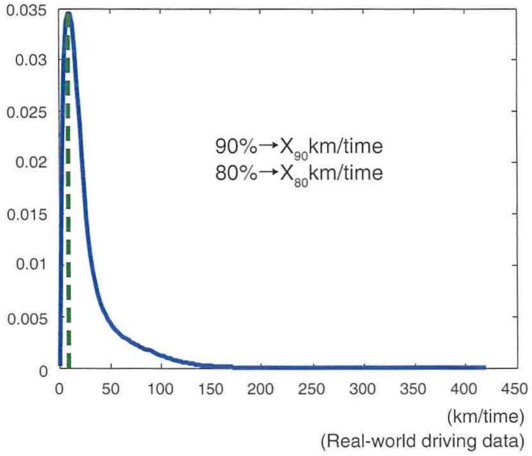

Fig. 16 90th and 80th Percentile of Trigger Actuating Frequency

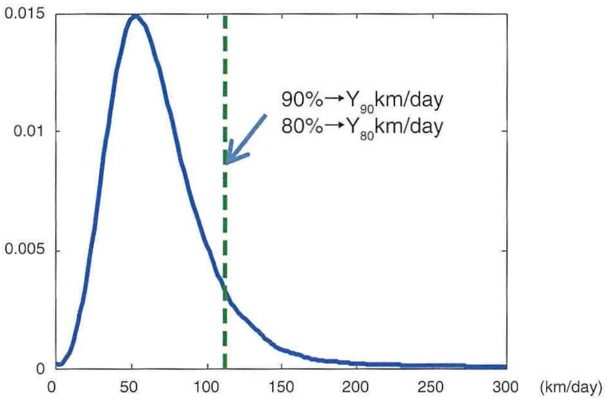

Fig. 17 **90th and 80th Percentile of Daily Driving Distance**

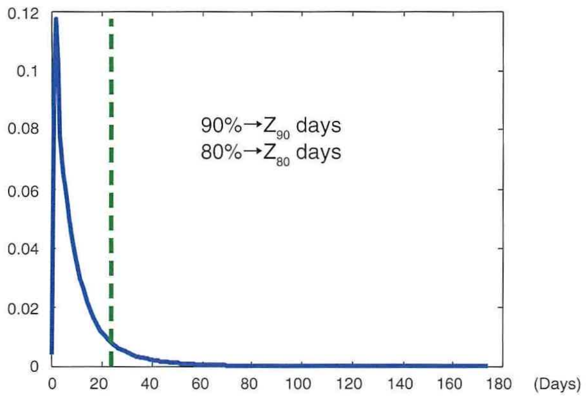

Fig. 18 **90th and 80th Percentile of Number of Days Until Vehicle Taken to Dealer**

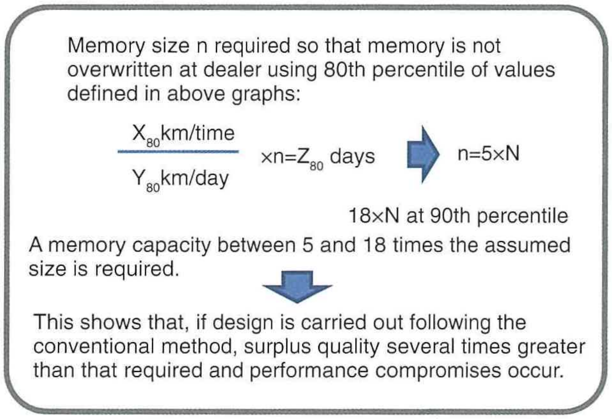

Memory size n required so that memory is not overwritten at dealer using 80th percentile of values defined in above graphs:

$$\frac{X_{80}\text{km/time}}{Y_{80}\text{km/day}} \times n = Z_{80}\text{ days} \Rightarrow n = 5\times N$$

18×N at 90th percentile

A memory capacity between 5 and 18 times the assumed size is required.

This shows that, if design is carried out following the conventional method, surplus quality several times greater than that required and performance compromises occur.

Fig. 19 **Required Memory Size Calculated by Conventional Method**

As described above, a model can be created by extracting and synthesizing various probability distributions of variance from driving data. Using this model to calculate the probability distribution of a target parameter enables design with an appropriate balance between quality and performance. This method calculates products, sums, and quotients of probability distributions and can be realized using the four basic arithmetic operations. Therefore, it should be possible to convert all models created by conventional numerical calculations to probability distribution models in this way. **Fig. 20** provides an overview of the calculations described above.

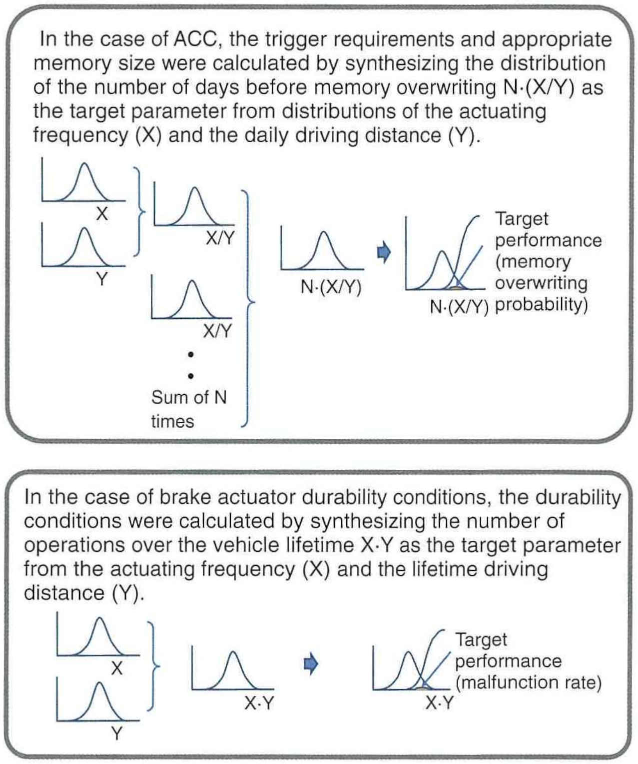

In the case of ACC, the trigger requirements and appropriate memory size were calculated by synthesizing the distribution of the number of days before memory overwriting N·(X/Y) as the target parameter from distributions of the actuating frequency (X) and the daily driving distance (Y).

In the case of brake actuator durability conditions, the durability conditions were calculated by synthesizing the number of operations over the vehicle lifetime X·Y as the target parameter from the actuating frequency (X) and the lifetime driving distance (Y).

Fig. 20 **Example of Four Basic Arithmetic Operations Applied to Probability Distribution**

4. Information Extraction from Measured Data

The previous section described how a model is created from probability distributions to enable optimum design. This section describes how data from real-world driving and system evaluations is extracted, processed, and used in design.

Real-world driving data that can be used in the development of driver assistance and other systems can now be collected in various formats. In addition to system control data, this includes vehicle state variables, radar recognition data, and images of the area in front of the vehicle. Although various measuring instruments are used in accordance depending on the supplier or objective when the data was recorded, all such instruments can output data as comma separated values (csv). Providing sufficiently rich information can be recorded in the csv format, such data has a high level of re-usability and it can be used for various purposes. For example, data measured in durability condition studies of brake actuators for ABS and TRC systems can be applied to different brake actuators or brake control systems. Therefore, additional real-world driving is not required even for reliability studies of unnecessary operations and or like.

This data can be processed using script processing languages such as AWK, Perl, and Python. These script processing languages use powerful search functions called normal expressions and various libraries to extract the required information from large volumes of csv data in a short period of time and a cross-sectoral manner. Despite this capability, these languages still require several days to process terabytes of data. Therefore, as an initial step, intermediate data is created in the proper format using only the necessary data. Once intermediate data has been created, the data can be processed and re-processed repeatedly in a short period of time in a format that can be handled by software such as MATLAB (**Fig. 21**).

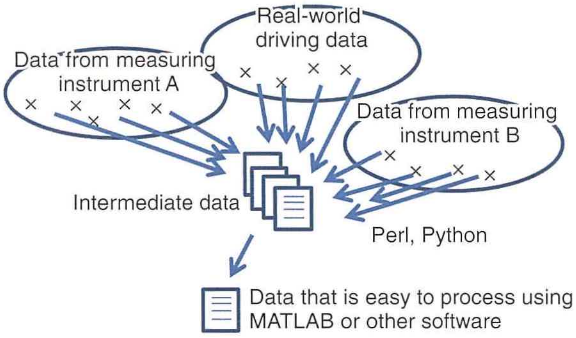

Fig. 21 Data Processing Flow

The processing sequence is described below. Steps (1) and (2) are performed by the script language and steps (3) and (4) are performed by MATLAB.

(1) csv data formats, which differ depending on the measuring instrument, are re-read using common data labels and units. This data is then searched using various triggers and data from those trigger timings are entered into intermediate files in various formats.

(2) To create frequency distributions, the average per-trip distance interval written into all the intermediate files is read to create files in a summarized list that are easy for MATLAB to process. Aside from frequency distributions, when studying settings, data volumes, or the like used by controls based on variances of control parameters or various state variables, files that can be processed by MATLAB are created from control data when trigger operations occur.

(3) These files are read by MATLAB and histograms are created. Kernel distributions are created from these histograms. All distributions are handled as point sequences. Interpolation is applied as necessary and it is necessary to ensure accuracy.

(4) In addition to probability distributions created from driving data, MATLAB is used to read statistical data such as the daily driving distance and vehicle lifetime driving distance, and calculate the distributions described in Sections 2 and 3 (**Fig. 22**).

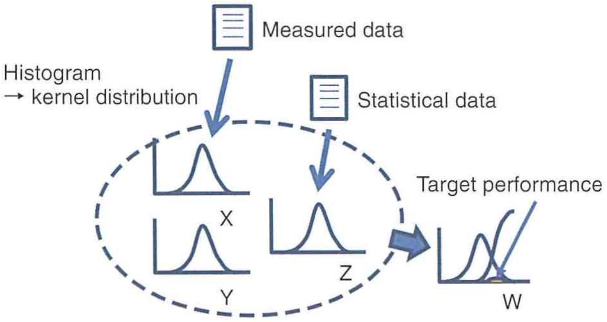

Fig. 22 Probability Distribution Creation Method

5. Conclusion

Sections 2 and 3 described how the developed method is capable of the handling of frequency distributions as probability distributions, the modeling of multiple probability distributions using the four basic arithmetic operations, and the synthesis of a probability distribution for a target parameter. Section 4 outlined the procedure by which large volumes of data from various measuring instruments is collected and used to create frequency distributions. These methodologies can be used to accurately design various systems containing large variance, thereby helping to efficiently ensure reliability and performance. Furthermore, the developed method is also capable of extracting various items of design data and hidden phenomena from large volumes of data.

Although this article has only described an outline of the developed method, it is hoped that communicating the requirements and inspirations (i.e., the needs and seeds) of the method in this way to a wider audience will help to facilitate its utilization and advancement in various fields.

Author

S. KOIKE

Research into Response Type Detection Technology for Active Listening Robot Using Machine Learning

Tatsuro Hori[*1]
Narimasa Watanabe[*1]

Abstract

This research is developing technology that switches the type of response made by active listening robots designed to help prevent or arrest the progress of senile dementia at an optimum timing. Conventional technologies permit users and robots to converse in an alternate question and answer format. In contrast, this research established a control method that allows the robot to make responses at appropriate timings by detecting the type of required response (silence, nodding, or an actual response) using randomized decision forests in machine learning characterized by the user's voice. Randomized decision forests are capable of achieving high identification performance through group learning using multiple decision trees. Quantitative indices were used to confirm that this method enables more rhythmical dialogues than conventional technology.

Keywords: *active listening robot, number of interruptions, machine learning, random forest*

1. Introduction

Japan faces a severe aging population problem as the proportion of elderly people 65 or over will exceed 33.4% in 2035, and with an estimated 25% of that group predicted to suffer from senile dementia.(1) The behavioral and psychological symptoms of dementia (BPSD), which include delusions, hallucinations, and violence or other agitation, strongly heighten the burden felt by caregivers.(2) Interviews with doctors and caregivers in field surveys conducted at Mifune Hospital and other care and medical facilities revealed that conversation was an essential part of providing care for dementia. Robotic conversation partners for elderly people afflicted with dementia must have a conversational ability oriented toward small talk that makes the user feel secure and appreciated, rather than task-oriented conversations such as those provided by Apple's Siri.

Toyota has already developed a conversation system that listens to the user receptively,(3) a small talk conversation system that uses Internet news to enrich the discussion,(4) and a small talk conversation system that searches for responses that match the topic brought up by the user.(5) The development of the Pocobee active listening robot (**Photo 1**), which consolidates those conversation technologies began in April 2016.

Photo 1 Pocobee

2. Overview of the Pocobee Active Listening Robot

With its ability to recognize words and facial expressions, and to move its eyes and body while conversing with the user, the Pocobee active listening robot aims to function as an everyday small talk partner that helps prevent the onset of dementia or slow its progress, and also contributes to reducing the burden on caregivers working with dementia patients. Using conversation that prompts reminiscences while looking at old photographs (the reminiscence method) as a base, the robot interprets the contents of the conversation while switching between talking, listening, responding, and asking questions at appropriate points, and its primary function is to hold a conversation while analyzing the emotional state of the user.

[*1] Z Frontier Div., Frontier Research Center

The reminiscence method calls for actively prompting the user to speak. This makes it necessary to resolve the problems of delays between the user talking and the robot responding (prolonged silences) and robot responses unnecessarily disrupting the user's speech (number of interruptions). To do so, technology that switches to an utterance type mode at appropriate times (turn-taking) was developed. Section **3** presents this turn-taking technology, and Section **4** describes its evaluation.

3. Turn-Taking Technology

Fig. 1 shows the processing flow for turn-taking, which consists of three modules (user utterance feature deduction, timing detection, and utterance type assessment). The utterance feature quantity and timing detection method were carefully designed to reduce the computation burden that leads to prolonged silences, and are respectively described in Sections **3.1** and **3.2**. The method used to determine the appropriate utterance type to reduce the impact of the number of interruptions is presented in Section **3.3**.

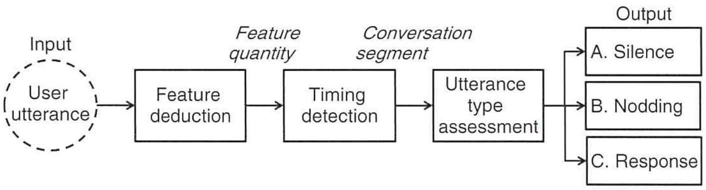

Fig. 1 Turn-Taking Processing Flow

3.1 User utterance feature deduction

The deduction of user utterance features involves extracting low-calculation feature quantities such as the pitch of the end of the phrase or of the overall segment of an utterance, its volume, or its length. Characteristics such as an utterance being likely to end when the user's voice drops in volume or rises in pitch, for example, can be identified. In addition, the use of the end of phrase feature quantity makes it possible to identify first-order changes (rising tone, e.g., "I'm looking forward to that") and second-order changes (rising and falling tone, e.g., "This weekend, you know") (**Fig. 2**). Typical conversation applications such as Siri rely on linguistic features such as voice recognition results, which is prone to longer delays than the phoneme feature-only approach presented in this article (Siri: approximately 2 seconds, this approach: approximately 0.8 seconds). Delays (prolonged silences) are shortened with the approach presented in this article.

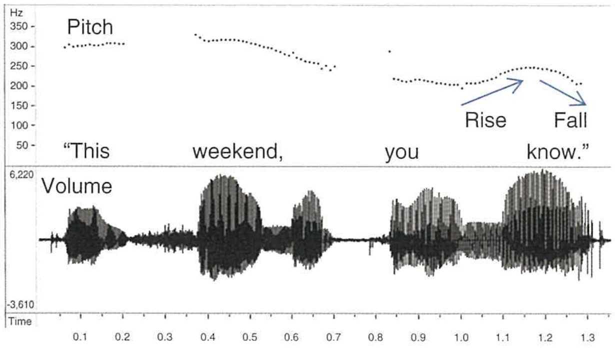

Fig. 2 Pitch and Volume Waveform

3.2 Timing detection

As a rule, a short pause in the other person's utterance represents the appropriate time to respond, and is often accompanied by nodding. In conversations such as the one in **Table 1** (at right), there is a short pause in the utterances after each unit of meaning, and a more natural conversation is achieved by nodding at those points. Cases such as these are envisioned, and breaks in user utterances are detected as the timing of the response. More specifically, as shown in **Fig. 3**, the timing of the response is detected as the point starting when the volume falls below and goes back over the threshold in a fixed segment T, and the number of times the 0 line is crossed also falls below N.

Table 1 Utterance Type Selection

User	Robot	Response type
"Well, I did it this morning..."		
	"Sounds great."	C. Response
"It might be dry by now."		
		A. Silence
"Maybe I'll check."		
	Uh-huh	B. Nodding

Random utterance type selection

User	Robot	Response type
"Well, I did it this morning..."		
	Uh-huh	B. Nodding
"It might be dry by now."		
	Uh-huh	B. Nodding
"Maybe I'll check."		
	"Sounds great."	C. Response

Appropriate utterance type selection

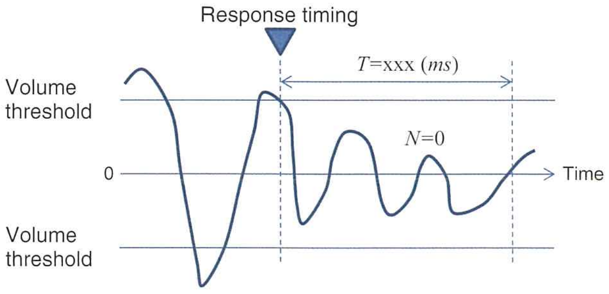

Fig. 3 Response Points

3.3 Utterance type assessment

Using the feature quantities deduced in Section **3.1** as inputs, the utterance type assessment identifies an appropriate utterance type.(6) As shown in **Table 1** (at left), random selection of the type of utterance may create a higher number of interruptions because the response is taking place while the user is still talking. With an appropriate assessment, the robot continues to listen when playing the role of the listener, and to speak when playing the role of the speaker, resulting in the more natural conversation presented in **Table 1** (at right).

In advanced research by Raveesh et al.,(7) utterance types were classified into silence or response, with a support vector machine (SVM) classifier used to discriminate between the two. The present research differs in terms of the number of types and the classifier.

As described in Section **3.2**, this project aims to achieve more natural conversation through the inclusion of nodding. This results in three types of utterances: silence, nodding, and response.

For the classifier, methods of obtaining higher discrimination accuracy were studied. There are three general approaches to classifiers. Decision trees (rules) and machine learning are used after specifying feature quantities to some extent, while deep learning involves relying on vast data sets to learn about feature quantity and discriminators at the same time. In this research, the absence of feature quantities with a notable contribution ratio makes it difficult to establish a decision tree. Conversely, turn-taking is already partially regulated, making vast amounts of learning data unnecessary. Given the additional difficulty of acquiring conversation data, the deep learning approach, which requires extremely large data sets, is not suited to this project. Consequently, machine learning was deemed appropriate in this case. Sections **3.3.1** and **3.3.2** respectively discuss the preparation of learning data for utterance type assessment, and the details of the classifier.

3.3.1 Preparation of learning data

Data collection was performed using the Wizard-of-Oz (WoZ) technique, which involves a hidden human operator using a button to determine the utterance type for the robot. This enabled the semi-automatic assignment of ideal utterance type training labels at an ideal timing for the conversation data, and facilitated the construction of the classifier.

However, even WoZ conversation contains response errors. Consequently, some training labels (approximately 5% of the whole dataset) were later corrected manually. The time required to assign training labels for conversation data for five subjects speaking for three minutes (a total of 15 minutes) was reduced from 150 minutes to 30 minutes, which represents a significant decrease in the work hours needed to prepare the training data compared to manual labeling of the whole dataset.

3.3.2 Comparison of approaches to utterance type discrimination models

A classifier for the data prepared in Section **3.3.1** was prepared. Logistic regression, SVM, and random forests were used as candidate classifiers. The base approach involved a random selection of the training label ratio (36% silence, 48% nodding, and 16% response) in the training data, which was also compared with the SVM base approach used in advanced research.

Fig. 4 shows the results of a comparative 10-fold cross validation of the candidates. The random forest approach had the most accurate results, followed by SVM and logistic regression as the order for the base approach. Given its higher accuracy of 27% relative to the base method and 15% relative to the advanced research in terms of discriminating between the three types of utterances, the random forest approach exhibited significantly better results. As shown in **Fig. 5**, the random forest approach is a machine learning method that involves applying ensemble learning using multiple decision trees to obtain high discrimination performance.

Adaptability to individual user types was another requirement. For example, there is a difference in how voice pitch changes between users who raise it at the end of words and those who do not, and this calls for a learning model with fine boundary distinctions. **Fig. 6** shows a comparison of the decision boundaries between the SVM and random forest approaches. The random forest approach is capable of finer boundary classification, and suited to the task.

In terms of both accuracy and adaptability to user types, the random forest approach was therefore proposed as the utterance type discrimination model.

Fig. 4 Comparison of Accuracy for Various Utterance Type Discrimination Models

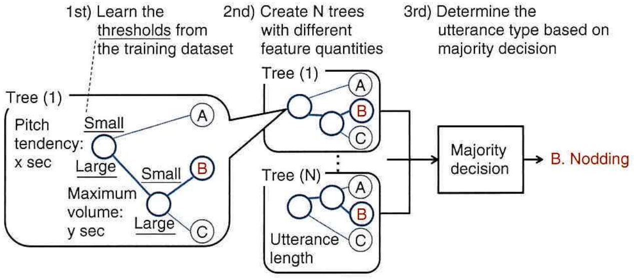

Fig. 5 Random Forest Learning and Discrimination Process

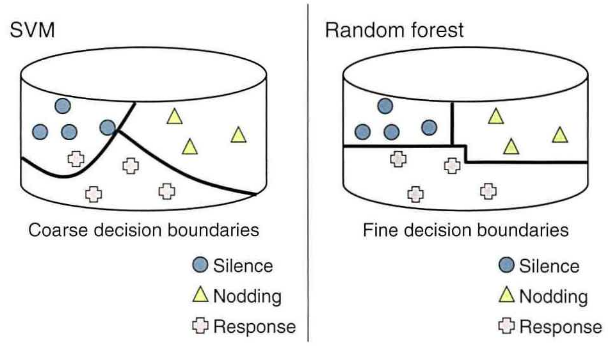

Fig. 6 Comparison of Decision Boundaries

4. Validation Experiment

This section presents the validation experiment. The evaluation data collection method, the quantitative evaluation, and the qualitative evaluation are respectively described in Sections **4.1**, **4.2**, and **4.3**.

4.1 Collection of evaluation data

Fifteen users were asked to have conversations with two types of systems (the base approach and the proposed approach). Eight users held the base approach conversation first, followed by the proposed approach conversation, while the remaining seven users held the conversations in the opposite order to remove bias due to the order of the conversations. A single conversation lasted approximately four minutes (for a total of 120 minutes).

4.2 Quantitative evaluation

The number of interruptions n (times/minute) was obtained with Equation (1), and the ratio of user utterances p_u (%) was calculated using Equation (2).

$$n = c/(t_u + t_r) \qquad (1)$$

$$p_u = 100 * t_u/(t_u + t_r) \qquad (2)$$

where,

c (times): cumulative number of interruptions
t_u (minutes): cumulative user utterance time
t_r (minutes): cumulative robot utterance time

Fig. 7 shows the average number of interruptions and average user utterance ratio for the fifteen users. Compared to the base approach, the proposed approach has a lower number of interruptions (p = 0.049 in a one-tailed t-test, 5% significance*), and a higher rate of user utterance (p = 0.045 in a one-tailed t-test, 5% significance*). In short, decreasing the number of interruptions during conversations between the user and the system is believed to have reduced discomfort and fostered proactive continued conversation.

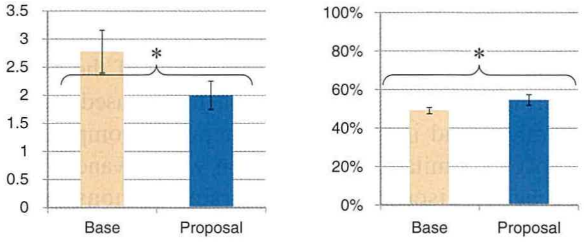

Fig. 7 Number of Interruptions and Utterance Ratio

4.3 Qualitative evaluation

After the experiment with the conversations systems, a subjective evaluation was conducted using the semantic difference method (SD) method. The evaluation asked (a) whether the robot had good utterance timing and, (b) whether the robot was a good listener. **Fig. 8** shows the results. The Wilcoxon signed-rank test was used to assign scores to (a) and (b). Although the proposed approach had a higher average score for (a), the difference could not be described as statistically significant. For (b), the proposed approach exhibited a higher score with a 1% statistical significance. This suggests that although there was no clear sense that the robot had good utterance timing, the proposed approach provided a good impression as a listener.

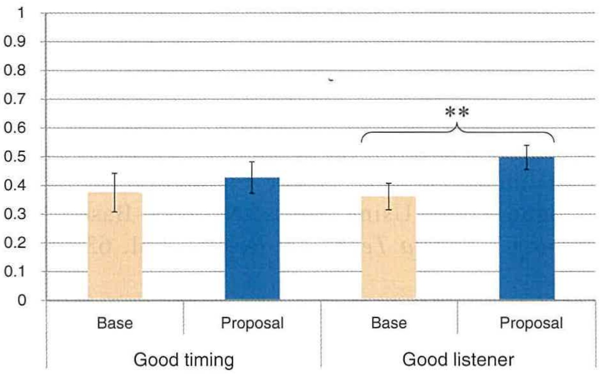

Fig. 8 SD Method-Based Subjective Evaluation Results for the Robot (Ranked from 0: Poor to 1: Good)

5. Summary and Further Development

This research focused on developing utterance type assessment technology that estimates the timing and type (silence, nodding, response) of the robot response from the user's utterance features, with the aim of creating an active listening robot that encourages proactive conversation in patients afflicted with dementia. The use of low-processing burden phoneme features and a random forest discrimination model made it possible to configure an accurate and user-friendly system despite the difficulty of acquiring conversation audio data. In addition, creating the learning dataset using the WoZ technique enabled the semi-automatic assignment of training labels and facilitated the construction of the classifier. The results of the evaluation tests confirmed that the proposed approach decreased the number of interruptions and increased user utterances compared to the base approach. Similarly, a comparison with advanced research provided better discrimination accuracy, demonstrating the validity of the proposed approach.

The next planned step is to apply the present research in the field and conduct tests to use data from conversations with patients suffering from dementia to rebuild the utterance type discrimination model.

The authors would like to extend their gratitude to Professor Joakim Gustafson, Associate Professor Gabriel Skantze, and Martin Johansson of the KTH Royal Institute of Technology in Sweden for their extensive assistance in the course of this research.

References

(1) 2016 Annual Report on the Aging Society. Cabinet Office, Government of Japan (in Japanese), http://www8.cao.go.jp/kourei/whitepaper/w–2016/zenbun/28pdf_index.html (2016).

(2) Scientific Research on Implementing Effective Support for the Care of People with Dementia (in Japanese), https://www.nri.com/~/media/PDF/jp/opinion/r_report/syakaifukushi/201503_report.pdf (2015).

(3) K. Shitaoka et al. "Active Listening System for a Conversation Robot" (in Japanese). *Journal of Natural Language Processing* Vol. 24 No. 1 (2017) pp. 3-47.

(4) N. Watanabe, Nakano. "Development of Dialogue Algorithms and Dialogue Learning Techniques for Nursing Robots." *Toyota Technical Review* Vol. 60 (2014) pp. 92-96.

(5) T. Takatani, Yamada. "Topic Estimation Technique for Dialogue Robot Using Neural-Network-Based Machine Learning." *Toyota Technical Review* Vol. 63 (2017) pp. 67-72.

(6) M. Johansson, Hori, Skantze, et al. "Making Turn-Taking Decisions for an Active Listening Robot for Memory Training." *International Conference on Social Robotics* (2016).

(7) R. Meena, Skantze, Gustafson: "A Data-Driven Model for Timing Feedback in a Map Task Dialogue System." *Proceedings of the SIGDIAL 2013 Conference* (2013) pp. 375-383.

Authors

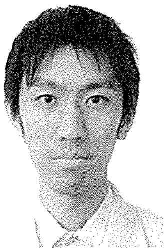

T. HORI

N. WATANABE

Particle Structural Analysis of Sulfide Solid Electrolyte

Shinya Shiotani*1
Hideyuki Yamamura*1

Abstract

The practical adoption of next-generation batteries will play an important role in the further popularization of environmentally friendly vehicles. One promising example is all-solid-state batteries, which have the potential to achieve both excellent safety performance and high energy density. Solid electrolytes with high ionic conductivity are necessary to realize high-performance all-solid-state batteries. To maximize the performance of sulfide-based solid electrolytes for all-solid-state batteries, the correlation between the internal structure and characteristics of particles must be identified to enable particle structural control. However, it has not been possible to establish an analysis method for the particle structures of sulfide-based solid electrolytes due to chemical instability and the assumption that these structures consist of a complex blend of crystals and glass. This research succeeded in quantitatively analyzing the structure of sulfide-based solid electrolytes through dark-field transmission electron microscopy (TEM).

Keywords: *all-solid-state battery, sulfide solid electrolyte, conduction mechanism, crystallization behavior, transmission electron microscopy (TEM)*

1. Introduction

1.1 Background

The development and popularization of high-performance storage batteries for environmentally friendly vehicles such as hybrid, plug-in-hybrid, and battery electric vehicles is required to help address environmental issues. One promising example is all-solid-state batteries, which have the potential to achieve both excellent safety performance and high energy density. Solid electrolytes with high ionic conductivity are necessary to realize high-performance all-solid-state batteries.

1.2 Current status and issues of solid electrolytes

Sulfide solid electrolytes with high ionic conductivity such as Li_2S-P_2S_5(1) and $Li_{10}GeP_2S_{12}$ (LGPS)(2) have already been discovered. With these electrolytes, although the crystalline phase can be precipitated by heat treatment from a glass precursor manufactured by mechanical milling, the correlation between ionic conductivity and the crystalline structure has been a matter for discussion.

Furthermore, ionic conductivity changes due to the heat treatment conditions. As an example, **Fig. 1** shows the correlation between the heat treatment conditions and ionic conductivity in LGPS and $75Li_2S$-$25P_2S_5$ (referred to as Li_3PS_4 below). Although the ionic conductivity of LGPS increases rapidly in accordance with the temperature, it increases before falling in the case of Li_3PS_4. This is because ionic conductivity is not controlled by the crystalline structure alone, and is affected by other factors, such as the size of nanocrystallites and degree of crystallization within the particles, as well as the distribution of crystals and glass. For this reason, controlling the internal particle structure is regarded as a promising means of increasing ionic conductivity. To formulate a design approach toward this objective, it is necessary to identify the correlation between the state and properties of these particles. X-ray diffraction (XRD), Raman spectroscopy, and the like have been studied as possible ways of analyzing sulfide solid electrolytes. However, these methodologies can only obtain averaged data and are not suited for particle analysis, which also requires the evaluation of distributions. Although direct observation by transmission electron microscopy (TEM) is regarded as a potentially effective means of analysis, sulfide solid electrolytes are vulnerable to electron beams and a methodology to analyze particle structures had yet to be developed.

[*1] Battery Material Engineering & Research Div., Advanced R&D and Engineering Company

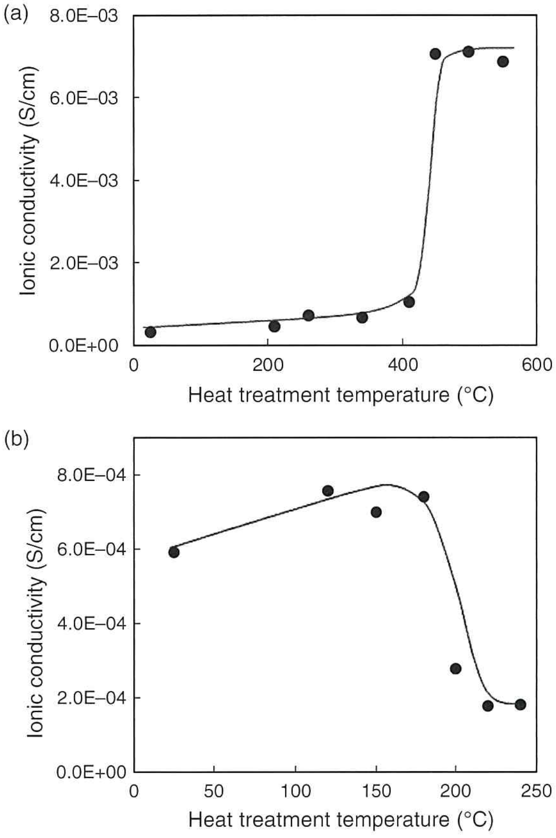

Fig. 1 Correlation between Heat Treatment Conditions and Ionic Conductivity: (a) LGPS, (b) Li_3PS_4

Therefore, this research developed a methodology capable of using TEM to evaluate the particle states (crystal/glass distribution and degree of crystallization) of sulfide solid electrolytes. Then, by using this methodology to analyze the behavior shown in **Fig. 1**, this research identified the correlation between structural changes and ionic conductivity in LGPS and Li_3PS_4, and formulated an approach for controlling the particle structure to increase ionic conductivity.

2. Proposed Structural Analysis Methodology

The main methods of observation using TEM are electron beam diffraction, high-resolution imaging, nano-electron beam diffraction, and bright field/dark field imaging. Of these, high-resolution imaging and nano-electron beam diffraction involve the acquisition of images at high magnifications or use convergent electron beams. These techniques are not regarded as suitable for sulfide solid electrolytes because electron beams unavoidably damage the sample. Therefore, the development focused on dark field imaging, which is capable of acquiring images at low magnifications and can selectively extract only crystalline components. **Fig. 2** shows an outline of observation using dark field imaging. This methodology forms images using electron beams that diffract when passing through the sample. More specifically, **Fig. 2**(b) (top view of the objective lens aperture) shows an image formed by selecting particular diffraction spots, i.e., information related to crystals. In this case, since only the regions that satisfy the diffraction conditions are shown brightly in the image, it is possible to define bright areas as crystals and dark areas as glass.

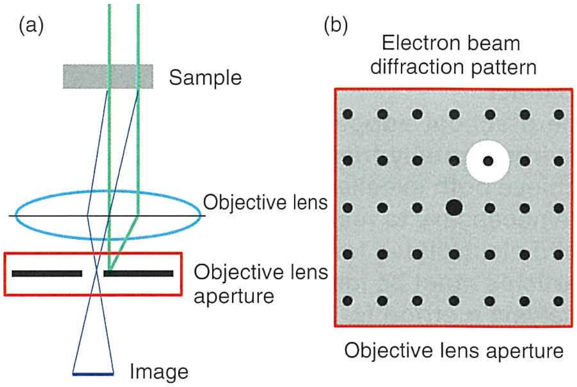

Fig. 2 Outline of Observation Using Dark Field Imaging: (a) Optical System, (b) Top View of Objective Lens Aperture

A new analysis methodology was proposed to apply this technique to sulfide solid electrolytes (**Fig. 3**). As shown in **Fig. 3**(a), multiple images are acquired of different selected spots. These images are superimposed on each other as shown in **Fig. 3**(b). This methodology is capable of obtaining images reflecting large volumes of information related to crystals, and can potentially visualize the crystal/glass distribution inside particles.

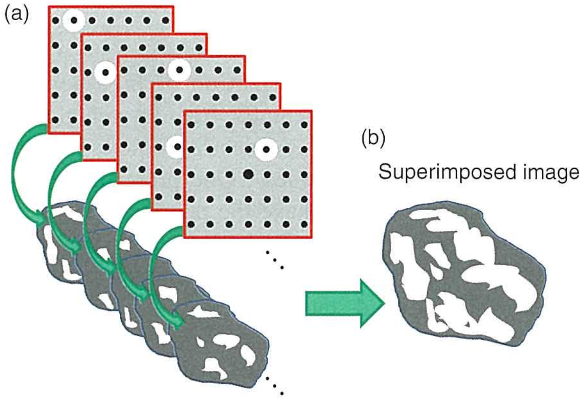

Fig. 3 Outline of Proposed Analysis Methodology: (a) Images Obtained from Multiple Spots, (b) Superimposed Image

3. Results and Discussion

3.1 Verification of structural analysis methodology

The TEM-based observation methodology was studied using a field-emission (FE) type JEM-2100F TEM system. The model material used in the study was Li_3PS_4 sintered at 240°C.

Fig. 4 shows the bright field image and the electron beam diffraction pattern obtained from each area circled in the image. The electron beam diffraction patterns shown in **Fig. 4**(b) consist of halos and spots, demonstrating that the observed areas contain a mix of crystals and glass. These results indicate that this material is suitable for the visualization of the crystal/glass distribution.

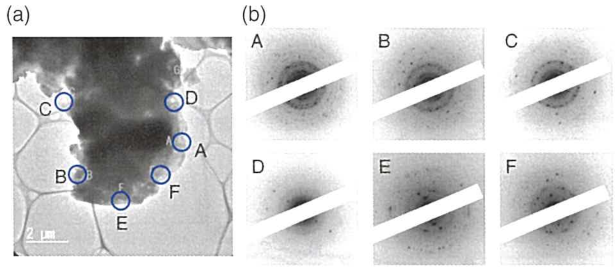

Fig. 4 TEM Observation Results of Sulfide Solid Electrolyte: (a) Bright Field Image, (b) Electron Beam Diffraction Pattern

Subsequently, analysis was carried out using the dark field imaging methodology proposed in **Fig. 3**. Obtaining and superimposing dark field images by selecting multiple spots of electron beam diffraction as shown in **Figs. 5**(a) and (b) enables the acquisition of mapping images in which the contrast of crystal areas in particles is clear (**Fig. 5**(c)). Since the bright areas of the image can be distinguished as crystals and the dark areas as glass, it was verified that the proposed methodology is an effective way of visualizing the crystal/glass distribution. Additionally, bright areas exist as masses sized between approximately 50 and 100 nm. Since this is the size of a nanocrystallite, this methodology can also be used to evaluate nanocrystallite sizes.

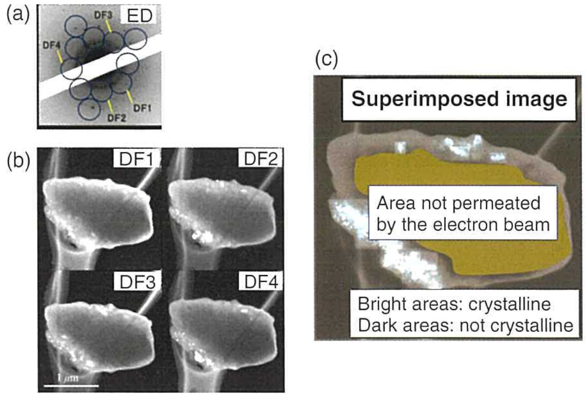

Fig. 5 Application Results of Proposed Methodology: (a) Electron Beam Diffraction Pattern and Selected Spots, (b) Dark Field Images Obtained from each Spot, (c) Superimposed Dark Field Image

The obtained mapping images were used to quantitatively study the degree of crystallization by image analysis. Since the bright pixels can be defined as crystals and other pixels as glass, the degree of crystallization χ_c can be expressed by Equation (1).

$$\chi_c = \frac{N_{pb}}{N_{pt}} \times 100 \tag{1}$$

where,

N_{pb}: number of bright pixels
N_{pt}: total number of pixels

This methodology was applied to **Fig. 6** to quantify the degree of crystallization. However, only areas (1) to (4) were studied since the shaded areas represent sample thicknesses through which the electron beam could not permeate. The table in **Fig. 6** shows the results. This analysis calculated that the degree of crystallization was approximately 60%, verifying that quantification was possible over an arbitrary area.

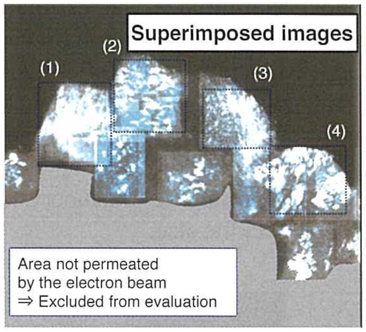

Area	χ_c (%)
(1)	62.79
(2)	53.65
(3)	60.94
(4)	70.21
Average	61.90

Fig. 6 Quantification of Degree of Crystallization from Mapping Images

3.2 Identification of crystallization behavior

The developed methodology was used to analyze structural changes during heat treatment of LGPS and Li_3PS_4. First, **Fig. 7** shows the changes in the electron beam diffraction pattern due to the sintering temperature as the analysis results for LGPS. The sintering temperature is shown in the top left of each figure. The analysis observed spots in the samples at all sintering temperatures, indicating the presence of crystals. Changes in the spots were observed from a temperature of around 410°C (the areas circled by the white dotted lines in **Fig. 7**). These indicate changes in the crystalline structure. Since previous research reported that phase transition to LGPS occurs in this temperature range,(3) it was concluded that the observed phenomenon was this phase transition to LGPS.

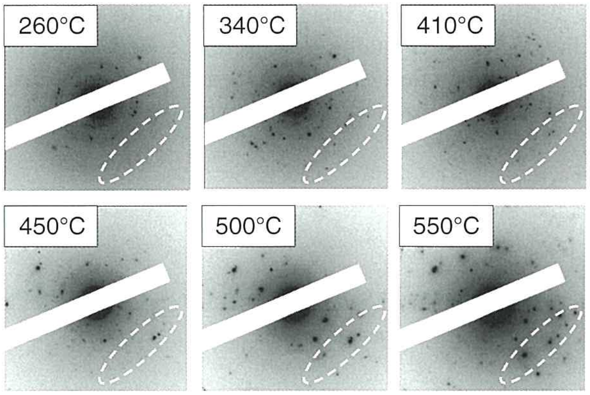

Fig. 7 Changes in Electron Beam Diffraction Pattern of LGPS due to Heat Treatment

The dark field images were observed to evaluate the crystallization behavior. **Fig. 8** shows the changes in the dark field images due to the sintering temperature. The developed methodology identified an increase in the crystal area as the temperature rose. The nanocrystallite size was estimated as being approximately 30 nm up to the phase transition (lower than 410°C) before growing to approximately 100 nm after the phase transition (around 410°C). However, the nanocrystallite did not change if the sintering temperature was increased beyond that. In other words, the crystal growth mechanism of LGPS is thought to depend on increases in the number of nanocrystallites rather than on increases in nanocrystallite size.

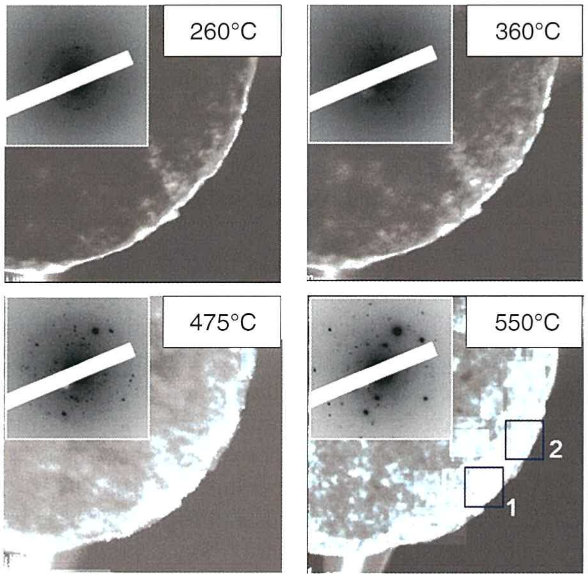

Fig. 8 Changes in Dark Field Images due to Heat Treatment of LGPS

The degree of crystallization at each sintering temperature was calculated to identify the correlation between the degree of crystallization and ionic conductivity. **Fig. 9** shows the correlation between temperature and the degree of crystallization and ionic conductivity. The rapid rise in ionic conductivity and the increase in the degree of crystallization close to 400°C coincide. In other words, the precipitated crystalline phase is a high ion-conducting phase and high ionic conductivity in LGPS is caused by crystalline phase formation and growth.

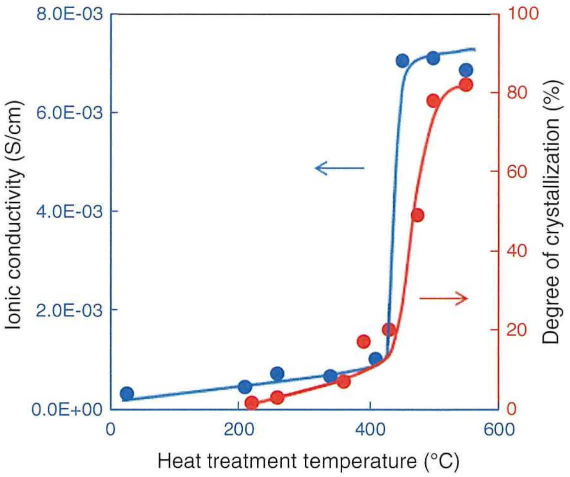

Fig. 9 Correlation between Ionic Conductivity and Degree of Crystallization of LGPS

Next, **Fig. 10** shows the changes in the electron beam diffraction pattern due to the sintering temperature as the analysis results for Li_3PS_4. Spots were observed from 180°C, confirming the occurrence of crystallization.

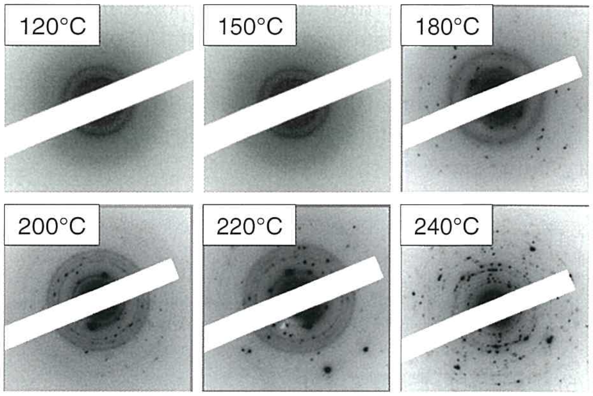

Fig. 10 Changes in Electron Beam Diffraction Pattern of Li_3PS_4 due to Heat Treatment

In the same way as the LGPS analysis, the dark field images were observed to evaluate the crystallization behavior. **Fig. 11** shows the changes in the dark field images due to the sintering temperature. As shown by the electron beam diffraction results in **Fig. 10**, slight crystallization was observed in the dark field images at 180°C. The crystal areas then increased at higher sintering temperatures.

The nanocrystallite size was estimated to be between 30 and 50 nm, regardless of the sintering temperature. In other words, it was found that the crystal growth mechanism of Li_3PS_4 also depends on increases in the number of nanocrystallites rather than on increases in nanocrystallite size.

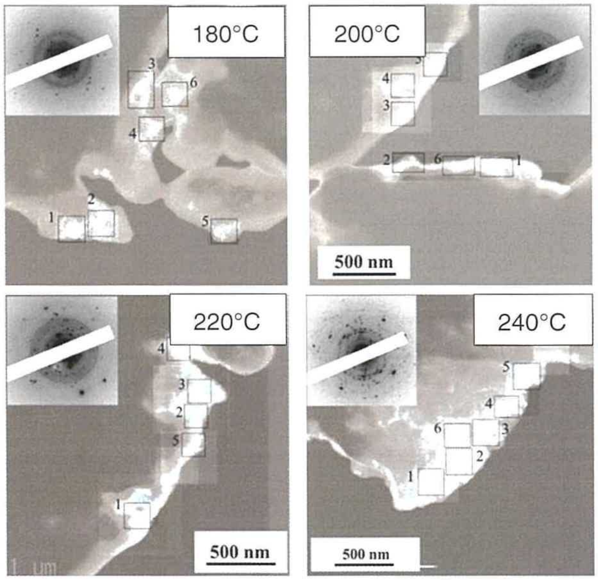

Fig. 11 Changes in Dark Field Images due to Heat Treatment of Li_3PS_4

Again, in the same way as the LGPS analysis, the degree of crystallization was calculated to identify the correlation with ionic conductivity. **Fig. 12** shows the correlation between the sintering temperature, degree of crystallization, and ionic conductivity. In the case of Li_3PS_4, the decrease in ionic conductivity coincided with the increase in the degree of crystallization. This is thought to be because the precipitated crystalline phase is a low ion-conducting phase and reduced ionic conductivity in Li_3PS_4 is caused by crystal growth. In contrast, in the sintering temperature range between 120 and close to 180°C, ionic conductivity increases slightly regardless of the formation of crystals from glass. This range cannot be explained simply in terms of crystal formation and growth. In other words, a change occurs in the internal particle conduction mechanism that leads to higher ionic conductivity. Although the causes of this phenomenon were inferred to be the following two factors, final confirmation was not possible within the limits of this research.

i) Heating causes the glass structure remaining inside the particles to change, contributing to higher conductivity.
ii) A third phase with high ionic conductivity is formed at the interface between the nanocrystallites and glass, contributing to higher conductivity.

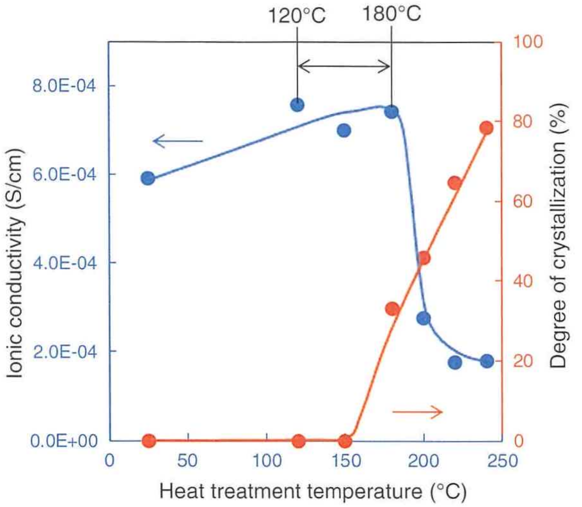

Fig. 12 Correlation between Ionic Conductivity and Degree of Crystallization of Li_3PS_4

This article has described the development of the world's first analytical technology capable of visualizing and quantitatively analyzing particle structures in sulfide solid electrolytes. This technology was used to identify the correlation between crystallization behavior and changes in ionic conductivity of LGPS and Li_3PS_4. Based on these results, the following two approaches were formulated to increase the ionic conductivity of sulfide solid electrolytes.

(1) When the precipitation crystalline phase is a high ion-conducting phase (such as LGPS), it is effective to increase the degree of crystallization of the particles, that is, to create a near monocrystalline state.
(2) When the precipitation crystalline phase is a low ion-conducting phase (such as Li_3PS_4), high ion conductivity may be achieved by controlling the remaining glass structure or by controlling the mixed crystal/glass phase state. However these control mechanisms have yet to be identified and further enhanced analytical technology will be required for future studies.

4. Conclusions

i) This research succeeded in visualizing the crystal/glass distribution and quantifying the degree of crystallization of sulfide solid electrolytes by combining TEM dark field imaging and image analysis.
ii) The correlation between crystallization behavior and conductivity of LGPS and Li_3PS_4 was evaluated and the following three points were identified.
  - The crystal growth mechanism of both LGPS and Li_3PS_4 is the same, and depends on increases in the number of nanocrystallites.

- In the case of LGPS, conductivity rises in accordance with increases in the degree of crystallization.
- In the case of Li_3PS_4, although conductivity decreases as the degree of crystallization increases, conductivity increases immediately before a rapid increase in the degree of crystallization.

Based on the these results, the following approaches were formulated for increasing ionic conductivity.

(1) Control of the degree of crystallization inside the particles
(2) Control of the glass structure or the mixed glass/crystal phase state

In addition to ionic conductivity, it should also be possible to apply the internal sulfide solid electrolyte state observation technology developed in this research to the analysis of degraded solid electrolyte structures, a phenomenon that remains unclear. As a result, this technology has the potential to greatly contribute to advancing the development of all-solid-state batteries.

Finally, everyone involved in this research would like to extend their sincere gratitude for the support provided by Professor Mori and Mr. Tsukasaki of Osaka Prefecture University in obtaining the results of this research.

References

(1) A. Hayashi et al. "Preparation of $Li_2S–P_2S_5$ Amorphous Solid Electrolytes by Mechanical Milling." *Journal of the American Ceramic Society* Vol. 84 Issue 2 (2001) pp. 477-479.
(2) N. Kamaya et al. "A Lithium Superionic Conductor." *Nature Materials* 10 (2011) pp. 682-686.
(3) S. Hori et al. "Phase Diagram of the Li_4GeS_4-Li_3PS_4 Quasi-Binary System Containing the Superionic Conductor $Li_{10}GeP_2S_{12}$." *Journal of the American Ceramic Society* Vol. 98 (2015) pp. 3352-3360.

Authors

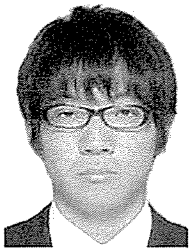

S. SHIOTANI

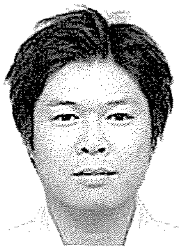

H. YAMAMURA

The New Technology Development Foundation: The 49th The Ichimura Prize in Industry for Distinguished Achievement

Research and Development of Thermo-Swing Wall Insulation Technology (TSWIN) for Engine Heat Loss Reduction

Akio Kawaguchi*1 Naoki Nishikawa*2 Yoshifumi Wakisaka*3

1. Introduction

Automakers are searching for ways to boost the thermal efficiency of internal combustion engines to help combat global warming. **Fig. 1** shows an example of the heat balance of energy generated from fuel in an engine. A large proportion of this energy escapes through the walls of the combustion chambers as cooling loss. To help reduce this loss, many studies were carried out in the 1980s into the feasibility of insulating combustion chambers using ceramic materials. However, these insulation methodologies did not provide a practical solution because the combustion chamber wall temperature would remain high at all times (see the conventional insulation line in **Fig. 2**), resulting in an elevated intake air temperature, which causes lower performance and greater emissions. Therefore, a completely new concept called Thermo-Swing Wall Insulation (TSWIN) was proposed and developed to resolve these issues.

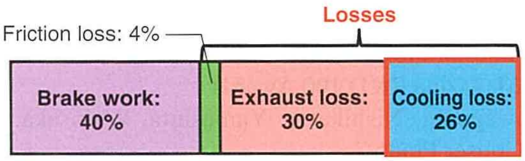

Fig. 1 Example of Engine Heat Balance

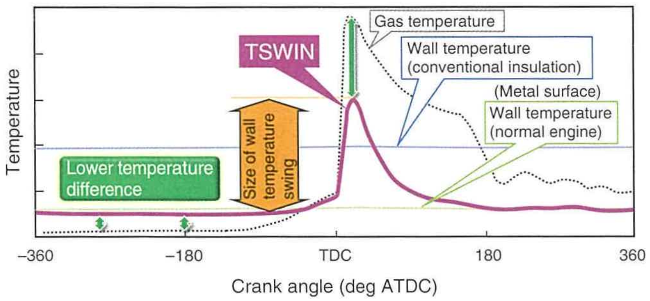

Fig. 2 Concept of TSWIN

2. Concept of TSWIN

TSWIN reduces the temperature difference between the gas and the combustion chamber walls by increasing or decreasing (i.e., "swinging") the wall temperature in accordance with changes in the gas temperature during the engine cycle. It aims to reduce cooling loss in the combustion stroke and prevent intake air heating from the walls during the intake stroke (**Fig. 2**).

3. Material Development

The insulating coating formed on the combustion chamber wall surfaces must have heat insulating properties and be capable of tracking the temperature of the gas inside the cylinder. Its thermophysical properties must include low thermal conductivity and low volumetric specific heat capacity. In other words, the coating material must contain a large proportion of voids and have an appropriate thickness. Material development focused on an anodized coating of an aluminum alloy. With this material, the voids created by crystals within the alloy can be used to increase the volume of voids compared to a conventional coating and improve the thermophysical properties. In addition, silica filler was added to the coating as reinforcement against the high stresses generated during engine operation (**Fig. 3**). The resulting newly developed coating was called Silica Reinforced Porous Anodized Aluminum (SiRPA) (**Fig. 4**).

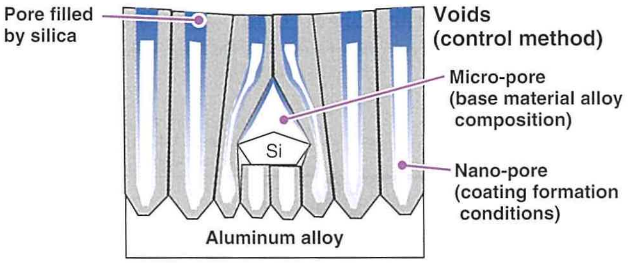

Fig. 3 SiRPA

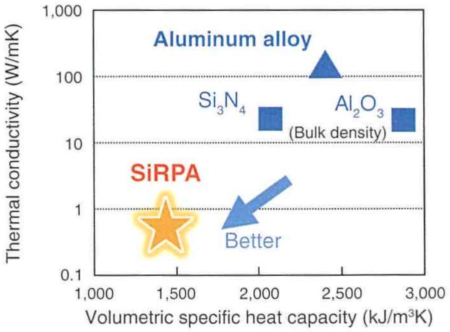

Fig. 4 Thermophysical Properties of SiRPA

---

*1 Advanced Powertrain Function Development Div., Powertrain Company

*2 Inorganic Material Engineering Div., Advanced R&D and Engineering Company

*3 Toyota Central R&D Labs., Inc.

4. Application to Diesel Engine

After forming the developed SiRPA coating on the piston surfaces of a diesel engine, the surface temperature of the coating was measured and its performance evaluated. The surface temperature of the coating was measured in an optically accessible single cylinder engine by laser-induced phosphorescence thermometry, which is capable of non-contact and rapid temperature measurement. As intended, the maximum temperature of the SiRPA coating increased to approximately 140K during combustion and decreased during the intake stroke (**Fig. 5**).

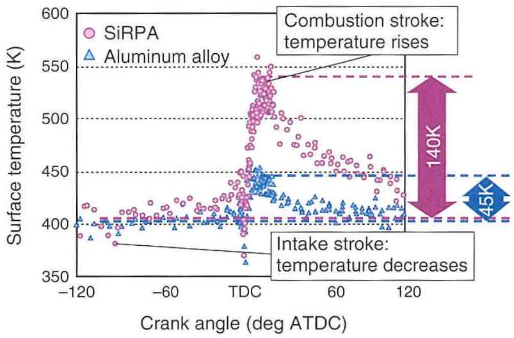

Fig. 5 Surface Temperature Measurement Results with and without SiRPA coating

Actual engine evaluations confirmed that SiRPA-coated pistons reduced cooling loss compared to normal aluminum pistons, while increasing brake work and exhaust loss (**Fig. 6**). These results verified the feasibility of the TSWIN concept under real-world engine operating conditions and confirmed that thermal efficiency increased. It was also confirmed that emissions cleared the target level with the same engine calibration regardless of whether TSWIN was adopted.

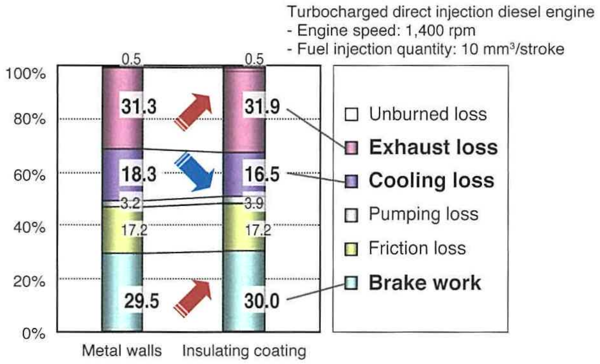

Fig. 6 Energy Balance with and without SiRPA Coating

5. Conclusion

This technology was adopted for the first time in the world in the newly developed 2.8-liter turbocharged diesel engine installed in the Land Cruiser Prado. **Photo 1** shows a piston coated with this technology.

Photo 1 Cut Model of SiRPA-Coated Piston

The authors would like to extend their sincere gratitude for the invaluable advice and support of the many people involved in this project. It is planned to adopt this technology on other engines, and to achieve further thermal efficiency gains by improving the insulating properties of the coating and expanding the area of insulation.

TSWIN has been awarded a number of prizes in addition to the Ichimura Prize in Industry. The titles of award-winning papers and the names of the authors are as follows.

◆ R&D Magazine R&D 100 Awards
A. Kawaguchi, Nishikawa, Yamashita, Wakisaka. "Toyota Land Cruiser Prado."

◆ JSME Medal for New Technology
A. Kawaguchi, Nishikawa, Yamashita, Wakisaka, Shimizu. "A Novel Cooling Loss Reduction Technique for Improving Engine Thermal Efficiency."

◆ The JSAE Technological Development Prize
A. Kawaguchi, Nishikawa, Yamashita, Wakisaka, Shimizu. "Development of Engine Cooling Loss Reduction Technology by Thermo-Swing Wall Insulation" (in Japanese).

◆ The JSAE Thesis Prize
Y. Wakisaka, Horie, Kawaguchi, Nishikawa, Yamashita. "Heat Insulation by "Temperature Swing" in Combustion Chamber Walls" (Second to Fourth Reports).

The JSAE Technological Development Prize (67th JSAE Awards)

Development of Lithium Ion Batteries for Hybrid Vehicle with World Class Fuel Efficiency

Kouichi Sato[*1] Hiroki Nagai[*2] Yasuhiro Takahashi[*2] Hiroyuki Akita[*1] Takayuki Tanahashi[*3]

1. Introduction

As the range of available fuel efficient technologies becomes increasingly diversified, the development of hybrid vehicles (HVs) is facing the challenge of meeting greater customer expectations for even higher fuel economy. To meet these expectations and to further enhance the product appeal of HVs, Toyota Motor Corporation initiated a program to develop technology capable of reducing the size of battery packs by improving the output power of lithium ion batteries (LIBs). This program focused on reducing LIB resistance as an effective means of increasing battery output power by revising the technical concept, particularly of the cathode active material, which is the predominant cause of resistance.

2. Details of Technology

A cathode active material was newly developed with hollow structural particles that reduce the resistance of each active material particle and greatly enhance the output power performance per unit area of the electrode. **Fig. 1** shows the concept of this technology, which increases output power by adopting hollow particles for the cathode active material. The cathode active material secondary particles are formed by aggregating primary particles. The primary particles are aggregated to form hollow areas in the center of the secondary particles. The aggregation of primary particles is controlled to provide through-holes that allow the electrolyte to penetrate to the center of the hollow space in the secondary particles. This enlarges the surface area of the active material exposed to the electrolyte, thereby reducing the internal resistance and increasing output power. Based on this concept, a process was developed from synthesis of the cathode active material precursor to create a hollow particle cathode active material. **Fig. 2** compares the output power characteristics of the first generation LIB, which used a conventional cathode active material, and the second generation LIB, which used the developed hollow particle cathode active material. **Table 1** lists the specifications of the developed battery. By adopting the new cathode active material, the output power per unit electrode area of the second generation LIB increased by 40%. As a result, these improved output power characteristics helped to reduce the size and weight of the second generation LIB by approximately 20% compared to the first generation LIB.

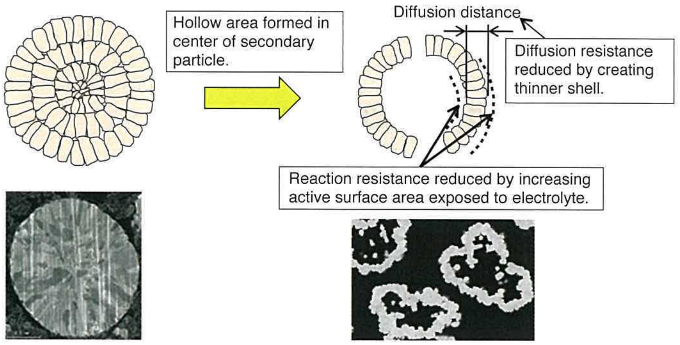

Fig. 1 Development Concept for Increasing Output Power of Second Generation LIBs by Adopting Hollow Particle Cathode Active Material

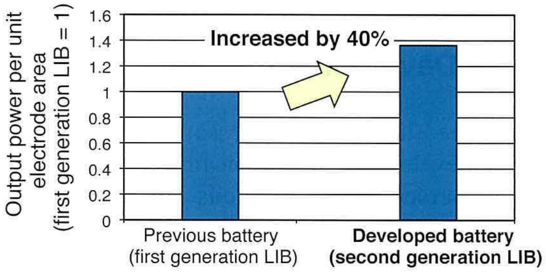

Fig. 2 Comparison of Output Power per Unit Electrode Area of First and Second Generation LIBs

Table 1 Specifications of Developed Battery (Second Generation LIB)

	Previous battery (first generation LIB)	**Developed battery (second generation LIB)**
		
Voltage (V)	3.6	3.7
Capacity (Ah)	5.0	3.6
Output power(W/kg)	2,950	3,920
Weight (g)	245	204
Dimensions (mm)	W: 111 × T: 14.1 × h: 91.8	W: 137 × T: 13.3 × h: 63.3

3. Conclusion

A hollow particle cathode active material was newly developed to increase the output power of HV LIBs. This technology enables the development of more compact batteries by increasing output power, thereby helping to improve the fuel economy and product appeal of HVs.

[*1] Battery Material Engineering & Research Div., Advanced R&D and Engineering Company

[*2] EHV Battery Design Div., Powertrain Company

[*3] Battery & Fuel Cell Production Engineering Div., Powertrain Company

67th JSAE Awards: Technological Development Award

Development of Stampable Thermoplastic Carbon Fiber Reinforced Plastic and its Application to Stack Frames

Koichiro Hayashi[*1] Koki Ikeda[*2]
Kiyoshi Hokazono[*3] Natsuhiko Katahira[*4]

1. Background and Purpose

The growing importance of reducing vehicle weight to comply with global CO_2 emissions regulations has drawn attention to carbon fiber reinforced plastic (CFRP), which has higher specific strength and specific rigidity than steel or aluminum. Until now, CFRP for automotive parts mainly consisted of thermoset epoxy resin and was subject to calls for higher productivity. The purpose of this research was to develop a stampable thermoplastic CFRP material for use in the stack frame of fuel cell vehicles (**Photo 1**).

2. Material Development

To obtain the flowability necessary to form shapes, the material was developed as a carbon fiber mat configured with randomly dispersed non-continuous fibers (**Photo 2**) and suitably loosened carbon fiber bundles. The fiber volume ratio was set to 30% to satisfy both the strength and flowability required by the part, and the fiber length was optimized. Polyamide 610 was used for the resin matrix to inhibit decreases in strength when water is absorbed at high temperatures.

Photo 1 External Appearance of Part

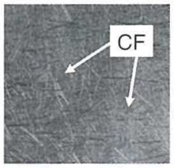

Photo 2 External Appearance of Material

3. Part Design

In addition to fulfilling part functions such as holding and protecting the fuel cells from external forces (e.g., road interference or collisions) and ensuring vehicle rigidity, the development also factored in the low fracture strain (approximately 2%) of CFRP and galvanic corrosion of steel components. As a result, the structure shown in **Fig. 1** was created, in which three layers of CFRP are bonded together to form a cardboard-like panel that is enclosed by a steel frame, with all fastening points between the fuel cell unit and the vehicle body consisting of steel members.

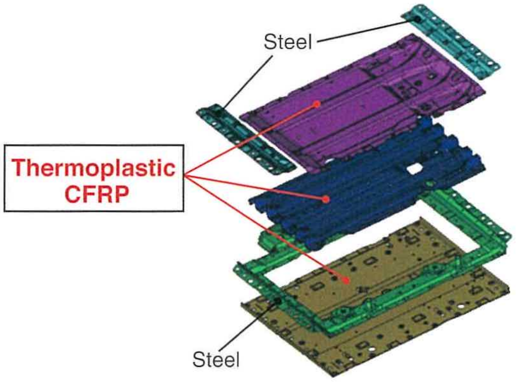

Fig. 1 Configuration of Fuel Cell Stack Frame

4. Production Engineering Development

Taking into account material strength and mass production capacity, and specifically the balance between the length of the carbon fibers and stamping time, press molding after preliminary heating of the CFRP sheets was selected as the molding method. Issues such as warpage and voids were resolved during prototyping before production began.

5. Conclusion

A stampable thermoplastic CFRP material with the potential for wider application has been developed. This world-first application to automotive parts satisfying the performance targets of the fuel cell stack frame was realized after overcoming a variety of issues. The use of thermoplastic CFRP eliminated fifteen components and achieved a weight reduction of approximately 11 kg compared to a part made only from steel.

[*1] Organic Material Engineering Div., Advanced R&D and Engineering Company
[*2] Advanced Body Technology Development Div., Advanced R&D and Engineering Company
[*3] CV Body Design Div., CV Company
[*4] Advanced Production Engineering Div., Advanced R&D and Engineering Company

The JSAE Thesis Prize (67th JSAE Awards)

In-Line Quality Monitoring System Using Multiple Regression Equation in Remote Laser Welding

Sachiko Nakajima[*1] Masaru Ochiai[*2] Atsushi Fukunishi[*1]

1. Introduction

Demand for hybrid vehicles (HVs) is increasing year-by-year as part of measures to address environmental issues. One of the key components of a hybrid system is the inverter, which converts direct current from the battery to alternating current and consists of semiconductors mounted into heat radiating modules. The module terminals and external bus bar are welded by remote laser welding, which is capable of joining these parts at high speed. To ensure a channel for large currents, the area of these welds must exceed a certain value. Therefore, a quality monitoring system that focuses on the process waveform during welding was developed to ensure that the required welding area is achieved.

2. Development of Laser Welding Monitoring

This welding procedure uses a pulse laser with a wavelength of 1,070 nm. The welding arc generated by this laser welding procedure is plasma light with a wavelength between 600 and 800 nm, and is obtained using an optical sensor circuit. When the welding quality is within normal parameters, the plasma light is strong and the voltage fluctuates greatly. An algorithm was formulated that judges welding quality by estimating the welding area from the plasma light using multiple regression analysis.

First, the factors affecting welding were identified based on the equipment and parts used, as well as from human observation. A direct relationship was then established between welding area and the plasma light wavelength by examining various levels of these factors. Subsequently, the characteristic points of the waveform were defined in accordance with welding process principles based on **Fig. 1** to completely quantify the obtained waveform.

Next, the characteristic points were converted into explanatory variables, and multiple regression analysis was carried out with the measured welding area as the target variable. During this process, each data item that adversely affected the sensitivity of the multiple regression equation was studied. For example, metallic vapor fumes that greatly distort the wavelength behavior were excluded from the area judgment, and a judgment window was created for the characteristic points. Characteristic points created by the effects of sputtering, which is defined as abnormal combustion, were also excluded from the explanatory variables. As a result, the relationship between the measured welding area and the welding area predicted by quantifying the plasma light using the multiple regression equation was found to correlate closely, with a high multiple correlation coefficient of 0.89 (**Fig. 2**).

Finally, to verify the quality judgment accuracy, test pieces were fabricated with welding areas within and outside the acceptable standard. The criterion value for welding area quality was defined as the upper limit of the welding area within a reliable range as derived using the multiple regression equation. It was confirmed that this system is capable of correctly judging the state of both the good-quality and sub-standard welding area test pieces.

The monitoring system was then incorporated into the welding equipment and applied to judge welding area quality. The plasma light wavelength is obtained using the laser irradiation signal as a trigger, and the welding area quality is judged simultaneously with the welding area calculation. It is planned to apply this monitoring technology to other process points.

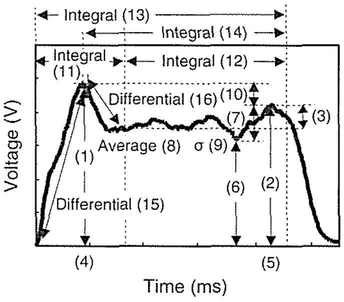

Fig. 1 Characteristic Points of Plasma Light

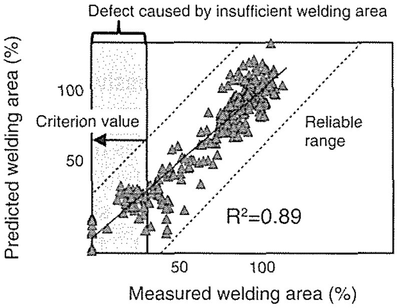

Fig. 2 Results of Multiple Regression Analysis

[*1] Electronic Components Production Engineering Div., Powertrain Company

[*2] E/E Architecture Development Div., Advanced R&D and Engineering Company

The JSAE Thesis Prize (67th JSAE Awards)

Analysis of Influence of Snow Melting Agents and Soil Components on Corrosion of Decorative Chrome Plating

Yuko Kajiyama[*1] Motohide Mori[*2] Masahiro Nakamura[*1] Tsuyoshi Sugimoto[*3]

1. Introduction

Some plastic automotive exterior parts are coated with a decorative copper-nickel-chromium (Cu-Ni-Cr) plating to create a metallic appearance. However, as the global automobile market grows, vehicle usage is expanding in Russia. In this market, chromium plating is affected by a particular type of corrosion that does not occur elsewhere, despite the presence of similar severe corrosive environments. Therefore, a study was carried out to identify the causes of this phenomenon that occurs specifically in this region. This research focused on soil components, and discovered that fulvic acid contained in the soil is one cause of this particular type of corrosion.

2. Details of Research

2.1 Particular characteristics of chromium plating corrosion in Russia

2.1.1 Mechanism and key points of chromium plating corrosion

Conventional plating corrosion is sacrificial corrosion that occurs at the bottom Ni layer before the surface Cr layer. However, the corrosion that occurs in Russia affects the Cr layer first. This research aimed to identify the causes of this particular Russian phenomenon.

2.1.2 Survey of environmental characteristics in Russia

This research focused on soil components. Soil types in Russia were found to have all three properties regarded as having an impact on corrosion: organic components, high ion exchange properties, and a highly acidic nature. After analyzing all the soil components and investigating each type of acid found in the soil, the research focused on corrosive organic fulvic acid, which interacts particularly strongly with metals.

2.2 Estimation of corrosion mechanism

2.2.1 Changes caused by fulvic acid to passivation film

The electric potential of Cr/Ni plating was measured inside and outside a saturated solution containing 11 mass% of fulvic acid (the same concentration as that found in soil in Russia) and calcium chloride (a snow melting agent). From the results, it was estimated that Cr formed a compound with the fulvic acid, and that this compound attached to the surface of the Cr and corroded the passivation film (**Fig. 1**).

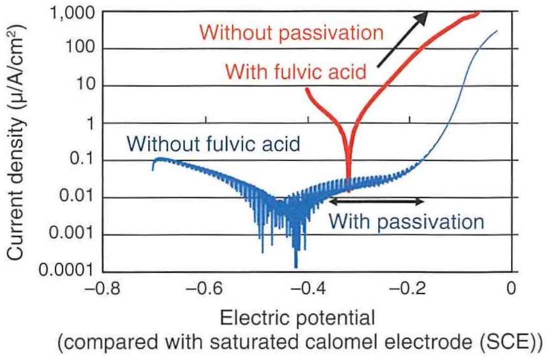

Fig. 1 Polarization Curve of Chromium Plating

2.2.2 Elimination of sacrificial corrosion effect of Ni by fulvic acid

Fulvic acid was gradually added to a saturated calcium chloride solution up to a concentration of 20 mass%. The natural electric potential of Cr and Ni was then measured under the different acid concentrations. The research confirmed that the difference in potential between Cr and Ni disappeared at a fulvic acid concentration of 10 mass% or higher (**Fig. 2**).

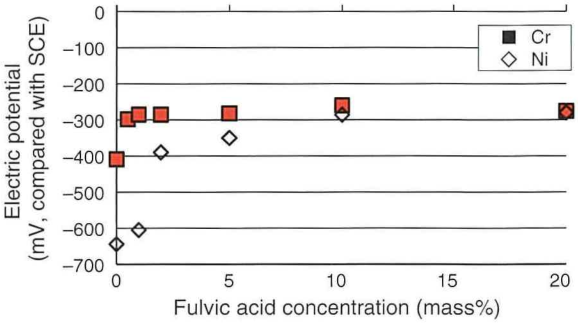

Fig. 2 Changes in Cr/Ni Electric Potential due to Fulvic Acid Concentration

For these two reasons, it was presumed that fulvic acid is the cause of the particular corrosion occurring in Russia.

3. Conclusion

This research examined the reasons for the particular corrosion of decorative chromium plating that only occurs in Russia. Through geological surveys and other investigations outside the field of corrosion, this research identified interaction between the fulvic acid in the soil and a snow melting agent as the mechanism causing this corrosion.

[*1] Organic Material Engineering Div., Advanced R&D and Engineering Company
[*2] Inorganic Material Engineering Div., Advanced R&D and Engineering Company
[*3] Material Platform Engineering Div., Advanced R&D and Engineering Company

Best Poster Paper Presentation Award at 2016 Annual Congress of
Society of Automotive Engineers of Japan, Inc.

Development of Highly Durable Fuel Cell Stack for New FCVs

Michito Norimoto*1 Hideki Kubo*1 Seiji Mizuno*1

1. Introduction

For its new mass-production fuel cell vehicles (FCVs), Toyota Motor Corporation took on the challenge of developing a fuel cell (FC) stack with the following characteristics, based on the approach of simplifying the FC system to reduce size and cost: (1) the world's first capability to generate power without a humidification system and (2) a substantially lower amount of precious metals by reducing the platinum (Pt) in the electrocatalyst by two-thirds and eliminating the gold (Au) plating surface treatment of the separator.

This FC stack has a world-class power density of 3.1 kW/L, and can be installed under the seats of a sedan-type FCV (**Fig. 1**). This article focuses on the measures adopted for (1) humidifier-free operation and (2) reducing the amount of Pt while ensuring the durability and maintaining the power of the FC stack.

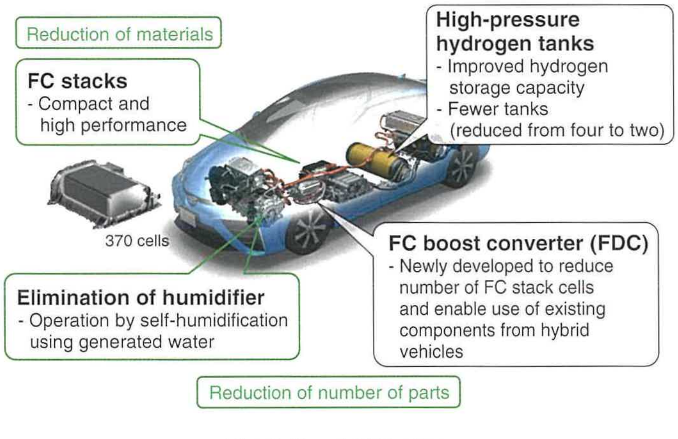

Fig. 1 New FC System

2. Maintenance of Power Level with Humidifier-Free Power Generation

One issue with a humidifier-free system is the concentration of hydroxyl (OH) radicals formed during power generation in the cells of the stack. These radicals cause sulfonic acid to be released from the electrodes and adversely affect power generation performance. The following countermeasures were adopted to address this issue: (1) reduce the thickness of the electrolyte membrane, (2) increase the amount of hydrogen circulation, and (3) flow the hydrogen and air in counter directions (opposing flows). These measures enhanced the self-humidification function of the stack and reduced the concentration of radicals at the air inlet, which is strongly susceptible to drying, without relying on an external humidifier or other humidification system. **Fig. 2** shows the power generation performance and resistance distribution with and without these countermeasures.

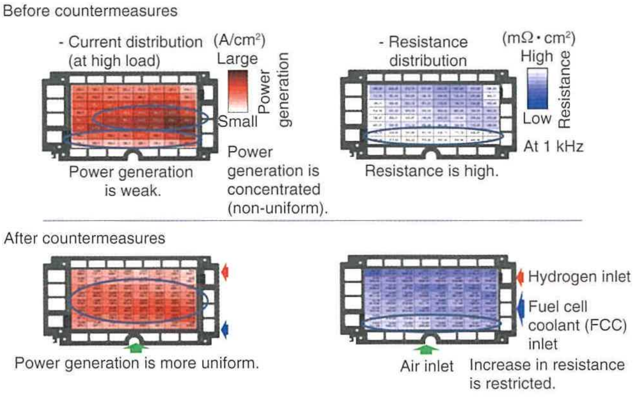

Fig. 2 Cell Current Distribution and Resistance Distribution after Power Generation Durability Test

3. Maintenance of Power Level with Reduced Pt Amount

Power is reduced by the dissolution of Pt particles, which occurs due to potential fluctuations and at high potentials when the FC system is started up, stopped, and during driving. When dissolution occurs, catalytic activity decreases as the Pt particle size increases, which increases the oxygen diffusion resistance and causes power to drop. Although dependent on how the FCV is used, this accounts for approximately 70% of power reduction in an FCV, and is the main cause of power deterioration.

During a power generation durability test, lowering the Pt content of the catalyst increased the oxygen diffusion resistance and led to further decreases in power. In response, a solid carbon catalyst support was adopted that maintains the Pt catalyst close to the carbon surface layer. This configuration helps the Pt catalyst to contribute more strongly to power generation (**Fig. 3**) and achieves approximately the same power drop characteristics with one-third the amount of Pt.

---

[1] Fuel Cell System Engineering & Development Div., Powertrain Company

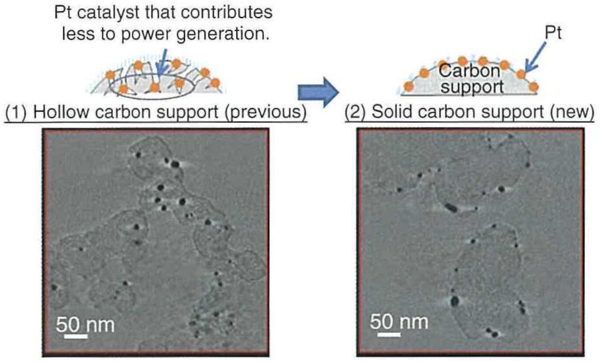

Fig. 3 State of Electrocatalyst Support

4. Conclusion

The FC stack countermeasures described above, and the adoption of an operation method that lowers the upper voltage limit while driving to avoid high potential states, helped to reduce the power drop in a system bench durability test by two-thirds compared to the previous model, thereby ensuring sufficient durability for mass production.

Best Poster Paper Presentation Award at 2016 Annual Congress of Society of Automotive Engineers of Japan, Inc.

Study of Enhancing the Ride Down Effect in Side Impacts

Masato Kunisada[*1] Hiroyuki Nagura[*2] Osamu Fukawatase[*3]
Takashi Hasegawa[*4] Hitoshi Kondo[*1]

1 Introduction

When a side impact occurs, the vehicle has little space in which to absorb the impact energy. Unlike in frontal impacts, the ride down effect, which helps mitigate injuries by transferring some of the kinetic energy of the occupants to the vehicle, has yet to be utilized in side impacts. However, the utilization of this effect is becoming more feasible as high-strength vehicle bodies and faster sensing technologies are adopted. As pre-collision sensors are becoming more widespread, this study provisionally calculated the ride down effect when pre-collision sensors are adopted for side impacts, as well as the injury-mitigation benefit of the ride down effect in real-world traffic accidents.

2. Details of Technology

2.1 Application of pre-collision sensors to side impacts

An effective means of mitigating injury by enhancing the ride down effect in a side impact is to constrain the vehicle occupants continuously and securely from a point in time before the collision occurs. This study proposed a system consisting of multiple occupant restraint devices, including a device activated by pre-collision signals (**Fig. 1**).

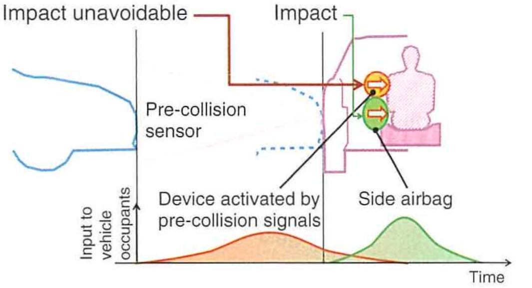

Fig. 1 Side Impact with Operation of Pre-Collision System

2.2 Ride down effect

A spring-mass model was used to simulate this occupant restraint system, which combines a device activated by pre-collision signals that operates continuously from before to immediately after the collision, and a side airbag that is activated by the impact of the collision. According to this model, the external force applied to the occupant was reduced by 17% and the ride down effect was 32% (**Fig. 2**). Furthermore, an equivalent occupant protection performance was obtained even when the impact speed was increased by 20%.

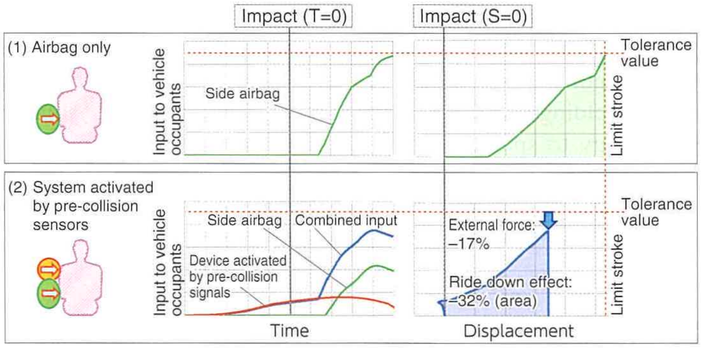

Fig. 2 Impact of Pre-Collision System on Simulated Wavelengths

3. Estimation of Injury Mitigation Effect

The number of severe or fatal injuries was calculated using a probability curve based on logistic regression analysis of side impact accident data. This calculation found that the maximum number of severe or fatal injuries was 0.7 when the vehicle was equipped with a system activated by pre-collision sensors, compared with 1 with only a side airbag. In other words, this system has the potential to help reduce the number of severe or fatal injuries caused by side impact accidents by a maximum of approximately 30% (**Fig. 3**).

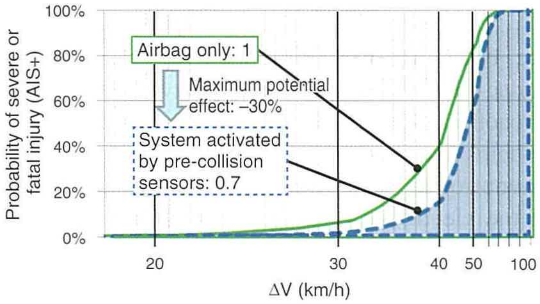

Fig. 3 Estimation of Injury Mitigation Effect

4. Conclusion

This study found that pre-collision sensors have the potential to help further mitigate injuries caused by side impacts. In anticipation of the wider adoption of side radars in automated driving systems, the results of this study should help to encourage the wider adoption and popularization of pre-collision safety systems.

[*1] Vehicle Engineering Development Div., Advanced R&D and Engineering Company
[*2] MS Vehicle Evaluation & Engineering Div., Mid-size Vehicle Company
[*3] Advanced Body Technology Development Div., Advanced R&D and Engineering Company
[*4] Advanced Safety Performance Engineering Div., Advanced R&D and Engineering Company

2016 JSME Medal for New Technology

Vehicle Frame Development Using Laser Screw Welding with Circular Scanning Method

Norimasa Koreishi*1 Junichiro Makino*2 Shuhei Ogura*2 Koushi Kumagai*3 Minghuang Cheng*3

1. Introduction

Spot welding accounts for most of the joints in a body in white (BIW), which forms the foundation of vehicle performance. However, the shunt current limits the number of spot welding joints that can be applied, which makes it difficult to fully utilize the strength and rigidity of the frame members. Therefore, laser screw welding (LSW) was developed as an alternative joining technology to spot welding. This is a joining technology that overcomes the major laser welding issue of sheet gap tolerance, and is capable of increasing the number of joints and welding application range while also improving productivity.

2. Outline of Technology

2.1 Development of laser welding process

The LSW process allows metallic zinc vapor to escape by scanning the laser in a circle and carefully agitating the molten steel through the correct welding conditions. This process achieves stable weld quality regardless of the presence of a sheet gap (**Fig. 1**). LSW allows laser welding to be applied widely throughout the BIW and makes a more positive contribution to vehicle performance than conventional laser welding.

2.2 Development of BIW using LSW

2.2.1 Innovation of BIW structure

Unlike conventional spot welding, LSW can create concentrated joints with a short pitch between welds. Adopting this approach in areas of the BIW that absorb high force in a collision helps to enhance passive safety.

In conventional spot welding, the weld has to be placed between the electrodes of the welding gun. Therefore, some locations of the BIW cannot be joined by this method. In contrast, as shown in **Fig. 2**, LSW can be applied to areas of the BIW with closed cross-sections. This enables the design of continuous structures in the BIW without any loss of productivity.

2.2.2 Innovation of welding process by high-speed joining

LSW is a faster process than spot welding, requiring between 0.3 and 0.8 seconds per weld. Replacing spot welding with LSW can shorten the welding process by 40% (**Fig. 3**).

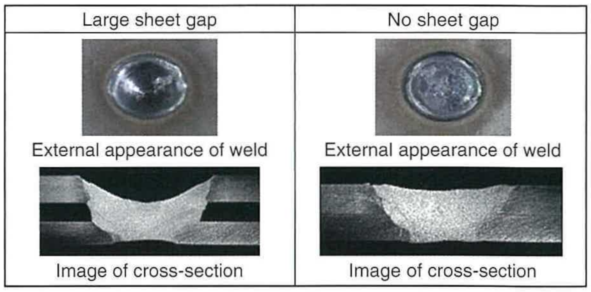

Fig. 1 Comparison of Weld Quality with Different Sheet Gaps

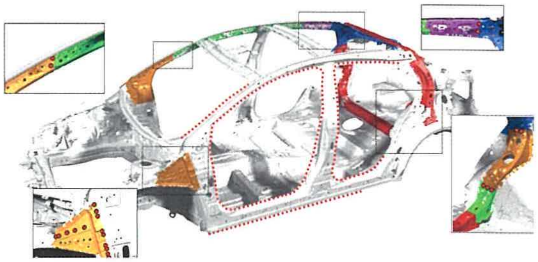

Fig. 2 Example of Areas of BIW Adopting LSW

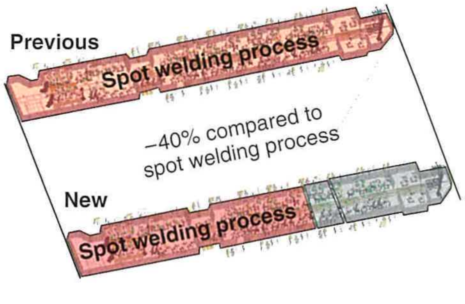

Fig. 3 Comparison of New and Previous Welding Processes

3. Conclusion

LSW is the world's first laser welding technology to overcome the issue of sheet gap tolerance and be applied to mass production, successfully satisfying requirements related to both productivity and performance. Toyota Motor Corporation intends to expand the number of models using LSW and to actively further enhance vehicle performance.

[*1] Advanced Body Technology Development Div., Advanced R&D and Engineering Company

[*2] MS Body Assembly Engineering Div., Mid-size Vehicle Company

[*3] Advanced CAE Div., Advanced R&D and Engineering Company

2016 JSME Medal for Outstanding Paper

Verification of Micro Pitting Formation Mechanism Considering Frictional Force at Gear Tooth Mesh Surface of Power Transmission Gears

Yuko Yasue[*1] Seiji Hiroshima[*2]
Yasushi Hayashida[*2] Susumu Matsumoto[*3]

1. Introduction

1.1 Issues of micro pitting design

Important development requirements for automotive transmissions include reducing weight and increasing transmission efficiency. However, decreasing the size of the gears to reduce weight increases the contact pressure on the gear face. Additionally, reducing lubricant viscosity to lower lubricant churning loss results in thinner oil films, creating severe lubricating conditions. These conditions have the potential to generate micro pitting. Micro pitting consists of collections of extremely small cracks that appear as a clouded finish on gear faces. This phenomenon may generate abrasion that worsens gear noise.

Various parameters have been proposed for application to micro pitting design, including the lubricating conditions and flash temperature of the gear face. However, these parameters are difficult to adopt in actual design methodologies due to unclear physical evidence and a lack of verification with respect to limit values for individual gear specifications.

1.2 Approach to resolve issues of micro pitting design

Clear sliding marks and extremely small cracks can be observed on gear faces affected by micro pitting. Since these phenomena are thought to be caused by frictional force between contact surfaces, it was necessary to measure the frictional forces occurring on a gear face to identify the factors directly affecting micro pitting. To verify the accuracy of this approach, micro pitting was generated under laboratory conditions. The distribution of this micro pitting was then compared with the theoretical distribution of frictional force generated on the gear face.

2. Verification of Micro Pitting Formation Mechanism

2.1 Test method and calculation of gear face frictional force

Five test specimens were prepared respectively of two types of gears and micro pitting was formed on each specimen.

The distribution of frictional force on the gear face was calculated using the method devised by Kubo and Umesawa. The value calculated using Matsumoto's formulae was adopted for the friction coefficient.

2.2 Comparison of micro pitting and frictional force distribution

Fig. 1 shows a photograph of micro pitting on a gear face and an example of the comparison with the results of the frictional force distribution calculation.

The area of micro pitting highlighted by the orange lines on the photograph matches the area of frictional force shown by the black lines in the frictional force calculation results. This confirms that micro pitting occurs in areas of high frictional force. It was also confirmed that the minimum frictional force in the areas in which micro pitting occurred on other gears was virtually the same, thereby verifying the existence of a frictional force value that results in micro pitting.

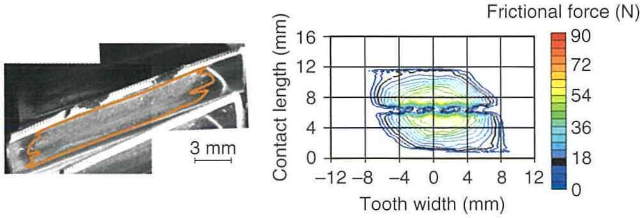

Fig. 1 Gear Face with Micro Pitting and Frictional Force Calculation Results

3. Conclusions

Experimental verification results confirmed the hypothesis that micro pitting occurs in areas of high frictional force, and identified a limit value for that force. These results demonstrated that the frictional force generated on a gear face can be applied to design methodologies for micro pitting without causing physical inconsistencies.

[*1] Drivetrain-EHV Design Div. No. 2, Powertrain Company
[*2] Drivetrain-EHV Design Div. No. 3, Powertrain Company
[*3] Waseda University

2016 Energy Conservation Grand Prize (Minister Prize of Economic, Trade and Industry)
of the Energy Conservation Center, Japan

Hybrid Technologies for the New Prius

Mitsumasa Fukumura[*1] Shunsuke Fushiki[*1] Michitaka Tsuchida[*1] Keiji Takizawa[*2]
Takaji Kikuchi[*3] Takanori Kumagai[*4] Koichiro Muta[*5]

1. Introduction

As the standard bearer for environmentally friendly and hybrid vehicles (HVs), advanced performance and unsurpassed fuel economy are indispensable attributes of the Prius. These requirements are satisfied primarily through hybrid system technologies.

A smaller, lighter, and more efficient next-generation hybrid system (**Fig. 1**) was developed for the fourth generation Prius. This article introduces the component parts of this system.

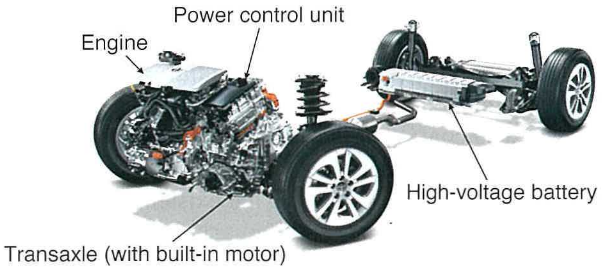

Fig. 1 Hybrid System of the Fourth Generation Prius

2. Details of Hybrid Technologies

Engine: a maximum thermal efficiency of 40% was achieved by improving combustion with a redesigned intake port shape and improved exhaust gas recirculation rate, and by adopting low-friction items in each component part.

Transaxle: the length of the transaxle was shortened by 47 mm and the mechanical loss reduced by approximately 20% by adopting a dual-axis structure for the motor and generator and a parallel axis layout for the motor speed reduction device.

Motor: copper loss was reduced by adopting a segment coil winding structure for the stator and optimizing the coil winding. Additionally, loss and weight were decreased by 20% respectively by developing magnetic steel sheets and a core structure that reduced iron loss and high-frequency loss.

Power control unit: loss was reduced by approximately 20% and volume by approximately 33% due to the development of new power semiconductors and the optimization of the cooling structure and high-voltage system wiring structure.

High-voltage battery: the size of the battery was reduced by 10% by refining the contact materials and case structure, as well as by expanding its charge/discharge performance.

Electronic four-wheel drive (4WD) system: a more fuel efficient 4WD system was achieved by adopting an induction motor and greatly reducing the drag loss that is a characteristic feature of 4WD systems.

Control system: various refinements were incorporated to maximize the performance of each component, such as expanding the vehicle speed range in which the engine can be stopped, and optimizing the voltage boosting control. These control refinements contributed one-quarter of the gains in vehicle fuel economy.

3. Conclusions

The fourth generation Prius achieved impressive environmental performance, as typified by its fuel economy of 40.8 km/L under the Japanese JC08 test cycle.

Fig. 2 Generational Improvements in Fuel Economy of the Prius

The development of a fuel-efficient electronic 4WD system also helped to expand the appeal of environmentally friendly vehicles to new markets.

[*1] Powertrain Product Planning Div., Powertrain Company
[*2] Drivetrain-EHV Design Div. No. 1, Powertrain Company
[*3] EHV Electricity Converter Design Div., Powertrain Company
[*4] Toyota Motor Engineering & Manufacturing (China) Co., Ltd.
[*5] Electric Powertrain System Development Div., No. 1, Powertrain Company

2016 Presidential Award for Patented Inventions

Seat Structure Having a Side Impact Air Bag Apparatus

Japanese Patent No. 3345279

Hisaaki Kato*1 Mitsuyoshi Ohno*2

1. Background of the Invention

Various countermeasures have been taken to better protect vehicle occupants against impacts occurring at the side of the vehicle (referred to below as simply "side impacts").

As one example, a structure in which a side impact air bag apparatus is incorporated into the side of a front seat of a vehicle has been developed in recent years. However, in this conventional structure, when a relatively easy-to-stretch material such as knit or the like is used for the surface layer of the seat back, the surface layer greatly stretches outwardly in the transverse direction of the seat in the initial stage of air bag deployment. As a result, the sewn portion to be broken, which is formed by a sewing thread, becomes hard to break. Consequently, the speed of air bag deployment slows down and the deployment shape becomes unstable.

2. Overview of the Invention

Fig. 1 is a perspective view that shows the structure of a seat with the side impact air bag apparatus described by this invention.

Fig. 2 is a horizontal cross-sectional view showing a side portion of the seat structure. A sewn portion, which is formed by sewing together the front terminal portion of the seat back side surface layer and the outer terminal portion of the front side surface layer, is positioned in the vicinity of the front side of the front edge of the air bag case lid. When the air bag deploys, the sewn portion is broken by the lid.

In addition, a cotton cloth is provided at the inner side of the seat back side surface layer as a hard-to-stretch fabric. The front terminal of this cotton cloth is sewn onto the sewn portion, and the rear terminal is connected to the fixing member on the seat side.

When the inflator of the air bag apparatus is activated by a side impact, the air bag is inflated by the flow of gas injected from the inflator. The air bag case lid is then pushed and opened in the direction indicated by arrow A in **Fig. 2**. When this occurs, the stress that pushes and opens the air bag case lid is concentrated at the sewn portion through the cotton cloth. Therefore, the sewn portion is instantaneously broken as indicated by the two-dot chain line in **Fig. 2** and the air bag deploys immediately.

Fig. 1 Seat Structure

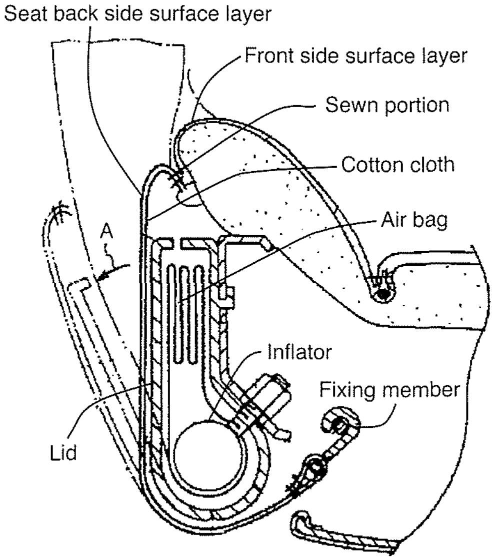

Fig. 2 Horizontal Cross-Sectional View of Side Portion

3. Effects of the Invention

This invention allows the side impact air bag to deploy promptly and smoothly.

[*1] Vehicle Engineering Development Div., Advanced R&D and Engineering Company

[*2] Advanced Body Technology Development Div., Advanced R&D and Engineering Company

2016 Presidential Award for Patented Inventions

Master Cylinder Device and Hydraulic Brake System Using the Same

Japanese Patent No. 5626414

Hiroshi Isono*1

1. Background of the Invention

As shown in **Fig. 1**, some conventional master cylinder devices include a pressure receiving piston, which is moved forward by the pressure of brake fluid introduced into an input chamber from a high pressure source, and an input piston, which is fitted in a rearward opening blind hole of the pressure receiving piston and which is moved forward by brake operation. In this type of conventional device, an inter-piston chamber is formed between the bottom portion of the blind hole and the front end face of the input piston, which enables the pressure receiving piston and the input piston to move independently from each other. However, in this master cylinder device, when the pressure receiving piston is moved by the high-pressure brake fluid, a seal between the pistons generates frictional force. This generates a force that causes the input piston to move, which has an adverse effect on brake operation feeling.

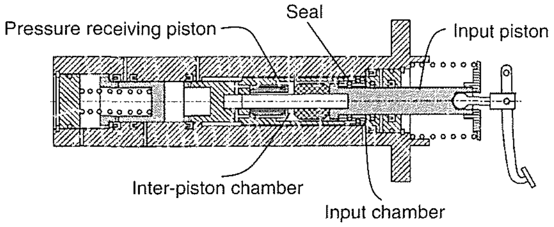

Fig. 1 Conventional Master Cylinder Device

2. Overview of the Invention

Fig. 2 shows a hydraulic brake system including the master cylinder device described by this invention.

The housing of the master cylinder device includes a partition portion, which separates the interior of the housing into a front side chamber and a rear side chamber, and has an opening that passes through it. The pressure receiving piston includes a flange formed at the rear end. The main body of the pressure receiving piston is fitted in the housing with seals at the flange and at a portion in front of the flange, and the pressure receiving piston is also fitted in the partition portion of the housing with a seal. Through this configuration, the pressure receiving portion consists of: (1) a pressurizing chamber located in front of the main body portion of the pressure receiving piston for the brake fluid to be supplied to the brake device, (2) an input chamber located between the rear end of the main body portion and the partition portion, into which the brake fluid from the high pressure source is introduced, and (3) an opposing chamber located around the main body, which opposes the input chamber and has the flange interposed between it and the input chamber.

The master cylinder device described by this invention includes an inter-piston chamber between the input piston and pressure receiving piston, which faces both pistons. Since this device is provided with seals between the input piston and housing, the input piston and the pressure receiving piston are therefore not fitted to each other with any seal.

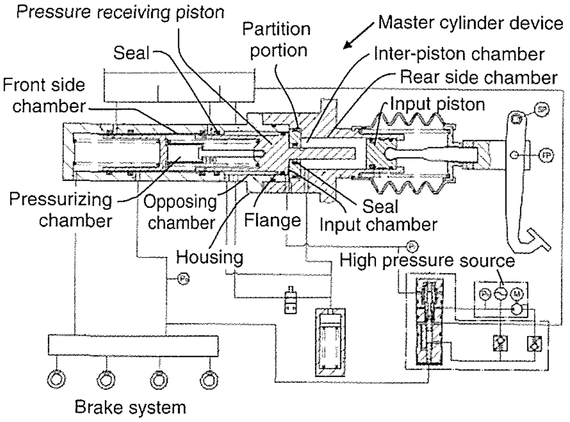

Fig. 2 Hydraulic Brake System

3. Effects of the Invention

In the master cylinder device described by this invention, the input piston is not fitted to the pressure receiving piston by any seal. Therefore, no force generated by the friction of a seal is applied to the input piston, even when the pressure receiving piston is moved by the brake fluid in the input chamber. As a result, this invention enables excellent brake operation feeling because drag is not applied to either the input piston or the brake pedal by the movement of the pressure receiving piston.

---

[1] Technology Development Management Div., Advanced R&D and Engineering Company

TOYOTA Technical Review

Back Number Index

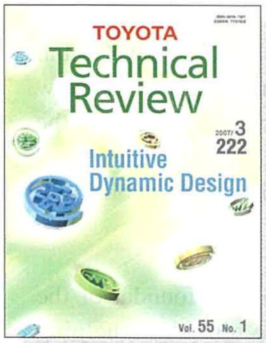

Vol. 55 No. 1 (2007)
Special Feature:
Intuitive Dynamic Design

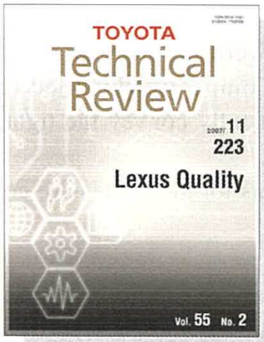

Vol. 55 No. 2 (2007)
Special Feature: Lexus Quality

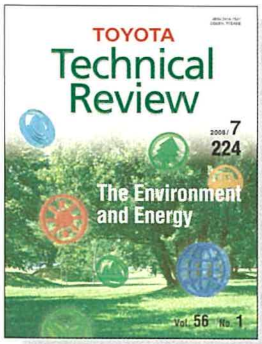

Vol. 56 No. 1 (2008)
Special Feature:
The Environment and Energy

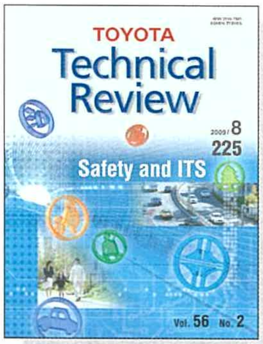

Vol. 56 No. 2 (2009)
Special Feature: Satety and ITS

Vol. 57 No. 1 (2010)
Special Feature: Prius

Vol. 57 No. 2 (2011)
Special Feature:
Next-Generation Electric Storage
and its Applications

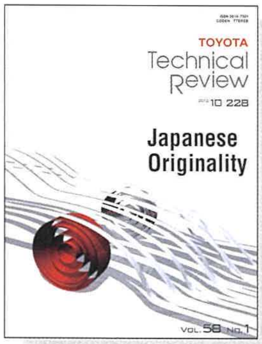

Vol. 58 No. 1 (2012)
Special Feature:
Japanese Originality

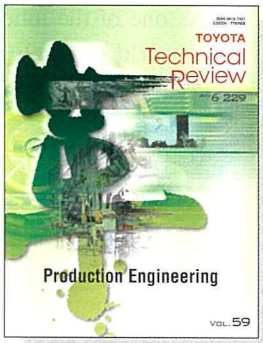

Vol. 59 (2013)
Special Feature:
Production Engineering

Vol. 60 (2014)
Special Feature: Powertrain

Vol. 61 (2015)
Special Feature 1: The Mirai FCV
Special Feature 2: ITS and
Advanced Driving Support Systems

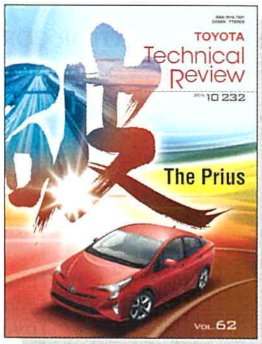

Vol. 62 (2016)
Special Feature: The Prius

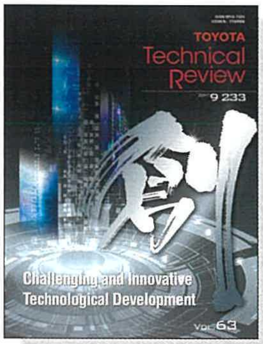

Vol. 63 (2017)
Challenging and Innovative
Technological Development

¥3,024 (excluding tax: ¥2,800)

Distributor: Ohmsha, Ltd.
Tel: 81-3-3233-0641
https://www.ohmsha.co.jp/magazine/partners_magazine.htm

Thank you for reading the *Toyota Technical Review*. It is my pleasure to present Volume 64, which is the 234th edition of the *Toyota Technical Review* since its publication began.

Constantly keeping in mind that a better approach exists, and to further promote the creation of ever-better cars and the training and nurturing of personnel, Toyota introduced the business unit system in 2013 and established in-house companies in 2016, thereby implementing a major adjustment of the development framework from one centered on functions to one focused on products.

The special feature of this edition introduces the powertrain technologies of the Toyota New Global Architecture (TNGA) developed by the Powertrain Company, which led the transition into the new development framework. I hope that these articles will fully convey the tight collaboration between the engineering and production divisions during development.

I would like to express my sincere gratitude to the authors for their extensive cooperation in the publication of this edition of the *Toyota Technical Review*.

Last year was a milestone marking the 150th anniversary of the birth of Sakichi Toyoda, founder of the Toyota group. In retracing his footsteps, I realized that, having resolved to dedicate himself to helping society through his inventions, Sakichi followed through on his conviction that a product should never be sold unless it has been carefully manufactured and fully tested in commercial trials. He spent 30 some years perfecting Toyota's non-stop automatic shuttle change loom (the Type G automatic loom), which offered the best performance in the world at the time.

As one of the inheritors of Sakichi's legacy, I feel a renewed responsibility to play a part in invigorating real-world research and development through the introduction of new technologies. I hope that you will continue to read these articles with interest.

(Publisher: Matsumoto)

TOYOTA Technical Review Vol. 64

Publisher's Office	Technical Administration Div. TOYOTA MOTOR CORPORATION 1 Toyota-cho, Toyota, Aichi, 471-8572 Japan 81-565-28-2121 (Operator)
Publisher	Yasushi Matsumoto
Editor	Taku Kosaka Technical Operations Dept., Toyota Office Toyota Enterprise Inc.
Printer	Sasatoku Printing Co., Ltd. Owaki 7, Sakae-cho, Toyoake, Aichi, 470-1196 Japan
Distributor	Ohmsha, Ltd. 81-3-3233-0641 (Operator) http://www.ohmsha.co.jp/index_e.htm
Published	September 19, 2018

Printed on recycled paper.

The Summer Triangle asterism and Milky Way rising above the Shirabiso highlands in Nagano Prefecture

TOYOTA Technical Review

2018/9
VOL.64 234

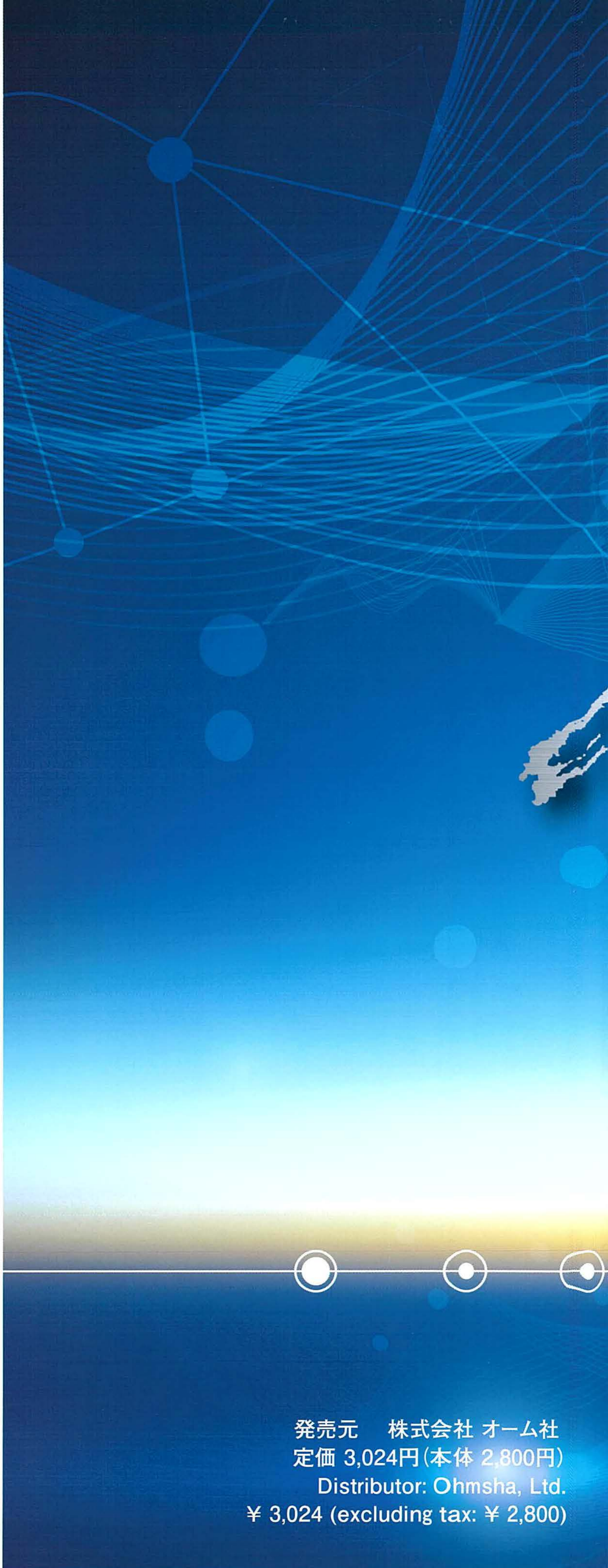

発売元　株式会社 オーム社
定価 3,024円（本体 2,800円）
Distributor: Ohmsha, Ltd.
¥ 3,024 (excluding tax: ¥ 2,800)